Dynamique et contrôle optique d'un spin individuel dans une boîte quantique

Claire Le Gall

UNIVERSITÉ DE GRENOBLE

THÈSE

Pour obtenir le grade de

DOCTEUR DE L'UNIVERSITÉ DE GRENOBLE

Spécialité : **Physique**

Arrêté ministériel : 7 août 2006

Présentée par

Claire LE GALL

Thèse dirigée par **H. Mariette**
et codirigée par **L. Besombes**

préparée au sein **de l'Institut Néel**
et de **l'Université de Grenoble**

Contrôle Optique et Dynamique d'un spin individuel dans une boîte quantique

Thèse soutenue publiquement le **4 novembre 2011**,
devant le jury composé de :

Mr Laurent SAMINADAYAR
Professeur de l'Université Joseph Fourier, Président
Mr Olivier KREBS
Chargé de Recherche CNRS au Laboratoire de Physique des Nanostructures, Rapporteur
Mr Christophe TESTELIN
Chargé de Recherche CNRS à l'Institut des Nano-Sciences de Paris, Rapporteur
Mr Denis SCALBERT
Directeur de Recherche CNRS au Groupe d'Etude des Semiconducteurs, Examinateur
Mr Henri MARIETTE
Directeur de Recherche CNRS à l'Institut Néel, Directeur de thèse
Mr Lucien BESOMBES
Chargé de Recherche CNRS à l'Institut Néel, Co-Directeur de thèse

b

UNIVERSITÉ DE GRENOBLE

THÈSE

Pour obtenir le grade de

DOCTEUR DE L'UNIVERSITÉ DE GRENOBLE

Spécialité : **Physique**

Arrêté ministériel : 7 août 2006

Présentée par

Claire LE GALL

Thèse dirigée par **H. Mariette**
et codirigée par **L. Besombes**

préparée au sein **de l'Institut Néel**
et de **l'Université de Grenoble**

Contrôle Optique et Dynamique d'un spin individuel dans une boîte quantique

Thèse soutenue publiquement le **4 novembre 2011**,
devant le jury composé de :

Mr Laurent SAMINADAYAR
Professeur de l'Université Joseph Fourier, Président
Mr Olivier KREBS
Chargé de Recherche CNRS au Laboratoire de Physique des Nanostructures, Rapporteur
Mr Christophe TESTELIN
Chargé de Recherche CNRS à l'Institut des Nano-Sciences de Paris, Rapporteur
Mr Denis SCALBERT
Directeur de Recherche CNRS au Groupe d'Etude des Semiconducteurs, Examinateur
Mr Henri MARIETTE
Directeur de Recherche CNRS à l'Institut Néel, Directeur de thèse
Mr Lucien BESOMBES
Chargé de Recherche CNRS à l'Institut Néel, Co-Directeur de thèse

d

Sommaire

Remerciements

Je tiens à remercier en premier lieu tous les membres de mon jury, pour l'intérêt qu'ils ont porté à mes travaux : Laurent Saminadayar pour avoir présidé ce jury, Denis Scalbert pour avoir accepté d'examiner cette thèse, Olivier Krebs et Christophe Testelin, pour leur lecture attentive du manuscrit et pour la pertinence de leurs remarques.

Je tiens particulièrement à remercier Lucien Besombes pour la qualité de son encadrement, son enthousiasme et ses savants conseils. Toujours disponible pour discuter de physique ou donner un coup de pouce pour les manips, il a, par son dynamisme, largement contribué à l'avancée de ma thèse. Lors de la rédaction, tu as également été remarquable par la justesse de tes remarques et ta rapidité dans les corrections. Je tiens à remercier Roman Kolodka et Adalberto Brunetti, qui sont venus en post-doc pendant un an dans notre équipe et ont participé à la réalisation de ce travail. Aussi, je tiens à remercier Henri Mariette pour sa gentillesse, son précieux soutient et la sagesse de ses conseils tout au long de mes travaux.

Ces trois ans de thèse se sont déroulées dans un cadre très agréable grâce à l'ensemble des membres de l'équipe NPSC. Je pense en particulier à Aurélien et Samir, mes colocs de bureau avec qui j'ai eu un réel plaisir à partager des discussions animées, des sessions cuisine à l'azote liquide et des bières à la bobine. Je remercie également Greg, Mathieu et Thomas, les grands frères qui terminaient leur thèse alors que j'arrivais en stage, et qui m'ont accueilli à bras ouvert. Je pense aussi à David, toujours enclin à se creuser la tête sur un problème de physique, à Signe, pour son enthousiasme, Max et Régis, les pédagogues discutant volontiers de leur travaux avec le novice ou celui qui n'est pas " du domaine ", Dang, Gilles, Jacek, Alexia, Stefano, JPP et tous les autres. Aussi, je souhaite un bon courage à ceux qui assurent la relève : Inah, Igor, Daniel, Piotr et Emilien.

Ce travail n'aurait pu aboutir sans la contribution de nombreuses personnes. Sincères remerciements pour Hervé Boukari, l'homme qui m'a fournit des échantillons de compét tout au long de ma thèse et qui sais courir sur la neige verglacée en dévers sans crampons et sans tomber. Parmi les gens extérieurs à l'équipe, je tiens à remercier Joachim Fernandez-Rossier, et Georges Bouzerar pour les explications théoriques ainsi que Benjamin Canal, pour m'avoir guidé du côté obscure de la force (le code) et avoir généreusement mis son ordi de calcul à disposition.

Enfin, cette thèse n'aurait pas été aussi heureuse sans les gens que j'ai rencontrés sur Grenoble...

Au boulot tout d'abord, les copains de la pause café, compagnons de poker, soirée nanar ou autre se reconnaitront. Et puis zut! Je vais quand même donner quelques noms... Grand Mika, Camille, Laeticia, Arno, Edouard (Et mon baptême de l'air? On se tient au jus!), Laulau,

Jérôme, Farid, les deux " Pierre M. " (le premier, pour l'approvisionnement en caféine de tout un batiment, le second pour ses encouragements et sa bienveillance), Raoul et Alexia (mes maîtres en skating), Roro (mon maître en ski de rando), Stef et Myriam (pour les déjeuner entre filles).

Mais également ceux rencontrés en dehors du boulot. Merci à Kerdon (l'homme de la situation), Merci à Mika, Noura, Albane et Flo (pour leur encouragements quotidients !), Merci à Sara, Emy, les Meltings Potes, les Bretons des grands boulevards et les Normands de Revel, et tous les autres qui m'ont accompagnés durant ces trois ans de thèse.

Enfin, un grand Merci à ma famille pour son soutient infaillible.

Introduction

The ability to control individual spins in semiconductors is a key but very challenging step for any spin-based solid-state quantum computing technology. In the last few years many techniques have been developed to initialize, manipulate and read-out the spin of individual carriers in semiconductor quantum dots. The improvement of experimental schemes allow to probe and to understand the quantum-mechanical processes which control the dynamics of a single spin.

Schematically, single-spin systems in the semi-conductor world fall into two categories: gate-defined quantum dots and optically active quantum dots. The former quantum dots are defined in a two-dimensional electron gas, where single electrons are confined using electric fields from surface gate electrodes. These quantum dots are studied electrically and coherent control of a single electron spin can be achieved using magnetic or electric fields [1, 2]. The coherent transitions between the electron states spin-up or spin-down can be performed in a few tens of ns. Coherent control over two-electron spin-states (two quantum dots with a tunnel coupling) has also been achieved in these systems. Optically active quantum dots are made of direct bang-gap semi-conductors in III-V or II-VI materials. This is the case of the samples studied in this thesis. In these systems, the optical selection rules can be used to initialize [3] and read out the spin of a resident carrier (electron [4] or hole). Remarkably, the spin of the resident carrier can be coherently manipulated on a few tens of ps time-scale using a combination of optical pulses and transverse magnetic fields [5, 6]. The coherent control of electrons and holes has been recently demonstrated in III-V MBE-grown quantum dots. However, in these system, the coherence is limited by nuclear spin effects and the charge noise bath to decoherence times ranging from several hundreds of ns to μs (depending on the dot) for resident holes [6] and electrons [7].

Alternatively, the spin of a magnetic impurity could be a promising candidate. A Manganese impurity in a II-VI crystal is a 5/2 spin with a well defined location in the crystal matrix. During the last decades, a number of studies have shown that, under magnetic field, the relaxation time of Manganese impurities in a II-VI crystal could reach the ms range for vanishing manganese-concentrations [8, 9]. The idea here, is to marry the advantages of diluted magnetic semiconductors with the atom-like optical properties of quantum dots. The manganese impurity at the center of a II-VI quantum dot is strongly coupled to the photo-created electron-hole pair. Compared to the case of a manganese impurity in a bulk crystal, this coupling, known as *spd* exchange, is further enhanced by the confinement of the photo-created electron-hole pair in the quantum dot. This coupling results in a remarkable property of the Mn-doped quantum dots: the optical spectra presents six lines, which provide a direct measurement of the Mn spin-state ($S_z = +5/2 ... -5/2$). Thanks to this single spin read-out, we have explored, in this thesis, the dynamics of a single Mn spin by optical means.

This manuscript is organized as follows:

In Chapter 1, we try to give a comprehensive presentation of the spectral properties of Mn-doped CdTe/ZnTe quantum dots. In order to do so, we will start with a description of the center of the Brillouin zone of II-VI semiconductors, non-magnetic semiconductor quantum-dots, and bulk diluted magnetic semiconductors. The elements of theory presented in these three topics will hopefully allow the reader to understand all the subtleties of Mn-doped quantum dots spectra.

In Chapter 2, we present our samples and the experimental techniques that were used throughout this thesis to study dynamical properties of Mn-doped quantum dots. We will report on the experimental evidence of photo-induced spin orientation of the localized Mn spin. In other words, we will show that the Mn-spin can be optically initialized and read-out.

In Chapter 3, we develop pump-probe experiments and use magnetic fields to explore the dynamics of the Mn spin alone. We investigate on the relaxation time of the Mn spin at $B = 0T$, and on the coherent evolution of the Mn atom in a strained crystal field. We will demonstrate that the coherent coupling of the Mn spin to its environment is essential to perform Mn-spin initialization at zero magnetic field.

In Chapter 4, we develop PLE experiments and perform a detailed study of the photo-induced orientation process to extract information on the microscopic mechanism controlling the initialization process. We will discuss possible mechanisms. A spin-flip of the hole is likely involved in the orientation process; however, we will evidence other relaxation channels within the XMn states, whose physical origin need to be clarified.

In Chapter 5, we will evidence strong coupling between the transition dipole of a Mn-doped quantum dot and a resonant continuous optical field. The results can be well understood in the dressed atom picture. We place ourselves in an experimental configuration where the strong coupling is detected from another level than the ones resonantly driven. This allows to evidence optical Stark shift of the Mn spin-states.

In Chapter 6, at last, we will study CdTe/ZnTe quantum dots with a resident electron. We investigate in the latter the electron-nuclear spin bath interaction. We will evidence that depolarization of the resident electron by a non-polarized nuclei ensemble is also an issue in this system. However, we will show that this depolarization can be bypassed thanks to the creation of dynamic nuclear spin polarization.

Introduction (French)

Notre habilité à contrôler un spin unique localisé dans un semi-conducteur est une étape clef vers le stockage d'information quantique. Ces dernières années ont vu l'essor des techniques de contrôle qui visent in fine à initialiser, manipuler et lire l'état d'un seul spin. En physique du solide ce spin individuel peut être un porteur confiné dans une boite quantique ou une impureté du cristal comme par exemple les centres colorés dans le diamant qui ont connu un réel engouement ces dernières années, et des développements expérimentaux considérables [10]. Le progrès de ces techniques expérimentales permet de comprendre et de sonder toujours plus finement les processus physiques qui régissent la dynamique d'un spin unique.

Le contrôle d'un spin individuel dans le monde des boites quantiques se classe de façon schématique en deux catégories suivant que le spin est adressé par des méthodes de transport ou par des moyens optiques. De façon générale, le confinement des porteurs est obtenu en utilisant deux semi-conducteurs de structure de bande différente: le matériau de plus petit gap agissant comme un puits de potentiel pour les porteurs. La réduction de la taille de ce puits de potentiel dans une direction permet de quantifier les niveaux d'énergie des porteurs.

En transport, le contrôle cohérent sur un spin unique a été démontré [1, 2]. Dans ce système, le confinement d'un électron individuel dans un petit volume du cristal est obtenu en combinant un confinement 1D (gaz bidimensionnel d'électron créé a l'interface entre GaAs/AlGaAs) avec des champs électriques créés par des électrodes posées sur la surface de l'échantillon typiquement 100 nm au-dessus du gaz 2D d'électrons. Par des méthodes de transport (mesure de courant dépendant de l'état de spin de l'électron résident dans la boite [1]), le contrôle cohérent sur un spin unique a été démontré. Le moyen le plus évident pour réaliser ce contrôle est d'utiliser des champs magnétiques: un champ magnétique statique qui lève la dégénérescence entre un état up et un état down, et un champ magnétique radiofréquence pulsé, dont l'amplitude et la phase permettent de créer n'importe quelle superposition d'état[2]. De façon plus indirecte, un champ électrique peut également être utilisé pour réaliser un contrôle cohérent [1]; l'action du champ électrique sur le spin étant médiée par l'interaction spin-orbite.

En optique, les nanostructures étudiées pour le contrôle cohérent d'un spin unique sont des boites quantiques auto-organisées où le matériau de plus petit gap va, dans des conditions de croissance bien choisies, spontanément former des ilots dans lesquels les porteurs sont confinés

[1] La méthode d'initialisation et de lecture repose sur l'utilisation de deux boites quantique couplées: une boite sur laquelle est réalisé le contrôle de spin, et une boite sonde. Pour la lecture, on fait tunneler l'électron résident de la boite étudiée vers la boite quantique sonde qui contient un électron résident de spin connu. D'après le principe de Pauli, l'énergie de l'état à deux électrons va être inferieure si les deux électrons sont de spins antiparallèles (singulet). Cette différence d'énergie entraine l'existence d'un courant tunnel seulement si l'électron mesuré a un spin opposé à celui situé dans la boite sonde

dans les trois directions. Dans ces systèmes, les règles de sélection optiques permettent de préparer par pompage optique [3] et de lire l'état de spin d'un porteur confiné dans la boite (électron [4] ou trou). Le contrôle cohérent de l'électron et plus récemment du trou ont été démontré [5, 6]. Dans le cas d'un électron résident par exemple, un photon polarisé $\sigma+$ ne peut être absorbé que par un électron up selon l'axe de croissance (axe z). Ainsi, une impulsion polarisée $\sigma+$ fortement désaccordée de la transition de la boite peut être utilisée pour ajouter une phase θ à l'état de spin up (effet Stark optique discuté au chapitre 5). Un état $\Psi = \alpha\uparrow + \beta\downarrow$ devient $\alpha\uparrow + e^{i\theta}\beta\downarrow$: l'impulsion optique est équivalente a un champ magnétique dirigé selon z qui permet de faire tourner le vecteur de Bloch en quelques fs autour de l'axe de croissance. Un champ magnétique extérieur perpendiculaire à z (notons le B_x) permet de faire précesser le spin selon l'axe x (période pouvant typiquement atteindre 10 ps). La rotation du spin de l'électron autour de deux axes distincts permet d'atteindre de façon contrôlée n'importe quel état de la sphère de Bloch.

Cependant, dans les systèmes décrit jusqu'ici, la cohérence est limitée par la présence de spins nucléaires (les noyaux dépolarisés d'une boite quantique couplés par interaction hyperfine au spin du porteur, agissent comme un champ magnétique aléatoire qui perturbe le spin électronique), de phonons (qui perturbent le spin via l'interaction spin-orbite et dont l'effet augmente avec la présence d'un champ magnétique extérieur en raison de l'augmentation de la densité de phonons à l'énergie nécessaire pour passer d'un état de spin à l'autre). Ces interactions avec l'environnement limitent la cohérence à des temps de l'ordre de quelques centaines de ns à quelques microsecondes pour des électrons [7] ou des trous résidents [6].

Au lieu d'utiliser le spin des porteurs résidents, une alternative serait d'utiliser le spin d'une impureté magnétique. Par exemple un atome de manganèse dans un cristal semi-conducteur II-VI constitue un spin 5/2, localisé, avec des temps de relaxation sous champ magnétique pouvant atteindre la ms [2][8, 9]. L'idée est de marier les propriétés de ce spin aux propriétés optiques des boites quantiques. Le spin d'un atome de manganèse situé dans une boite quantique II-VI (CdTe/ZnTe) est fortement couplé à la paire électron-trou photo-créée. Ce couplage vient d'une interaction d'échange (dite spd) entre l'électron, le trou et le spin 5/2 (électrons $3d^5$ du Mn). Dans une boite quantique, ce couplage, proportionnel à la probabilité de trouver l'électron ou le trou sur le Mn est fortement exacerbé par le confinement. Ces interactions d'échange modifient l'énergie d'émission de la boite quantique suivant l'état de spin du Mn: moyenné dans le temps, le spectre d'une boite quantique magnétique possède 6 raies : chacune correspondant, pour une polarisation donnée, à un état de spin du Mn ($S_z = +5/2 ... -5/2$). Allant ainsi sonder optiquement l'état de spin du Mn, nous avons dans cette thèse exploré la dynamique d'un spin unique.

Ce manuscrit est organisé comme suit:

Dans le premier chapitre, nous présentons les fondements théoriques et expérimentaux utiles à la compréhension du système Manganèse dans une boite quantique. Pour ce faire, nous commencerons par une description de la zone de Brillouin en nous attachant particulièrement à l'effet de contraintes inhérentes aux boites-quantiques auto-assemblées. Nous en déduirons les propriétés optiques des boites quantiques (cas simple des boites sans Mn). Puis, nous présenterons quelques résultats du vaste sujet d'étude que sont les semiconducteurs magnétiques dilués,

[2] d'après des mesures d'ensembles sur des échantillons de faible concentration en Mn, ou les impuretés de manganèse sont suffisamment éloignées les unes des autres pour avoir un comportement analogue a celui d'un spin unique dans la matrice cristalline

pour discuter de l'interaction d'échange *spd* entre l'électron le trou et l'atome de manganèse. Ce premier chapitre devrait permettre au lecteur de comprendre la richesse et la diversité des propriétés spectrales de ces boites magnétiques.

Dans le deuxième chapitre, nous présentons la fabrication des échantillons et le montage de micro-photoluminescence résolue en temps qui nous a permis d'étudier les propriétés dynamiques des boites quantiques dopées Mn. Nous mettons en évidence la possibilité d'initialiser le spin de Mn par l'injection de porteurs polarisés ou l'excitation résonnante sur un des états de spin (pompage optique).

Dans le troisième chapitre, nous développons des expériences pompe-sonde résolues en temps, et une étude en champ magnétique du processus de pompage optique, dans l'idée de mieux comprendre la dynamique du Mn lorsqu'il est seul dans la boite. Nous nous intéresserons à son temps de relaxation en champ nul et à l'évolution cohérente d'un spin de Mn dans un environnement cristallin contraint (ce qui est le cas des boites étudiées ici). Nous verrons que la prise en compte de ce champ cristallin contraint est essentielle pour expliquer l'observation d'une initialisation du Mn en champ nul.

Dans le quatrième chapitre, nous discutons de la dynamique du système exciton-manganèse, qui contrôle le processus d'initialisation. Afin d'identifier un mécanisme microscopique d'orientation, nous réalisons une étude en puissance du mécanisme de pompage et mettons en évidence des canaux de relaxation de spin au sein du complexe exciton-Manganèse. Nous discuterons en nous appuyant sur ces études expérimentales, des mécanismes possibles.

Dans le chapitre 5, nous mettrons en évidence l'habillage par un champ laser d'une des transitions optiques d'une boite quantique magnétique. C'est la signature d'un couplage cohérent entre un laser continu et la transition d'une boite quantique dopée Mn, qui est rappelons-le, liée a un état de spin du Mn. Cette observation expérimentale implique, qu'à l'instar de l'électron et du trou, une impulsion laser pourrait être utilisée pour contrôler la rotation du spin de Mn selon l'axe optique. Le contrôle du manganèse par l'utilisation d'impulsions lumineuses et d'un champ magnétique transverse a d'ailleurs été proposé théoriquement [11]. Sa réalisation expérimentale est pour l'instant ardue (un problème de taille est notamment l'initialisation en champ transverse), mais s'inscrirait dans la suite de ce travail.

Enfin, dans le chapitre 6, nous étudions des boîtes CdTe/ZnTe possédant un électron résident. Nous nous intéressons au couplage de cet électron aux spins nucléaires de la boite. Nous montrons que la relaxation du spin de l'électron par un bain de noyaux non-polarisés est également rapide dans les boites II-VI. Cependant, nous montrons que cette décohérence peut être évitée grâce à la création d'une polarisation dynamique nucléaire dont nous étudions la dynamique de formation et de relaxation par des mesures du taux de polarisation de la photoluminescence résolue en temps.

Résumé (French)

Chapitre 1

Le manganèse est un dopant iso-électronique dans les semi-conducteurs II-VI. Cette impureté a éveillé l'intérêt de la communauté scientifique dès les années 70, avec la découverte de l'effet Zeeman géant : l'évolution en champ magnétique de l'énergie d'émission de l'exciton dans un semi-conducteur magnétique dilué présente un effet Zeeman plus important que prévu du au champ effectif créé par la polarisation sous champ des impuretés magnétiques présentent dans le cristal. Ce champ effectif résulte des interactions d'échanges entre les porteurs et les électrons localisés du Manganèse.

L'introduction d'un atome magnétique dans une boîte quantique permet de localiser des porteurs, et offre donc la possibilité de faire interagir de façon contrôlée un spin unique avec ces derniers. Les boîtes quantiques sont souvent surnommées atomes artificiels, en raison de la quantification des niveaux d'énergie de la paire électron-trou, qui résulte en des raies d'émission et d'absorption à des énergies discrètes. Les propriétés optiques d'une boite quantique sont intimement liées à la structure de bande du semi-conducteur. La bande de conduction possède un moment orbital nul : un électron est une quasi-particule de spin 1/2. En revanche, la bande de valence possède un moment total $J = 3/2$, et donc le trou possède a priori quatre états de spin possible. Dans une boîte quantique, en raison de la forme du confinement (Hamiltonien de Luttinger) et de la présence de contraintes biaxiales (Hamiltonien de Bir et Pikus), les états $\pm 1/2$ (trous légers) sont rejetés à plus haute énergie. Ainsi, au degré d'approximation le plus bas (approximation du trou lourd), le trou confiné dans une boîte quantique possède un spin anisotrope $J_z = \pm 3/2$. En fait, cette approximation est souvent insuffisante pour expliquer les propriétés magnéto-optiques de nos boîtes. Comme l'ont montré Y. Léger, L. Besombes *et al.* [12], le mélange trou lourd-trou léger peut typiquement atteindre 20% dans les boîtes étudiées ici à cause d'une anisotropie des contraintes et du potentiel de confinement.

Dans l'approximation du trou lourd, le trou agit comme un champ magnétique effectif, fixé selon z, qui par l'interaction d'échange électron-trou lève la dégénérescence entre des états des excitons dits brillants, et des excitons noirs. Par l'interaction d'échange trou-Manganèse (et dans une moindre mesure l'échange électron-Manganèse), l'énergie de cet exciton va aussi dépendre de l'état de spin Sz du Manganèse. Dans cette approximation du trou lourd, une boîte magnétique présente donc six raies, deux fois dégénérées (symétrie $z \longleftrightarrow -z$): l'énergie du photon émis lors de la recombinaison de la paire électron-trou dépend de l'état de spin S_z du Mn. En présence d'un mélange de bande de valence, les boites quantiques dopées Mn présentent des raies additionnelles liées à un mélange des états exciton-Mn noirs et brillants. Alors, la correspondance entre une raie d'émission et un état de spin du Mn n'est plus parfaite.

Chapitre 2 La croissance des boites II-VI n'est pas une croissance Stanski-Krastanov classique : la transition 1D-3D de la couche de CdTe est induite par la déposition de Te amorphe qui modifie l'énergie de surface et favorise la formation d'ilots. L'incorporation de Mn s'effectue

durant la croissance de CdTe. La densité surfacique de Mn est ajustée pour être égale à celle des boites, ce qui aboutit statistiquement à une proportion de boites magnétiques (un seul Mn proche du centre de la boite) de l'ordre de quelques %. L'étude d'une boite magnétique individuelle s'effectue grâce à un montage de micro-spectroscopie confocale. L'échantillon est placé dans un cryostat à doigt froid (5K), surmonté d'une lentille à immersion solide, afin d'augmenter l'efficacité de collection.
Afin de mettre en évidence le contrôle optique d'un spin de Manganèse, nous avons développé une mesure résolue en temps de la population (mesure statistique) d'un état de spin du Mn sous excitation modulée en polarisation ($\sigma+/\sigma-$) ou en longueur d'onde (pompage optique par une impulsion résonante puis lecture par une impulsion quasi-résonante). La résolution temporelle de notre détection est fixée par le jitter de l'APD ($50ps$). Le temps de montée des éléments permettant la mise en forme des trains d'onde (AOM et EOM) se situe entre 5 et $10ns$ ce qui nous cantonne à des dynamiques plus lentes.
Dans la Figure 2.2 (p.43), nous considérons l'orientation du Mn par l'injection de porteurs polarisés, ce qui en pratique est le cas lorsque le laser est résonant avec un des états excités de la boite. Sous excitation modulée $\sigma+/\sigma-$, nous détectons la luminescence d'une raie associée à un Mn dans l'état $-5/2$. L'observation d'un transitoire dans ce signal de photoluminescence suite à un changement de polarisation de l'excitation reflète une évolution de la probabilité de détecter le Mn dans cette état. On observe une augmentation de la probabilité de détecter $-5/2$ sous excitation $\sigma+$: le Mn se polarise selon $-z$, ce qui peut s'interpréter comme une polarisation du Mn dans le champ magnétique effectif crée par le trou. Cependant, si ce mécanisme permet bien d'expliquer le sens de la polarisation effectivement observé, il est trop lent[3] pour rendre compte de la vitesse du processus (quelques dizaines de ns), ce qui correspond plutôt à une dynamique rapide médiée par une relaxation de spin des porteurs. Le pompage optique d'un état de spin (excitation résonante entrainant une déplétion de 75% de sa population d'équilibre) est également présentée dans la Fig. 2.6 (p. 49)

Chapitre 3

Ayant mis en évidence un moyen d' " initialiser " et de " lire " l'état de spin du Manganèse, nous effectuons des expériences pompe-sonde pour aller mesurer le temps de relaxation (T_1) du spin du Manganèse en l'absence d'excitation optique (Fig 3.1, p.54). Nous observons que ce temps de relaxation est supérieur à une dizaine de μs (pour des raisons expérimentales, nous n'avons pu sonder la relaxation sur des temps plus longs.), résultat encourageant pour un éventuel stockage d'information sur le spin du Mn.
Cela dit, les observations faites jusqu'alors-pompage optique et mémoire de spin en champ nul-sont en fait non-triviales. Le spin électronique du Mn n'est pas parfaitement isotrope et découplé de son environnement : d'une part, les orbitales $3d$ du Manganèse sont affectées par la présence des atomes voisins (champ cristallin); d'autre part, le spin électronique du Manganèse est couplé a son propre noyau (interaction hyperfine). En symétrie cubique (cristal non-contraint), l'Hamiltonien qui contrôle l'évolution du spin électronique du Mn (S) et du noyau du Mn (I) est donné par :

$$H_{FS} = A\vec{I}.\vec{S} + \frac{1}{6}a\left[S_x^4 + S_y^4 + S_z^4 - \frac{1}{5}S(S+1)(3S^2+3S-1)\right]$$

Où la constante hyperfine A vaut $0.71\mu eV$ et la constante de champ cristallin vaut $a = 0.36\mu eV$. Il est clair que le nombre quantique S_z n'est pas état propre de cet Hamiltonien : la

[3]Le temps de spin-flip du Mn dans le champ d'échange du trou est contrôle par l'interaction du Mn avec les phonons, ce qui aboutit à des temps supérieurs à la μs

polarisation créée selon z pendant la durée de vie de l'exciton est " effacée " en quelques ns par la précession du Mn dans le champ cristallin et le champ hyperfin. Les observations faites jusqu'ici ne semblent alors compatibles avec la théorie que si une anisotropie magnétique (terme de champ cristallin lié à la présence de contraintes biaxiales) bloque cette précession. Le terme d'anisotropie magnétique que l'on doit alors ajouter à H_{FS} s'écrit :

$$H_{Anis} = D_0 \left[S_z^2 - \frac{1}{3} S(S+1) \right]$$

Avec D_0 pouvant atteindre jusqu'à $12\mu eV$ pour une couche de CdTe parfaitement contrainte sur ZnTe. La présence d'une anisotropie magnétique dans les boites étudiées est démontrée par des mesures de pompage optique en champ magnétique faible. En substance, nous observons une faible augmentation de l'efficacité du pompage optique sous champ Faraday, ce qui indique qu'une anisotropie magnétique domine déjà l'évolution cohérente du Mn à $0T$. En champ magnétique transverse (effet Hanle), nous observons une dépolarisation du Mn contrôlée par cette anisotropie. Ces mesures nous permettent d'évaluer l'anisotropie magnétique à $6\mu eV$, valeur consistante avec une relaxation partielle des contraintes dans les boites.

Chapitre 4

Nous cherchons à mettre en évidence expérimentalement un mécanisme microscopique permettant d'expliquer l'orientation du Manganèse. A cette fin, nous nous intéressons aux processus de relaxation de spin au sein du complexe XMn : une excitation laser est balayée sur les transitions haute-énergie du complexe XMn, tandis que nous détectons la photoluminescence des transitions basse énergies (expérience de PLE). Nous mettons ainsi en évidence que les canaux de relaxation dominant font intervenir le spin-flip de deux particules simultanément (électron-trou ou trou-Mn ou encore électron-Mn). La dépendance de ces processus avec l'écart énergétique entre les deux niveaux XMn impliqués semblent indiquer qu'ils sont médiés par les phonons. Cependant, le calcul des taux de spin-flips induits par l'action conjointe des phonons et de l'interaction courte-portée conduit a des temps de spin-flip trop longs pour expliquer nos observations, et l'origine physique de ces processus mériterait d'être creusée.
Nous discutons ensuite des mécanismes d'orientation possibles. Récemment, la relaxation du spin du trou a été invoquée comme pouvant être responsable du processus de photo-orientation. Cependant, l'observation d'une dominance de processus de spin-flips à deux particules sous excitation résonante nous pousse à présenter un autre mécanisme possible pour expliquer l'orientation du Mn sous excitation résonante. Il nous semble que de plus amples investigations sont nécessaires pour trancher la question.
Enfin, nous terminons par une étude en puissance du processus d'orientation du Mn sous excitation résonante sur un des états du complexe XMn et sous excitation résonante sur un état excité de la boite. Nous montrons que l'injection de porteurs sur un état excité conduit à une orientation significativement plus rapide que sous excitation résonante. Ce résultat peut être lie à une relaxation du spin du trou lors de la relaxation vers le niveau fondamental de l'exciton.

Chapitre 5

Nous présentons ensuite l'habillage par un champ laser des transitions optiques d'une boite quantique magnétique (Fig 5.2, p.92). Cette expérience a pu être réalisée grâce à l'utilisation d'un laser monomode et peut être décrite quantitativement (étude en puissance et en fonction du désaccord avec la transition) par le formalisme de l'atome habillé : La présence d'un champ laser couple de façon cohérente l'état fondamental de la boite à un état XMn par absorption et émission stimulée, ce qui résulte en un dédoublement de Rabi de chacun des deux niveaux

de la transition. Ce dédoublement est proportionnel au couplage dipolaire électrique entre la transition et le laser, et est donc proportionnel à l'amplitude du champ électrique i.e. à la racine carrée de la puissance. La fluorescence résonante d'une transition habillée donne ainsi lieu au triplet de Mollow.
Ici, nous mettons en évidence l'éclatement de Rabi à l'aide d'une seconde transition-peuplée par un laser non-résonant- qui partage un niveau avec la transition habillée : nous détectons un doublet d'Autler-Townes. Nous atteignons à résonance des éclatements de Rabi de l'ordre de 300 μeV. Nous montrons ainsi que chaque état de spin du manganèse peut être adressé individuellement, nonobstant le mélange noir-brillant induit par les termes non-diagonaux d'échange trou-Mn ou électron-Mn. Ces résultats constituent, comme détaillé dans l'introduction, une démonstration importante en vue du contrôle cohérent du spin du Mn dans une boite quantique par des moyens optiques.

Chapitre 6

Enfin, nous quittons les boites quantiques magnétiques pour des boites quantiques contenant un électron résident. Ce système nous a permis d'étudier la dynamique du système électron-noyaux, assez mal connue pour des boites II-VI. La présence d'un (seul) électron résident dans les boites étudiées est confirmée par la présence en PLE de la structure fine du trion chaud résolue en polarisation. A des énergies d'excitation supérieures, nous observons un taux de polarisation négatif, lié à la dynamique d'injection et de relaxation des porteurs photo-créés. Nous mettons en évidence cette dynamique par l'étude résolue en temps du taux de polarisation sous excitation pulsée. Cette dynamique, contrôlée par les interactions d'échanges électrons-trou et des processus de relaxation de spin, est analysée quantitativement afin d'en extraire des grandeurs physiques. En particulier, les constantes d'échanges trouvées sont consistantes avec celles trouvées dans la littérature pour des systèmes analogues.
Dans un deuxième temps, nous nous focalisons plus spécifiquement sur les effets liés aux noyaux. Nous mettons d'abord en évidence la relaxation du spin électronique induite par les fluctuations du champ Overhauser, et la possibilité de l'éviter grâce à la création d'une polarisation nucléaire dynamique ou à l'utilisation d'un champ magnétique extérieur. La construction d'une polarisation nucléaire est directement observée en champ nul et sous faible champ extérieur. Celle-ci est plus rapide (d'un facteur 10^3) que dans les boites III-V. Nous imputons ceci au faible volume de nos boites. Nous nous sommes également intéressés au temps de relaxation de la polarisation nucléaire et à son évolution sous faible champ. Un effort théorique reste à faire pour comprendre certaines de nos observations.

Chapter 1

A Mn spin in a CdTe/ZnTe Quantum Dot: Single Spin Addressing

Contents

The purpose of this chapter is to present the physical properties of CdTe/ZnTe quantum dots containing a single Mn atom. We begin with a description of the bulk properties of CdTe and ZnTe, focusing on the band extrema. We detail the conduction and valence states at $k = 0$, we present elements of $k.p$ theory and the Luttinger Hamiltonian and we discuss the effect of strains, which are described using the Bir-Pikus Hamiltonian. Then, we describe carrier confinement, energy level structure and the optical properties of a semiconductor quantum dot. The energy levels structure is strongly modified by the exchange interactions between the confined carriers. We present these exchange interactions and how the geometry of the confining potential and the strain environment affect them, and affect the optical spectra. At last, we discuss the origin of the interaction of photo-created carriers with the magnetic moment of an isolated manganese atom, and present the optical spectra of a Mn-doped quantum dot. The spin operators used in this Chapter are resumed in Appendix A.

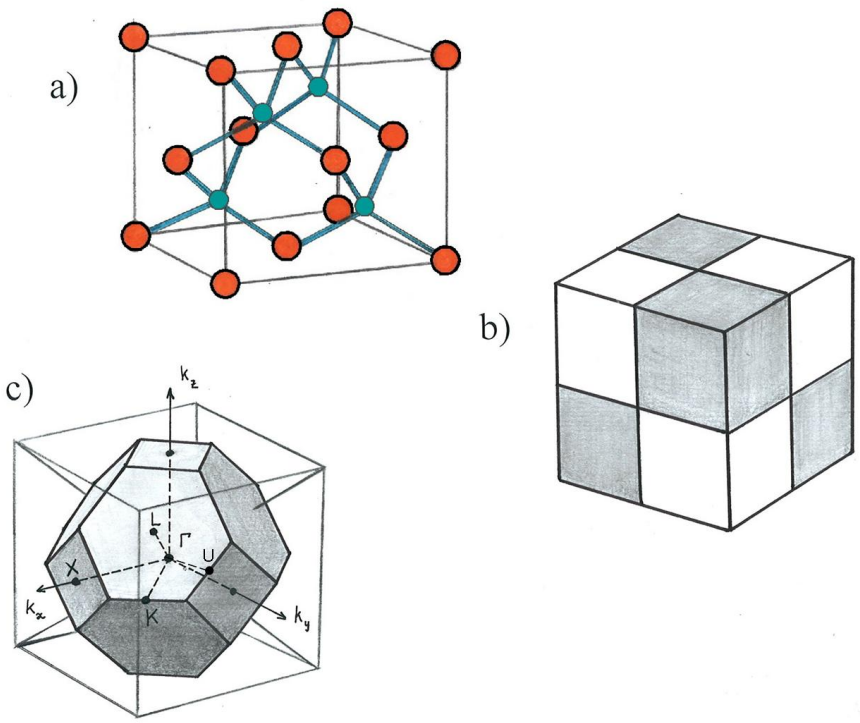

Figure 1.1: (a) Elementary cell of a CdTe or ZnTe (Zinc-Blende structure).(b) Illustration of the T_d symmetry. (c) Brillouin zone of the CdTe crystal, and main points in $2\Pi/a$ unit: $\Gamma = (0,0,0)$, $X = (1,0,0)$,$L = (1/2,1/2,1/2)$, $K = (3/4,3/4,0)$ and $U = (1/4,1,1/4)$.

1.1 II-VI Semiconductors

This paragraph aims at giving a quick introduction to semiconductor physics, presenting the band structure of CdTe. CdTe and ZnTe belong to II-VI materials, so called because they are comprising elements of group II and group VI of the Periodic Table. They are insulators at $0K$, and present a small gap ($1.6eV$ for CdTe and $2.3eV$ for ZnTe). As part of direct band gap semiconductors, radiative recombination is the dominant process for free carrier relaxation and their physical properties can be investigated through optical experiments.

1.1.1 Band Structure of CdTe and ZnTe

These materials present a Zinc-Blende structure (Fig. 1.1): each atomic species is on a face-centered cubic crystal, one of the lattice is shifted from the other by a quarter of the [111] diagonal. Hence, the environment of each atom is tetrahedral and the space-group of the zinc-blende structure is T_d.

The band structure of these semi-conductors can be intuitively understood if we consider the linear combination of atomic orbitals from the valence electrons of the cation ($4d^{10}5s^2$ for Cd or $3d^{10}4s^2$ for Zn) and the anion ($4d^{10}5s^25p^4$ for Te): the s level and three p levels of each atom hybridize to form eight levels out of which four are bonding and four are anti-bonding. A crystal with N unit cell presents $8N$ valence electrons. $2N$ fill the lowest band issued from s-atomic states and $6N$ fill the 3 bands issued from p-atomic states. At higher energy, the first empty

band (i.e. bottom of the conduction band) is issued from the anti-symmetric combination of the s-atomic levels and 3 bands issued from the anti-bonding combination of p states at even higher energies. At the Γ point (center of the Brillouin zone), the T_d symmetry of the crystal does not 'affect' s and p orbitals (it does not mix them or lift up the degeneracy between the p levels, contrary to d levels), so that we can still reason as if the symmetry was spherical, and attribute an 'orbital momentum' L to the band-states ($L = 1$ for the top of the valence band and $L = 0$ for the bottom of the conduction band). A more elaborate approach would be to use group theory, the extrema of each band can be described by a representation of the T_d group corresponding to their symmetry Γ_1 (resp. Γ_5) for bands issued from s (resp p) atomic states.

If we now include Spin-Orbit coupling, the conduction band extrema takes the name Γ_6 (now that the 1/2 spin is included, the eigenstates acquire a π phase in a 2π rotation, contrary to Γ_1 eigenstates which are unchanged); and (similarly to angular momentum composition in atom physics) the valence band maximum with $L = 1$ is split into a quadruplet with $J = 3/2$ (Γ_8) and at lower energy, a doublet with $J = 1/2$ (Γ_7). The energy splitting at the Γ point between the valence band and the split-off band Γ_7 is $\approx 0.9eV$ for CdTe and ZnTe. The valence band eigenstates at the Γ point can be expressed as a function of the three electronic states $|X\rangle$, $|Y\rangle$, $|Z\rangle$ and the spin-states $|+\rangle$, $|-\rangle$. Eigenstates of $L_z = 0, \pm 1$ are:

$$\begin{aligned} |+1\rangle &= -\frac{|X\rangle + i\,|Y\rangle}{\sqrt{2}} \\ |0\rangle &= |Z\rangle \\ |-1\rangle &= \frac{|X\rangle - i\,|Y\rangle}{\sqrt{2}} \end{aligned} \tag{1.1}$$

And composition with the 1/2 spin leads to:

$$\begin{aligned} \Gamma_8: \quad \left|\frac{3}{2},\frac{3}{2}\right\rangle &= |+1\rangle\,|+\rangle \\ \left|\frac{3}{2},\frac{1}{2}\right\rangle &= \sqrt{\frac{2}{3}}\,|0\rangle\,|+\rangle + \sqrt{\frac{1}{3}}\,|+1\rangle\,|-\rangle \\ \left|\frac{3}{2},-\frac{1}{2}\right\rangle &= \sqrt{\frac{2}{3}}\,|0\rangle\,|-\rangle + \sqrt{\frac{1}{3}}\,|-1\rangle\,|+\rangle \\ \left|\frac{3}{2},-\frac{3}{2}\right\rangle &= |-1\rangle\,|-\rangle \end{aligned} \tag{1.2}$$

$$\begin{aligned} \Gamma_7: \quad \left|\frac{1}{2},\frac{1}{2}\right\rangle &= \sqrt{\frac{2}{3}}\,|1\rangle\,|-\rangle + \sqrt{\frac{1}{3}}\,|0\rangle\,|+\rangle \\ \left|\frac{1}{2},-\frac{1}{2}\right\rangle &= \sqrt{\frac{2}{3}}\,|-1\rangle\,|+\rangle + \sqrt{\frac{1}{3}}\,|0\rangle\,|-\rangle \end{aligned} \tag{1.3}$$

These eigenstates give directly the optical selection rules at $k = 0$ in the semiconductor, but we will come back to that later. We are now going to focus on the non-trivial behavior of the Γ_8 band, near $\vec{k} = 0$[4]. Near the band edge, and for a given direction $\vec{k}$ the curvature of the energy $E(\vec{k})$ of the bands can be described by an effective mass $m_v(\vec{k})$:

[4]We limit our discussion to the few % of the Brillouin zone near $k = 0$ that are relevent k's in Quantum Dots.

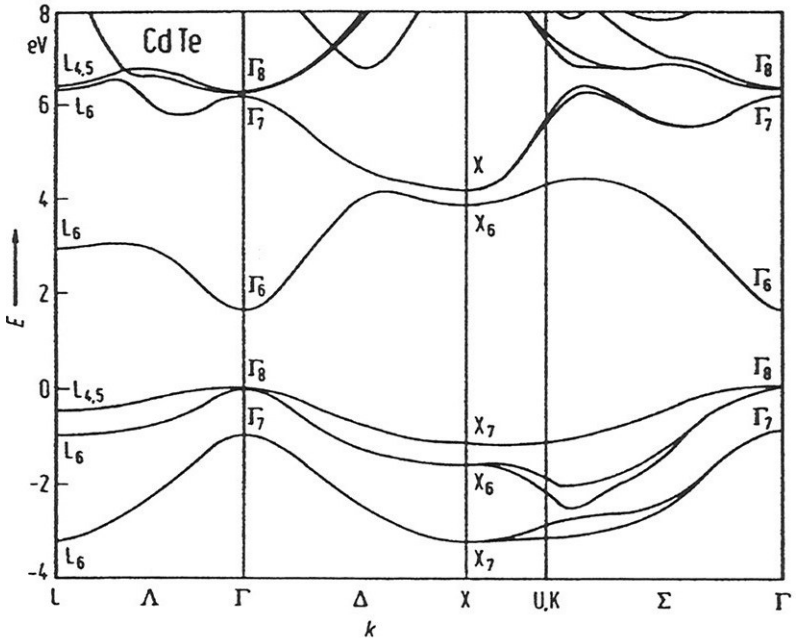

Figure 1.2: Band structure of CdTe

$$E_v(\vec{k}) \quad = \quad -\frac{(\hbar k)^2}{2m_v(\vec{k})} \tag{1.4}$$

As shown Fig. 1.2, as we move out from the Γ point, the valence band splits into two branches. The one with the smallest curvature (and highest mass) is called the heavy-hole band, the other is the light-hole band.

The difference of curvature can be understood in the so-called $\vec{k}.\vec{p}$ approximation, which was first proposed by Kane in 1957 [13]. The Kane model permits to estimate the electronic band structure starting from the exact solution and energy levels of the Schrödinger equation at the center of the Brillouin zone (i.e. we suppose in the following that $\psi_{n,0}$ and $E_{n,0}$ are known). We are looking for the solutions $\psi_{n,\vec{k}}$ to the equation:

$$\left(\frac{p^2}{2m_0} + U(\vec{r})\right)\psi_{n,\vec{k}} = E_{n,\vec{k}}\psi_{n,\vec{k}} \tag{1.5}$$

where n is the band index, $\vec{p}$ is the $-i\hbar\vec{\nabla}$ operator, $U(\vec{r})$ is the potential of the crystal and $\psi_{n,\vec{k}}$ is the Bloch wave, which is the product of a periodic part $u_{n,\vec{k}}(\vec{r})$ and a plane-wave $e^{i\vec{k}\vec{r}}$. The gradient of $\psi_{n,\vec{k}}$ is:

$$\vec{\nabla}\psi_{n,\vec{k}}(\vec{r}) = e^{i\vec{k}\vec{r}}\vec{\nabla}u_{n,\vec{k}}(\vec{r}) + i\vec{k}\psi_{n,\vec{k}}(\vec{r}) \tag{1.6}$$

Therefore, equ. 1.5 is equivalent to:

$$H_{kp}u_{n,\vec{k}}(\vec{r}) = \left(\frac{p^2}{2m_0} + U(\vec{r}) + \frac{\hbar^2k^2}{2m_0} + \frac{\hbar}{m_0}\vec{k}.\vec{p}\right)u_{n,\vec{k}}(\vec{r}) = E_{n,\vec{k}}u_{n,\vec{k}}(\vec{r}) \tag{1.7}$$

Then, Kane's idea is to expand $u_{n,\vec{k}}$ on the $\{u_{n,0}\}_n$ basis: $u_{n,\vec{k}} = \sum_{n'} c_{n'} u_{n',0}$. Under the assumption that we know the exact solutions $u_{n,0}(\vec{r})$, we can calculate the following matrix elements:

$$\langle u_{n,0} | H_{kp} | u_{n',0} \rangle = \left(E_n + \frac{\hbar^2 k^2}{2m_0} \right) \delta_{n,n'} + \left\langle u_{n,0} \left| \frac{\hbar}{m_0} \vec{k}.\vec{p} \right| u_{n',0} \right\rangle \tag{1.8}$$

The $\{u_{n,0}\}_n$ basis is infinite. In practice, we have to consider a limited number of n. In his original work, Kane limited his calculation to 8 bands : he calculated the matrix elements for $u_{n,0}$ belonging to the Γ_7, Γ_8 valence band, and the Γ_6 conduction band. Here, to illustrate the difference of curvature within the Γ_8 band, we will only consider the Γ_8 and Γ_6 bands[5] and a $\vec{k}$ in the [001] direction (equivalent to the dispersion of $E(k)$ along the $\Gamma \to X$ path). A natural basis is:

$$u_{\Gamma_8,+3/2},\ u_{\Gamma_8,+1/2},\ u_{\Gamma_8,-1/2},\ u_{\Gamma_8,-3/2},\ u_{\Gamma_6,\uparrow},\ u_{\Gamma_6,\downarrow};$$

where $\uparrow$, $\downarrow$ correspond to the spin of the Γ_6 states, and $\pm 3/2$,$\pm 1/2$, the angular momentum projection J_z of the Γ_8 states. The diagonal terms are simply equal to $E_i + (\hbar k_z)^2/2m_0$ where $E_i = E_v$ for a Γ_8 state, and E_c for a Γ_6. The non-diagonal terms are given by the matrix elements of the type:

$$\left\langle u_{\Gamma_6,\downarrow} \left| \frac{\hbar}{m_0} k_z p_z \right| u_{\Gamma_8,+1/2} \right\rangle = \frac{\hbar}{m_0} k_z \left\langle u_{\Gamma_6,\downarrow} | p_z | u_{\Gamma_8,+1/2} \right\rangle \tag{1.9}$$

These matrix elements are trivial in the basis $|X\rangle$, $|Y\rangle$, $|Z\rangle$ and $|S\rangle$. Only one matrix element is different from zero, we name it Π:

$$\begin{aligned} \langle S | p_z | Z \rangle &= \Pi \\ \langle S | p_z | Y \rangle &= 0 \\ \langle S | p_z | X \rangle &= 0 \end{aligned}$$

Then, using the definitions given in Equs. 1.1, 1.2, the calculation of 1.9 is straightforward. Only few non-diagonal matrix elements are different from zero. These matrix elements couple the $u_{\Gamma_8,\pm 1/2}$ states with the conduction band states, and the problem reduces to the diagonalization of a 2×2 Hamiltonian H' in the subspaces $u_{\Gamma_8,-1/2}, u_{\Gamma_6,\downarrow}$ or $u_{\Gamma_8,+1/2}, u_{\Gamma_6,\uparrow}$:

$$H'_{k_z p_z} = \begin{pmatrix} E_v + \frac{\hbar k_z^2}{2m_0} & \frac{\sqrt{2}\hbar}{\sqrt{3}m_0} \Pi k_z \\ \frac{\sqrt{2}\hbar}{\sqrt{3}m_0} \Pi^* k_z & E_c + \frac{\hbar k_z^2}{2m_0} \end{pmatrix} \tag{1.10}$$

Treating the non-diagonal term as a perturbation yields at the second order:

$$\begin{aligned} E_c(k_z) &= E_c + \frac{\hbar^2 k_z^2}{2m_0} + \frac{2}{3} \frac{\hbar^2 |\Pi|^2 k_z^2}{m_0^2 (E_c - E_v)} \equiv E_c + \frac{\hbar^2 k_z^2}{2m_c} \\ E_{v,\pm\frac{1}{2}}(k) &= E_c + \frac{\hbar^2 k_z^2}{2m_0} - \frac{2}{3} \frac{\hbar^2 |\Pi|^2 k_z^2}{m_0^2 (E_c - E_v)} \equiv E_v - \frac{\hbar^2 k_z^2}{2m_{lh}} \\ E_{v,\pm\frac{3}{2}}(k) &= E_v + \frac{\hbar^2 k_z^2}{2m_0} \end{aligned} \tag{1.11}$$

[5] Mathematically, the Γ_7 valence band cannot be neglected: its contribution to the curvature of the Γ_6 band is only ≈ 4 times smaller than the one we are about to calculate.

We see from these equations 1.11 that due to the $k_z p_z$ coupling, the $|\pm 1/2\rangle$ doublet from Γ_8 and the Γ_6 band repel each other. This results in an effective mass m_c for the electron[6] which is approximately ten times smaller than m_0, and for the light hole band, an effective mass m_{lh} close to the one of the conduction electrons. In practice, the value of Π used to calculate the effective mass is known experimentally (the same matrix element rules the optical properties of the semiconductor). However, we see that the treatment at this point is too rough: the heavy-hole band has the positive curvature of a conduction band! This is because we should take into account the coupling between this band and higher conduction bands, which will repel it and give a negative curvature. This curvature will be smaller (i.e. the effective mass will be higher) since the levels are further away. Moreover, the $\vec{k}.\vec{p}$ theory permits to calculate the wave-functions at $k \neq 0$. For instance, in the limit of small k_z (and still neglecting the Γ_7 band), the wave-function of the conduction-band is given by:

$$u_{\Gamma_6,k_z,\uparrow} = u_{\Gamma_6,\uparrow} + \sqrt{\frac{2}{3}} \frac{\hbar \Pi^* k_z}{m_0 (E_c - E_v)} u_{\Gamma_8,+1/2} \tag{1.12}$$

The diagonalization of the Hamiltonian (like the one given in Eqn. 1.10) gives the dispersion beyond the parabolic approximation (i.e. beyond the effective mass approximation). Including more bands (typically 30), one can predict accurately the dispersion of the bands in a large region of the Brillouin zone [14]. In particular, we see in Fig. 1.2, that the curvature of the Γ_8 band is highly anisotropic (it is quite clear if we compare the dispersion along the $\Gamma \to X$ and $\Gamma \to L$ path). This so-called warping of the valence band is described by $\vec{k}.\vec{p}$ calculations.

In the previous discussion, if we had considered a $\vec{k}$ along the [100] axis, without changing the spin-quantization axis (along z), we would have found a Hamiltonian H_{kp} much more complicated. We know from symmetry that the eigenvalues would be the same, but the eigenstates would not be simple combination of the ($u_{\Gamma_8,\pm 1/2}$, $u_{\Gamma_8,\pm 3/2}$). This means we cannot attribute an effective mass to a given Γ_8-state. Even for small $\vec{k}$'s, we have to describe them as a whole, taking in account all the Γ_8 wave-functions at $k = 0$ (i.e. using a sort of effective-mass matrix in the Γ_8 subspace).

1.1.2 Description of the Γ_8 band around $k = 0$: The Luttinger Hamiltonian

Rather than diagonalizing a $k.p$-Hamiltonian for each $\vec{k}$, the matrix describing the Γ_8 can be found using symmetry considerations. As shown by Luttinger in 1956 using group theory [15], the only Hamiltonian fulfilling the cubic symmetry is:

$$H_L = -\frac{\hbar^2}{2m_0} \left(\gamma_1 k^2 I_4 - 2\gamma_2 \sum_i k_i^2 \left(J_i^2 - \frac{1}{3} J^2 \right) - 2\gamma_3 \left(k_x k_y (J_x J_y + J_y J_x) + c.p. \right) \right) \tag{1.13}$$

Where γ_1, γ_2, γ_3 are the Luttinger parameters (we will discuss numerical values shortly after), I_4 is the 4×4 identity matrix, $\vec{k}$ is a vector of the Brillouin zone, $\vec{J}$ is the orbital momentum operator (J_x, J_y, J_z are the 4×4 matrix satisfying $[J_x, J_y] = iJ_z$ etc.), x, y, z are the axis of the Brillouin zone shown in Fig. 1.1 and '*c.p.*' stands for circular permutation. Now, we introduce new parameters (A B C) in order to re-write the Luttinger Hamiltonian in a physically transparent way:

[6] It is not difficult to see that if we had considered the Γ_7 valence band, we would have found $E_c(k_z) = E_c + \frac{\hbar^2 k_z^2}{2m_0} + \frac{2}{3} \frac{\hbar^2 |\Pi|^2 k_z^2}{m_0^2 (E_c - E_v)} + \frac{1}{3} \frac{\hbar^2 |\Pi|^2 k_z^2}{m_0^2 (E_c - (E_v - \Delta))}$ while the other equations in 1.11 are unaffected

$$\begin{aligned} A &= \gamma_1 + \frac{5}{2}\gamma_2 \\ B &= 2\gamma_2 \\ C &= 2(\gamma_3 - \gamma_2) \end{aligned} \tag{1.14}$$

$$H_L = -\frac{\hbar^2}{2m_0}\left(Ak^2 I_4 - B\left(\vec{k}\vec{J}\right)^2 + C\left(k_x k_y (J_x J_y + J_y J_x) + c.p.\right)\right) \tag{1.15}$$

The first term alone attributes the same effective mass for all the Γ_8 states. The addition of the B-term lifts up the four-fold degeneracy into two sub-bands, and is invariant under arbitrary rotation. We are in the spherical approximation: the Luttinger Hamiltonian has two eigenvalues (that we can guess simply by taking $\vec{k}$ and $\vec{J}$ along the same axis):

$$\begin{aligned} E_{hh} &= -\frac{\hbar^2 k^2}{2m_0(A-2.25B)^{-1}} = \frac{\hbar^2 k^2}{2m_0(\gamma_1 - 2\gamma_2)^{-1}} \\ E_{lh} &= -\frac{\hbar^2 k^2}{2m_0(A-0.25)^{-1}} = \frac{\hbar^2 k^2}{2m_0(\gamma_1 + 2\gamma_2)^{-1}} \end{aligned} \tag{1.16}$$

The effective masses $m_{hh} = m_0(\gamma_1 - 2\gamma_2)^{-1}$ and $m_{lh} = m_0(\gamma_1 + 2\gamma_2)^{-1}$ do not depend on the direction of $\vec{k}$. The iso-energies are spheres. The C-term in Equ. 1.15 describes the warping of the valence band.

The Luttinger Hamiltonian is usually expressed in a matrix form. In the basis ($u_{\Gamma_8,3/2}$, $u_{\Gamma_8,-1/2}$, $u_{\Gamma_8,1/2}$, $u_{\Gamma_8,-3/2}$), the Luttinger Hamiltonian 1.15 is equivalent to:

$$H_L = -\frac{\hbar^2}{2m_0}\begin{pmatrix} a_{hh} & c & b & 0 \\ c^* & a_{lh} & 0 & -b \\ b^* & 0 & a_{lh} & c \\ 0 & -b^* & c^* & a_{hh} \end{pmatrix} \tag{1.17}$$

with:

$$\begin{aligned} a_{hh} &= (\gamma_1 - 2\gamma_2)k_z^2 + (\gamma_1 + \gamma_2)k_{||}^2 \\ a_{lh} &= (\gamma_1 + 2\gamma_2)k_z^2 + (\gamma_1 - \gamma_2)k_{||}^2 \\ c &= -\sqrt{3}\left(\gamma_2(k_x^2 - k_y^2) - 2i\gamma_3 k_x k_y\right) \\ b &= -2\sqrt{3}\gamma_3\left(k_x - ik_y\right)k_z \end{aligned} \tag{1.18}$$

The values of the Luttinger parameters and of the corresponding effective mass are given in Table 1.1.2 for CdTe and ZnTe.

1.1.3 Effect of strain: The Bir-Pikus Hamiltonian

Because of the lattice mismatch between CdTe and ZnTe, the effect of strain cannot be ignored in nanostructures. We briefly present the notations we use, we give Hooke's law for a cubic

	CdTe	ZnTe
E_g	1606 meV	2391 meV
ϵ_r	10.6	9.7
a_0	6.48Å	6.10Å
Δ_{so}	0.90 eV	0.91 eV
γ_1	4.8	4.07
γ_2	1.5	0.78
γ_3	1.9	1.59
$m_{hh,z}$	0.556	0.398
$m_{hh,\perp}$	0.159	0.206
$m_{lh,z}$	0.128	0.178
$m_{lh,\perp}$	0.303	0.303
m_e	0.096	0.116

Table 1.1: Physical parameters in CdTe and ZnTe.

crystal, and at last, we present the Bir-Pikus Hamiltonian, which models how strains affect the Γ_8 band.

We consider the arbitrary transformation of an elementary cubic volume $V = (x\vec{u_x} + y\vec{u_y} + z\vec{u_z})^3$ into a volume $V' = (x\vec{u_x}' + y\vec{u_y}' + z\vec{u_z}')^3$. While the $\{\vec{u_i}\}_{i=x,y,z}$ is an ortho-normalized basis, the $\{\vec{u_i}'\}_{i=x,y,z}$ are defined by:

$$\begin{aligned}
\vec{u_x}' &= (1+\varepsilon'_{xx})\vec{u_x} + \varepsilon'_{xy}\vec{u_y} + \varepsilon'_{xz}\vec{u_z} \\
\vec{u_y}' &= \varepsilon'_{yx}\vec{u_x} + (1+\varepsilon'_{yy})\vec{u_y} + \varepsilon'_{yz}\vec{u_z} \\
\vec{u_z}' &= \varepsilon'_{zx}\vec{u_x} + \varepsilon'_{zy}\vec{u_y} + (1+\varepsilon'_{zz})\vec{u_z}
\end{aligned} \tag{1.19}$$

The term ε'_{ij} ($\ll 1$) describes an expansion of the vector i in the direction j. This arbitrary transformation can be decomposed in a symmetric part and an anti-symmetric part. The symmetric part is the strain tensor. We note it $\overline{\overline{\varepsilon}}$ (it is defined by $\varepsilon_{ii} = \varepsilon'_{ii}$ and $\varepsilon_{ij} = 1/2(\varepsilon'_{ij} + \varepsilon'_{ji})$). In the linear regime, the strain tensor is proportional to the stress tensor $\overline{\overline{\sigma}}$. The stress tensor is also symmetric. σ_{ij} describes a force parallel to i on a surface perpendicular to j. Hence σ_{kk} corresponds to an elongation stress, while σ_{kl} ($k \neq l$) describes a shear stress. Since these tensor are symmetric, only 6 coefficients (out of 9) are independent. They are related in the linear regime through Hooke's law which reads in a cubic crystal:

$$\begin{bmatrix} \sigma_{xx} \\ \sigma_{yy} \\ \sigma_{zz} \\ \sigma_{yz} \\ \sigma_{zx} \\ \sigma_{xy} \end{bmatrix} = \begin{bmatrix} C_{11} & C_{12} & C_{12} & 0 & 0 & 0 \\ C_{12} & C_{11} & C_{12} & 0 & 0 & 0 \\ C_{12} & C_{12} & C_{11} & 0 & 0 & 0 \\ 0 & 0 & 0 & 2C_{44} & 0 & 0 \\ 0 & 0 & 0 & 0 & 2C_{44} & 0 \\ 0 & 0 & 0 & 0 & 0 & 2C_{44} \end{bmatrix} \cdot \begin{bmatrix} \varepsilon_{xx} \\ \varepsilon_{yy} \\ \varepsilon_{zz} \\ \varepsilon_{yz} \\ \varepsilon_{zx} \\ \varepsilon_{xy} \end{bmatrix} \tag{1.20}$$

Physically, the use of only two diagonal coefficients C_{11} and C_{44} is evident since x, y, z and xy, yz, zx are equivalent. The presence of C_{12} means that if the cube lattice is compressed in one direction (for e.g. $\varepsilon_{zz} < 0$) and that we do not allow a strain of the elementary volume in the other directions ($\varepsilon_{yy} = \varepsilon_{xx} = 0$), we need to apply a stress σ_{xx}, σ_{yy} in the x and y directions to maintain the lateral sides of the cube at the same position (while the cube tends to expand along x and y to minimize the elastic energy). Therefore, we expect physically $C_{12} > 0$.

An important example is the presence of biaxial strains. This example corresponds to the case of a coherently grown quantum well. For instance, we consider a $2D$ CdTe layer grown on ZnTe along the z axis. The strain in the xy plane is:

$$\varepsilon_{xx} = \varepsilon_{yy} = \frac{a_{ZnTe} - a_{CdTe}}{a_{CdTe}} \tag{1.21}$$

While the CdTe crystal is free to expand in the z direction in order to minimize the energy. Mathematically, $\sigma_{zz} = 0$, from which we deduce using Hooke's law 1.20:

$$\varepsilon_{zz} = -\frac{2C_{12}}{C_{11}} \frac{a_{ZnTe} - a_{CdTe}}{a_{CdTe}} \tag{1.22}$$

For a 2D CdTe layer grown over ZnTe, we have $\varepsilon_{xx} = \varepsilon_{yy} < 0$ and we find $\varepsilon_{zz} > 0$, as expected physically. All the other strain terms are equal to zero. We can decompose this strain into two components: a hydrostatic part which describes a variation of the volume that preserves the cubic symmetry and a shear part which introduces an anisotropy (i.e. a breaking of the cubic symmetry):

$$\begin{aligned} \overline{\overline{\varepsilon}}_{hyd} &= \frac{1}{3}\left(\varepsilon_{xx} + \varepsilon_{yy} + \varepsilon_{zz}\right) I_3 \\ \overline{\overline{\varepsilon}}_{sh} &= \overline{\overline{\varepsilon}} - \overline{\overline{\varepsilon}}_{hyd} \end{aligned} \tag{1.23}$$

The strain $\overline{\overline{\varepsilon}}$ induces a shift of the energies of the bands that we can describe through a Hamiltonian. A strain element ε_{xy} has the same symmetry as xy, or $k_x k_y$. Hence, the strain-Hamiltonian is formally identical to the quadratic terms of the Hamiltonian given by Luttinger. To describe these effects in the Γ_8 subspace, we just need to replace in the Luttinger Hamiltonian (Eqn. 1.13) the $k_i k_j$'s by the ε_{ij}'s and the γ_j by the Bir and Pikus parameters called a_v, b_v and d_v. The Bir-Pikus Hamiltonian [16] is given by:

$$H_{BP} = a_v \varepsilon I_4 + b_v \sum_i \varepsilon_{ii} \left(J_i^2 - \frac{1}{3} J^2 \right) + \frac{d_v}{\sqrt{3}} \left[\varepsilon_{xy} \left(J_x J_y + J_y J_x \right) + c.p. \right] \tag{1.24}$$

with $\varepsilon = \varepsilon_{xx} + \varepsilon_{yy} + \varepsilon_{zz} = tr\overline{\overline{\varepsilon}} = tr\overline{\overline{\varepsilon}}_{hyd}$

Following the convention used so far, we take an electron Hamiltonian and we have with the chosen notation a_v, b_v, $d_v > 0$. In CdTe [17], the Bir-Pikus parameters are:

$$\begin{aligned} a_v &= 0.91eV \\ b_v &= 0.99eV \\ d_v &= 2.76eV \end{aligned}$$

The effect of the hydrostatic term is to shift the Γ_8 energy through the a_v parameter (the gap increases with a hydrostatic compression i.e. $\varepsilon_{hyd} < 0$). The shear strain due to non-equal ε_{ii} lifts up the degeneracy between the two Γ_8 sub-bands through the b_v parameter (similarly to the situation in $\vec{k} \neq 0$ in the Luttinger Hamiltonian). So does 'pure shear' (i.e. ε_{ij} with $i \neq j$) through the d_v parameter. The Bir-Pikus Hamiltonian is independent on $\vec{k}$. The dispersion in a strained semi-conductor is simply given by the sum of H_L and H_{BP}. But let us discuss the effect of strain with an example.

In the case of biaxial strain discussed above, we see that the Bir-Pikus Hamiltonian reduces to:

$$\begin{aligned} H_{BP} &= a_v \varepsilon I_4 + \frac{b_v}{3}\left(\varepsilon_{||} - \varepsilon_z\right)\left(J_x^2 + J_y^2 - 2J_z^2\right) \\ &= \left(a_v\varepsilon + \frac{5}{4} b_v \left(\varepsilon_{||} - \varepsilon_z\right)\right) I_4 - b_v\left(\varepsilon_{||} - \varepsilon_z\right) J_z^2 \end{aligned} \tag{1.25}$$

Where we have used $J_x^2 + J_y^2 + J_z^2 = J(J+1)I_4$ with $J = 3/2$ to simplify the first expression. It is now clear that, as explained earlier, the degeneracy of the Γ_8 band has been lifted at $k = 0$ by the anisotropy of the strains. Using 1.22, we find:

$$E_{\pm\frac{3}{2}} - E_{\pm\frac{1}{2}} = 2b_v\left(1 + \frac{2C_{12}}{C_{11}}\right)\frac{a_{CdTe} - a_{ZnTe}}{a_{CdTe}} \tag{1.26}$$

In a fully strained layer of CdTe over ZnTe, the heavy-mass Γ_8 sub-band is $300meV$ above the light-mass sub-band, so that, in first approximation, light-holes in these nano-structures can be neglected. For thorough explanations on the elements of semiconductor theory developed in this section we recommend [18].

1.2 Quantum Dots

A quantum dot is a nanometer size volume of a semiconductor (here CdTe) embedded in a larger gap semiconductor (ZnTe). As the valence band (resp. conduction band) of CdTe is at higher (resp. lower) energy than the one of ZnTe, the quantum dot behaves as a 3D potential well for the free carriers. This results in a quantization of the energy levels of the carriers and a discretization of the optical properties. Due to these features, quantum dots are often nicknamed 'artificial atoms', the potential created by the barrier, being the analogue of the Coulomb potential in atoms. However, as we will see, the analogy has its limit: when an electron is promoted from the valence band to the conduction band, a hole is left in the valence band. Coulomb interaction between these two (quasi-)particles plays an important role: it consists of an attractive term that shifts the single particle energy levels and an exchange interaction (due to Pauli's exclusion principle). Indeed, although the two particles look different in a naive approach, a hole is the absence of a valence band electron. The hole's energy, charge, spin, orbital momentum, $\vec{k}$ and mass are, by definition, taken opposite to the missing valence electron. Hence, the promotion of an electron from the state $u_{\Gamma_8,3/2}$ will leave in the valence band a hole with an orbital momentum $J_z = -3/2$ that we will note $\Downarrow$.

1.2.1 Energy Levels and Optical Selection Rules

The wave-function of a carrier can be developed on the Bloch states:

$$\Psi(\vec{r}) = \sum_{n,k} c_{n,k} u_{n,k}(\vec{r}) e^{i\vec{k}\cdot\vec{r}} \tag{1.27}$$

Because of confinement, only Bloch states around $\vec{k} = 0$ need to be considered. The single-particle energy levels (for the electron or the hole) can be determined in the effective-mass approximation (i.e. inter-band wave-function mixing is neglected): The periodic crystal potential and the free-electron kinetic energy are replaced by the effective Hamiltonian describing the band extrema (effective mass m_e for the conduction band or $H_L + H_{BP}$ for the Γ_8 band) and the expansion on Bloch states is replaced by an expansion on the $u_{n,0}(\vec{r})e^{i\vec{k}\cdot\vec{r}}$. The valence band and conduction band electronic wave-function can be written as a function of slowly varying envelope functions:

$$\begin{aligned}
\Psi_c(\vec{r}) &\approx \sum_k c_k u_{\Gamma_6,0}(\vec{r}) e^{i\vec{k}\cdot\vec{r}} \\
&= u_{\Gamma_6,0}(\vec{r}) F_e(\vec{r}) \\
\Psi_v(\vec{r}) &\approx \sum_{J_z=\pm 3/2,\pm 1/2,k} c_{J_z,k} u_{\Gamma_8,J_z}(\vec{r}) e^{i\vec{k}\cdot\vec{r}} \\
&= \sum_{J_z=\pm 3/2,\pm 1/2} u_{\Gamma_8,J_z}(\vec{r}) F_{J_z}(\vec{r})
\end{aligned} \tag{1.28}$$

This allows us to work with the very intuitive picture of an effective mass carrier trapped in a potential $V_{c,v}(\vec{r})$ created by the band-offset between the two semi-conductor materials with an envelope function F_c for the electron or a linear combination of the envelope functions $F_{\pm 3/2}, F_{\pm 1/2}$ for the hole. These envelope function satisfy the Schrödinger equation:

$$\begin{gathered}
\left(\frac{\hbar^2}{2m_e}\Delta\right) F_e(\vec{r}) + V_e(\vec{r}) F_e(\vec{r}) = E F_e(\vec{r}) \\
\left[\tilde{H}_{BP} + \tilde{H}_L + V_h(\vec{r})\right] \begin{pmatrix} F_{3/2}(\vec{r}) \\ F_{-1/2}(\vec{r}) \\ F_{1/2}(\vec{r}) \\ F_{-3/2}(\vec{r}) \end{pmatrix} = E \begin{pmatrix} F_{3/2}(\vec{r}) \\ F_{-1/2}(\vec{r}) \\ F_{1/2}(\vec{r}) \\ F_{-3/2}(\vec{r}) \end{pmatrix}
\end{gathered} \tag{1.29}$$

Where in $\tilde{H}_L$, the k-terms transform into a gradient of the envelope function ($\vec{k} \to -i\nabla$). Note that now, $\tilde{H}_L$ and $\tilde{H}_{BP}$ are hole Hamiltonians (i.e. opposite to the electron Hamiltonians defined earlier). From now on we will drop the $\tilde{}$, although we are talking of a hole Hamiltonian. The derivation of the effective mass approximation can be found in [19].

A few approximations are usually made to solve this problem:

- *Approximation already made in Eqn. 1.29*: we take the same effective mass in CdTe and ZnTe, otherwise we would need to consider more complicated equations (the latter are discussed in [18] for instance).
- Considering the presence of biaxial strain, non-diagonal terms in H_L (coupling heavy and light holes) can be neglected compared to the lift of degeneracy due to H_{BP} (c.f. section 1.1.3). This is the heavy hole approximation: The four differential equations become

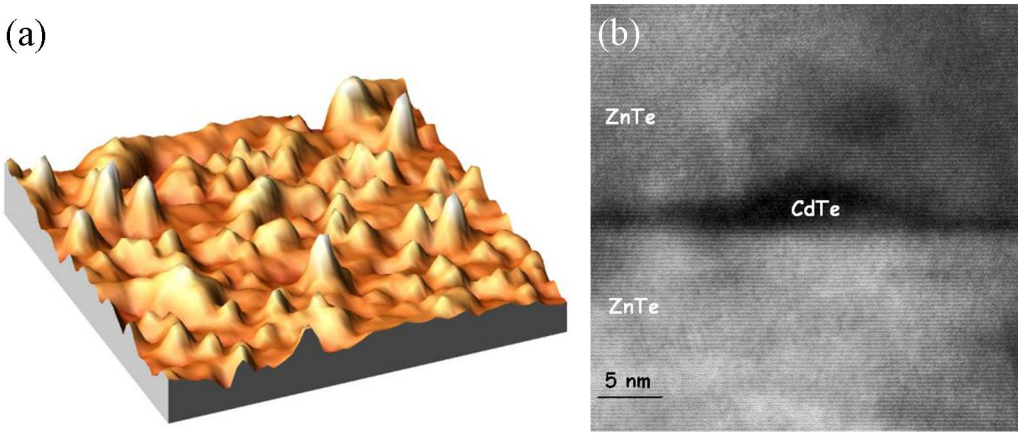

Figure 1.3: (a) AFM Image ($250nm^2$) of CdTe/ZnTe quantum dots before capping (quantum dot density $\approx 3.10^{10}$). (b) TEM Image of a CdTe/ZnTe quantum dot.

uncoupled, only the ground states $|\pm 3/2\rangle$ are considered, and their effective mass is given by the diagonal term in the Luttinger Hamiltonian: $m_{h,||}$ in the plane, $m_{h,z}$ along the growth axis.

At this point, the problem is still too complicated for analytical resolution, but we can make it simple by choosing a textbook potential (i.e. one we know how to solve!). The true shape of a quantum dot is lens-like, with a height L_z much smaller than its radius ρ (c.f. Fig 1.3). Consequently, solutions of the form $\chi(z)\phi_{n,m}(\rho,\theta)$ are a good approximation of the real functions. We suppose $V_{c,v}(\vec{r}) = V_{c,v}(z) + V_{c,v}(\rho)$, where $V_{c,v}(z)$ is a $1D$ harmonic oscillator, and $V_{c,v}(\rho)$ is a $2D$ harmonic oscillator:

$$\begin{aligned} V_{c,v}(z) &= 4\Delta E_{c,v}\frac{z^2}{L_z^2} \\ V_{c,v}(\rho) &= 4\Delta E_{c,v}\frac{\rho^2}{L_\rho^2} \end{aligned} \tag{1.30}$$

We introduce for the $2D$ harmonic oscillator the characteristic spatial width $\sigma_\rho^{e,h} = \sqrt{\frac{\hbar}{m_{e,h||}\omega_{e,h}}}$ and the characteristic frequency $\omega_\rho^{e,h} = \sqrt{8\Delta E_{c,v} m_{e,h||} L_\rho^2}$ and their analogue $\sigma_z^{e,h}$, $\omega_z^{e,h}$ for $V_{c,v}(z)$. The ground state (GS) and the first two degenerate excited states $Exc, \pm 1$ can be found in any textbook, (e.g. [20]):

$$\begin{aligned} F_{c,v}^{GS}(z,\rho,\theta) &= \frac{1}{(\sqrt{\pi}\sigma_z)^{1/2}}\exp\left(-\frac{z^2}{2\sigma_z^2}\right)\frac{1}{\sqrt{\pi}\sigma_\rho}\exp\left(-\frac{\rho^2}{2\sigma_\rho^2}\right) \\ F_{c,v}^{Exc,\pm 1}(z,\rho,\theta) &= \frac{1}{(\sqrt{\pi}\sigma_z)^{1/2}}\exp\left(-\frac{z^2}{2\sigma_z^2}\right)\frac{1}{\sqrt{\pi}\sigma_\rho}\exp\left(-\frac{\rho^2}{2\sigma_\rho^2}\right)\frac{\rho}{\sigma_\rho}\exp\left(\pm i\theta\right) \end{aligned} \tag{1.31}$$

The ground state and the first two excited states have the same envelope function along the z axis. This comes from the fact that $L_z \ll L_\rho$, and consequently, a node along the z axis is

at much higher energies that the states considered above. The first energy state, at an energy $E^S_{e,h} = \hbar(\omega_z^{e,h} + \omega_\rho^{e,h})/2$ for the electron or the hole, will be commonly called S state. The second energy state, $E^P_{e,h} = \hbar(\omega_z^{e,h} + 3\omega_\rho^{e,h})/2$, is referred as P state and is only twice degenerate with an angular momentum $l_z = \pm 1$, contrary to atom physics (where p-states are 3-times degenerate). This is, as we have explained already a consequence of the geometry $L_z \ll L_\rho$, or in other words, the symmetry of the dot. Each of these states has an additional degeneracy due to spin (or, strictly speaking, atomic angular momentum regarding the hole): there are two possible spin projection for the electron ($\pm 1/2$) which we will note $|\uparrow\rangle$ and $|\downarrow\rangle$ and two spin projections for the heavy-hole ($\pm 3/2$) which we will note $|\Uparrow\rangle$ and $|\Downarrow\rangle$. A hole $|\Downarrow\rangle$ corresponds to the absence of a valence electron $\Psi_v(\vec{r}) = u_{\Gamma_8,3/2}(\vec{r})F_{3/2}(\vec{r})$.

The basic optical properties of a quantum dot can be determined considering the coupling through the operator $\vec{p}$. Indeed, the coupling to light in the dipole approximation is given by $H = -q\vec{p}.\vec{A}/m$ or $H = -\vec{d}.\vec{E}$, depending on the chosen gauge. As usual, $\vec{A}$ is the vector potential, $\vec{d}$ is the dipole operator, and $\vec{E}$ the electrical field. This coupling can be calculated between the state 'empty dot' $|\emptyset\rangle$ and an electron-hole pair state (which we will call exciton, to keep it short). Alternatively, we will consider the interband matrix element between the two electronic states Ψ_c and Ψ_v introduced previously:

$$|\langle\Psi_v|\,\vec{p}\,|\Psi_c\rangle|^2 = |\langle F_v|F_c\rangle|^2\,|\langle u_{\Gamma_8,J_z}|\,\vec{p}\,|u_{\Gamma_6,\sigma}\rangle|^2$$

We see from this expression that optical transitions are a product between the overlap integral over the envelope functions, and an interband matrix element depending on the symmetry of the periodic Bloch wave. The latter can be calculated using the results given in subsection 1.1.1. It is straighfoward to demonstrate that in the heavy hole approximation, there are only two optically active transitions: between $u_{\Gamma_8,-3/2}$ and $u_{\Gamma_6,\downarrow}$ (coupled through the $p_+ = p_x + ip_y$ operator, corresponding to $\sigma+$ photon absorption or emission) and the transition between $u_{\Gamma_8,+3/2}$ and $u_{\Gamma_6,\uparrow}$ (coupled through the $p_- = p_x - ip_y$ operator, corresponding to $\sigma-$ photon absorption or emission). The overlap integral over the envelope functions implies that the envelope function of the empty valence state and the conduction state have the same symmetry and forbids crossed transition between, for instance, a valence state of the P shell to a conduction state of the S shell.

Coming back to an electron-hole pair description, the general result is that for S-electron-hole pair, we have two bright states ($|\downarrow\Uparrow\rangle$ with $J_z = +1$ and $|\uparrow\Downarrow\rangle$ with $J_z = -1$) optically active and two dark states ($|\uparrow\Uparrow\rangle$ with $J_z = +2$ and $|\downarrow\Downarrow\rangle$ with $J_z = -2$) which cannot recombine radiatively. For now, within a given shell, the states are all degenerate, but we will see this is no longer the case if we take into account the real symmetry of the dot and Coulomb interactions.

The harmonic potential approximation overestimate greatly the single-particle energy levels, since they overestimate the confinement. However, the wave-functions Equ. 1.31 can be used as trial wave-functions for variational calculation in a more realistic potential, in order to estimate correctly the energy levels. Another improvement compared to the simple model we have presented, is to take into account the mixing between the bands, which is commonly done using $\vec{k}.\vec{p}$ theory. Experimentally, in our system the P shell is typically 30 to $35meV$ higher than the S shell. In between, we often find the LO-phonon replica, $25meV$ above the exciton ground-state.

1.2.2 Corrections due to Coulomb interactions: Binding energy and Exchange Interactions

Fundamentally, the evaluation of Coulomb interactions is a complex many-body problem between an electron of the conduction band and $N-1$ electrons from the valence band. However, as shown in [21], this interaction reduces to an effective interaction between the electron and the hole with a direct term and an exchange term. The Hamiltonian matrix elements are:

$$\langle e,h\,|H|\,e',h'\rangle = \delta_{h,h'}\delta_{e,e'}(\epsilon_e-\epsilon_h) - K_{h'ee'h} + J_{eh'e'h} \tag{1.32}$$

ϵ_e and ϵ_h are the single-particle energy levels, $K_{h'ee'h}$ and $J_{eh'e'h}$ represent the direct and the exchange Coulomb interaction. The latter are given by:

$$\begin{aligned} K_{h'ee'h} &= \frac{e^2}{4\pi\varepsilon}\int d\vec{r}_1 d\vec{r}_2 \frac{\Psi^*_{v'}(\vec{r}_1)\Psi^*_c(\vec{r}_2)\Psi_{c'}(\vec{r}_2)\Psi_v(\vec{r}_1)}{|\vec{r}_1-\vec{r}_2|} \\ J_{eh'e'h} &= \frac{e^2}{4\pi\varepsilon}\int d\vec{r}_1 d\vec{r}_2 \frac{\Psi^*_c(\vec{r}_1)\Psi^*_{v'}(\vec{r}_2)\Psi_{c'}(\vec{r}_2)\Psi_v(\vec{r}_1)}{|\vec{r}_1-\vec{r}_2|} \end{aligned} \tag{1.33}$$

In these expressions, ε is the dielectric constant of the material. Ψ_c is the wave-function of the electron in the conduction band and Ψ_v is the electronic wave-function of the missing electron in the valence band. The direct term is attractive, as expected from the common picture of a positively charged hole interacting with a negatively charged electron. It lowers the excitonic levels by a few tens of meV, depending on the envelope function of the electron-hole pair, while the exchange term dramatically influences the structure of the levels within a spin-degenerate multiplet. Indeed, J_{eheh} is different from zero only if the spin of Ψ_v and Ψ_c are the same (and the electron and hole spin are opposite). Hence, the exchange term can be expressed as a spin-dependent effective Hamiltonian that increases the energy of bright states compared to dark states which remain unaffected. The picture is that the Coulomb interaction between electrons of identical spin is lower because they avoid each other due to Pauli exclusion principle. Therefore, as a $\Uparrow$-hole is an absence of an electron with spin down, the Coulomb interaction between the valence band and the conduction electron is lower if this conduction electron is $\uparrow$ than spin $\downarrow$. In other words, the electron-hole exchange interaction gives rise to a ferromagnetic effective Hamiltonian which lifts up the degeneracy between bright and dark states.

In fact, the approach above does not take into account the true symmetry of the crystal so that the effective Hamiltonian presents additional terms. Bir and Pikus have intensively studied how the bulk-exciton exchange interaction could be modeled. They demonstrated that the exchange integral could be decomposed into two terms.

- The short-range exchange interaction, which corresponds to the case when the electron and the hole are in the same Wigner cell. For a $3D$ exciton, it can be treated by an effective Hamiltonian in the Γ_8, Γ_6 subspace: $J_{sr} = \delta_0^{sr,3D}\vec{\sigma}.\vec{J} + \delta_2\sum_{i=x,y,z}\sigma_i J_i^3$. The first term of the short-range exchange interaction lifts up the degeneracy between exciton states of total angular momentum $J_{tot}=2$ degenerate 5 times and $J_{tot}=1$ degenerate 3 times. The second term, predicted on symmetry considerations, results in a fine-structure of the dark states ($J_{tot}=2$ multiplet). This dark exciton fine structure has never been observed experimentally for bulk semiconductors but is expected to be much smaller than δ_0 which is equal to $0.07meV$ in CdTe and $0.28meV$ in ZnTe [22].

- A long-range exchange interaction, which depends on the envelope wave-function of the exciton. For a $3D$ exciton, this lifts up of the degeneracy between transverse exciton states (exciton dipole perpendicular to the center of mass wave-vector $\vec{k_{ex}}$) and longitudinal exciton states (exciton dipole parallel to the center of mass wave-vector $\vec{k_{ex}}$), independent of k_{ex}, for $k_{ex} > 2\pi/\lambda$. A $0.65meV$ transverse-longitudinal splitting was measured in CdTe [23]. For $k_{ex} < 2\pi/\lambda$, we are in the light-matter strong-coupling regime of polariton, that we will not discuss here. We now understand that $k_{ex} \neq 0$ corresponds more precisely to $k_{ex} \gg \lambda^{-1}$, where λ is the wavelength of the photon emitted during the exciton recombination.

We are now going to focus on exchange interactions in quantum dots. A general trend is that the magnitude of the exchange energies increases with confinement as the overlap between the carriers wave-function is greater than in bulk semi-conductor. Regarding the symmetry of a quantum dot, the fine structure of the heavy hole exciton can be predicted. For the ground state, the exchange Hamiltonian can be written:

$$H_{eh}^{ex} = 2\delta_0 j_z \sigma_z + \frac{\delta_1}{2}\left(e^{2i\phi_1} j_+ \sigma_- - e^{-2i\phi_1} j_- \sigma_+\right) + \frac{\delta_2}{2}\left(e^{2i\phi_2} j_+ \sigma_+ + e^{-2i\phi_1} j_- \sigma_-\right) \tag{1.34}$$

Where δ_0, δ_1 and δ_2 are parameters, which represent respectively the dark/bright exciton energy splitting, the energy splitting between bright exciton states, and the energy splitting between dark states. j_i and σ_i are the Pauli matrices for the electron spin and the hole pseudo-spin. In CdTe/ZnTe quantum dots, δ_0 is typically $1meV$, and δ_1 varies between a few tens and a few hundreds of μeV. The splitting of dark states δ_2 is governed by short-range exchange interaction. Both short-range and long-range interactions contribute to δ_0. In an anisotropic quantum dot, δ_1 is controlled by long-range exchange (we neglect strain-induced valence band mixing that we will discuss in the next section). The eigenstates observed optically (bright exciton states) are linearly polarized along the ϕ_1 direction and $\phi_1 + 90°$:

$$\begin{aligned} |\pi_{\phi_1}\rangle &= \frac{1}{\sqrt{2}}\left(e^{-i\phi_1}|+1\rangle + e^{i\phi_1}|-1\rangle\right) \\ |\pi_{\phi_1+90°}\rangle &= \frac{1}{\sqrt{2}}\left(e^{-i\phi_1}|+1\rangle - e^{i\phi_1}|-1\rangle\right) \end{aligned} \tag{1.35}$$

This exchange Hamiltonian results from the fact that the highest possible symmetry of a real dot is C_{2v}. This favors two axis, perpendicular to the growth axis. Even in an ideally lens-shaped quantum dot, Bester, Zunger *et al* ([24], [25]) show using a microscopic approach that (i) interface between the dot material and the barriers, (ii) atomic relaxation (i.e. strain) induced by the lattice mismatch and (iii) the piezo-electric field arising from these strain result already in a fine structure splitting. For InGaAs/GaAs quantum dots with $L_x = L_y = 25.2nm$, $L_z = 3.5nm$, they calculate a $4\mu eV$ splitting of the bright states. This can be compared to the $30\mu eV$ splitting they calculate for a small shape anisotropy of a similar dot ($L_x = 26nm$, $L_y = 20nm$, $L_z = 3.5nm$) [25]. Such fine structure splittings are also predicted considering a potential anisotropy, and the short and long-range interaction in the frame of $\vec{k}.\vec{p}$ theory [26]. However, as it is impossible to check if the potential anisotropy chosen in the calculation corresponds to the one of the dot under optical study, the contribution of confinement anisotropy, strain anisotropy, interdiffusion of the barrier material in the quantum dot, randomness at an atomic scale of this interdiffusion, and the long range and short range exchange interaction resulting from these effects is still debated.

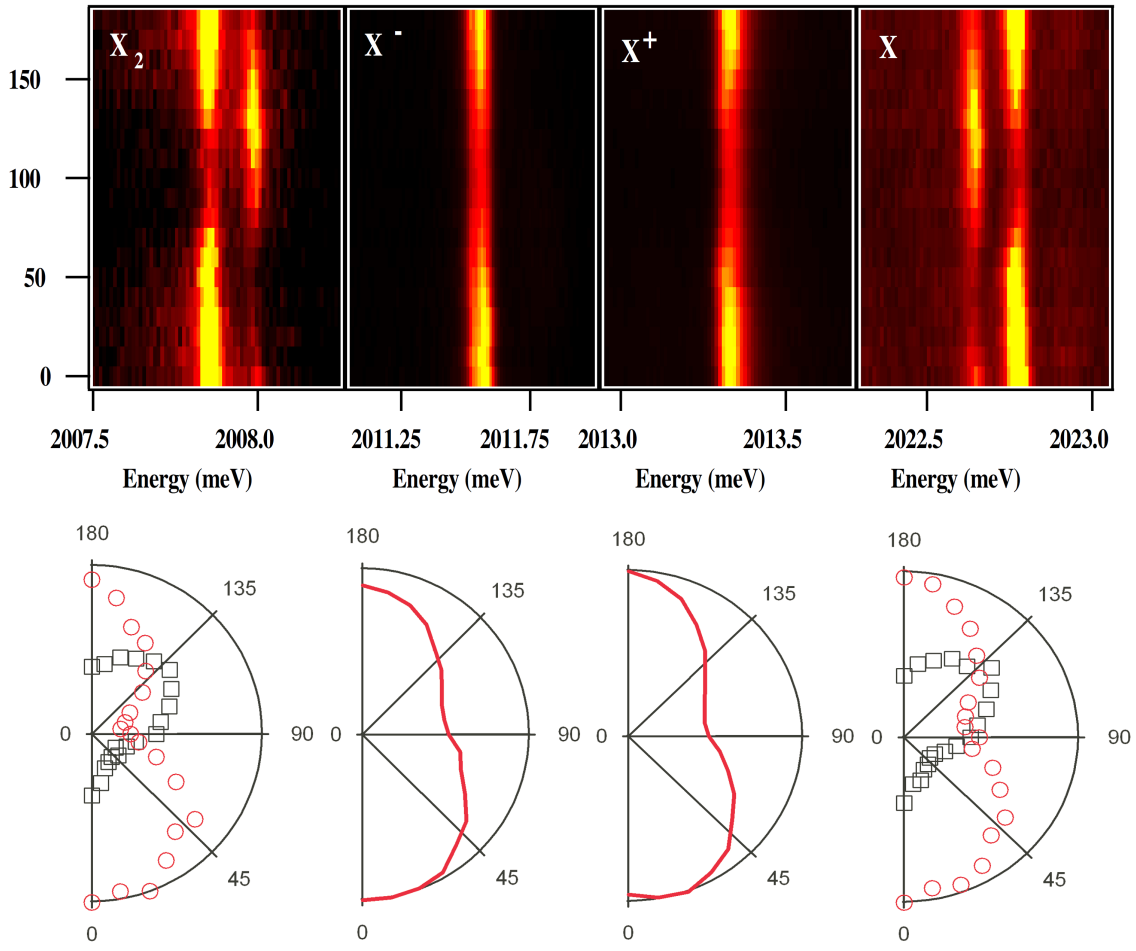

Figure 1.4: PL intensity of the lines of the biexciton, the charged excitons and the neutral exciton of a CdTe/ZnTe quantum dot as a function of the angle of the linearly polarized detection (taken from Yoan Leger's PhD thesis [27])

1.2.3 Polarisation anisotropy and Valence Band Mixing

Another experimental observation (Fig. 1.4) hurts the simple description of a heavy hole exciton given in subsection 1.2.1: in the majority of CdTe/ZnTe quantum dots, we observe that the linearly polarized bright states of the neutral exciton do not have the same intensity. Moreover, the angle between the two linearly polarized states is not 90°, as predicted earlier. This anisotropy of the oscillator strength is also observed in charged quantum dots, which present a linear component in the PL emission. This appears to be in complete contradiction with what has been stated earlier.

For instance, we consider the case of a negatively charged quantum dot. The ground state of the dot is degenerate twice ($|\uparrow\rangle$ or $|\downarrow\rangle$). So are the ground excitonic states X^- which are also twice degenerate ($|\uparrow\downarrow\Uparrow\rangle$, $|\uparrow\downarrow\Downarrow\rangle$). In charged quantum dots, exchange interactions vanish for the X^- ground state, as the hole interacts with two electrons in the same spatial state but with opposite spins. According to the heavy-hole approximation, the transitions are purely circularly polarized $\sigma+$ or $\sigma-$ so that no linear polarization should be observed.

However, we have seen that the heavy hole approximation relied on the presence of biaxial strain. An anisotropic distribution of strains (i.e. $\varepsilon_{xx} \neq \varepsilon_{yy}$ or $\varepsilon_{ij} \neq 0$ with $i \neq j$) can break down this hypothesis and mix the heavy-hole state $J_z = +3/2$ with $J_z = -1/2$ and $J_z = -3/2$ with $J_z = +1/2$ through the Bir-Pikus Hamiltonian. A light-hole/heavy-hole mixing (i.e. valence band mixing) can also occur through the Luttinger Hamiltonian if the dot is asymmetric ($L_x \neq L_y$), however, the mixing expected theoretically is too small compared to the polarization anisotropy observed here.

To fix ideas and show how Valence Band Mixing (VBM) can affect the polarization properties of the dot, we neglect the envelope function difference between the light and heavy hole, and consider a phenomenological parameter $\eta e^{2i\theta}$ describing the light part of the hole state[7].

$$\begin{aligned} \left|\widetilde{\Uparrow}\right\rangle &\propto |+3/2\rangle - \eta e^{2i\theta} |-1/2\rangle \\ \left|\widetilde{\Downarrow}\right\rangle &\propto |-3/2\rangle - \eta e^{-2i\theta} |+1/2\rangle \end{aligned} \tag{1.36}$$

In the hypothesis of a small strained-induced VBM:

$$\eta e^{-2i\theta} = \frac{id\varepsilon_{xy} - b\frac{\sqrt{3}}{2}(\varepsilon_{xx} - \varepsilon_{yy})}{\Delta_{lh}} \tag{1.37}$$

Where Δ_{lh} is the light-hole heavy-hole splitting given by the average in-plane bi-axial strain $b(\varepsilon_{xx} + \varepsilon_{yy} + 2\varepsilon_{zz})$. In our quantum dots, Δ_{lh} is expected to be approximately ten times smaller than the $300meV$ measured in the case of fully strained CdTe layer over ZnTe, because of partial relaxation of the strain [12]. However, this is a minimum estimate. As we will see, the only parameter accessed experimentally is η (Eqn. 1.37), which is a ratio of the in-plane anisotropy of the strain and light-hole/heavy hole splitting.

First, we consider the simplest case of a charged exciton where exchange interactions do not play a role because the hole is interacting with a spin singlet. The oscillator strength $\Omega(\alpha)$ of the transition (where the vector $\vec{e}_\alpha = \cos(\alpha)\vec{e}_x + \sin(\alpha)\vec{e}_y$ is the polarization of the detection) is given by:

$$\begin{aligned} \Omega(\alpha) &\propto \left|\left\langle \uparrow |\cos(\alpha)p_X + \sin(\alpha)p_Y| \uparrow\downarrow \widetilde{\Uparrow}\right\rangle\right|^2 \\ &= 1 + \frac{\eta^2}{3} + \frac{2}{\sqrt{3}}\eta\cos(2(\theta - \alpha)) \end{aligned} \tag{1.38}$$

Contrary to what is expected in the heavy hole approximation, the charged exciton can have a strong linear component, depending on the strength of the light/heavy hole mixing governed by η. In our quantum dots, the linear polarization rate P defined by:

$$P = \frac{I_{max} - I_{min}}{I_{max} + I_{min}} = \frac{4/\sqrt{3}\eta}{2 + 2\eta^2/3} \tag{1.39}$$

[7] Here, we have only considered admixtures of $|\pm 3/2\rangle$ with $|\mp 1/2\rangle$. This is often the case in the literature. This is not evident at the first sight of H_L and H_{BP} which also present non-diagonal terms coupling $|\pm 3/2\rangle$ with $|\pm 1/2\rangle$. This is because the coupling between envelope functions arising from the b term (in Eqn. 1.17) of H_L and their analogue for H_{BP} (due to the shear strain ϵ_{zx} and ϵ_{zy}) are neglected. For H_L, this comes from the decoupling approximation, whereby the wave-function can be separated in the z and $x-y$ coordinates. Therefore the b term in H_L does not couple envelope functions because $\langle \chi_i(z) | k_z | \chi_j(z) \rangle = 0$ by symmetry. For H_{BP}, our assumption is based on an experimental observation: the shear strain ϵ_{zx} and ϵ_{zy} was found to be negligible in the majority of the Mn-doped quantum dots ($p.88 - 91$ of [27]).

can reach 40%, which corresponds to strong light/heavy hole mixing ($\eta = 0.24$). Experimentally, there are no correlation between the polarisation axis of different quantum dots, even if they are spatially close to each other (and of course no correlation with the crystallographic axis). Such behaviour can be explained considering the anisotropic relaxation of strain during the growth [12]. A similar behaviour is observed in III-V compounds at low quantum dot density (near the 2D to 3D transition). Again, it is attributed to the effect of strains [21]. For this system, this hypothesis is supported by AFM studies showing that, in such growth conditions, the dots are preferentially nucleating near structural defects [28]. In the case of II-VI materials, a strained-induced heavy/light hole mixing is not surprising: the dislocation formation energy is low in this system [29].

For neutral excitons, the competition of the exchange interaction (which tends to favor linear emission along ϕ_1 and $\phi_1 + 90°$) and the effect of strains (which tends to favor linear emission along θ and $\theta+90°$) explains that the angle between the two linearly polarized X lines is not equal to 90°. Moreover, the VBM results in a fine structure splitting through short-range interaction that can either enhance or decrease the fine structure splitting due to long range interaction. In order to illustrate our point, we continue to omit subtleties, due to envelope function overlap and consider an isotropic short-range exchange interaction between the electron (spin σ) and the light or heavy hole (spin J):

$$H_{sr} = -\frac{\delta_0^{sr}}{3/2}\vec{J}.\vec{\sigma} \tag{1.40}$$

Where δ_0^{sr} still corresponds to the energy splitting between bright and dark exciton due to the short-range exchange. The coupling between the bright states $\left|\downarrow \widetilde{\Uparrow}\right\rangle$ and $\left|\uparrow \widetilde{\Downarrow}\right\rangle$ through H_{sr} can be calculated using eqns. 1.36:

$$\left\langle \downarrow \widetilde{\Uparrow} \left| H_{sr} \right| \uparrow \widetilde{\Downarrow} \right\rangle = \frac{2}{\sqrt{3}}\delta_0^{sr}\eta e^{-2i\theta} \tag{1.41}$$

Hence, valence-band mixing through short-range interaction splits the bright states into two linearly polarized states along axis defined by the strains. As a result of the competition between this effect and the long-range exchange interactions, the angle between the two linearly polarized states is not necessarily 90°. Also, dark states are coupled to each other to second order in η and acquire a weak oscillator strength (with a dipole along z, that are not detected in the configuration of our set-up.) A thorough investigation of these effects has been carried out in Yoan Leger's PhD thesis [27] and in [12], where envelope functions of the effective mass carriers have been taken into account, and calculations brought beyond the perturbative limit of small VBM.

1.3 Exchange interactions between carriers and a localized Mn spin

1.3.1 Exchange interactions in bulk Diluted Magnetic Semi-conductors

In order to understand the effect of adding a Mn atom in a CdTe quantum dot, a good starting point is to consider a Mn atom in a CdTe crystal and hence the case of Diluted Magnetic Semiconductors (DMS) at the limit of low concentrations which have been intensively studied

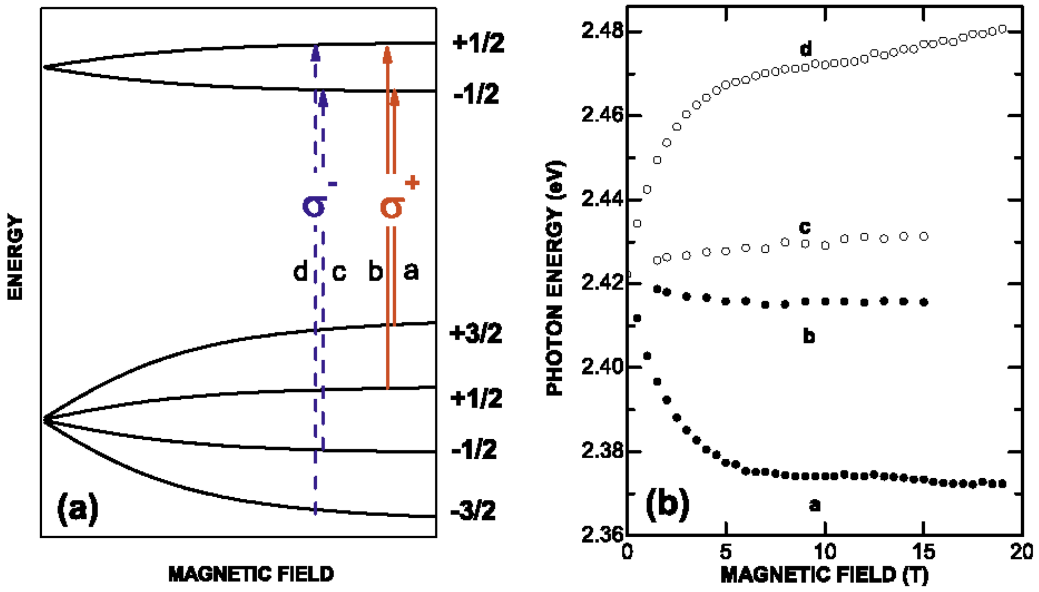

Figure 1.5: (a) Scheme of band energy close to the band gap ($k \approx 0$) as a function of a magnetic field B_z along the growth axis. The spin states of electrons (σ_z) and holes (J_z) as well as the optical transitions are displayed. (b) Experimental transition energies in a $Zn_{0.95}Mn_{0.05}Te$ sample, as a function of the applied magnetic field B_z. (Taken from [33, 34])

for the past decades. In such case, we can consider that the band states of the crystal are the ones of a pure crystal without the Mn impurity, while the presence of the Mn atom introduces localized d electronic states around the Mn nucleus: when the Mn atom ($3d^5 4s^2$) replaces a Cd atom $3d^{10}4s^2$, the 2 electrons of the s shell participate to the crystal bond, while the 5 electrons of the d shell remain localized around the Mn^{2+} ion. Consequently, the presence of the Mn impurity in a II-VI crystal does not strongly modify the crystal potential seen by free carriers contrary to a Mn impurity in a III-V semiconductor where the Mn atom is also an acceptor (The Mn^{2+} ion, which is a negatively charged center in the III-V crystal, binds a hole from the valence band to form a hydrogenic-like state [30]). The half filled $3d$ shell of the Mn atom in the ground electronic state satisfies according to Hund's rule $S = 5/2$ and $L = 0$: each electron occupies a d orbital ($L_z = -2, -1, 0, 1, 2$) with parallel spins. The lowest excited state $3d^{5*}$ with $S = 3/2$ and $L = 4$ (which corresponds schematically to the inversion of one of the electron's spin) lies $2.2eV$ above the electronic ground state. These intra-ionic optical transition (observed in ZnMnTe [31]) should be forbidden by parity rules and spin-conservation but are dipole allowed by the lack of inversion symmetry of the tetrahedral crystal field and spin-orbit interaction. The same mixing is responsible for spin-lattice relaxation of an isolated Mn atom. Since this mixing is small, we will consider in the following that the Mn is a 5/2 pure spin.

In DMS, a strong spin-dependent coupling was discovered in 1977 [32] between the effective mass-carriers (electron from the s band and holes from the p band) and the localized d electrons of the Mn atom called *spd* exchange. One of the most striking consequences of these interactions is the so-called giant Zeeman effect: the splitting produced by a magnetic field is more than an order of magnitude larger than the intrinsic Zeeman splitting of the exciton optical transitions, reflecting an energy shift of the conduction and valence band edge (Fig 1.5).

In order to explain it, a shift induced by the effective field created by polarized Mn atoms

needs to be considered. Since carriers near the band edge are delocalized, a mean field approximation is performed (it is the so-called virtual-crystal approximation): the carriers are only sensitive to the mean value of the Mn spins $\langle S_z \rangle$, and to their average density xN_0 where x is the percentage of Mn in the alloy, and where N_0 is the number of unit cells in a normalized volume (i.e. $N_0 = \frac{N}{V} = \frac{4}{a^3}$ where N is the number of unit cell and V is the volume of the crystal. a is the size of the cubic cell in the zinc-blende structure.). This *spd* exchange-induced shift was found to be proportional to the Mn magnetization:

$$\begin{aligned} E_{sd} &= -N_0 x\alpha \langle S_z \rangle \sigma \\ E_{pd} &= -N_0 x\frac{\beta}{3} \langle S_z \rangle J_z \end{aligned} \tag{1.42}$$

α (resp. β) is a coupling constant between the s carriers (resp. p carriers) and the d electrons of the Mn spin. In CdTe, $N_0\alpha \approx 0.2eV$ and $N_0\beta \approx -0.88eV$. These values can be extracted from experiments like the one shown in Fig. 1.5 thanks to the presence of both light holes and heavy holes excitons which split proportionally to $N_0(\alpha + \beta/3)$ and $N_0(\alpha - \beta)$. The law equ. 1.42 is well satisfied in II-VI DMS with moderate band gap and a Zinc-Blende structure such as (Cd,Mn)Te, (Zn,Mn)Te or (Zn,Mn)Se. Generally, $N_0\alpha$ is fairly independent from the material, while $N_0\beta$ is large, negative and proportional to N_0 (i.e. increases as the size of a unit cell shrinks, for e.g. $N_0 |\beta_{CdTe}| < N_0 |\beta_{ZnTe}|$).

These spin-dependent coupling result from short-range exchange interactions between the effective mass-carriers (electron from the s band at a position $\vec{r}_e$ and holes from the p band, at $\vec{r}_h$) and the localized d electrons at $\vec{R}$ which take a Kondo-like form[8]:

$$H_{spd} = -J_{sd}(\vec{R} - \vec{r}_e)\vec{\sigma}_e \cdot \vec{S} - J_{pd}(\vec{R} - \vec{r}_h)\vec{\sigma}_h \cdot \vec{S} \tag{1.43}$$

Following the conventional notations, the Kondo Hamiltonian is expressed as a function of the pure spin of the free carriers, but it can also be expressed as a function of $\vec{J}$ (by replacing $\vec{\sigma}_h \mapsto \vec{J}$ and $J_{pd} \mapsto J_{pd}/3$).

Two mechanism contribute to this exchange coupling:

- A ferromagnetic coupling resulting from direct exchange interaction: Two electrons with parallel spins tend to avoid each other due to the Pauli exclusion principle, thus the Coulomb repulsive interaction is reduced compared to the case of anti-parallel spins.
- A spin-dependent hybridization of the Mn electrons with the free carriers which results in an anti-ferromagnetic coupling between the free carrier and the Mn spin, called kinetic exchange.

The hybridization is forbidden for an electron from the s band at $k = 0$ because of symmetry (s and d wave-functions are orthogonal in zinc-blende structures). The s-d exchange is only governed by direct exchange. But p-d hybridization is allowed, and has the main contribution to the hole-Mn exchange. Hybridization is modeled by the Anderson Hamiltonian, which describes

[8] The Kondo Hamiltonian is directly linked to the energy shift discussed previously: Applying the virtual crystal approximation to the matrix element $\langle \psi_{n,\vec{k}} | H_{spd} | \psi_{n,\vec{k}} \rangle$, where $\psi_{n,\vec{k}}$ is a delocalized states ($\psi_{n,\vec{k}}(\vec{r}) = \frac{1}{\sqrt{V}} e^{i\vec{k}.\vec{r}} u_{n,\vec{k}}$, $k \approx 0$), we find that the energy shift is proportional to the number of Mn atom (Nx), to the probability for the carrier to be on the Mn site $1/V$, and to $\alpha = \int_V d\vec{r} u^*_{\Gamma_6,0}(\vec{r}) J_{sd}(\vec{R}-\vec{r}) u_{\Gamma_6,0}(\vec{r})$, $\beta = \int_V d\vec{r} u^*_{\Gamma_8,0}(\vec{r}) J_{pd}(\vec{R}-\vec{r}) u_{\Gamma_8,0}(\vec{r})$. Eqns. 1.42 are recovered.

hopping from valence states to the Mn d-shell and vice-versa. The Anderson Hamiltonian can be transformed into a Kondo Hamiltonian as done for the first time by Schrieffer and Wolf in 1966 [35]. It can be seen as a second-order perturbation-theory effect[9] involving virtual transitions of an electron between the d orbitals of the Mn and valence band states. Assuming the Mn spin is in $S_z = +5/2$ (Mn electrons up), the energy shift of a Bloch state can be expressed as a function of[10]:

- ϵ_d: the one-electron energy of a $3d$ orbital ($\approx -3.7eV$).
- U: the Coulomb repulsion energy between opposite spin electrons located on the same d orbital ($\approx 9eV$).
- ϵ_v: the energy of the valence-band maximum ($= 0eV$).
- V_{pd}: the transfer integral between a neighboring p orbital and the d states ($= 1.1eV$).
- V: the volume of the crystal

Using these quantities, the energy shift for a given spin-projection of the valence electron are given by:

$$\Delta E_\uparrow \approx \frac{V_{pd}^2}{V}\frac{1}{\epsilon_v - \epsilon_d} \tag{1.44}$$

$$\Delta E_\downarrow \approx \frac{V_{pd}^2}{V}\frac{1}{\epsilon_v - (\epsilon_d + U)} \tag{1.45}$$

Hence:

$$\Delta E_\uparrow - \Delta E_\downarrow \propto -\frac{V_{pd}^2}{V}\frac{U}{(\epsilon_v - \epsilon_d)\,(\epsilon_v - (\epsilon_d + U))} \geq 0 \tag{1.46}$$

This coupling is anti-ferromagnetic, as stated earlier. It corresponds, apart from a numerical factor[11], to the exchange interaction derived from the Schrieffer-Wolf transformation. The expression of $N_0\beta$ in DMS can be derived from this microscopic approach:

$$N_0\beta = \frac{(4V_{pd}^2)}{S}\frac{U}{(\epsilon_v - \epsilon_d)\,(\epsilon_v - (\epsilon_d + U))} \tag{1.47}$$

where $S = 5/2$.

[9] It can be seen, but it cannot be treated mathematically by perturbation theory. This is all the point of the Schrieffer-Wolf transformation, which is a canonical transformation.

[10] The numerical values are adapted from the donor and acceptor energies and the transfer integral given in [36].

[11] This factor varies in the literature, depending on how V_{pd} is defined.

1.3.2 Effect of Confinement on Exchange Interactions

Knowing what are the exchange constants α and β in bulk DMS, what should we expect in a Mn-doped quantum dot? Compared to the case of bulk materials, the hole-Mn interaction cannot be considered isotropic, because of the strained-induced light-hole/heavy-hole splitting. In the heavy-hole approximation, a flip of the pure spin of the hole from $J_z = 3/2$ leads to a light-hole state at a different energy so hole-Mn flip-flop are energetically forbidden. This means we have to consider a Hamiltonian of the form:

$$H = -I_{e-Mn}\vec{\sigma}.\vec{S} + I_{h-Mn}J_z.S_z - \frac{2}{3}I_{e-h}J_z.\sigma_z \tag{1.48}$$

This equation gives the exciton-Mn (XMn) levels in a first approximation: we have neglected anisotropic long-range exchange interaction and valence band mixing. However, this degree of approximation is often sufficient. Typically, $I_{e-h} \approx 0.8meV$, and the carrier-Mn exchange constants can reach $I_{h-Mn} \approx 300\mu eV$, $I_{e-Mn} \approx 100\mu eV$. Considering electron-hole exchange, bright excitons are split from dark excitons by I_{e-h}. Then, considering the interaction with the Mn, these levels are further split into six levels depending on the relative projection the Mn and the exciton spin. These six lines are equally split by $1/2(3I_{h-Mn} + I_{e-Mn})$ for a bright exciton, and $1/2(3I_{h-Mn} - I_{e-Mn})$ for a dark exciton. The energy levels are twice degenerate (as the energy does not change if we reverse simultaneously S_z, σ_z and J_z). This level structure (depicted in Fig. 1.6) accounts well for the spectra observed experimentally: the Mn doped quantum dot presents six lines, as the spin-state of the Mn atom fluctuates during the time-averaged PL measurement. The remarkable property of this system is that the spin-state of the Mn can be accessed optically: single-shot detection of a photon at a given energy and with a given polarization is a measurement of the spin-state of the Mn atom. The biexciton-states are degenerate as the Mn atom is interacting with two spin-singlets. Recombination from the X_2Mn levels to the non-degenerate XMn levels also results in a sextuplet structure of the biexciton PL.

What are the values expected for I_{e-Mn} and I_{h-Mn}? As the exchange interaction is short-range, in first approximation, we can consider that the exchange constants are proportional to the probability of presence of the carrier at the Mn site[12]:

$$\begin{aligned} I_{e-Mn} &= \alpha \left|F_e(\vec{R})\right|^2 \\ I_{h-Mn} &= -\beta/3 \left|F_h(\vec{R})\right|^2 \end{aligned} \tag{1.49}$$

From these relation, we can derive the order of magnitude of the exchange interaction expected. We will consider that the envelope function of the carriers is given by:

$$F_{e,h} = \sqrt{8/V}\cos(k_x x)\cos(k_y y)\cos(k_z z)$$

where the quantum dot is approximated by a square-box potential with infinite barriers. If we take $V = 2 * 10 * 10nm^3$, a Mn atom at the center of the dot ($\vec{R} = 0$) and knowing that $\alpha = -15meV.nm^3$ and $\beta = 50meV.nm^3$, we obtain $I_{e-Mn} \approx 60\mu eV$ and $I_{h-Mn} \approx 80\mu eV$. This simple estimation fails to predict the observed exchange constants CdTe/ZnTe quantum dots

[12]Such relation is straightforward to obtain using Eqn. 1.43 and the envelope function formalism (assuming that the variation of the envelope function can be neglected on the space-scale of the exchange interaction)

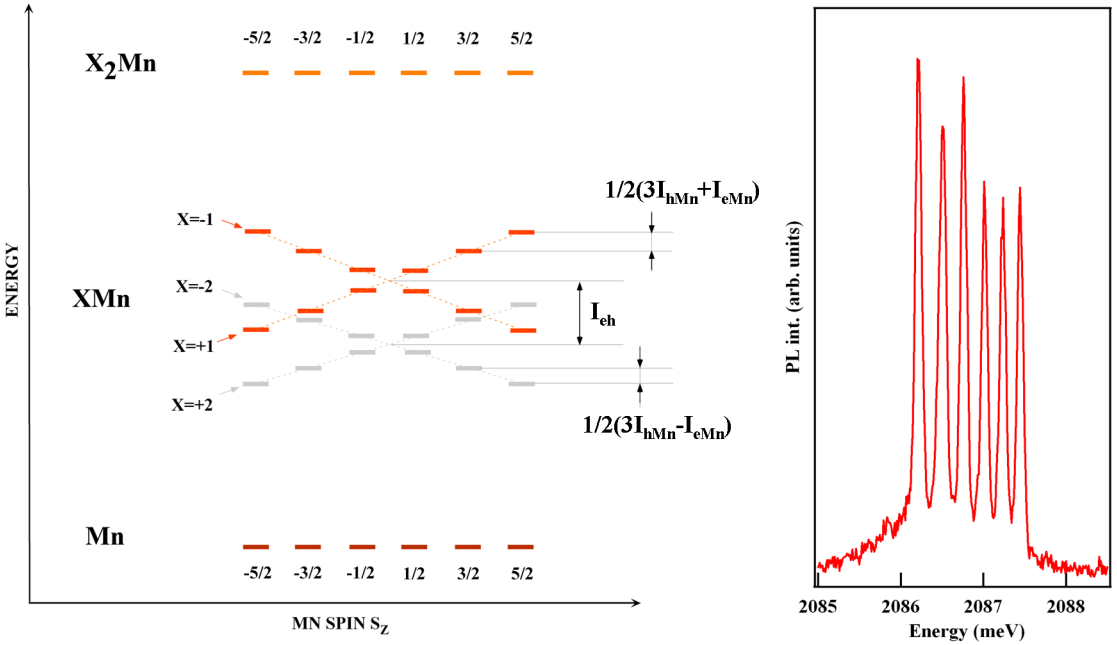

Figure 1.6: Energy levels of the ground-state, the exciton and the biexciton in a Mn-doped quantum dot. The levels are sketched as a function of the Mn spin S_z. Dark states are represented in grey. Optical transitions from the bright states of the XMn complex result in a six-line PL spectra shown on the right.

[27], where I_{h-Mn} is typically *three times larger* than I_{e-Mn} while the ratio expected in this simple approach is $\beta/(3\alpha) \approx 4/3$. The ratio is more relevant than the absolute values which depend a lot on the quantum dot's volume.

This could be because our estimation is too rough: as pointed out earlier, the exchange constants accessed optically result from exchange interactions between the magnetic atoms and effective mass carriers from the edge of the bands that is to say $\vec{k} = 0$. However, localized carriers (in quantum dots or quantum wells) have a finite wave-vector $\vec{k}$: considering an infinite confinement along z, of height L, the lowest wave-vector is $k_z = \pi/L$. Now, at finite $\vec{k}$, a mixing between the conduction and valence band occurs as we have seen from the elements of kp-theory presented earlier. For the electron, the consequence is a decrease of the ferromagnetic constant J_{e-Mn} with increasing confinement as the electron acquires a valence-band character which interacts antiferromagnetically with the Mn. More precisely, the reduction of the coupling constant with increasing $\vec{k}$ is the sum of two contributions: (i) kinetic exchange allowed by the mixing with the valence band [37] (ii) a reduction of the direct exchange term (calculated using a tight-binding model initially developed in [38]). But (i) dominates. In the case of a heavy hole, it is the k-dependence of the kinetic exchange [38], and not the mixing with the conduction band that dominates the decrease of the overall exchange. As proposed by Battacharjee [39], and developed by L. Maingault in his PhD thesis [40], these effects can be included in the envelope function formalism[13]:

$$I_{e-Mn} = \alpha \left| F_e(\vec{R}) - A(\partial_z^2 F_e(\vec{R}) + \partial_\rho^2 F_e(\vec{R})) \right|^2 + \beta \left((C-B) \left| \partial_z F_e(\vec{R}) \right|^2 + C \left| \partial_\rho F_e(\vec{R}) \right|^2 \right)$$

[13] As k terms are included in reciprocal space, they can be expressed as derivatives of the envelope function in real space.

$$I_{h-Mn} = -\beta \left| F_h(\vec{R}) - G(\partial_z^2 F_h(\vec{R}) + \partial_\rho^2 F_h(\vec{R})) \right|^2 \quad (1.50)$$

with $A = 10.3$ Å^{-2}, $B = 0.781$ Å^{-2}, $C = 19.8$ Å^{-2} and $G = 4.23$ Å^{-2}. A and G arise from the k-dependence of the coupling constants and B and C arise from the mixing with electron states, F_e and F_h are the electron and hole envelope functions which were calculated in [40], using a variational calculation in a realistic energy potential, and Coulomb interaction between the electron and the hole. The main results are that if we neglect the effect of the $\vec{k}$ dependence of the exchange constants and mixing between the conduction and the valence band, I_{h-Mn} should be two times smaller than I_{e-Mn}, because the hole is weakly confined in the quantum dots considered here (this is so true that most of the confinement comes from the attractive Coulomb interaction with the electron). Then, if eqn. 1.50 are considered, the $e-Mn$ exchange interaction is diminished by 15% due to $e-h$ hybridization, while I_{h-Mn} is mostly unaffected. Hence, even with this elaborate approach, the expected ratio is around 0.6, which does not match with what is observed experimentally. Further investigation is needed. However, the effective Hamiltonian is still a very good tool to describe the observed magneto-optical behaviour of our quantum dots. We have restricted ourselves to a qualitative description of the interactions between the Mn and free-carriers but we recommend to a curious reader the book of G. D. Mahan [41] where, starting from a microscopic description with Coulomb interactions, an effective spin-spin Hamiltonian is derived. We also recommend Laurent Maingault's PhD thesis [40] where exchange interactions with the Mn in CdTe/ZnTe quantum dots have been quantitatively studied using variational calculations. At last, in [33], chap 13, a detailed review on DMS can be found.

The last ingredient we need to add is the light/heavy hole mixing, which has important consequences on the spectra observed experimentally.

1.3.3 Beyond the Heavy-Hole Approximation and Isotropic Electron-Hole Exchange

In order to take into account valence-band mixing (VBM), a projection of the $\vec{J}$ operator in the heavy-hole subspace is performed. The operator $\tilde{J}_+$ for instance is defined by:

$$\tilde{J}_+ = \begin{pmatrix} \left\langle \tilde{\Uparrow} \right| J_+ \left| \tilde{\Uparrow} \right\rangle & \left\langle \tilde{\Uparrow} \right| J_+ \left| \tilde{\Downarrow} \right\rangle \\ \left\langle \tilde{\Downarrow} \right| J_+ \left| \tilde{\Uparrow} \right\rangle & \left\langle \tilde{\Downarrow} \right| J_+ \left| \tilde{\Downarrow} \right\rangle \end{pmatrix} \quad (1.51)$$

Which yields:

$$\tilde{J}_+ = \eta \begin{pmatrix} 0 & -2\sqrt{3}e^{-2i\theta'_s} \\ 0 & 0 \end{pmatrix} + \eta^2 \begin{pmatrix} 0 & 0 \\ 2e^{4i\theta'_s} & 0 \end{pmatrix} \quad (1.52)$$

$$\tilde{J}_- = \eta \begin{pmatrix} 0 & 0 \\ -2\sqrt{3}e^{2i\theta'_s} & 0 \end{pmatrix} + \eta^2 \begin{pmatrix} 0 & 2e^{-4i\theta'_s} \\ 0 & 0 \end{pmatrix} \quad (1.53)$$

$$\tilde{J}_z = \begin{pmatrix} 3/2 & 0 \\ 0 & -3/2 \end{pmatrix} + \eta^2 \begin{pmatrix} -1/2 & 0 \\ 0 & 1/2 \end{pmatrix} \quad (1.54)$$

Using eqn. 1.36, the energy spectra is then given by:

$$\begin{aligned} H_{XMn} = & -\tfrac{2}{3} I_{eh} \left(J_z \sigma_z + \tfrac{1}{2} \left(\tilde{J}_+ \sigma_- + \tilde{J}_- \sigma_+ \right) \right) - I_{eMn} \vec{S} \vec{\sigma} \\ & + I_{hMn} \left(J_z S_z + \tfrac{1}{2} \left(\tilde{J}_- S_+ + \tilde{J}_+ S_- \right) \right) + H_{LR}^{anis} \end{aligned} \quad (1.55)$$

In this expression, we have neglected the contribution of the long-range exchange interaction in the dark-bright exciton splitting $I_{eh}^{lr} = 0$. This assumption is somewhat arbitrary (there is no general consensus on the respective contribution of long range and short-range to the exchange term $J_z\sigma_z$.). Since we assume that all the diagonal electron-hole exchange comes from the short range exchange, we overestimate the non-diagonal s-p exchange term induced by the VBM at a given η. H_{LR}^{anis} is the non-diagonal term of the long-range exchange interaction (due to an anisotropy of the confinement) introduced earlier. It is given by:

$$H_{LR}^{anis} = \frac{1}{2}\left\{\delta_1 e^{2i\phi_1} \left|\Downarrow\uparrow\right\rangle \left\langle\Uparrow\downarrow\right| + \delta_1 e^{-2i\phi_1} \left|\Uparrow\downarrow\right\rangle \left\langle\Downarrow\uparrow\right|\right\} \tag{1.56}$$

Experimentally, H_{LR}^{anis} is responsible for a linear polarization-rate in the emission and modifies the spacing between the six PL lines. Similarly to neutral non magnetic quantum dots, the observed polarization-rate and the exact level structure also depends on the VBM through short-range exchange. Only a detailed analysis of the anisotropy of polarization and a magneto-optical study[14] can help discriminating the two effects. The overall effect is particularly visible when the Mn is not at the center of the dot. Then, I_{h-Mn} and I_{e-Mn} can be smaller than δ_1 or $\eta I_{e-h}/2$, and the latter dominate the PL structure.

The Hamiltonian H_{XMn} presents terms in $\tilde{J}_-S_+$ et $\tilde{J}_+S_-$ which admix bright and dark states through a hole-Mn flip-flop: the first order in η couples $|-2, S_z\rangle$ with $|+1, S_z - 1\rangle$. Yet, as we see in the scheme of Fig. 1.7, for $S_z < 0$, these levels correspond to the highest dark levels and the lowest bright levels, which are close in energy, leading to dark-bright mixing. Eventually, when $|-2, -1/2\rangle$ is almost degenerate with $|+1, -3/2\rangle$ (Fig. 1.7) or when $|-2, -3/2\rangle$ is almost degenerate with $|+1, -5/2\rangle$, the quantum dot presents an additional PL line which results from the coherent coupling of these two states. This effect is particularly visible when I_{h-Mn} and I_{e-Mn} are large, leading to an overlap between dark and bright uncoupled states. Dark-bright mixing can also occur through electron-Mn flip-flop (terms in $\sigma_+S_- + c.h.$). However, at $B = 0T$, levels coupled through an electron-Mn flip-flop cannot be degenerate. The mixing induced by this coupling shortens the lifetime of a dark exciton (which recombines through its bright part) but does not modify the PL structure at $B = 0T$.

At last, to perfectly match the experimental spectra, an additional Hamiltonian term is considered for the exciton:

$$H_v = -\zeta S_z^2 \tag{1.57}$$

and for the biexciton,

$$H_v' = -2\zeta S_z^2 \tag{1.58}$$

This term reproduces an experimental feature that is clearly observed in Fig. 1.7: the exciton lines are unequally spaced, and a fine analysis shows that the biexciton states are twice as much shifted [42]. This feature results from virtual transitions of the hole towards the P-shell, which result, in second order perturbation theory to a correction of the XMn levels in S_z^2 [43]. We find that ζ can typically reach $20\mu eV$ in our quantum dots. These terms will be taken in account in future experiments, where the position of the XMn levels needs to be determined with a high precision.

[14] The use of a high magnetic-field B_z is used to evidence dark/bright exciton anti-crossing. The splitting of the anti-crossing, either proportional to I_{e-Mn} or ηI_{h-Mn}, allows to determine precisely these quantities.

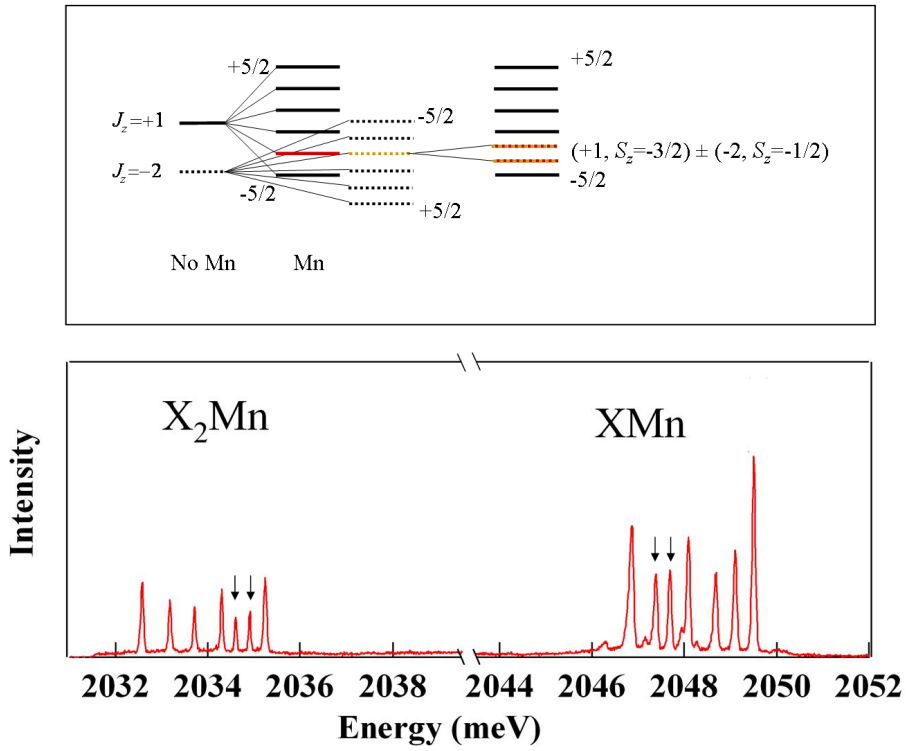

Figure 1.7: XMn and X_2Mn PL spectra of a Mn-doped quantum dot presenting seven lines. As a result of VBM, $|+1,-3/2\rangle$ is coherently coupled to $|-2,+1/2\rangle$ by a hole-Mn flip-flop. Since these levels are degenerate (c.f. scheme displayed above) it results in two admixed states which share the oscillator strength of the bright state $|+1,-3/2\rangle$. Recombination from the X_2Mn level ($|X_2,-3/2\rangle$) to these admixed states and recombination from these admixed states to the ground state are indicated by arrows.

Chapter 2

Optical control of a single spin: spin initialization and read-out

Contents

We present in this chapter the micro-photoluminescence experiment and the samples studied in this thesis. After that, we will present the achievement of optical orientation of the localized Mn spin using quasi-resonant excitation and optical-pumping of a Mn spin-state using resonant excitation. We will limit ourselves to a descriptive analysis and a qualitative explanation of the physics ruling these two processes.

2.1 Sample Growth

The samples used in this thesis are CdTe/ZnTe quantum dots. The growth is performed on a [001] ZnTe substrate in a II-VI Molecular Beam Epitaxy (MBE) chamber. 6.5 monolayers of CdTe are deposited by ALE (Atomic Layer Epitaxy) at $280°C$. The 2D to 3D transition is induced by the deposition of amorphous tellurium. The amorphous Te layer decreases the surface-energy cost associated to the creation of 3D islands. Without this deposition, a further increase of the CdTe layer results in a plastic relaxation of the strains (creation of dislocations) rather than an elastic relaxation of the strains (formation of coherent 3D islands). This is due to the low dislocation formation energy in II-VI materials.

The growth technique has slightly evolved compared to the one presented in [44, 29]:

- The Mn is now included during the growth of the CdTe layer (instead of growing a $Zn_{0.94}Mn_{0.06}Te$ buffer and using segregation of the Mn atom in a thin ZnTe spacer between the ZnMnTe buffer and the CdTe quantum dot layer).

- The amorphous tellurium is deposited around $150-160°C$ (instead of room temperature).
- In some samples, Mg has been included in the barriers to increase the confinement of the hole.

Then, the dots are capped by a 100 nm ZnTe layer. The Mn concentration is adjusted to optimize the probability of detecting one Mn per dot, which corresponds roughly to a density of Mn equal to the density of quantum dots.

2.2 Experimental set-up

Spatial and spectral selection are the two basic requirements to achieve micro-photoluminescence experiments i.e. to study physical properties at a single dot level.

The spatial resolution fixed by the limit of diffraction of the microscope objective ($N.A. = 0.55$) is $d = \lambda/N.A.$ which gives a spot diameter of $d \approx 1.1\mu m$. The average density of quantum dots is $50\text{QDs}/\mu m^2$. The spatial resolution obtained using a microscope objective can be further improved. One option is to use aluminum masks obtained by electronic lithography. Optical excitation is performed through apertures which can be as small as $0.2\mu m$. High spatial resolution can be achieved thanks to this technique. However, it presents a few drawbacks that pushed us to abandon it and to develop an other technique: the use of micro-lens (i.e. solid immersion lens). The problems with aluminum masks were that the search for Mn-doped quantum dots was fastidious, and that reflected laser light became a real issue when excitation and detection were close in energy.

A micro-lens is a hemisphere with a refractive index ($n \approx 2.25$) close to the one of the semiconductor ($n_{ZnTe} \approx 3$ [45]). The focusing action allows a decrease of the diffraction limit of the focal spot area and an increase of the collected signal by a factor of 4 [46]. The $1mm$ mico-lens is held on the bare surface of the sample using a $800\mu m$ pinhole screwed on the sample-holder. It is possible to study a given quantum dot for an arbitrary time using irregularities of the sample surface such as silver-paint particles as points of reference. However, once the micro-lens is dismounted, the quantum dot is lost, which is a disadvantage compared to aluminium masks.

A schematic view of the optical set-up is given in Fig. 2.1. The laser sources are two rhodamine 6G CW dye lasers pumped by a 532nm diode-pumped solid-state laser. These were used for the experiments in Chapter 2, 3, 4 and 6. More recently, a single mode CW dye ring laser was installed. It was used for the experiments in Chapter 5. At last, a pulsed Ti-Sapphire laser coupled to an OPO (Optical Parametric Oscillator) was used to perform PL decay measurements.

To realize the optical orientation and optical pumping experiments described in the following chapters, we need to produce trains of light of controlled helicity and duration ($\approx$ 100's of ns). This was achieved using an Electro-Optic-Modulator (EOM) and Acousto-Optic Modulators (AOM). The AOMs permit to switch the laser excitation ON or OFF[15] with a rise time of 10 ns,

[15] An AOM is made of a crystal in which a high frequency generator ($f = 80MHz$) produces a sound-wave with a wavelength $\lambda = C/f \approx 50\mu m$, where C is the speed of sound in the crystal $C \approx 4000m.s^{-1}$. By such means, a standing wave of pressure that creates a periodic modulation of the crystal's refractive index is generated. The light sent trough the crystal experiences Bragg diffraction. The intensity of the diffracted light depends on the amplitude of the sound wave. Collecting the first diffracted order, the light is turned ON or OFF depending if a sound-wave is created by the high frequency generator or not. The optical rise-time is a function of the acoustic transit time across the optical beam. Therefore, to operate at the highest speed, we focus the optical beam down to a small spot inside the modulator.

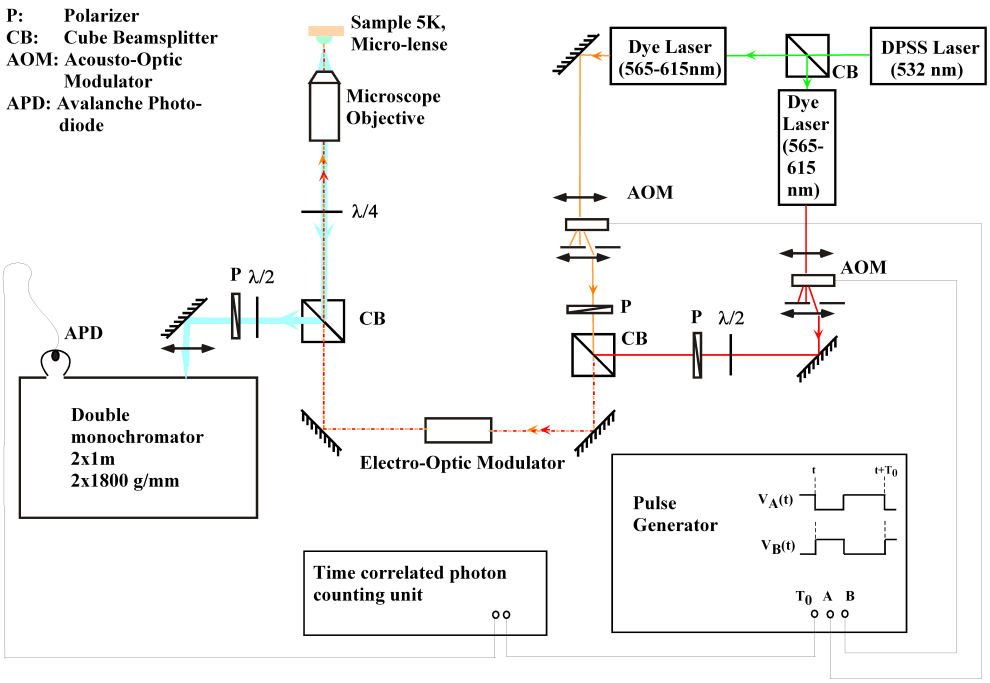

Figure 2.1: Schematic view of the micro-spectroscopy set-up used for time-resolved optical pumping experiments.

while the EOM[16] permits to switch the excitation polarization with a rise time of 5 ns[17]. Then, the laser beams go through wave-plates depending on the desired helicity, are overlapped and are focused on the sample using a microscope objective and a micro-lens. The circular polarization is obtained using a $\lambda/4$ located just before the microscope objective in order to avoid any ellipticity introduced by mirrors.

For two wavelength experiments (i.e. with two lasers), great care has to be taken so that the two beams overlap. Two pinholes distant by one meter are used as reference points. Then, the mode are spatially filtered[18] (not represented on Fig.2.1). The sample is either in a cold finger cryostat or in a helium bath cryostat, where superconductive coils can be used to apply a magnetic field up to $11T$ in a Faraday geometry. When using the cold-finger cryostat, a magnetic field up to $150mT$ can also be applied using permanent magnets in a Voigt or Faraday geometry. These magnets are mounted on a translation stage synchronized with the detection.

We work in a back-reflection geometry: the circularly polarized signal is collected through the same microscope objective, and converted into a linear polarization by the $\lambda/4$. Then, a $\lambda/2$ at 0 or 45° followed by a polarizer controls the helicity of the detection (either co or cross-circularly polarized with the detection). After that, the signal is focused on the monochromator slits. Then,

[16]The principle of operation of an electro-optic modulator is based on the modification of the refractive index of a nonlinear crystal by an electric field in proportion to the field strength. It can thus be seen as a voltage-controlled half-waveplate. Its risetime is controlled both by the crystal's capacitance and the electronic driver. As the crystal is also piezo-electric, the applied voltage can introduce mechanical vibrations, which themselves can affect the refractive index. The consequence is that around certain modulation frequencies, the EOM shows a sinusoidal noise around the desired polarization.

[17]Using a polarizer on its output, the EOM can also be used as an ON/OFF switch, faster than the AOMs.

[18]A microscope objective is used to focus the beams on a $10\mu m$ pinhole. After the pinhole, a lens collimates the diffraction pattern, and a pinhole only allows the Airy disk to go through.

it is either detected on a camera for sample imaging or dispersed twice by 1800g/mm gratings and sent on a low noise CCD camera[19] or an APD[20]. Alternatively, the two circular polarization of the PL can be detected simultaneously on two areas of the CCD, adding , before the $\lambda/2$ a birefringent prism to the detection path. One of the dye lasers Lyot filter[21] is motorized and synchronized with the CCD allowing automatized PLE measurement[22]. In time-resolved optical pumping experiments, a pulse generator drives the AOMs and the EOM and gives the clock counts to a time correlated photon-counting unit. The latter allows to integrate APD counts as a function of the delay between the photon arrival-time and the clock signal.

Using these samples and set-up, we have developed an initialization and and read-out scheme, demonstrating that the spin of a Mn atom embedded in a quantum dot could be manipulated optically. In the following, we present these experiments.

2.3 Optical orientation

2.3.1 A Simple Picture of Photo-induced Spin-orientation

Photo-induced spin orientation of a Mn spin was theoretically considered in [47]. The underlying idea in this paper to explain Mn spin-orientation, is the existence of thermalization processes within the XMn complex. Let us imagine that the Mn spin is continuously excited with $\sigma+$ light and that the spin of the photo-created carriers is well conserved during the relaxation to the ground exciton state (XMn). The Mn spin coupled to the photo-injected electron-hole pair is subject to an effective magnetic field. The direction of this magnetic field is controlled by the spin of the hole (anti-ferromagnetic interaction with the Mn, giving rise to an effective magnetic field along $-\vec{u}_z$, if the light is $\sigma+$). Due to thermalization among the XMn levels, the Mn spin should become polarized (down). This polarization should be understood as a dynamic equilibrium: when an electron-hole pair is injected, the Mn spin tends to be polarized; once the electron-hole pair has recombined, relaxation of the Mn spin tends to equilibrate the population of the six Mn spin-states. Considering that the polarization due to spin-flips within the XMn levels takes place on a characteristic time-scale τ_{XMn}, while the relaxation of the Mn alone takes place on a time-scale of τ_{Mn}, the condition to obtain optical orientation of the Mn spin is $\tau_{XMn} < \tau_{Mn}$.

2.3.2 Experimental Evidence of Optical Orientation

Optical orientation of the Mn spin is performed using circularly polarized light, tuned on an excited state of the quantum dot. These conditions of excitation will be hereafter referred to as *quasi-resonant* excitation (as opposed to *resonant* excitation, that we will use for an excitation tuned on one of the ground-XMn levels). Experimentally, we search for excited states presenting an important polarization-rate.

In order to observe photo-induced spin orientation, the linear polarization of the excitation laser was modulated between two orthogonal states by switching an electro-optic modulator with a rise time of $5ns$, and converted to circular polarization with a quarter-wave plate. The circularly

[19] The CCD camera is 1600×200 pixel silicium array cooled at $-50°$C by a Peltier.

[20] The APD is a $50\mu m^2$ chip with a $50ps$ jitter.

[21] A Lyot filter is an optical monochromatic filter controlling the laser wavelength.

[22] Photoluminescence excitation spectroscopy (PLE) consists in shining laser light of well-known wavelength on a quantum dot. When the laser energy corresponds to an optically active excited state of the system, the light is absorbed. Then, the system relaxes and re-emits a photon at the energy of the ground exciton state. Hence, scanning the laser wavelength while detecting the photoluminescence from the ground state allows to probe the excited states of the system.

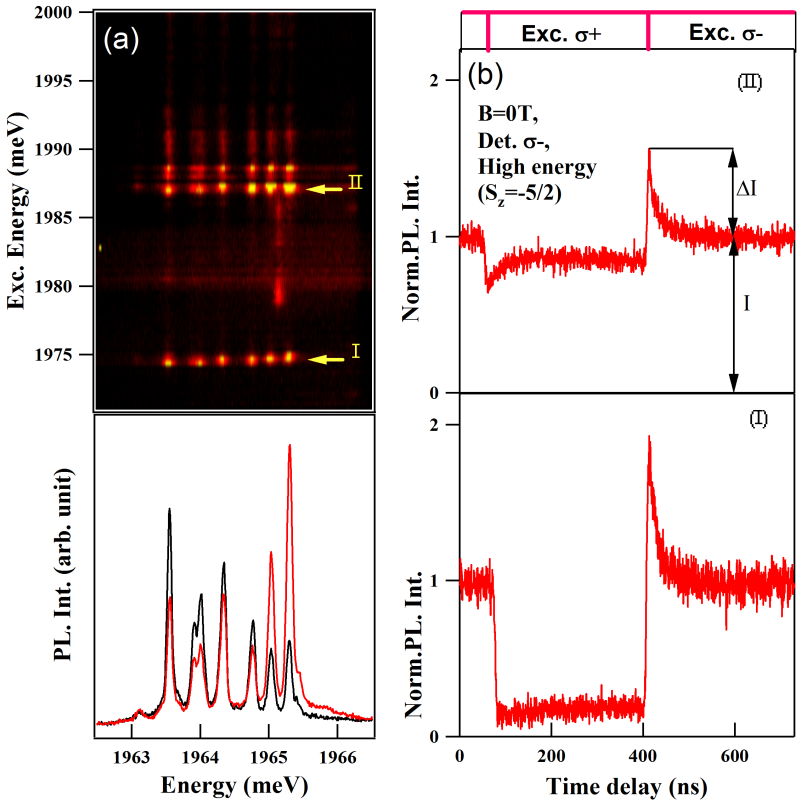

Figure 2.2: (a) PL and PLE spectra of a Mn-doped quantum dot at $B = 0T$. The PL spectra are taken at two different energies of excitation, and detected in circular polarization under alternate $\sigma - /\sigma+$ excitation. For the black (resp. red) curve, the laser excitation is at $1987meV$ (resp. $1987.4meV$). (b) The $\sigma-$ PL of the high energy line (corresponding to $S_z = -5/2$) is time-resolved under $\sigma + /\sigma-$ modulated excitation. The excitation sequence is displayed above. The PL transient labeled (I) (resp. (II)) was observed under resonant excitation at $1975meV$ (resp. $1987meV$).

polarized PL of a given XMn line is detected by a fast avalanche photodiode in conjunction with a time correlated photon counting unit with an overall resolution of $50ps$.

The time-evolution of the $\sigma-$ PL of the high energy line (corresponding to $S_z = -5/2$) is shown in Fig. 2.2 b) for two different excitation energies: $\approx 35meV$ (resp. $\approx 20meV$) above the PL energy for the curve (I) (resp. (II)).

First, we focus on the common features of these two curves. Under the conditions of excitation displayed in Fig. 2.2, switching the circular polarization of the excitation produces a change of the σ^- PL intensity with two transients: first an abrupt one with the same sign for all six lines, reflecting the population change of the spin polarized excitons; then a slower transient reflecting an increase or a decrease of the occupation of the detected spin state. This slow transient has an opposite sign for the two extreme PL lines (*i.e.*, when monitoring the Mn spin states $S_z = +5/2$ and $S_z = -5/2$, Fig. 2.3). This confirms that the slow transient observed corresponds to a photo-induced orientation of the Mn spin.

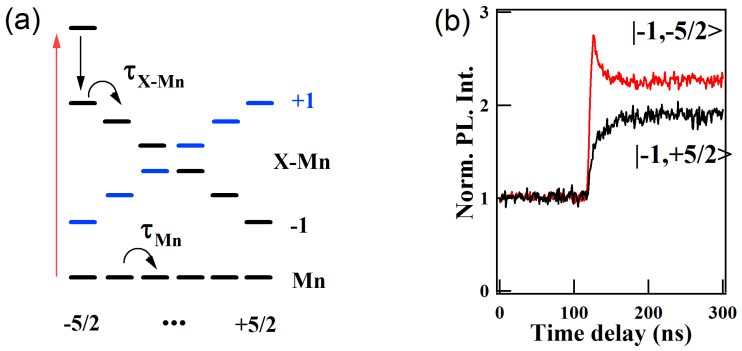

Figure 2.3: (a) Simplified level diagram of a Mn-doped quantum dot, as a function of the Mn spin projection S_z. Only the bright exciton are represented. (b) PL transients recorded in $\sigma-$ polarization on the high ($S_z = -5/2$) and low ($S_z = +5/2$) energy lines of the XMn complex as the laser excitation is switched from $\sigma+$ to $\sigma-$.

Injection on the bright XMn levels of spin-polarized excitons is schematized in Fig. 2.3(a). For the sake of simplicity, we omit the dark exciton states which should be included for a quantitative analysis. Following the simple picture described earlier, we consider that the dynamics can be described by two spin relaxation times, one for the Mn alone τ_{Mn} and one within the X-Mn complex τ_{X-Mn}. As spin orientation results from a cumulative effect of relaxation in presence of the exciton, it can be performed only if τ_{X-Mn} is shorter than τ_{Mn}. When exciting one of the low energy excited states of the QD, spin-relaxation of the photo-created carriers is slow enough to consider that the injected exciton is $|+1\rangle$. Considering thermalization among the XMn levels, relaxation of the Mn spin within the X-Mn system is driven by the anti-ferromagnetic interaction with the spin polarized carriers which have been injected. As shown in Fig. 2.3, where we focus on the spin-transient corresponding to a $\sigma+/\sigma-$ switch, the observed orientation of the Mn spin is consistent with this process. We observe an increase of the $|-1,+5/2\rangle$ PL reflecting an increase of the population of the $+5/2$ Mn spin state, while the population of $-5/2$ decreases: the Mn spin aligns along the effective field of the photocreated exciton (opposite to the exciton spin $|-1\rangle$).

2.3.3 Spin Selectivity of the Excitation

The photo-induced spin orientation also depends on the energy of the quasi-resonant excitation. As shown in Fig.2.2, the amplitude of the transient $\Delta I/I$ observed under co and cross-polarized excitation, and the overall polarization rate of the PL line strongly vary with the laser energy. The photo-induced Mn spin orientation is not only controlled by the polarization of the injected carriers but also by spin selectivity (which Mn spin-states are preferentially absorbent).

To illustrate spin-selectivity, we present in Fig. 2.2 (a), two PL spectra obtained by changing the laser excitation of only $0.4meV$ around the excited state (II). This energy difference is smaller than the width of the excited state (II). We can see a dramatic change between the relative heights of the six PL lines. At $1987meV$ (black curve), the injection is mainly on the low energy line. As the laser is set $0.4meV$ above, we observe the opposite: the injection is predominantly on the high energy XMn levels. Moreover, it appears clearly that at this energy (red curve), the spin state $\pm 5/2$ are selectively excited: the overall PL on the high and low energy lines is higher than

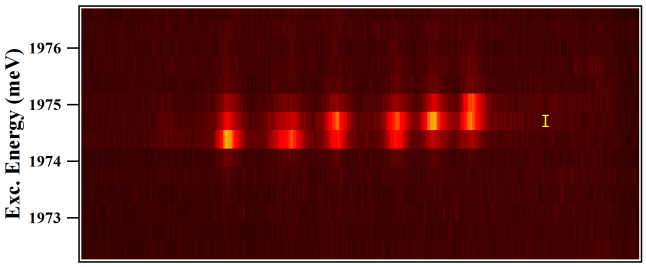

Figure 2.4: Detailed circularly co-polarized PLE of the excited state labeled (I) in Fig. 2.2.

for the overall PL corresponding to $\pm 3/2$ and $\pm 1/2$. Spin selectivity is also clearly observed on the lowest excited state (I) (Fig. 2.4): a laser excitation tuned on the low energy side of the excited state mainly excites the low energy lines. When the laser excitation is on the high energy side, PL from the high XMn levels is larger.

Spin selectivity is already well understood in our system [48]. It is controlled by the exchange interaction of the photo-created carriers on an excited level with the Mn spin. The *spd* exchange in the latter is considerably lower than *spd* exchange for an exciton in the ground state. Indeed, the interesting quantum dots from an experimental point of view are the ones with a maximum inter-level splitting corresponding to a Mn located close to the center of the dot. A P-shell carrier for instance, presents a wave function with a node at the center so that it is only weakly coupled to the Mn (and not coupled at all if the Mn is at the center of the dot). This explains that $\sigma+$ excitation on the high energy side of the excited state tends to excite selectively the quantum dot when the Mn is in the $|+5/2\rangle$ spin state and to create a $|+1;+5/2\rangle$ exciton. However, in an anisotropic quantum dot, the fine structure of an excited state can be dominated by non-diagonal terms in the electron-hole exchange due to long-range exchange in an anisotropic potential. Then, the excited state presents an elliptically polarized fine structure which can be an issue for the injection of polarized excitons with a ± 1 spin.

Spin selectivity leads to a dynamical process similar to optical pumping (in which, as it will be further discussed, the selective optical excitation of a spin-state diminishes the probability to detect it). Both mechanisms, absorption selectivity and spin injection, depend on the structure of the excited states, resulting in a pumping signal which depends on the excitation energy (Fig. 2.2). An efficient pumping of the Mn spin can be performed within a few tens of ns, showing that at $B = 0T$, the spin relaxation time of the Mn alone is long enough compared to orientation process within the XMn levels.

2.4 Optical pumping

2.4.1 Efficient Initialization of a Mn Spin

After demonstrating that optical orientation is achievable, the next step is naturally to head toward a real initialization of the Mn spin. Optical initialization of resident carriers (electrons [49] or holes [3]) has been successfully achieved in semiconductor quantum dots. Optical pumping involves resonant excitation of a spin-selective transition. Under these conditions of excitation, any recombination to the other spin-state (mediated by hyperfine interaction for the optical

pumping of a hole or light/hole heavy hole mixing for the optical pumping of an electron) initializes the spin: the quantum dot no longer absorbs light, the resident carrier has been controllably brought to a spin-state opposite to the one coupled to the laser excitation.

To perform optical pumping on the Mn spin, we proceed similarly (Fig. 2.5). A laser tuned on the high energy line with a $\sigma-$ helicity drives resonantly the $|-1, S_z = -5/2\rangle$ transition. The photons address the Mn only if it is in the $S_z = -5/2$ state. The resultant exciton can radiatively recombine via the same channel, or a relaxation process can project the X-Mn system in a state with $S_z \neq -5/2$. Hence after a certain number of absorption-emission cycles, the probability of detecting the Mn in the $S_z = -5/2$ state should decrease. Again, the overall scheme depends on the same requirements than for optical orientation: the relaxation rate of the Mn spin when the quantum dot is empty ($\Gamma_{Mn,G}$) must be smaller than the relaxation rate of the Mn spin within the ground XMn complex ($\Gamma_{Mn,X}$). The efficiency of the process will be probed monitoring the $\sigma+$ PL from the low energy line, corresponding to the same Mn spin-state. PL from this low energy line relies on a spin relaxation of the exciton ($\Gamma_{X,Mn}$). We expect to be able to detect the spin initialization in real-time if $\Gamma_{X,Mn} > \Gamma_{Mn,X}$ (otherwise the spin initialization is faster than the detection path).

2.4.2 Experiment

The main features of the experiment are presented in Fig. 2.6 (ii). The quantum dot is periodically excited with a two color pump-probe sequence. The pump, tuned on the high energy line depletes $S_z = -5/2$. Then, a linearly polarized probe pulse, tuned on an excited state of the quantum dot injects excitons independently of the Mn spin state S_z[23] , driving back the Mn atom in a state where all spin states are roughly equiprobable. $\sigma+$ PL from the low energy line (also corresponding to $S_z = -5/2$) is recorded. During the pump pulse, spin relaxation of the exciton within its lifetime gives rise to a weak PL on the detected line. The intensity of the detected PL depends on the absorption of the pump laser, which is controlled by the occupation of $S_z = -5/2$. Therefore, the decrease of the PL observed during the pump pulse reflects the efficiency of the optical pumping process. The efficiency is then given by $\Delta I/I_0 \approx 75\%$. During the probe pulse, the amplitude of the PL depends on the population of $S_z = -5/2$, and increases overtime as the probe restores an even probability of having $S_z = -5/2$. The PL level at the beginning of the quasi-resonant pulse is a probe of the pumping efficiency reached at the end of the pump pulse. This is illustrated in Fig. 2.6(i) which presents the difference of the signal produced by the quasi-resonant probe when the pump was ON or OFF (the steady-state quasi-resonant PL is normalized to one). This difference reflects the population difference caused by optical pumping and its height, which reaches 75%, is another way to measure the efficiency of the optical pumping. The rapidity of the transient observed in Fig. 2.6(i) during the probe pulse depends on the intensity of the probe, whereas the transient observed during the pump pulse is controlled by the pump power. Experimentally, for this measure, the probe power is 10 times smaller than the pump pulse. The processes responsible for the orientation of the Mn spin are faster under quasi-resonant excitation than under resonant excitation (since the observed transient time is similar for very different powers). This point will be studied in depth in Chapter 4.

The process does not lead to pumping efficiencies as high as the one observed in the case of resident carriers initialization (above 99%). Reasonning with the simple picture of a dynamics controlled by incoherent processes (with characteric time-constants $\tau_{Mn,X}$ and $\tau_{Mn,G}$, Fig.

[23] We choose excited states with a weak spin-selectivity.

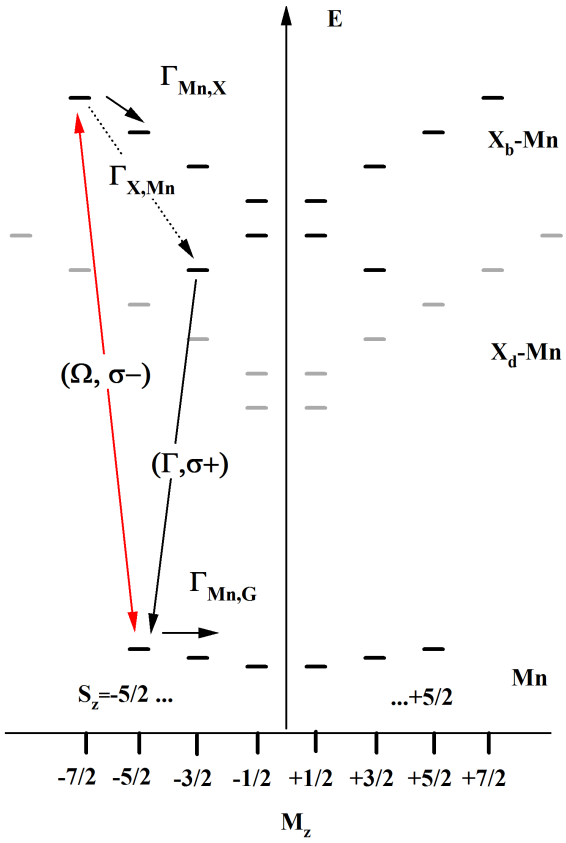

Figure 2.5: Energy levels of a Mn-doped quantum dot and experimental configuration. The states are displayed as a function of their total angular momentum M_z (Mn+Exciton) and energy E. The bright excitons X_b are displayed in black, the dark excitons are displayed in gray. For the resonant optical pumping, the quantum dot is resonantly excited on the state $S_z = -5/2$ with a $\sigma-$ laser with a Rabi frequency Ω. The scattered photons obtained after a spin-flip of the exciton (rate $\Gamma_{X,Mn}$) are recorded in the $\sigma+$ PL of the low energy line. The intensity of this PL is proportional to the population of the Mn spin state $S_z = -5/2$ and is used to probe the optical pumping efficiency.

2.5), this could be attributed to a fast relaxation of the Mn spin when it is in the ground state ($\tau_{Mn,G}$). However, this is ruled out by the following experiment: performing the same sequence as before without the probe pulse, we observe a completely flat PL signal (curve (iii) of Fig. 2.6). No transient is observed. This is the signature that the optical pumping performed by the resonant excitation is fully conserved over a few hundreds of ns. The optical pumping needs to be destroyed by a quasi-resonant excitation, in order to observe an optical pumping spin-transient. The full conservation of the Mn spin distribution will be further-confirmed by a straight-foward experiment discussed in the next chapter. At this point, the 75% efficiency is unclear. This shows that an ingredient is missing to fully understand the dynamics of the system which cannot be simply described by two relaxation rates. We leave this question for now and focus on further experimental insights on the optical pumping mechanism.

The figure 2.7 presents the amplitude and the time-evolution of the fluorescence signal detected on the low energy line $|+1, S_z = -5/2\rangle$ for different pump wavelength around the high-energy level $|-1, S_z = -5/2\rangle$. A clear resonant behavior is observed in the initial amplitude I_0 of the fluorescence signal (Fig. 2.7 (c)). The measured width of the resonance ($80\mu eV$) is a convolution of the width of the quantum dot's absorption (probably power-broadened) and of the linewidth of the excitation laser ($60\mu eV$). The efficiency of the optical pumping $\Delta I/I_0$, presents a similar resonance demonstrating the strong excitation energy dependence of the optical pumping process. However, the efficiency of the optical pumping and the fluorescence does not follow exactly a Lorentzian shape. A weak optical pumping, with a pumping efficiency of $\approx 20\%$ can still be observed for detunnings as large as $400\mu eV$. This is probably due to phonon-assisted absorption from the state $|+1, -5/2\rangle$.

In Fig. 2.8, we present the time-resolved PL recorded on the low-energy line during an optical pumping sequence, for both polarizations of the detection. For cross circularly polarized pump excitation and PL detection, the PL probes the Mn spin state resonantly excited by the pump laser ($S_z = -5/2$ for a $\sigma-$ pump). In this case, the pumping effect is both observed in the transient of the resonant fluorescence and as a decrease in the initial PL intensity in the probe signal. For copolarized pump excitation and PL detection ($\sigma-$), the PL intensity of the low-energy line is proportional to the population of $S_z = +5/2$. As evidenced by the PL of the probe pulse, the population of this state is not significantly affected by the resonant pump laser. The resonant PL during the pump is dominated by the direct absorption from the acoustic phonon side band of this low energy line [50]. Surprisingly, a small transient is observed. Possibly, the $S_z = -5/2$ is not completely shielded from the laser by optical selection rules, contrary to what would be expected in the heavy hole approximation. Such effect could be induced by valence band mixing for instance. This is a small effect though. As expected for a Mn pumping process, the influence of a $\sigma-$ resonant laser tuned on the high-energy X-Mn level mainly affects the population of the state $S_z = -5/2$.

We have invoked phonon-assisted absorption twice already. To illustrate what is the phonon side-band in our quantum dots, we present in Fig. 2.9 a PLE measurement carried on the high energy side of a non-magnetic quantum dot line. We observe that the line is absorbent although the laser is not strictly resonant, which is due to coupling to acoustic phonons. This phonon-assisted absorption is efficient in the first $1-2meV$ around the PL emission. Also, as the circularly polarized laser is resonant with the excitonic line labeled Y on the scheme of Fig. 2.9, we observe a dip in the PLE. We attribute this to the direct absorption of the laser by the other excitonic line (Y), which is more efficient than the phonon-assisted absorption from the detected line (X). Note that this is a rather indirect but efficient way of measuring the absorption (and

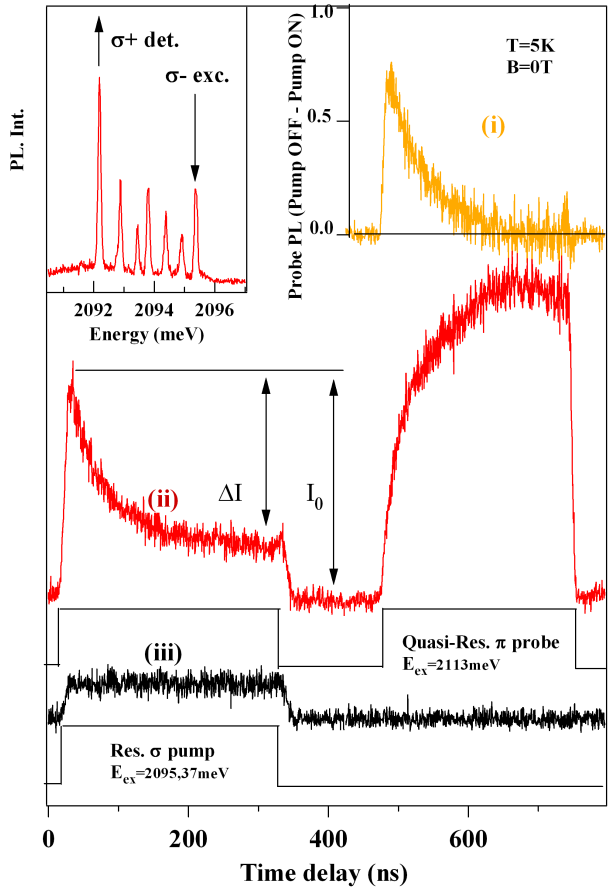

Figure 2.6: The left-inset presents the quantum dot PL under non-resonant excitation, and the configuration of the resonant excitation and detection. (ii) and (iii) are the PL transients recorded on the low energy line of the quantum dot, the quantum dot is excited using resonant and quasi-resonant (i.e. resonant on an excited state) excitation. The excitation sequence is displayed below each curve. In (ii) the optical pumping process is directly observed on the resonant fluorescence produced by the pump and on the PL from the probe. $\Delta I/I_0$ is the efficiency of the pumping process. The transient related to the destruction of the pumping by the probe can be evidenced by subtracting to the curve (ii) the PL signal obtained when the pump is OFF (which is a square signal apart from the rise-time of the set-up). This is how the curve (i) is obtained, reflecting a measure of the efficiency on the probe pulse. In (iii), no signature of a transient is observed, as a consequence of the Mn spin memory in the absence of injected carriers.

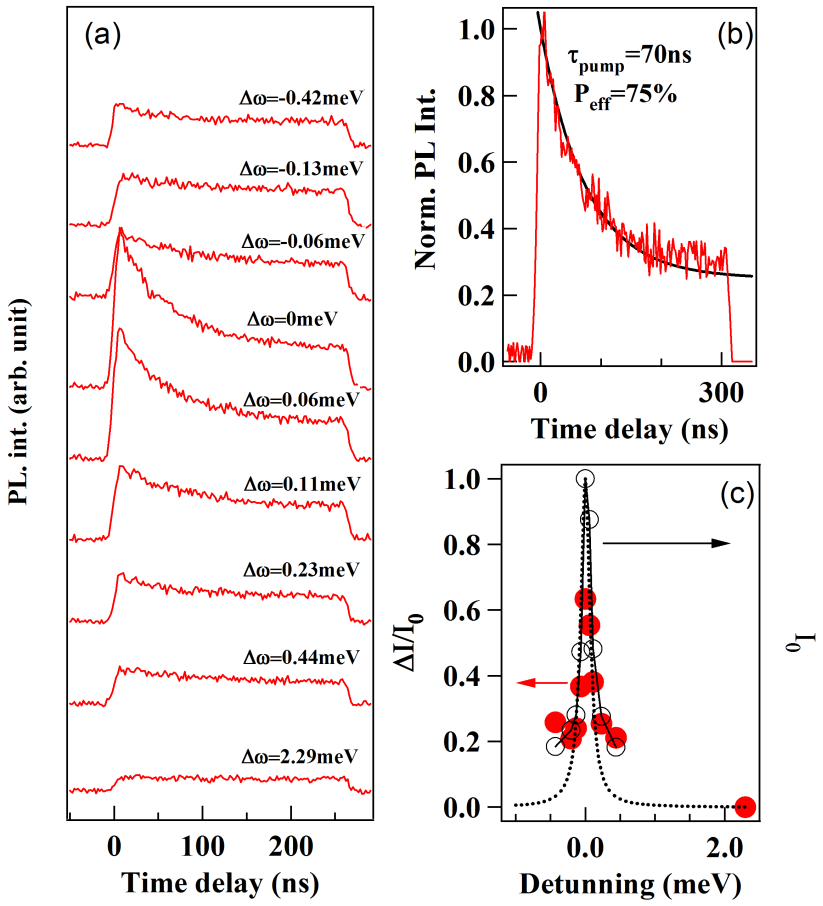

Figure 2.7: (Same quantum dot as in Fig. 2.6)(a) Excitation energy dependence of the resonant fluorescence signal obtained for cross circular excitation-detection on the high- and low-energy line respectively (positive detuning corresponds to an excitation on the hight energy side of the line). (b) Detail of the resonant fluorescence transient recorded during the optical pumping process. The exponentiel fit (black line) gives an optical pumping efficiency P_{eff}≈75% and a pump time of 70 ns. (c) Amplitude of the resonant fluorescence signal as the excitation is tuned around the high energy line of X-Mn. The Lorentzian fit give a full width at half maximum of $80\mu eV$, which is a convolution with the laser width $60\mu eV$ and the quantum dot linewidth.

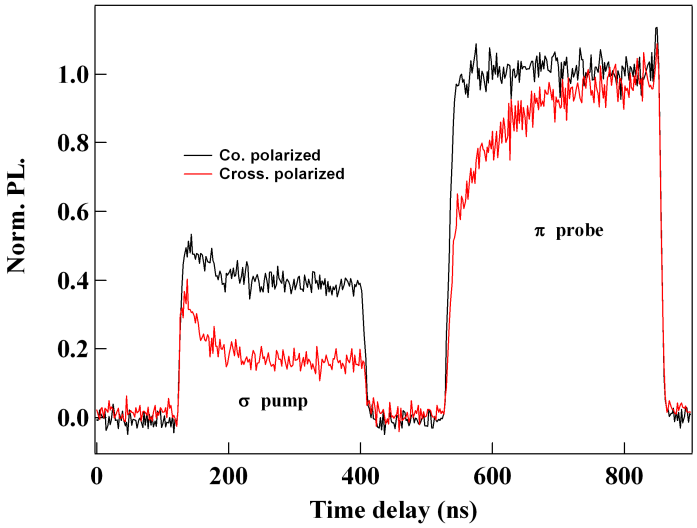

Figure 2.8: Circularly polarized PL obtained during the optical pumping sequence for co and cross circularly polarized pump.

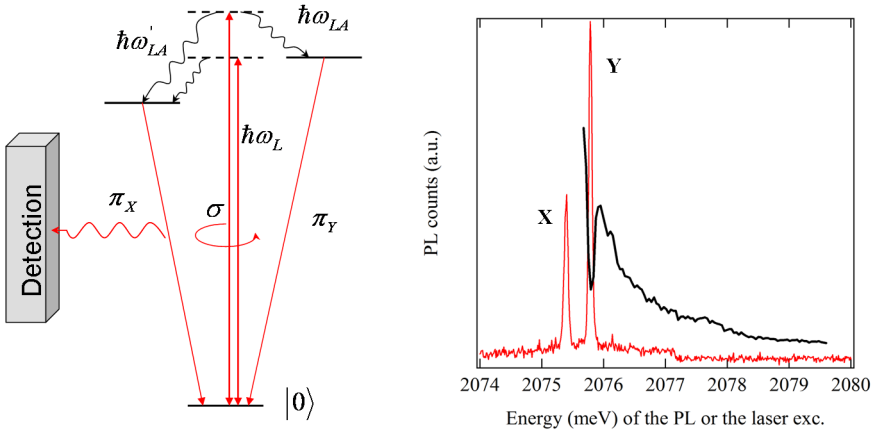

Figure 2.9: Phonon side-band in a non-magnetic II-VI quantum dot. The bright states are split into a linearly polarized doublet due the interplay of VBM and short-range exchange interaction as shown by the PL spectrum obtained under quasi-resonant excitation (red curve). Detecting the low energy line (as shown on the scheme), we perform a PLE measurement with a circularly polarized laser. The detection is cross-polarized to minimize scattered laser. Phonon-assisted absorption is visible in the first few meV on the high energy side of the PL line. Also, a dip occurs as the laser excitation is resonant with the other excitonic state.

the line-width[24]) of a line.

Conclusion

In this chapter, we have demonstrated for the first time that a Mn spin in a solid-state environment could be individually addressed and efficiently prepared in a non equilibrium spin distribution using optical excitation. Spin orientation of the Mn is achievable using injection of polarized carriers on an excited state of the quantum dot. Under resonant excitation on the high energy line, we were able to deplete the $-5/2$ spin-state of the Mn spin with an efficiency reaching $\approx 75\%$. The optical pumping process can be directly observed during the resonant excitation, or probed by a quasi-resonant probe.

This intuitive picture of the orientation of a single Mn spin in the effective field created by the exciton has been widely used in this chapter. We have seen that it is quite intuitive, and explains well the observed behavior under quasi-resonant excitation. However, it has its limits. It fails to predict the saturation of the efficiency of the process under resonant excitation. This raises fundamental questions: what are the exact microscopic mechanisms ruling the photo-induced spin-orientation and optical pumping; what limits the spin initialization?

[24] The measurement presented here are performed with a laser presenting a $60\mu eV$ FWHM, which has not a real interest. But the same measurements with a single-mode laser allow to measure line-width below the resolution of our set-up (which is $30\mu eV$).

Chapter 3

Dynamics of the Mn spin

Contents

This chapter deals with the dynamics of the Mn atom revealed by the optical pumping experiments. To begin with, we present pump-probe experiments which enable us to give a minor bound to the Mn spin relaxation time. Then, we will discuss mechanisms which allow optical pumping at $B = 0T$. We will show that the presence of a magnetic anisotropy is primordial to explain the observed dynamics. This magnetic anisotropy is clearly evidenced by the magnetic field dependence of the optical pumping. At last, we will discuss possible effects due to hyperfine coupling of the Mn spin with its nucleus.

3.1 Mn spin memory

Having established a method for preparing Mn spins, we perform pump-probe experiments to observe how the Mn polarization is conserved (Fig. 3.1 (b)). In this experiment, a non-equilibrium distribution of the Mn spin is prepared with a $\sigma-$ train of quasi-resonant excitation. The pumping laser is then switched off and switched on again after a dark time t_{dark}. The appearance of a PL transient after t_{dark} would mean that the Mn spin distribution has partially relaxed towards thermal equilibrium, the amplitude of the transient being a probe of this relaxation. However, for the quantum dot presented in Fig. 3.1 (b), no transient is observed with t_{dark} in the μs range showing a conservation of the prepared Mn spin distribution.

To further confirm this conclusion, we perform the reciprocal experiment: We prepare the Mn spin using a $\sigma+$ light, switch off the laser during t_{dark}, and switch it on again with the opposite helicity ($\sigma-$). If the distribution prepared by the $\sigma+$ illumination is fully conserved over t_{dark}, a spin transient, identical to the one observed for a $\sigma+/\sigma-$ switch, should be observed. This is exactly verified in Fig. 3.1 (a).

However, as expected from previous measurements of a single Mn spin dynamics under CW optical excitation [51], the injection of high energy carriers in the vicinity of the QD significantly increases the Mn spin relaxation rate. This is illustrated in Fig. 3.1 (c): When free carriers are

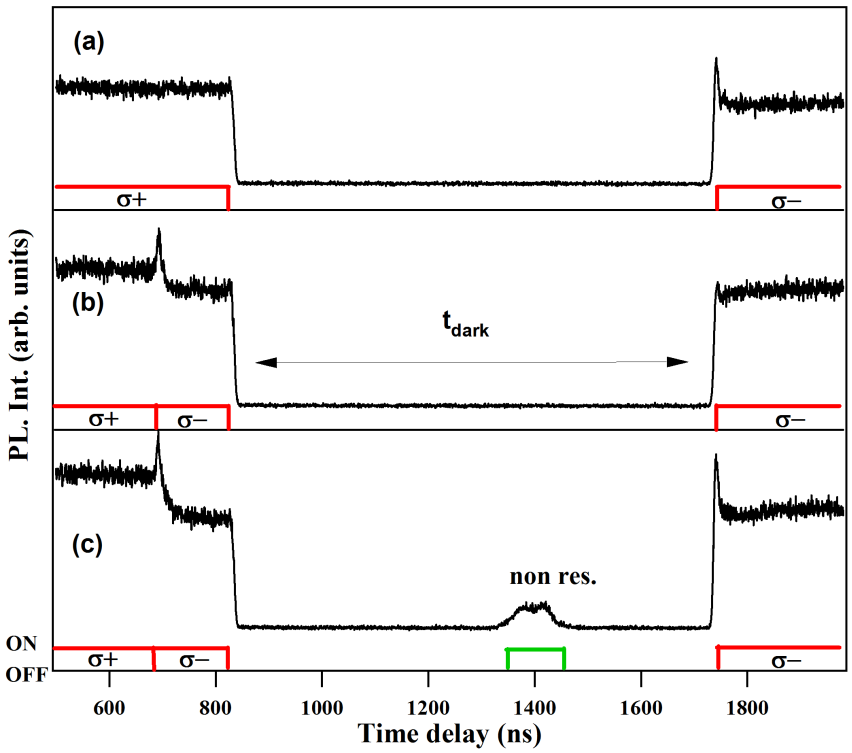

Figure 3.1: PL transients recorded under the optical transients displayed at the bottom of each plot. The prepared Mn spin is conserved during t_{dark}: in (a) and (b), a transient is observed only for a different helicity of the pump and the probe. (c) The injection of carriers with a non-resonant excitation ($514nm$) forces the relaxation of the Mn spin.

injected with a second non-resonant laser during the dark time, the PL transient is observed when the probe laser is switched on after t_{dark}. This result confirms that the exchange coupling with carriers in the wetting layer is a very efficient way to erase the Mn spin orientation. As it can be seen from the low non-resonant PL, the process requires very few non-resonant photons. Surprisingly, even this vanishing small non-resonant excitation slightly shifts the PL emission of the dot, because of a change in the electro-static environment.

We present in Fig. 3.2 analogue experiments carried out on two other quantum dots. With the top curve (QD1), we show another example of Mn spin memory, where τ_{dark} has been increased up to $\approx 3\mu s$. Again, no relaxation of the spin distribution is observed. Probing the relaxation on longer time-scales is difficult experimentally. The integration time is proportional to the duration of the sequence, and the illumination time has to be comparable to the dark time (in order to have enough signal to correct the drifts of the set-up). We have reached dark times up to $10\mu s$ and have not observed any relaxation. For all the investigated quantum dots the relaxation time is longer than experimentally accessible times. All, except one! This example is shown at the bottom of Fig. 3.2. We have estimated the Mn relaxation time for this quantum dot by measuring the amplitude of the pumping transient for increasing delays. We observe a relaxation time $\tau_{Mn,G} \approx 700ns$. On this quantum dot we observe an efficient pumping process in quasi-resonant excitation and resonant excitation. The relaxation process is too slow to affect the efficiency of the Mn spin orientation. The origin of this relaxation could be tunnel coupling

with charged defects around the dot.

3.2 Fine structure of the Mn spin

To understand the dynamics observed on a few μs timescale, we need to consider the evolution of the Mn spin when the dot is empty, i.e. once the photo-created carriers have recombined optically. We consider at $t = 0$ a given S_z spin state of the Mn spin, given by the energy and helicity of the emitted photon. The Mn spin evolution is given by a master equation of the general form:

$$\frac{d\rho}{dt} = -\frac{i}{\hbar}[H, \rho] + L(\rho) \tag{3.1}$$

where ρ is the density matrix of the manganese atom, H is the Hamiltonian which governs the coherent evolution of the manganese atom, and $L(\rho)$ describes the non-hermitian evolution of the system due to its coupling to the environment, responsible for irreversible relaxation of the Mn spin. $L(\rho)$ would include processes such as phonon assisted spin relaxation or coupling to a fluctuating reservoir of charges. The fluctuating reservoir of charges could result from the p-doping by surface states or photo-created carriers in the quantum dot's vicinity. The effect of surface can be neglected if the capping layer is sufficiently thick. The relaxation induced by photo-created carriers is very rapid when exciting above the barriers but it can be neglected otherwise. The other spin relaxation process, is a spin relaxation process caused by a deformation of the lattice (phonon). The picture here, is that the lattice deformation induced by the phonon shakes the electronic wave-function of the Mn $5d$ electrons, which can, through spin-orbit coupling cause a spin relaxation of the Mn spin. However, since the orbital momentum of the Mn spin is $L = 0$, phonon assisted spin-relaxation is a second order process, and the time of the phonon-mediated relaxation is expected in the ms range [9]. This is much longer than the time-scale accessed experimentally (which is given in optical pumping experiments by the time between the injection of two excitons ($\approx 1ns$) or by τ_{dark} in pump-probe memory experiments). Last but not least, the absence of relaxation processes is also consistent with experimental observations discussed in the last section.

Another question to address, is the presence of pure dephasing, which can also affect the coherent dynamics. We will assume that the effect of pure dephasing can be neglected and focus on the coherent evolution of the Mn spin. The Hamiltonian controlling the Mn spin is well known from electron paramagnetic resonance in CdTe/ZnTe superlattices [52]:

$$H_{FS} = A\vec{I}.\vec{S} + \frac{1}{6}a\left[S_x^4 + S_y^4 + S_z^4 - \frac{1}{5}S(S+1)(3S^2+3S-1)\right] + D_0\left[S_z^2 - \frac{1}{3}S(S+1)\right] \tag{3.2}$$

The first term in the Hamiltonian is the hyperfine interaction which results from the magnetic dipolar interaction between the Mn $5d$ electrons forming a spin $\vec{S}$ and the spin of the Mn nucleus $\vec{I}$. The latter is also a 5/2 spin. The hyperfine constant A is equal to $+0.71\mu eV$ ([53]). This term leads to a coherent evolution of the Mn spin state which flip-flops with its nucleus on a characteristic time-scale of $0.5ns$. Considering that the total spin $\vec{S} + \vec{I}$ is conserved[25], this flip-flop process reduces the possibility to perform optical pumping. The only spin-state configuration that conserves S_z are $(I_z = 5/2, S_z = 5/2)$ or $(I_z = -5/2, S_z = -5/2)$. Otherwise, starting from a given $(I_z,\ S_z)$, the expectation value of S_z averaged over time falls down to one half of its initial value.

[25] Relaxation processes for the nuclear spin can be neglected on the time-scale of $10\mu s$ considered here [54].

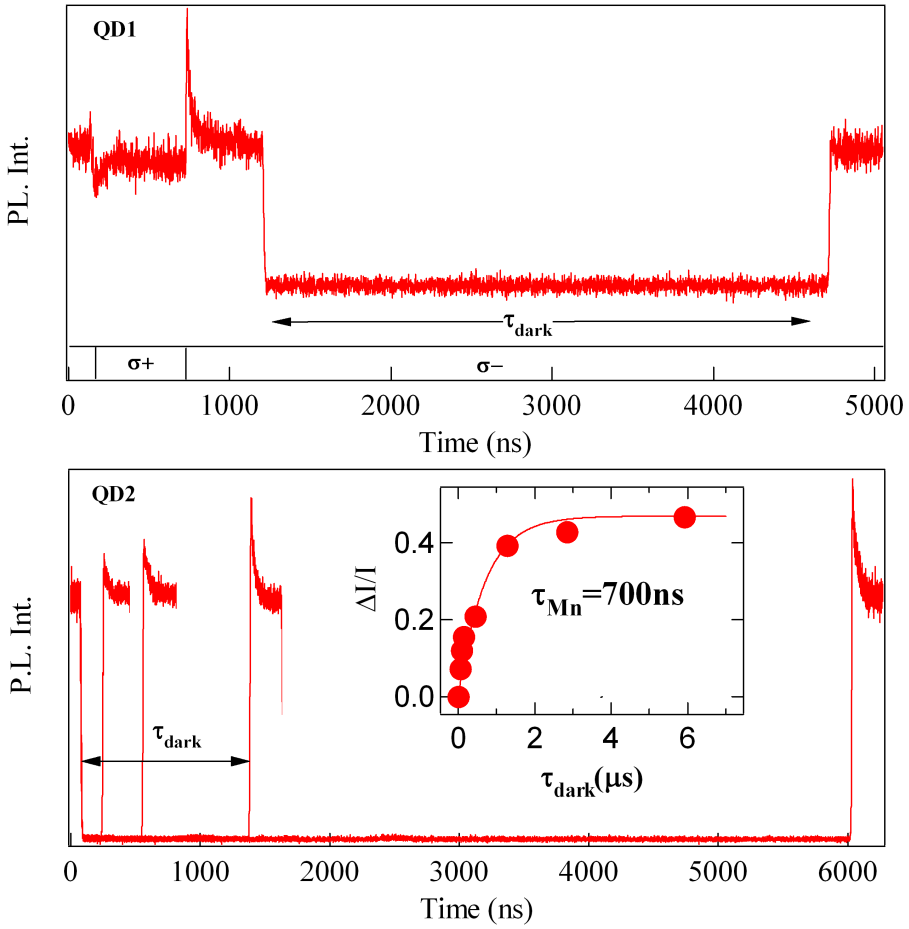

Figure 3.2: Relaxation time of the Mn spin: (QD1) PL transients recorded on the $\sigma-$ high energy line under the optical pumping sequence displayed at the bottom of the plot. The spin distribution prepared by optical pumping is fully conserved during $\tau_{dark} = 3.5\mu s$. (QD2) PL transients recorded under $\sigma-$ excitation, switched off during τ_{dark}. The amplitude of the pumping signal is fully restored after $\tau_{dark} \approx 3\mu s$. From the delay dependence of this amplitude, we deduce a Mn spin relaxation time $\tau_{Mn,G} \approx 700ns$.

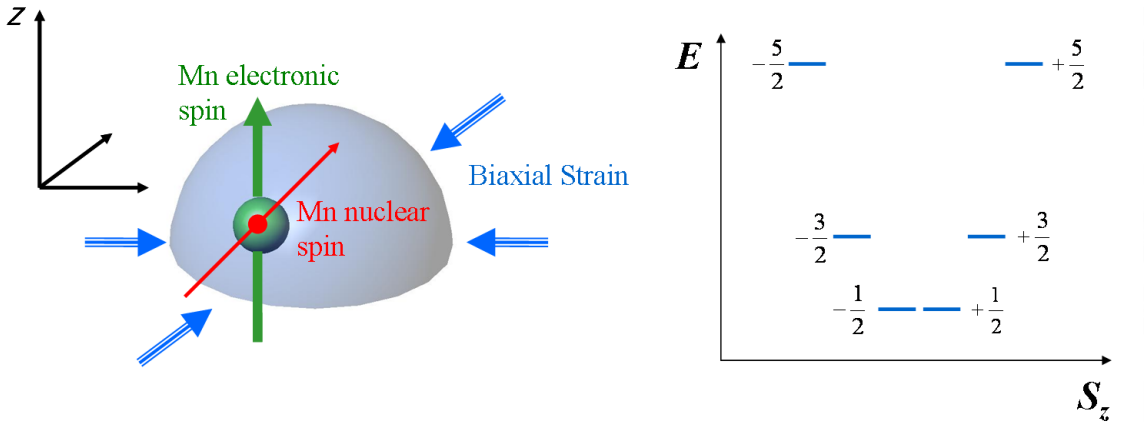

Figure 3.3: Schematic view of a Mn atom in a quantum dot. The fine structure of the electronic spin is controlled by the hyperfine interaction with the Mn nucleus, a cubic crystal field and a magnetic anisotropy arising from the presence of biaxial strain. The magnetic anisotropy results in the Mn energy level structure displayed on the right.

The second term of the Hamiltonian results from cubic crystal symmetry and mixes different S_z of the Mn spin. We have $a = 0.36\mu eV$ according to [53]. If we consider only this second term (and neglect hyperfine coupling), a Mn spin-state $S_z = 5/2$ at $t = 0$ coherently oscillates between $S_z = 5/2$ and $S_z = -3/2$ (as expected from the exponent 4 in the Hamiltonian) with a $\approx 4ns$ period. Thus, this term can lead to the impossibility of performing optical orientation.

The third term, commonly called 'magnetic anisotropy' arises from the existence of bi-axial strains. These strains induce an additional component to the crystal field which has an axial symmetry. We are going to give an estimation of the maximum D_0 expected in our samples. The lattice constant of an unstrained CdTe crystal is $a_{CdTe} \approx 0.648nm$ while for a ZnTe crystal, $a_{ZnTe} \approx 0.610$. According to [52], the magnetic anisotropy D_0 for a strained layer grown along the [001] axis is given by:

$$D_0 = -\frac{3}{2}G_{11}\left(1+\frac{2C_{12}}{C_{11}}\right)\frac{a_{xy}-a_{CdTe}}{a_{CdTe}} \tag{3.3}$$

where G_{11} is the spin-lattice coefficient describing the energy-shift of spin levels per unit strain, C_{11} and C_{12} are elastic constants, and a_{xy} is the common in-plane lattice constant of the strained-layer. According to [53], $G_{11}/(2\pi\hbar c) = 0.46cm^{-1}$, and according to [55], $C_{11} = 5.62 \cdot 10^{10} N.m^{-2}$ and $C_{12} = 3.93 \cdot 10^{10} N.m^{-2}$ at 77K. Considering a_{xy} is determined by the ZnTe lattice, we can estimate $D_0 \approx 12\mu eV$.

Note that if we take into account the hyperfine coupling, the Mn atom is described by a 36×36 density matrix. This coupling is always included in our modeling. In the following we will loosely call '5/2 population' or '$\rho_{5/2}$' what corresponds to the sum of the six diagonal coefficients of the density matrix corresponding to an electronic spin $S_z = 5/2$ (the sum runs over the spin-states of the nucleus $I_z = +5/2... - 5/2$).

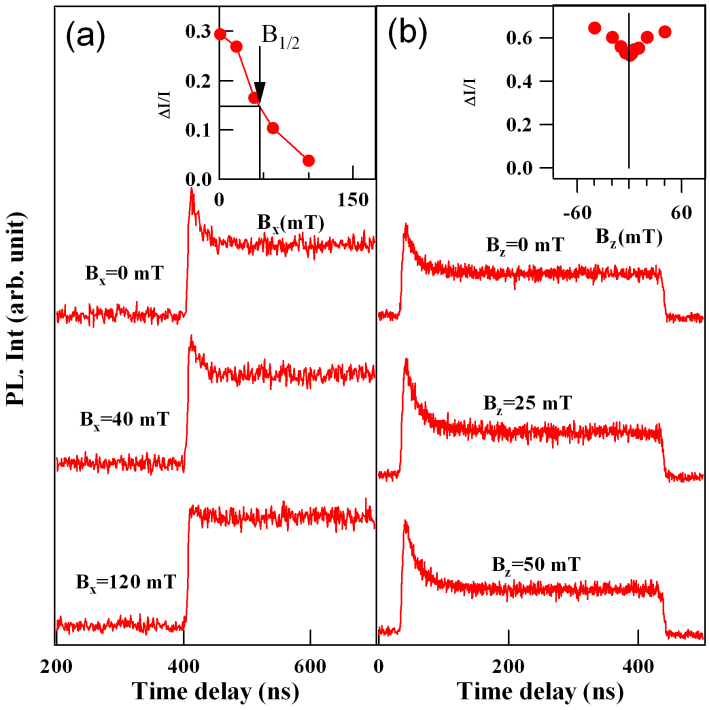

Figure 3.4: Mn spin transient as a function of a magnetic field applied in-plane (a) and out-of-plane (b). Inset: magnetic field dependence of the transient amplitude $\Delta I/I$ (see Fig. 2.2). $B_{1/2}$ is the half width at half maximum.

3.3 Magnetic Field dependence of the optical pumping: evidence of a magnetic anisotropy

More information on the Mn local environment can be obtained from the magnetic field dependence of the optical pumping signal. Depending on the direction, a magnetic field either stabilizes the spin-state S_z (through the Zeeman splitting) or induces a precession of the Mn spin. In the present case, a magnetic field in the Faraday configuration (B_z) does not change significantly the PL transients (Fig. 3.4): a weak increase of the spin orientation efficiency is observed as soon as a field of a few mT is applied. By contrast, an in-plane field (B_x) induces coherent precession of the Mn spin away from the optical axis (= quantum dot's growth axis), so that the average spin polarization, and therefore the amplitude of the optical pumping signal, decay (Fig. 3.4). For an isotropic Mn spin, the decoherence of the precessing spin in a transverse field gives rise to the standard Hanle depolarization curve with a Lorentzian shape and a width proportional to $1/T_2$ [56]. However, a detailed analysis of the magnetic field dependence (Fig. 3.4) shows that the transverse magnetic field dependence is not only ruled by T_2 but mainly by the Mn fine structure.

Let us discuss qualitatively how the Mn fine structure is expected to rule the magnetic field dependence of the optical pumping process. At zero field, in the absence of magnetic anisotropy, the precession of the electronic spin of the Mn in its own hyperfine field and in the cubic crystal field should erase any information stored on the electronic spin. In the presence of an anisotropy,

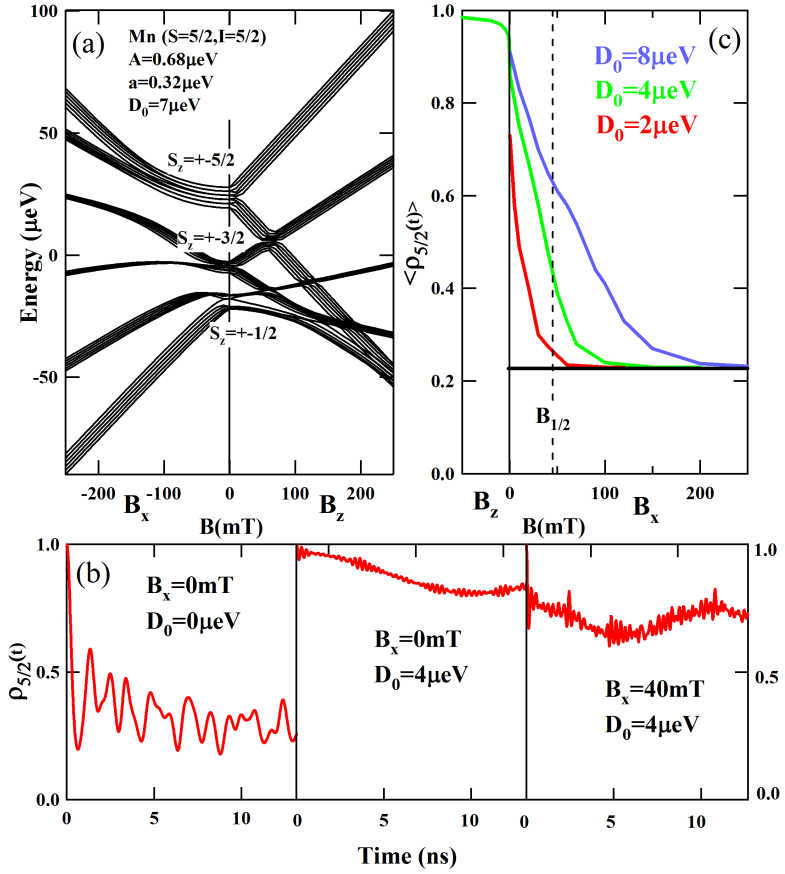

Figure 3.5: (a) Magnetic field dependence of the fine structure of the Mn spin with a magnetic field in the Faraday (right panel) and Voigt (left panel) geometry, calculated with hyperfine coupling $A = 0.68\mu eV$, a magnetic anisotropy $D_0 = 7\mu eV$, and a crystal field parameter $a = 0.32\mu eV$. (b) Time evolution of $\rho_{5/2}(t)$ calculated for different values of D_0 and B_x with $\rho_{5/2}(0) = 1$ and an unpolarized Mn nucleus. (c) Time-averaged value of $\rho_{5/2}(t)$ versus B_x for different values of D_0. Spin dephasing and relaxation is neglected ($T_2 = \infty$). The $B_{1/2}$ found experimentally is indicated with the dashed line.

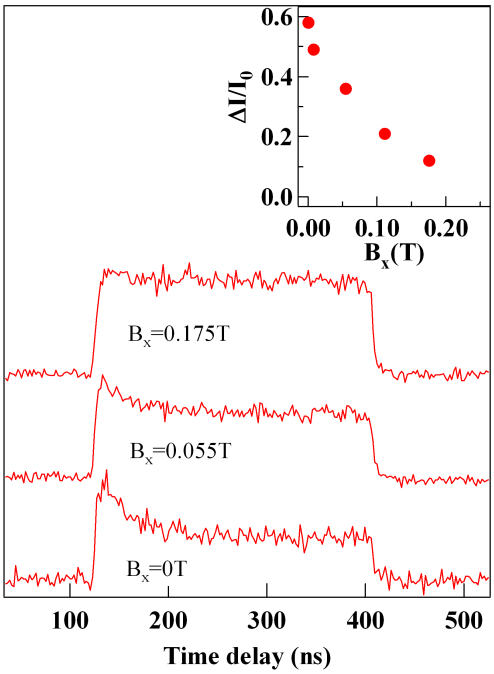

Figure 3.6: Transverse magnetic field (B_x) dependence of the resonant fluorescence signal under cross polarized excitation-detection. The inset presents the amplitude of the optical pumping signal as a function of transverse magnetic field.

the precession of the Mn spin in the nuclear field and the cubic crystal field is blocked even at $B = 0T$. In a weak transverse field: if D_0 is larger than a, A and $g_{Mn}\mu_B B_x$, the Mn electronic spin is still quantized along the growth axis, *i.e.* mixing between the S_z spin states induced by the hyperfine coupling or by B_x is small enough to have a partial memory of the S_z spin state between the emission of a photon and the absorption of another one. Then, the cumulative process controlling the optical pumping mechanism can take place. On the other hand, if the non diagonal terms in H_{FS} (Eqn. 3.2) or the transverse field are strong enough to overcome the magnetic anisotropy, the Mn spin starts to precess and no orientation can be performed. The presence of a magnetic anisotropy also explains the weak influence of an out-of-plane field (B_z): The Zeeman splitting cancels the residual non-diagonal coupling induced by crystal field or anisotropic strains and slightly improves the Mn spin conservation, thus accounting for the increase of the optical pumping efficiency experimentally observed in weak field (Fig. 3.4).

In order to verify quantitatively these assertions, we model the time-evolution of the Mn spin as given by Eqn. 3.2 and 3.1. We also add a Zeeman term to the Hamiltonian 3.2:

$$H_{Zeeman} = g_{Mn}\mu_B \vec{B}.\vec{S} \tag{3.4}$$

Fig. 3.5(c) presents the magnetic field dependence of the time average value of the diagonal density matrix element $\langle\rho_{5/2}(t)\rangle$ for $\rho_{5/2}(0) = 1$[26], $T_2 = \infty$ and varying values of D_0. This quantity describes the probability for the state $S_z = +5/2$ to be conserved after the recombination of an exciton leaving the electronic Mn spin to freely evolve in the hyperfine field, the crystal field and the applied magnetic field. A decrease in this spin conservation progressively destroys the cumulative process controlling the optical pumping mechanism. For a free precessing spin, $\langle\rho_{5/2}(t)\rangle \approx 0.23$ as soon as a transverse field[27] is applied and the depolarization is controlled by T_2. The presence of a magnetic anisotropy strongly modifies the depolarization curve in transverse magnetic field: the precession of the Mn spin only occurs if the transverse magnetic field overcomes the magnetic anisotropy. The half width at half maximum observed experimentally ($B_{1/2} \approx 45mT$, Fig. 3.4) is consistent with a magnetic anisotropy $D_0 \approx 6\mu eV$ in the modeling (Fig. 3.5). At large B_x, all the curves asymptotically tend towards the value of a free precessing Mn spin, as expected physically. The dephasing time is expected to be long enough to neglect its contribution to the observed experimental width. Scheibner *et al.* [57] have indeed measured in $Cd_{1-x}Mn_xSe/ZnSe$ quantum dots ensemble a $T_2^* = 630 \pm 70ps$. In the quantum dots studied here, because of the lower Mn concentration, we do not expect the dephasing time to be shorter. In other words, the contribution to the Hanle depolarization width should not exceed $\delta B = \hbar(T_2^* g_{Mn}\mu_B)^{-1} \approx 8mT$. Therefore, we tend to think that the Hanle depolarization curve is mainly controlled by D_0. Microwave excitation between the levels of the fine structure of the Mn atom could be a way of measuring directly D_0.

Under resonant excitation, the magnetic field behavior of the optical pumping process is also controlled by the Mn fine structure when the Mn atom is alone in the dot. Therefore, we do not expect the magnetic field dependence to change significantly. The transverse magnetic field dependence under resonant excitation is presented in Fig. 3.6. We indeed observe a similar behavior: the efficiency of the pumping process $\Delta I/I$ decreases with increasing transverse magnetic field (inset of Fig. 3.6) or, equivalently, we observe an increase of the steady-state resonant

[26] In this model, we neglect optical pumping of the Mn nucleus. We consider that all the spin-states of the Mn nucleus are equiprobable.

[27] This value is calculated by numerical means.

fluorescence (i.e. at the end of the resonant pulse). The steady-state fluorescence (equivalent to the resonant fluorescence under CW excitation) can be used to probe a change in the optical pumping efficiency.

We use the amplitude of the resonant fluorescence to probe variations of the optical pumping efficiency with an external magnetic field in the Faraday geometry (B_z). In Fig. 3.7 PLE spectra detected on the low-energy line when the excitation laser is tuned around the high-energy level are presented for different magnetic fields in Faraday geometry. The PL intensity is divided by two for a magnetic field of about $100mT$. This reduction could either be explained by a reduction in the spin-flip rate of the exciton or an increase in the efficiency of the optical pumping of the Mn spin. A priori, the Zeeman energy of the exciton in this weak magnetic field is not significant compared to the exchange field with the Mn: the dynamics of the exciton coupled with the Mn is unlikely to be affected by this small energy change. Thus, the magnetic field dependence can be attributed to an increase in the optical pumping efficiency. Indeed, the Zeeman splitting of the Mn in an empty dot cancels the non-diagonal coupling induced by the tetragonal crystal field or an anisotropic strained distribution at the Mn atom location (which gives rise to a magnetic anisotropy in $E(S_x^2 - S_y^2)$). It improves the Mn spin conservation thus accounting for the increase in the optical pumping efficiency in a Faraday magnetic field.

3.4 Mn steady-state under optical pumping

The PL transients obtained experimentally can be qualitatively reproduced considering laser excitation and relaxation from the bright state to a Mn spin-state different than the one under excitation[28]. Laser excitation can be included considering 6 other levels corresponding to a given XMn state (i.e. $|-1;-5/2\rangle$) with six spin-states for the nuclei ($I_i = -5/2... + 5/2$) following[29]:

$$\left(\frac{\partial\rho}{\partial t}\right)_{laser} = -\sum_{i=1}^{6} i\Omega(\sigma_{(XS_z,I_i),(S_z,I_i)}\rho + \sigma_{(S_z,I_i),(XS_z,I_i)}\rho - \rho\sigma_{(XS_z,I_i),(S_z,I_i)} + \rho\sigma_{(S_z,I_i),(XS_z,I_i)}) \tag{3.5}$$

Were $\sigma_{ij} =| i\rangle\langle j |$. We further add pure dephasing (γ_{XMn}) of the transition (although strictly speaking, the linewidth of the transitions could also come from spectral diffusion) and radiative recombination (Γ). Finally we consider that the excitonic state (XS_z, I_i) can recombine via an incoherent process toward $(S_z + 1, I_i)$ with a characteristic time τ_{pump}. The hypothesis of this particular recombination channel is a way of treating effectively the pumping process given Fig. 4.6. This process will be discussed in detail in the next chapter. This process is included considering an evolution term in the Lindblad form:

$$\left(\frac{\partial\rho}{\partial t}\right)_{pump} = -\sum_{i=1}^{6} \frac{1}{2\tau_{pump}}(2\sigma_{(S_z-1,I_i),(XS_z,I_i)}\rho\sigma_{(XS_z,I_i),(S_z-1,I_i)} - \sigma_{(XS_z,I_i),(XS_z,I_i)}\rho - \rho\sigma_{(XS_z,I_i),(XS_z,I_i)}) \tag{3.6}$$

[28] We will give abruptly a few equations to describe the density matrix evolution. One can refer to the first pages of Annex B where we manipulate the same equations on a simpler system, and take the time to discuss them.

[29] Bloch equation in the rotating frame.

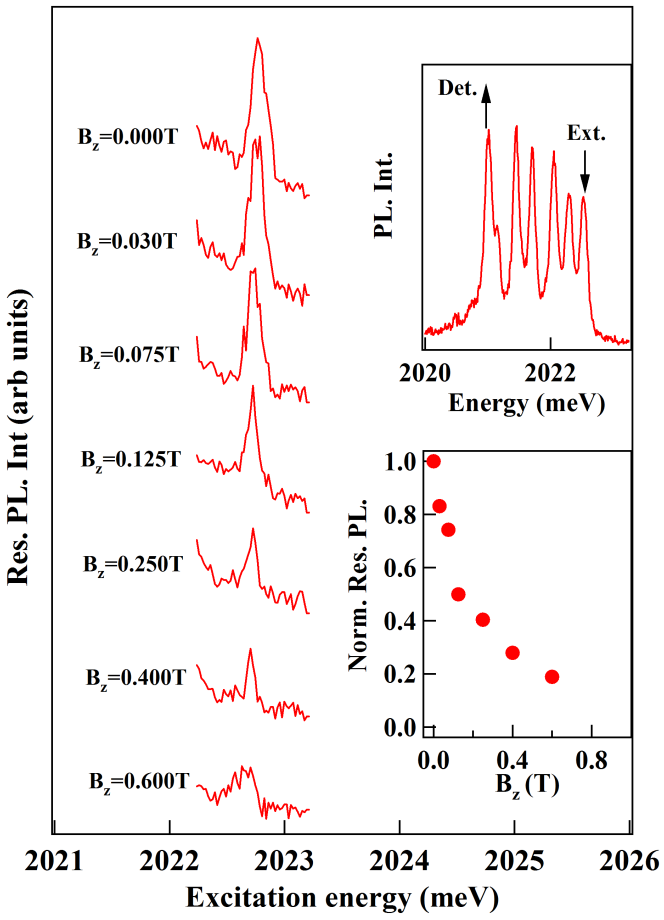

Figure 3.7: Magnetic field dependence of the photoluminescence excitation (PLE) spectra obtained on the ground state of a Mn doped QD (QD3)under circularly cross-polarized excitation-detection. The insets present a PL spectra of QD3 (arrows point the excitation and detection wavelength) and the magnetic field (B_z) dependence of the amplitude of the resonant PL signal.

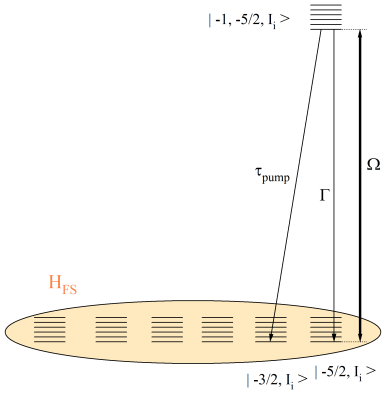

Figure 3.8: Schematic view of the modeling of the optical pumping experiments. We consider 36 levels corresponding to the uncoupled Mn-nuclei states. The evolution of these states is governed by the Hamiltonian describing the Mn fine structure (H_{FS}) defined Eqn. 3.2. We add a dipole-laser coupling characterized by the Rabi Ω. Radiative recombination occurs at a rate $\Gamma = 200ps$. The pumping process is modeled by a recombination toward the state $-3/2$ (The spin of the nuclei is conserved).

A schematic view of this model is shown in Fig. 3.8. The evolution of the density matrix is computed numerically. Experimentally, the PL signal is monitored through a spin-flip of the exciton in the exchange field of the Mn. This PL is proportional to the population of the state $|-1;-5/2\rangle$ (summed over the six nuclei spin-states). The population of this state (which we will call abusively PL) is shown in Fig. 3.9 for different τ_{pump} and magnetic anisotropy D_0. First we discuss the top panel of Fig. 3.9, were all the parameters of the modeling are kept constant, except for D_0. We see that the efficiency of the pumping process and the memory depend on D_0. Interestingly, a D_0 of $2\mu eV$ already allows an efficient pumping process. Moreover, for $D_0 = 6\mu eV$, a highly non-exponential transient is observed. This is still the case if τ_{pump} is increased (lower panel of Fig. 3.9). For $\tau_{pump} = 5ns$, the evolution of the transient presents two characteristic times: a quick decrease as the $-5/2$ population is transferred towards the $-3/2$. At this point the process is incomplete because population of the $-3/2$ can coherently evolve towards the $-5/2$ spin state via a flip-flop with the nuclei. The wave-function mixing is small though, because D_0 is large. The major part of the pumping process is performed. On a longer time-scale, the population is transferred toward states which are less coherently coupled to the $-5/2$ spin state involving higher projections of the nuclei spin state I_i. However, an absorption always remains because of the cubic crystal field (in theory, without the cubic crystal field ($a = 0$), the $-5/2$ spin state can be fully depleted at $D_0 = 0\mu eV$). A non-exponential transient has never been observed experimentally. This could arise as the fast transient is within the resolution of our set-up. This is plausible considering a fast τ_{pump} (which is, as we will see, expected to be controlled by the spin-flip of the hole). This model accounts well for the limit of the optical pumping efficiency observed experimentally, a memory effect on a hundred of ns and the role of a magnetic anisotropy.

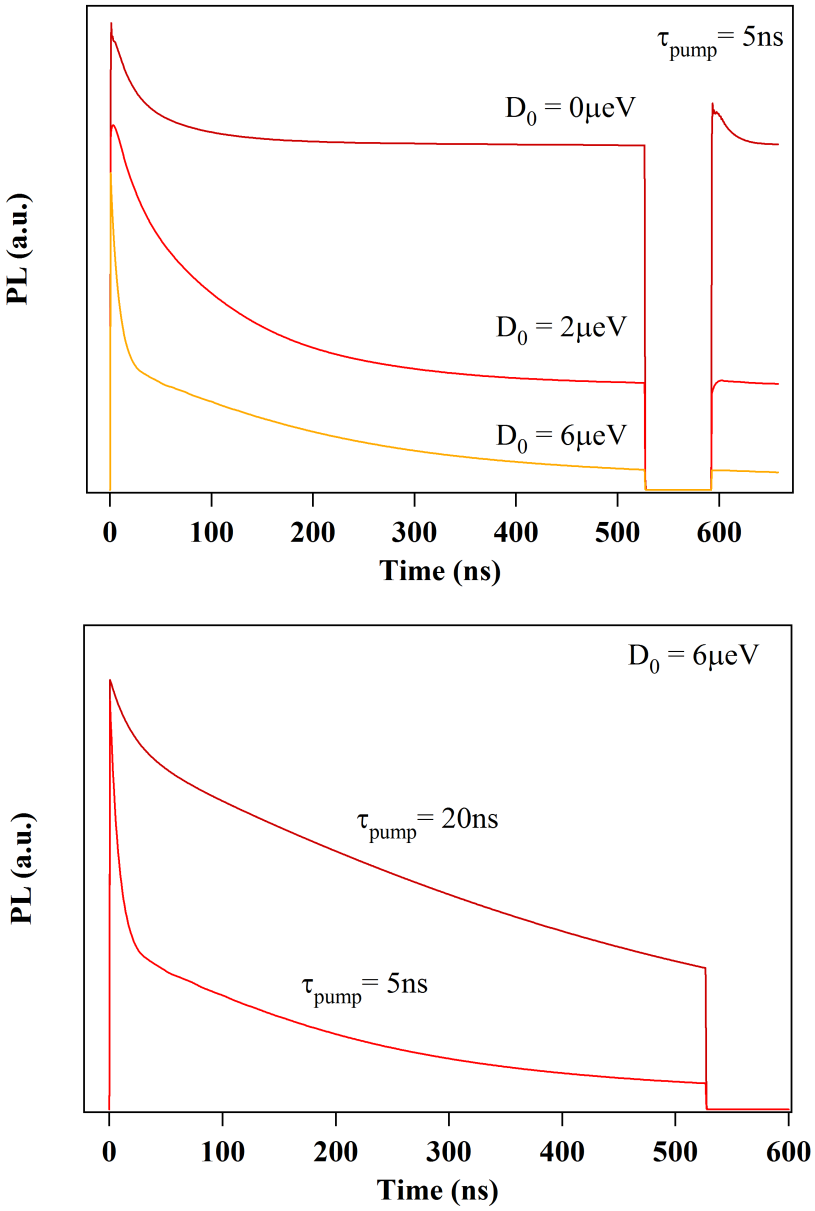

Figure 3.9: Modeling of the optical pumping experiments with $\Omega = (200ps)^{-1}$, $\Gamma = (200ps)^{-1}$, $\gamma_{XMn} = (20ps)^{-1}$. Upper panel: PL signal for varying values of D_0, at a fixed τ_{pump}. Lower pannel: PL signal for varying values of τ_{pump}.

Conclusion

We have discussed in this chapter the dynamics of the Mn atom in the absence of charged carriers in the dot. Through pump-probe experiments, we demonstrated that the relaxation time of the Mn atom is typically longer than the μs range. This is in full accordance with the relaxation rates measured by Dietl *et al.* for Mn spins in DMS at the limit of low concentration [9]. We have also demonstrated that the Mn fine structure, resulting from the inter-play of hyperfine coupling with the Mn nucleus and a magnetic anisotropy plays a key-role: it explains the saturation of the optical pumping of the $+5/2$ spin-state at $\approx 75\%$ in the best cases, and controls the magnetic field dependence of photo-induced spin orientation.

Chapter 4

Dynamics of the Exciton-Mn complex

Contents

This chapter is dedicated to the study of Exciton-Mn dynamics. First we study, using resonant fluorescence the most efficient spin relaxation channels within the ground state of the Exciton-Mn complex. We clearly observe a non-linear dependence of the spin-flip rate with the inter-level splitting, which suggests an acoustic-phonon mediated process. Spin-flips towards dark states are also observed. Regarding these spin-relaxation processes, we discuss recent theoretical proposal on the optical pumping mechanism in a Mn-doped quantum dot. Then, we will discuss relaxation processes from an excited state based on polarization-resolved PL-decay measurements. Relaxation of the exciton-spin during the injection is evidenced. This is in agreement with the faster optical initialization of the Mn spin under quasi-resonant excitation compared to resonant excitation.

4.1 Spin Relaxation within the Ground-State of the XMn Complex

In this section, we answer the following question: what are the main relaxation channels within the XMn complex? In order to address it, we perform resonant excitation on a given line of the XMn complex, and detect the PL emitted on the other lines. The spectral distribution of the scattered photons during the resonant excitation of a given line reveals the spin-flip processes within the exciton-Mn system.

4.1.1 Experiment

First, we report results on a quantum dot (QD1) presenting a weak optical pumping at $B = 0T$. This poor efficiency of the optical pumping is attributed to the local strain environment. This case is interesting for a study of the X-Mn dynamics: the quantum dot line is always absorbent and the scattered photons reflect the fastest spin relaxation channels.

In Fig. 4.1, we present the following PLE measurements: the detection window is set on the low energy side of the XMn PL, while a circularly cross-polarized laser scans the high energy lines. A PL spectrum under quasi-resonant excitation is displayed at the bottom to facilitate line identification. This spectrum is also displayed vertically in order to indicate the correspondence between the excitation energy and the PL lines. The two PLE maps differ by the detection window (controlled by the two slits of the double monochromator). For the top-map, the detection window (centered on the low energy line $|-1,+5/2\rangle$) is small, allowing the energy of the excitation to be very close to the detection. The energy of the laser excitation is determined with high precision using the scattered laser light[30].

On these two PLE maps we have labeled 6 resonances. We are going to discuss all of them in detail, starting with the easiest to identify. Before that, we highlight the fact that this quantum dot presents seven lines as a result of a strong admixing of the states $|+2,+1/2\rangle$ and $|-1,+3/2\rangle$ (Fig. 4.2). The position of the XMn levels labeled in Fig. 4.2 are confirmed by calculations shown in Fig. 4.3. We will safely based our reasoning on the XMn states labeled in Fig. 4.2.

Resonance 1 (equivalent to 4): Strong PL on the lowest energy line ($|-1,+5/2\rangle$) is observed when the cross-polarized laser is tuned on the highest line $|+1,+5/2\rangle$.

Resonance 5: As the laser is tuned on $|+1,+3/2\rangle$, the two lines corresponding to ($|+2,+1/2\rangle \pm |-1,+3/2\rangle$) present a resonance.

Resonance 6: This strong resonance appears as the laser is resonant with $|+1,+1/2\rangle$. Strong PL is observed from a dark state. Using Fig. 4.2, we can attribute this dark state either to $|-2,+3/2\rangle$ or $|+2,-3/2\rangle$. To discriminate between the two, we have to consider their admixture with bright states, through non-diagonal spd-exchange terms. $|-2,+3/2\rangle$ for instance, is admixed with $|-1,+1/2\rangle$ via a electron-Mn flip-flop term and with $|+1,+1/2\rangle$ through a hole-Mn flip-flop term. The admixtures α_+ (with $|+1,+1/2\rangle$) and α_- (with $|-1,+1/2\rangle$) scale as[31]:

$$\begin{aligned} \alpha_+ &= \frac{\sqrt{2} I_{eMn}}{\Delta E_+} \\ \alpha_- &= \frac{2\sqrt{6}\eta I_{hMn}}{\Delta E_-} \end{aligned} \tag{4.1}$$

where, as usual, η is the parameter describing the heavy-light hole mixing, I_{eMn} the electron-Mn exchange, I_{hMn} the hole-Mn exchange. $\Delta E_\pm$ are the energy splitting between the corresponding bright states with the dark state. $\eta I_{hMn} \approx 24 \mu eV$ can be estimated from the energy splitting

[30] $E_{laser} \approx E_{det} + 2\Delta E_{scat}$, where E_{laser} is the laser energy, E_{det} is the energy at the center of the detection window. ΔE_{scat} is the energy between the scattered laser and the detection window. Note that using this relation, one can find which line is excited, only using the bottom spectra (the vertical spectra are only displayed for comfort).

[31] Using a perturbative approach.

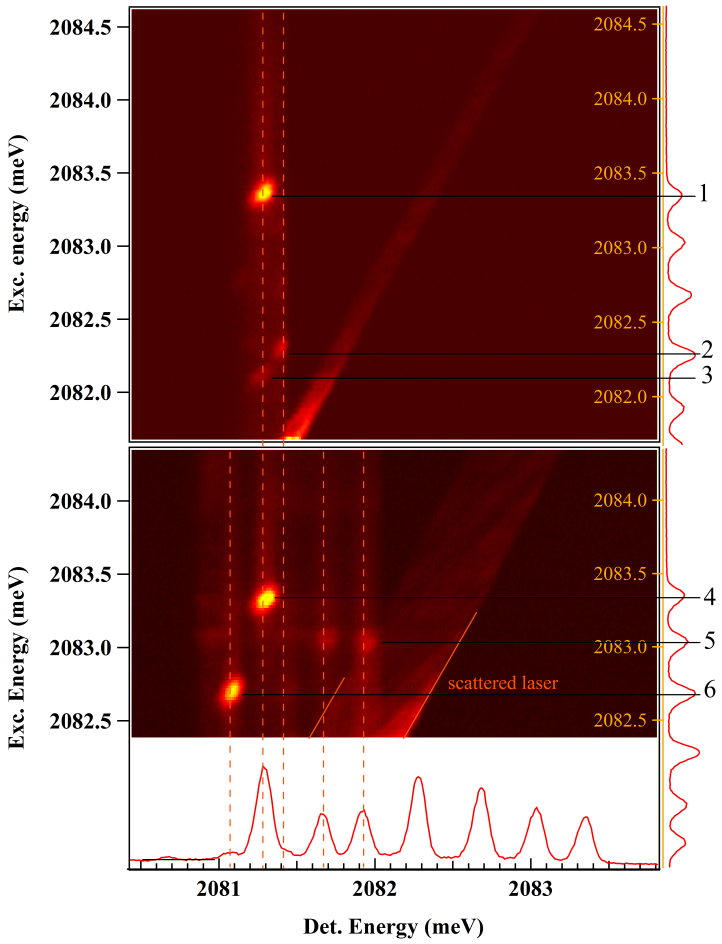

Figure 4.1: PLE maps of QD1. It can be seen from the quasi-resonant PL spectra that the laser excitation is scanned across the high energy lines of the XMn complex, while the detection is performed on the low energy lines. Excitation and detection are circularly cross-polarized. This quantum dot presents seven lines originating from a dark-bright admixture (see Figs. 4.2 and 4.3). The different resonances $(1-6)$ are discussed in detail in the text.

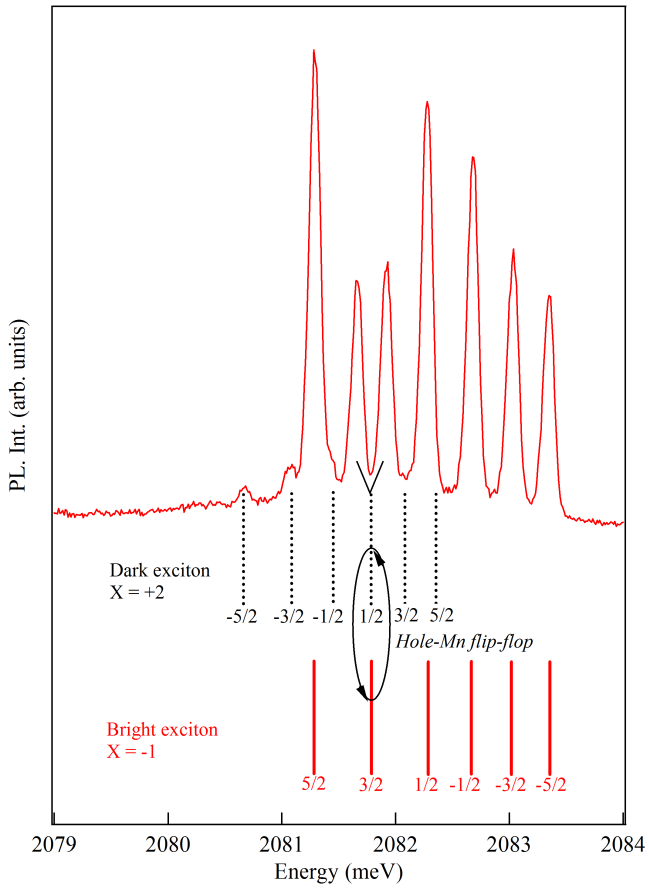

Figure 4.2: PL spectrum of QD1 under quasi-resonant excitation. Below are displayed the uncoupled levels of bright and dark states. The accidental degeneracy of the dark state $|+2, +1/2\rangle$ and the bright state $|-1, +3/2\rangle$ results (through valence band mixing and hole-Mn exchange) in two PL lines of equal oscillator strength.

of the two lines resulting from the dark/bright admixed lines ($|+2,+1/2\rangle$ and $|-1,+3/2\rangle$) [32]. $I_{e-Mn} \approx 70\mu eV$ can be estimated using two lines with the same Mn and hole spin projection and substracting the electron-hole exchange (but a precise estimation requires a spectra modeling as done in Fig. 4.3). Finally a rough estimation of these admixture, considering $\Delta E_+ \approx 1200\mu eV$ and $\Delta E_- \approx 1590\mu eV$ is:

$$\alpha_+ = 0.08$$
$$\alpha_- = 0.08$$

The admixtures are similar. Basing ourselves on polarization considerations, we cannot discriminate which of the two dark states ($|-2,+3/2\rangle$ or $|+2,-3/2\rangle$) is observed.

Resonance 3: A weak PL is observed from the $|-1,+5/2\rangle$ line, as the laser is tuned at a slightly lower energy than the $|+1,-1/2\rangle$ energy line. This must correspond to a dark state. Indeed the dark states $|+2,+3/2\rangle$ and $|-2,-3/2\rangle$ are expected at this energy (Fig. 4.2). Once again, the dominant admixture is ambiguous: for $|+2,+3/2\rangle$ the admixture via a hole-Mn flip-flop ($|-1,+5/2\rangle$) slightly dominates over the electron-Mn ($|+1,+5/2\rangle$).

Resonance 2: As the laser is tunned on $|+1,-1/2\rangle$ we clearly observe a resonance. Referring to Fig. 4.2, the PL either comes from $|-2,+1/2\rangle$ or $|+2,-1/2\rangle$. The dominant admixture with bright states is via a hole-Mn flip-flop (with $|+1,-1/2\rangle$ for $|-2,+1/2\rangle$). Since the detection is $\sigma-$, what we detect corresponds mainly to $|+2,-1/2\rangle$. This could be the signature of a hole spin-flip. However, the states $|+1,+1/2\rangle$ and $|-1,+1/2\rangle$ (or $|+1,-1/2\rangle$ and $|-1,-1/2\rangle$) are admixed by short range and long range exchange through valence band mixing or anisotropy of the confining potential, resulting in an absorption partially linearly polarized. Let us highlight the fact that this effect is particularly strong for the $\pm 1/2$ bright states because they are less split by the exchange interaction with the Mn (see [58] or *p.*81 of [27]). Consequently, the Mn spin-state under excitation is not well defined and we cannot affirm or infirm a spin-flip of the hole compared to the other process which would be a simultaneous hole-Mn flip-flop.

If we resume the observed resonance, we can distinguish two type of resonances:

- Resonances (4, 1 and 5) between two bright states, which involve a change of the spin of the exciton, while the Mn spin-state is unaffected. The transition between the two bright states corresponding to the Mn spin state $S_z = 1/2$ which has not been discussed so far, is shown in Fig. 4.3.
- Resonances (2, 3 and 6) involving a transition from a dark to a bright state or vice-versa. The exact XMn states involved in the transition could not be determined unambiguously for the latter. However, there is one possible path that unifies all these transitions: a hole-Mn flip-flop.

Before we comment on these conclusions, let us note a few other features of these transitions and briefly comment on another quantum dot. In Fig. 4.3, we see that the intensity of the resonant PL (which reflects more or less the probability of the transition during the life-time of the exciton) increases with the inter-level splitting of the two-states involved in the transition.

[32] Since the two lines are degenerate, we find from the model discussed in the first chapter that this energy splitting is $4\sqrt{(6)}\eta I_{hMn}$.

We also note that the acoustic phonon-side band can be observed in the PLE which reflects the absorption of the excited line. The effect is particularly clear on the resonance 1 (or 4) involving the 5/2 lines, since there is no absorption at higher energy.

In Fig. 4.4, we present an analogue experiment carried out on a different quantum dot. Similarly to the first example, we observe a XMn relaxation between bright states corresponding to the same Mn spin states. Again, relaxation from $|+1,+5/2\rangle$ to $|-1,+5/2\rangle$, is faster than relaxation from $|+1,+3/2\rangle$ to $|-1,+3/2\rangle$ resulting in a stronger PL signal. However, the efficiency of the optical pumping has not been investigated on this quantum dot. It is possible that the latter also plays a role in the relative height of the PL peaks.

We also observe relaxation toward the dark states: as the laser excitation is tuned on the high energy line corresponding to $|+1,+3/2\rangle$, two weak PL lines appear: we attribute them to dark states. A modeling[33] allows to attribute the corresponding XMn states ($|-2,+5/2\rangle;|+2,+1/2\rangle$). We will not detail all the transitions and simply highlight that the transitions between the bright state under resonant excitation and the observed dark state involve hole-Mn *and* electron-Mn flip-flop. Also, the PL from the dark states is very weak (it barely emerges from the background), contrary to what was observed for QD1. This second example illustrates that the rapidity and the nature of the dominant channels (e-Mn or h-Mn flip-flop) within the XMn states vary from dot to dot.

4.1.2 Phonon Assisted Spin Relaxation of the Exciton

Exciton spin relaxation through phonon-assisted processes has attracted attention both theoretically and experimentally. For typical quantum dots at low temperature, the zero-magnetic field exciton spin-relaxation is usually negligible compared to the radiative lifetime. Apart from [59] and [60], the relaxation time is expected to be longer than the tens of ns range, both theoretically [61] and experimentally [62]. However, it is well understood that the exciton spin-relaxation considerably increases with external magnetic field [63, 64]. This effect is due to the increase of the acoustic phonon density of states at the energy of the interlevel splitting. So far, the mechanisms identified by theoretical studies involve (i) the interplay of short-range exchange interaction and the distortion of the crystal by the phonon and consequently a distortion of the band described through the Bir-Pikus Hamiltonian or (ii) the combined action of spin-orbit coupling and the phonon. The former is expected to dominate spin relaxation processes for small quantum dots. We try, in the following to give an idea of how these spin-flip rates can be calculated and to describe the evolution of these phonon-assisted spin-flip as a function of the energy splitting between the two excitonic states. We will focus on the transitions linked to a spin-flip of a hole in the exchange field of the Mn. Our approach is based on [65] and [64].

The elastic properties of the two materials are similar, thus the bulk acoustic-phonon modes are considered here. We will make the approximation that the acoustic phonon dispersion is isotropic. Also, we will neglect the presence of anisotropic built-in strain. We will consider strain terms ε_{ij}, which are no longer built-in strain, but strain terms induced by the phonons.

As we have seen in Chap. 1, a crystal deformation leads to a shift of the energy of the conduction and the valence band, and shear strain ($\varepsilon_{ij} \neq 0$ or $\varepsilon_{ii} - \varepsilon_{jj} \neq 0$ with $i \neq j$)

[33] Because bright/dark admixture is not strong enough to identify the presence of a seventh line, the model does not allow strictly speaking to determine the position of the dark states (a change of I_{eh} shifts in block the position of the dark states). Contrary to QD1, a magneto-optic study would be required here. However, the values of I_{eh} are well known. Taking a value of I_{eh} in the average, there is only few ambiguity in the attribution of the dark sates.

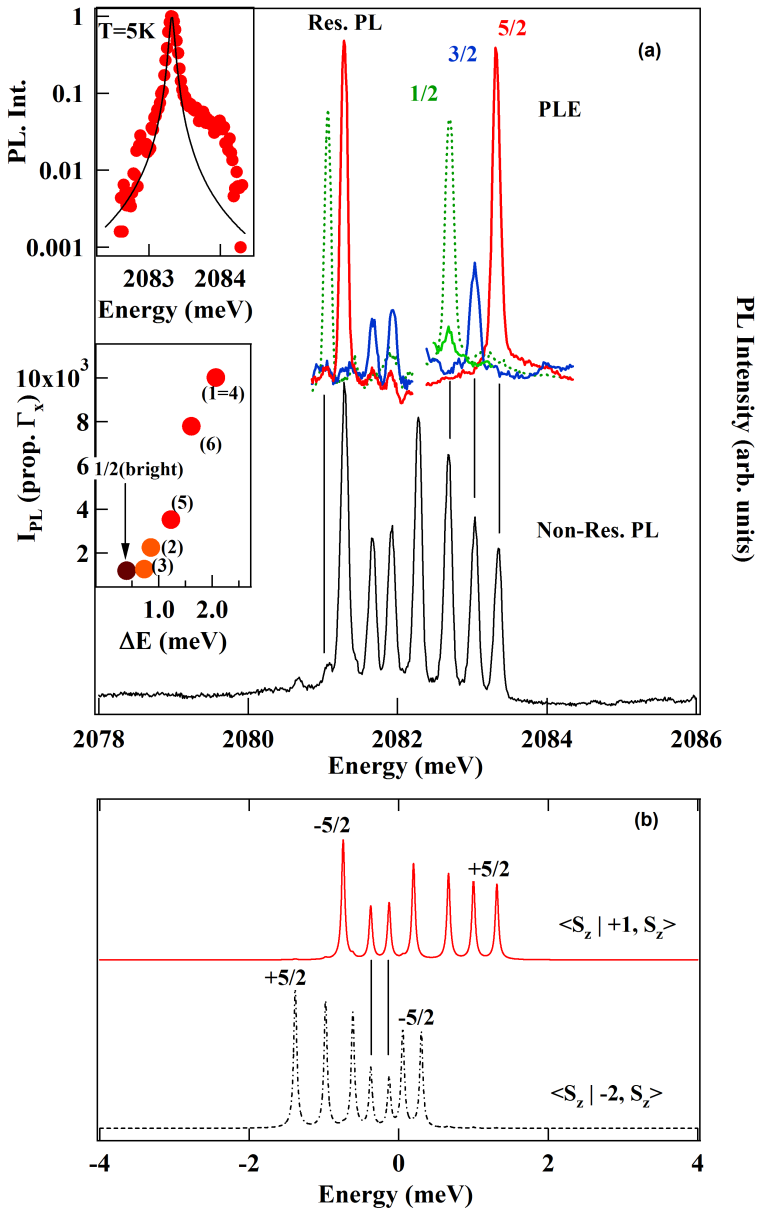

Figure 4.3: Photoluminescence excitation (PLE) spectra and resonant photoluminescence obtained on the ground state of QD1. The resonant PL is obtained under circularly cross-polarized excitation-detection. The top-inset presents an enlarged view of the PLE obtained under excitation and detection on the S_z=+5/2 state. The black line is a Lorentzian fit with a half width at half maximum of 80μeV. The asymmetry of the absorption line comes from a coupling with acoustic phonons. The lower inset presents the evolution of the intensity of the PL as a function of the energy splitting between the two states involved in the transition. Data points of the same color are issued from the same PLE measurement. The labels (1-6) refer to the resonances given in the text. (b) Calculated bright $|+1\rangle$ and dark $|-2\rangle$ energy levels with I_{eMn}=0.07 meV, I_{hMn}=0.245 meV, I_{eh}=825 meV, $\eta = 0.11$ and ζ=20μeV (all these constants are defined Chap. 1). The contribution of long-range exchange is neglected. Because of the large carrier-Mn exchange coupling, the dark exciton levels overlap with the bright excitons. The valence band mixing couples the states $|+1,-3/2\rangle$ and $|-2,-1/2\rangle$ and gives rise to an additional PL line.

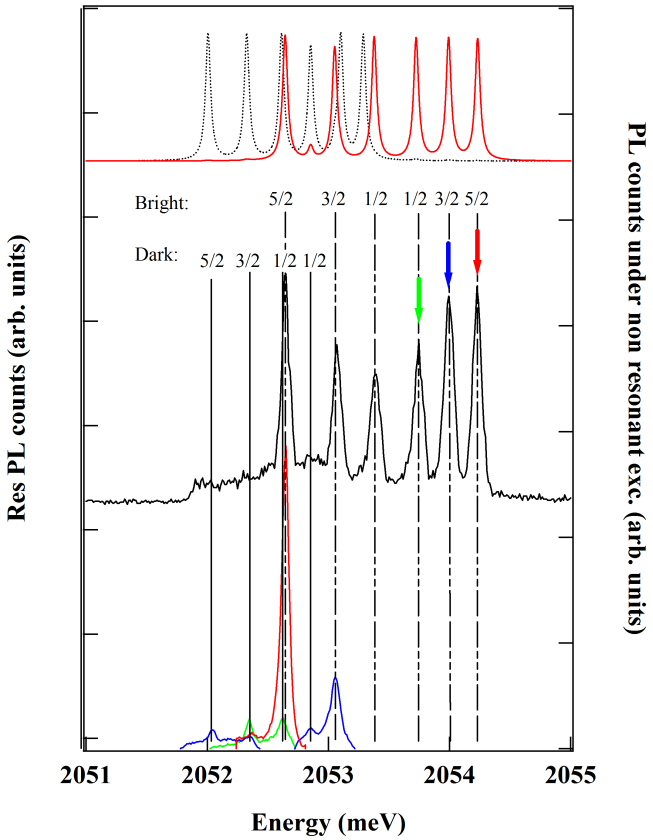

Figure 4.4: Black curve: PL under non-resonant excitation. Colored curves: $\sigma-$ PL spectra recorded under $\sigma+$ resonant excitation on the high energy lines (shown by the arrows) corresponding to $S_z = +5/2$ (red), $+3/2$ (blue) and $+1/2$ (green). Dashed or filled lines are used to highlight the position of the bright or dark lines. The XMn states (bright states in red, dark states in dashed-black) are modeled using I_{eMn}=0.06 meV, I_{hMn}=0.190 meV, I_{eh}=0.788 meV, $\eta = 0.07$ and ζ=17μeV. Long-range exchange is neglected.

modifies light/heavy hole mixing and changes (through short-range exchange interaction) the wave-function mixing between the different excitonic states. The strain components ε_{ij} are directly linked to the displacement field $\vec{u}$ induced by the phonon through the relation:

$$\varepsilon_{ij} = \frac{1}{2}\left(\frac{\partial u_i}{\partial r_j} + \frac{\partial u_j}{\partial r_i}\right) \tag{4.2}$$

In second quantization, the displacement field is given by:

$$\vec{u}(\vec{r}) = i\frac{1}{\sqrt{N}}\sum_{\vec{k}}\sqrt{\frac{\hbar}{2\rho V\omega(k)}}\vec{\epsilon}_{\vec{k}}\left(b_{\vec{k}} + b^{\dagger}_{-\vec{k}}\right)e^{i\vec{k}.\vec{r}} \tag{4.3}$$

where ρ is the crystal density, $\omega(k)$ is the frequency of the phonon mode, V is the volume of a unit cell (NV is the volume of the crystal), $b_{\vec{k}}$ and $b^{\dagger}_{\vec{k}}$ are the phonon creation and annihilation operators. $\vec{k}$ is the phonon wavevector and $\vec{\epsilon}_{\vec{k}}$ is the unit vector giving the polarization of the phonon.

Similarly to what we have seen in Chap. 1 (Eqn. 1.37), the strain terms due to phonons couple through short-range exchange interaction the bright states $|+1\rangle$ and $|-1\rangle$ (see Eqn. 1.41). The deformation potential Hamiltonian (H^{DP}) which describes the exciton-phonon coupling is given by:

$$\langle +1|\, H^{DP}\, |-1\rangle = \frac{\delta_0^{sr}}{\Delta_{lh}}\,\langle +1|\, i\frac{2}{\sqrt{3}}d\varepsilon_{xy} - b(\varepsilon_{xx} - \varepsilon_{yy})\,|-1\rangle \tag{4.4}$$

where δ_0^{sr} is the short-range exchange constant defined in Eqn 1.40, b, d are the Bir-Pikus parameter and Δ_{lh} is the energy splitting between light and heavy holes. This expression holds to describe the coupling in the limit of long wavelength phonons [65]. This expression also holds if we consider a magnetic quantum dot, and states corresponding to the same Mn spin-state ($|+1, S_z\rangle$ and $|-1, S_z\rangle$). In the following, we will not write S_z in the exciton state for brevity. We can deduce using Eqn. 4.2 and 4.3 that the coupling between these two states and the phonon modes is:

$$\langle +1|\, H^{DP}\, |-1\rangle = \frac{\delta_0^{sr}}{\Delta_{lh}}\,\langle +1|\, -\frac{1}{\sqrt{N}}\sum_{\vec{k}}\sqrt{\frac{\hbar}{2\rho V\omega(k)}}k\left(bM_b(\vec{k},\vec{\epsilon}_{\vec{k}}) + id\frac{2}{\sqrt{3}}M_d(\vec{k},\vec{\epsilon}_{\vec{k}})\right)$$
$$\left(b_{\vec{k}} + b^{\dagger}_{-\vec{k}}\right)e^{i\vec{k}.\vec{r}}\,|-1\rangle \tag{4.5}$$

In this expression, $M_b(\vec{k},\vec{\epsilon}_{\vec{k}})$ and $M_d(\vec{k},\vec{\epsilon}_{\vec{k}})$ are the so-called geometrical factors which depend on the direction of the phonon momentum $\vec{k}/k$ and polarization $\vec{\epsilon}_{\vec{k}}$, and are found replacing Eqn. 4.3 in Eqn. 4.2:

$$kM_b(\vec{k},\vec{\epsilon}_{\vec{k}}) = \left(k_x\epsilon_{\vec{k},x} - k_y\epsilon_{\vec{k},y}\right) \tag{4.6}$$

$$kM_d(\vec{k},\vec{\epsilon}_{\vec{k}}) = \frac{1}{2}\left(k_x\epsilon_{\vec{k},y} + k_y\epsilon_{\vec{k},x}\right) \tag{4.7}$$

$$\tag{4.8}$$

Where k_i, $\epsilon_{\vec{k},i}$ are the component of vector $\vec{k}$ or $\epsilon_{\vec{k}}$ along the i-axis. Assuming that the spatial wave-function of the carriers can be written:

$$\Psi_{e,h} = \frac{1}{\pi^{3/4} l_z^{1/2} l_\rho} e^{-\frac{1}{2}\left(\left(\frac{\rho}{l_\rho}\right)^2 + \left(\frac{z}{l_z}\right)^2\right)} \tag{4.9}$$

The matrix element 4.5 can be written:

$$\begin{aligned} \langle +1| H^{DP} |-1\rangle &= \int_{-\infty}^{\infty} d^3 r \Psi_h^*(\vec{r}) H^{DP}(\vec{r}) \Psi_h^*(\vec{r}) \\ &\propto -\frac{1}{\sqrt{N}} \sum_{\vec{k}} \sqrt{\frac{\hbar}{2\rho V \omega(k)}} k \left(b M_b(\vec{k}, \vec{\epsilon}_{\vec{k}}) + id \frac{2}{\sqrt{3}} M_d(\vec{k}, \vec{\epsilon}_{\vec{k}}) \right) \left(b_{\vec{k}} + b^\dagger_{-\vec{k}} \right) F(\vec{k}) \end{aligned} \tag{4.10}$$

Where $F(\vec{k})$ is commonly called form-factor, and is nothing else but the Fourier transform of the wave-function $\Psi(r)^2$:

$$F(\vec{k}) = e^{-\frac{1}{4}\left((k_\rho l_\rho)^2 + (k_z l_z)^2\right)} \tag{4.11}$$

We see from Eqn. 4.10, and the expression of the form factor that only phonons near the center of the Brillouin zone are coupled: if $k \gg 1/l_z, 1/l_\rho$, the coupling is negligible. Therefore, we will not make a big error considering a linear dispersion for the phonons: $\omega(k) = c_S k$, with $S = L, T$ corresponding to longitudinal or transverse phonons.

The phonon assisted spin-flip rate is given by Fermi's golden rule (the contribution of each phonon branch will be summed):

$$\Gamma_{-1\to+1} = \frac{2\pi}{\hbar^2} \sum_{\vec{k}} \left| \langle +1| H^{DP} |-1\rangle \right|^2 \delta(\omega_{-1\to+1} - \omega_k) \tag{4.12}$$

Alternatively written:

$$\Gamma_{-1\to+1} = 2\pi R_{ph}(\omega_{-1\to+1})(1 + n_B(\omega_{-1\to+1})) \tag{4.13}$$

where n_B is the Bose-Einstein distribution (equal to $(e^{-\beta E} - 1)^{-1}$), $\omega_{-1\to+1}$ is the frequency difference between the two bright levels and $R_{ph}(\omega)$ is spectral density of phonons, defined by:

$$R_{ph}(\omega) = \frac{1}{\hbar^2} \frac{\delta_0^2}{\Delta_{lh}^2} \frac{1}{N} \sum_k \frac{\hbar k}{2\rho V c_S} \left(b^2 M_b(\vec{k}, \vec{\epsilon}_{\vec{k}})^2 + d^2 \frac{4}{3} M_d(\vec{k}, \vec{\epsilon}_{\vec{k}})^2 \right)^2 F(\vec{k})^2 \delta(\omega - \omega_k) \tag{4.14}$$

We perform the continuum limit ($\sum_k \to \frac{NV}{(2\pi)^3} \int d^3k$ and switch to spherical coordinates: $\vec{k} = k(\sin\theta\cos\phi, \sin\theta\sin\phi, \cos\theta)$). Considering the following polarization vectors:

$$\begin{aligned} \vec{\epsilon}_{L,\vec{k}} &= \vec{k}/k \\ \vec{\epsilon}_{T_1,\vec{k}} &= (-\sin\phi, \cos\phi, 0) \\ \vec{\epsilon}_{T_2,\vec{k}} &= (\cos\theta\cos\phi, \cos\theta\sin\phi, -\sin\theta) \end{aligned} \tag{4.15}$$

for the transverse and longitudinal modes, we can calculate the geometrical factors M_b and M_d, integrate over ϕ and find in fair agreement with [64, 66]:

$$\begin{aligned}
R_{ph,L}(\omega) &= \frac{(\delta_0^{SR})^2\,(b^2+d^2/3)}{\Delta_{lh}^2}\frac{\omega^3}{16\pi^2\hbar\rho c_L^5}\int_0^\pi \sin\theta d\theta \sin^4\theta e^{-\frac{\omega^2}{c_L^2}\left(l_\rho^2\sin^2\theta+l_z^2\cos^2\theta\right)} \\
R_{ph,T_1}(\omega) &= \frac{(\delta_0^{SR})^2\,(b^2+d^2/3)}{\Delta_{lh}^2}\frac{\omega^3}{16\pi^2\hbar\rho c_L^5}\int_0^\pi \sin\theta d\theta \sin^2\theta e^{-\frac{\omega^2}{c_L^2}\left(l_\rho^2\sin^2\theta+l_z^2\cos^2\theta\right)} \\
R_{ph,T_2}(\omega) &= \frac{(\delta_0^{SR})^2\,(b^2+d^2/3)}{\Delta_{lh}^2}\frac{\omega^3}{16\pi^2\hbar\rho c_L^5}\int_0^\pi \sin\theta d\theta \sin^2\theta\cos^2\theta e^{-\frac{\omega^2}{c_L^2}\left(l_\rho^2\sin^2\theta+l_z^2\cos^2\theta\right)}
\end{aligned} \tag{4.16}$$

We calculate the phonon reservoir density by numerical means using the ZnTe sound velocities[34]: $c_L = 4\times10^3 m.s^{-1}$, $c_T = 2.6\times10^3 m.s^{-1}$ and the mass density [67, 50]. We take $\Delta_{lh} = 30meV$, $\delta_0^{SR} = 0.5meV$, $b = 1meV$ and $d = 2.76meV$.

4.1.3 Comparison with the Experiment

The shape of the spectral density of phonons depends a lot on the form-factor defined in Eqn. 4.11. If the wave-function is localized on a length l, the form-factor is equal to ≈ 1 for wave-vectors $k \ll 1/l$, while it is equal to zero for $k \gg 1/l$. Consequently, the spectral density of phonons first increases proportionally to ω^3 for $k \ll 1/l$, and decreases for $k \gg 1/l$.

We use localization parameters $l_z = 1.5nm$ and $l_\rho = 2.8nm$, found by Laurent Maingault using variational calculations in a II-VI quantum dot of typical size ($L_z = 2.6nm$ and a total width $L_\rho = 9nm$).

In Figure 4.5, we present the spin-flip rate between the two bright states as a function of the energy splitting. First, we note that this spectral density is less spread spectrally for transverse phonons than for longitudinal phonons. This is mainly due to the difference of velocity between transverse and longitudinal phonons $c_L > c_T$. The maximum of the spectral density is in $q \approx 1/l$, or equivalently $E \approx \hbar c_S/l$. The main contribution in this spin-flip mechanism is given by transverse phonons. These results can be compared with the results of Roszak *et al* [66]: we find a dynamics even slower than the one they report. The spin-flip rate found here is unable to explain the observed PL, contrary to what we thought in [68]. However these curves illustrate well how a phonon assisted process is expected to increase with the interlevel splitting in the first $\approx 1.25meV$ as a result of the increase of the phonon density.

Now, we compare the shape of the phonon density in Fig. 4.5 to the shape of the phonon side-band observed experimentally for the QD1 (see the inset of Fig. 4.3). Experimentally, the cut-off frequency is observed roughly around $1meV$ (compared to $\approx 3meV$ in the model). QD1 should evidently be modeled with larger localization parameters[35]. Considering the experimental phonon side-band of QD1, we would therefore expect a single phonon spin-relaxation process to decrease as the inter-level splitting increases from $1meV$ to $2meV$. Experimentally we observe the opposite.

[34] We use the elastic coefficients given in [67] and the fact that $c_T \approx \sqrt{C_{11}/C_{44}}c_L$.

[35] Note that the localization parameters chosen in the model are consistent with the strong hole-Mn exchange interaction observed for this quantum dot. Considering larger localization parameters for the hole to be in agreement with the acoustic phonon side-band observed experimentally would lead to a strong discrepancy with the observed exchange interaction.

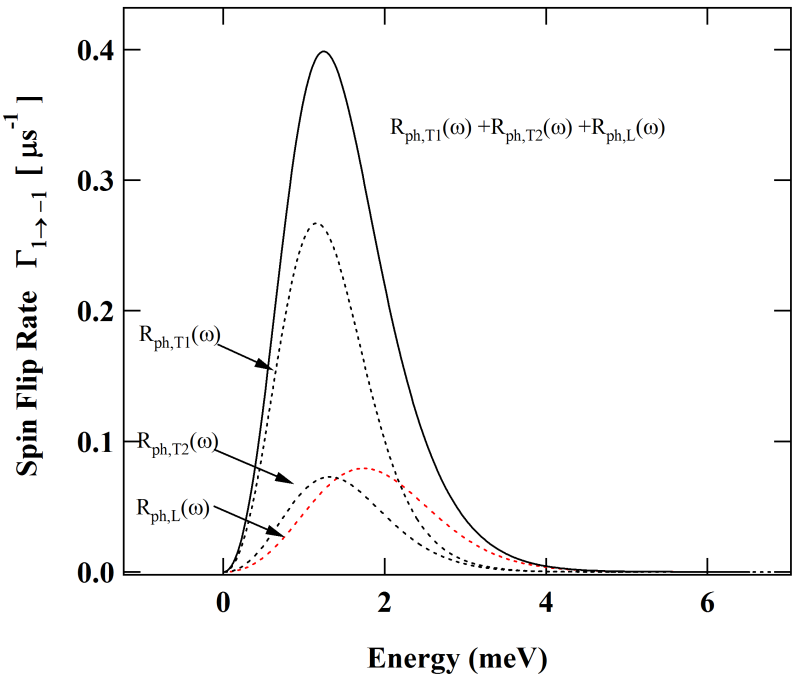

Figure 4.5: Phonon-assisted spin-flip rate corresponding to a direct transition between the two bright excitonic states (black curve) as a function of the energy splitting between the initial and final state. The contribution of the longitudinal branch and the two transverse phonon-branch are shown in dashed line. The spectral density of phonons are calculated with $l_z = 1.5nm$ and $l_\rho = 2.8nm$

To our knowledge, taking into account phonon spin-flips mediated by spin-orbit interaction would not help the understanding of the observed resonant fluorescence. Liao *et al.* [61] calculate the phonon assisted spin relaxation in (In,Ga)As quantum dots focusing on spin admixtures induced by spin-orbit coupling. They find that the dominant spin relaxation channel in a neutral quantum dot is a relaxation of the hole spin (i.e. $|+1,\rangle$ to $|-2\rangle$ and $|-1\rangle$ to $|+2\rangle$) which exceeds by a factor 10 to 100 the electron spin-relaxation in small quantum dots ($l_\rho \approx 3-6nm$). They extract a value of a few hundreds of ns. In our dots, the weak confinement of the hole could further reduce the relaxation time for the hole (this point should be checked carefully). Still, we do not see how an extension of their model applied to Mn-doped quantum dots would explain the transitions towards dark states, where a hole-Mn flip-flop is the fastest spin relaxation channel (resonance 2 3 and 6 in QD1).

4.2 Photo-Induced Orientation: Which Physical Mechanism?

4.2.1 State of the Art

The off-diagonal term of the *sp-d* exchange interaction are essential, they allow simultaneous spin-flips of carriers and the Mn spin. Cywinski [69] developed a model to clarify the physical origin of the optical pumping. He considered spin relaxation of the carriers (electron or hole). Let's consider excitation on the XMn state $|+1;+5/2\rangle$. An electron spin relaxation can be excluded from our experimental observations: electron spin relaxation from the high energy line $|+1;+5/2\rangle$ would lead to a dark state $|+2;+5/2\rangle$, which is not admixed to any other states considering the usual admixing[36]. This would not lead to any pumping process of the Mn spin. Thus, a hole spin-flip has to be considered. Once the hole has flipped, the XMn state is dark ($|-2;+5/2\rangle$), and its recombination is expected to be controlled by the admixtures with bright states. As discussed already, the dominant admixture (non-diagonal *s-d* or *p-d* exchange) depends on the dark state considered and the light/hole heavy hole mixing. However the main point is that whatever the admixture, the Mn spin decreases by one unit if the $|-2\rangle$ XMn state recombines optically through his bright part (Fig. 4.6). Cywinski showed that for realistic valence-band mixing and exchange constants, this could explain our experimental observations (apart from the saturation at 75%, which is, as we have seen a result from the coherent evolution of the Mn in the crystal field and the Mn nucleus).

In the same time, Goryca *et al.* [70], also looking for a mechanism for photo-induced spin orientation, have performed experiments in an interesting configuration: they observe the PL of a Mn-doped quantum dot at high magnetic field. This allows them to split the dark states $|-2,S_z\rangle$ from $|+2,S_z\rangle$ and so, to distinguish them. Under $\sigma-$ excitation[37], they report observing clearly the luminescence of the XMn dark states with an exciton $|+2\rangle$ explaining that the Mn spin tends to be oriented up. On the other hand, under $\sigma+$ excitation, they clearly observe the absence of luminescence on the $|+2\rangle$ XMn states. They would expect a high population transfer towards the $|-2\rangle$ XMn states. However this cannot be evidenced experimentally because the $|-2\rangle$ states overlap with the bright states at these high magnetic fields. The observation of an absence of +2 excitons under $\sigma+$ excitation is already a relevant indication: relaxation of the hole spin seems to be the preferential relaxation channel.

[36] admixtures with usual light hole/heavy hole mixing: $\left|+\tilde{3}/2\right\rangle = |+3/2\rangle + \eta\,|-1/2\rangle$

[37] The conditions of excitation are not explicitly mentioned. We assume it is quasi-resonant excitation, since the authors propose that their observations could explain experiments carried out under quasi-resonant excitation.

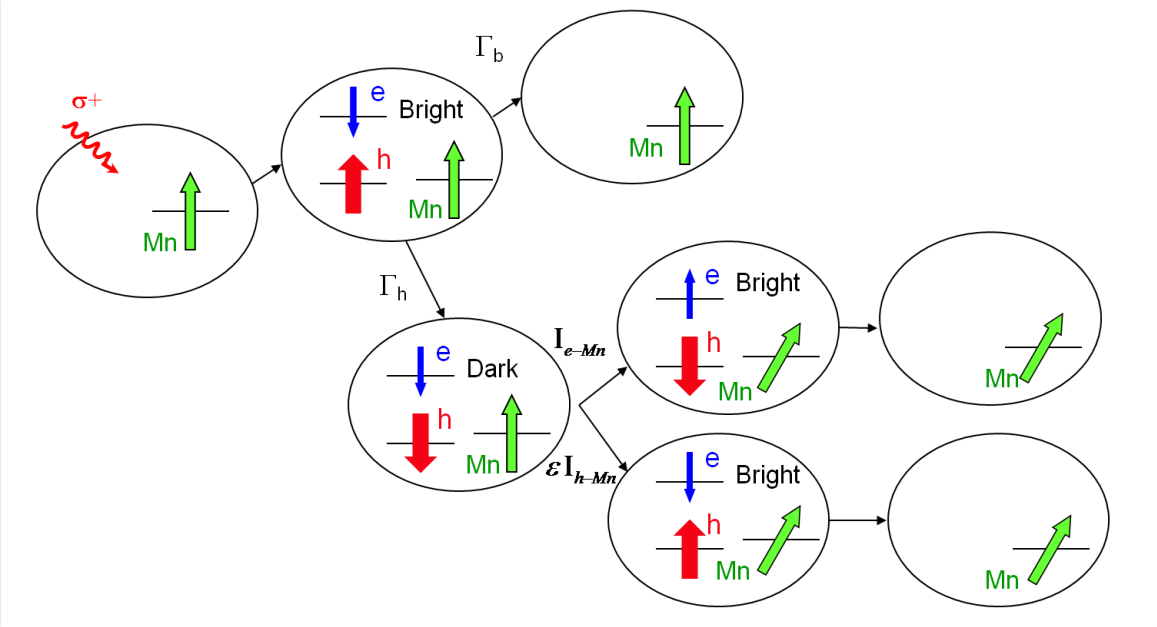

Figure 4.6: Schematic view of the mechanism proposed by Cywinski, allowing the pumping of the Mn spin under $\sigma+$ excitation. Spin relaxation of the hole at a rate Γ_h causes relaxation towards a dark state. This dark state is admixed with a bright state (through an electron-Mn or a hole-Mn flip-flop term). Recombination of the dark state through its bright part changes the Mn spin by one unit ($S_z \longrightarrow (S_z - 1)$)

4.2.2 Is the Role of Hole Spin Relaxation opened to doubt?

The XMn relaxation channels discussed in the previous section do not evidence a spin-flip of the hole. The hole spin-flip could simply be too long to be directly observed in PL. More importantly, could the observed relaxation channels within the XMn complex pave the way to a different mechanism of optical pumping? The fact that we do not fully understand the origin of these transitions does not facilitate the answer. We are going to show that another mechanism is indeed possible and could contribute to orientation of the Mn spin under resonant excitation.

The transitions evidenced in the subsection 4.1.1 correspond to a carrier-Mn relaxation. Let us suppose that both e-Mn and h-Mn spin relaxations can be involved. Experimentally, we perform optical pumping on the high energy line (say $|+1,+5/2\rangle$). Starting from the XMn state $|+1,+5/2\rangle$, an e-Mn spin relaxation leads to the dark state $|+2,+3/2\rangle$ while the hole-Mn spin relaxation via a flip-flop is forbidden (since the hole and the Mn spin are parallel). From the state $|+2,+3/2\rangle$, we need to consider the following recombination path:

- Optical recombination through a hole-Mn admixture (i.e. small admixture with the state $|-1,+5/2\rangle$)
- Optical recombination through an e-Mn admixture (i.e. small admixture with the state $|+1,+5/2\rangle$)
- Optical recombination through the light hole component of the exciton: $\left|\widetilde{+2}\right\rangle$ is in fact equal to $|J_z=+3/2,\sigma_z=+1/2\rangle+\eta\,|J_z=-1/2,\sigma_z=+1/2\rangle$. Optical recombination is expected through the emission of a photon linearly polarized along the z axis (that is to say parallel to the detection axis).

The first two recombination path are not expected to play any role on the optical orientation of the Mn spin, contrary to the last one. Recombination through the light hole component is not expected to be negligible. It leads to a recombination of the exciton with a Mn spin-state $S_z = +3/2$, different from the initial one ($S_z = +5/2$), thus leading to an optical pumping of the Mn spin. This process could also be involved in the observed spin-orientation of the Mn under resonant excitation, where experimentally, spin relaxation of the hole was not found to be the dominant relaxation channel within the XMn system.

Further investigations are required to understand the exact microscopic mechanism. An experiment that could help to discriminate between the two mechanism would be to perform optical pumping on different XMn lines (with $S_z = 5/2, 3/2, 1/2$). If Cywinski's mechanism is dominant, one would expect that the Mn spin is always driven from the state S_z to the state $S_z - 1$ (under σ_+ excitation). On the other hand, if carrier-Mn spin relaxation combined with recombination through the light-hole part is involved, one should expect more complex dynamics depending on the Mn spin-state.

4.3 Comparative Study of the Optical Orientation and Optical Pumping Dynamics

4.3.1 Power Dependence of the Optical Pumping

As displayed in Fig. 4.7, the characteristic time and the amplitude of the optical pumping signal depend on the excitation intensity. In the low excitation regime, as expected for a spin optical pumping process, the transient characteristic time τ_{pump} is inversely proportional to the pump laser intensity. However, a saturation behavior is clearly observed both for the amplitude and the characteristic time of the resonant fluorescence transient. Here, the rate of the spin optical pumping saturates around $0.025ns^{-1}$ (Fig. 4.7). The saturation of the optical pumping process results from a saturation of the absorption of the resonantly excited excitonic level. Indeed, the population of the excited state of a two level system driven by a resonant excitation laser is given by:

$$n = \frac{1}{2} \frac{\Omega^2 \frac{T_1}{T_2}}{\delta^2 + \frac{1}{T_2^2} + \Omega^2 \frac{T_1}{T_2}} \tag{4.17}$$

where Ω is the Rabi frequency, δ the frequency detuning between the excitation laser and the excitonic transition, and T_1 and T_2 the lifetime and the coherence time of the exciton, respectively. The rate of the spin optical pumping process, which is proportional to n, is expected to increase with the excitation Rabi frequency until it reaches a saturation value when the Rabi frequency is larger than the spontaneous emission rate $\Omega \gg (T_2 T_1)^{-1/2}$. The saturation curve obtained with this equation, $T_1 = 180ps$, $T_2 = 10ps$, and $\delta = 0$ is compared with the optical pumping signal. A good agreement with this simple model describing the population of a two level system resonantly excited by a cw laser is obtained.

As the intensity of the pump is increased, saturation of the absorption of the quantum dot and of the optical pumping rate is observed. Lets come back to a simple rate equation approach (neglecting the Mn fine structure). At saturation, if $S_z = -5/2$, the quantum dot is filled with an exciton half of the time and, assuming that $\Gamma_{Mn,X} \gg \Gamma_{Mn,G}$, the rapidity of the transient is simply governed by the rate of the relaxation process which depletes $S_z = -5/2$ ($\Gamma_{Mn,X}$). At saturation, the optical pumping rate observed in Fig. 4.7 (c) leads to a relaxation time

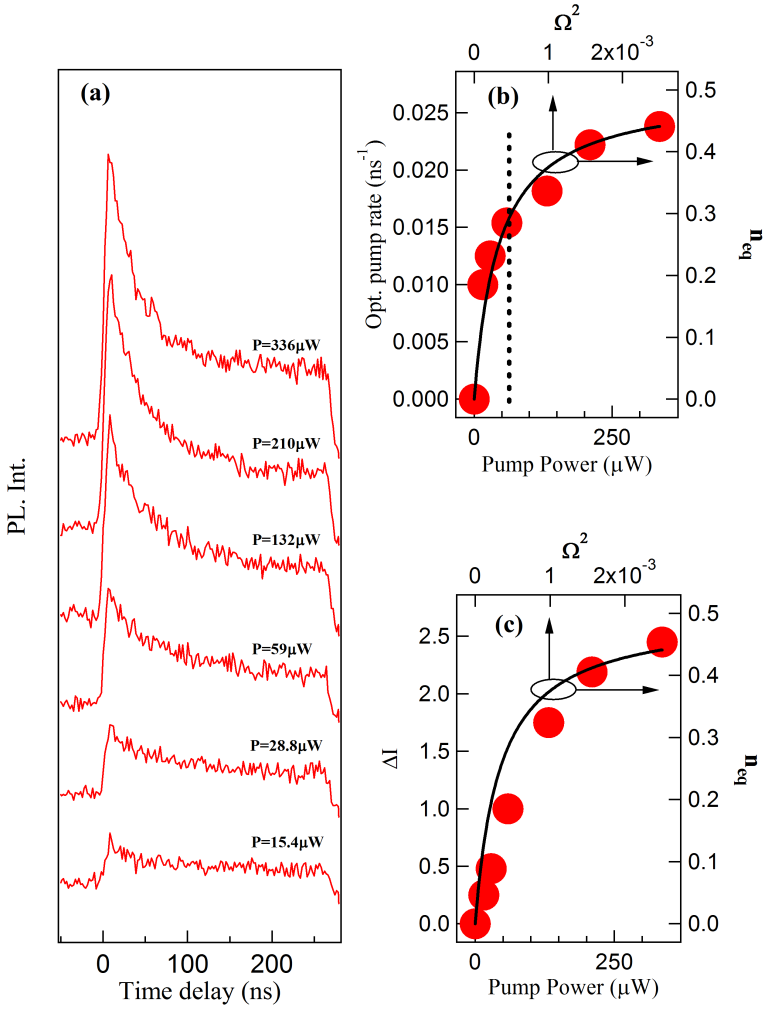

Figure 4.7: (a) Excitation power dependence of the resonant fluorescence signal. (b) Excitation power dependence of the optical pumping rate. (c) Excitation power dependence of the amplitude of the optical pumping signal. The solid line describe the population saturation of a resonantly excited two level system.

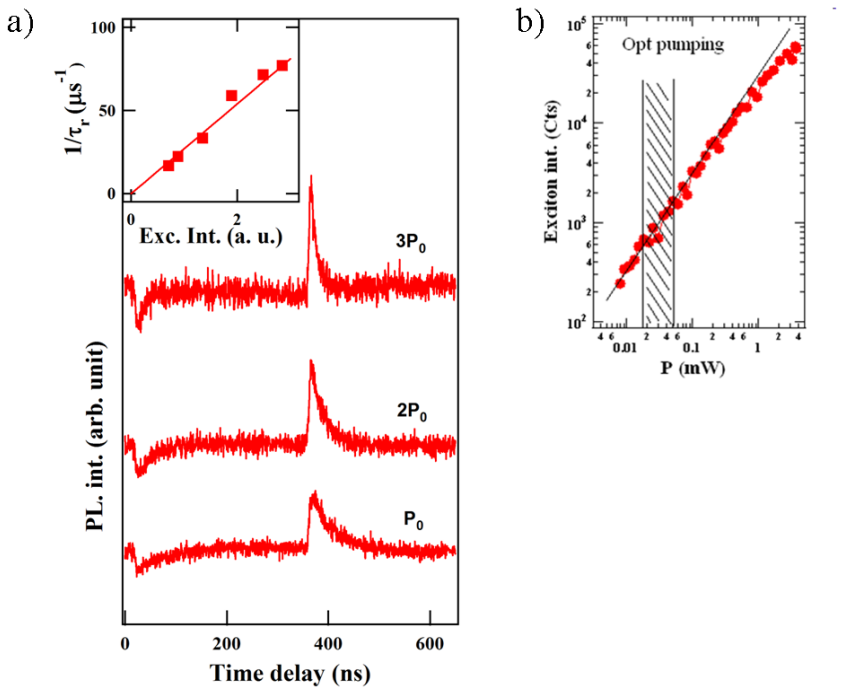

Figure 4.8: (a) PL transients at different values of the excitation power. In inset is shown the power dependence of the inverse of the response time τ_r, taken at the $1/e$ point the PL transient. (b) PL counts as a function of the excitation power. The black line is a guide to the eye showing a linear power dependence. The striped zone shows the power range in which the experiments were performed.

$\Gamma_{Mn,X} \approx 20ns$. In the microscopic process proposed by Cywinski [69], $\Gamma_{Mn,X}$ is governed by the relaxation time of the hole. However, considering the modeling presented in the section 3.4, we highlight the fact that the Mn fine structure is also expected to play a role in the transient time observed experimentally.

4.3.2 Power Dependence of the Optical Orientation

The power dependence of the optical orientation process is displayed in Fig. 4.8. In the power-range investigated here, the characteristic time of the transient is inversely proportional to the power. This is the expected behavior for a pumping process far from saturation (Fig. 4.8 (b)). The power-range cannot be further increased: at low power, we are limited by the insufficient signal to noise ratio, and at high power, the transient reaches the rise-time of the excitation modulation.

However, it is obvious that compared to the dynamics of optical pumping, optical orientation using quasi-resonant excitation is an extremely fast process ($\tau_r \approx 13ns$ for the highest power accessed experimentally which is far below the saturation).

This major difference is attributed to a spin flip of the hole during the relaxation of the carriers from the excited (XMn)*-state to the ground XMn-state. Under $\sigma+$ excitation, this leads to a high population of the $|-2\rangle$ exciton, and a decrease of the S_z through non-diagonal *spd* exchange terms. Spin relaxation of excited carriers is faster compared to when they are

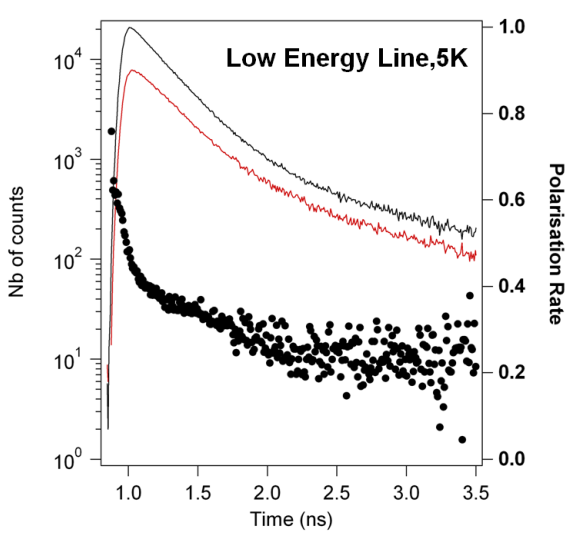

Figure 4.9: Polarization rate decay of the low energy line of a Mn-doped quantum dot under quasi-resonant excitation.

in the ground excitonic state. This can be evidenced through polarization rate measurements. We present in Fig. 4.9 the time-resolved PL observed under quasi-resonant pulsed excitation. The polarization rate presents an abrupt decrease in the first tens of ps, followed by a slower decrease. The initial diminution of the polarization rate is attributed to relaxation of the exciton during the thermalization of the photo-created carriers. The slower transient likely comes from relaxation of the exciton spin within the ground XMn complex. Hole spin relaxation is expected to follow the same trend. Relaxation of the hole during the thermalization process injects dark excitons and would explain why the optical orientation process is faster than the optical pumping process.

Conclusion

In this chapter, we have evidenced unexpectedly rapid transitions between the XMn levels. We clearly observe a dependence with the inter-level splitting of the two XMn states involved, which points out at a phonon mediated process. The transitions we observe are:

- A relaxation of the bright exciton in the exchange field of the Mn spin (i. e. from $|+1, S_z\rangle$ to $|-1, S_z\rangle$)
- A relaxation from bright do dark states or vice-versa. The relaxation channels involve a hole-Mn or an electron-Mn flip-flop. The dominant relaxation channels seem to depend on the spin-states admixtures. For instance, only hole-Mn flip-flops are observed on a quantum dot presenting strong valence-band-mixing.

The rapidity of these processes cannot be addressed considering a short-range mediated single-phonon spin relaxation.

We have discussed possible mechanism that could explain photo-induced spin-orientation. In agreement with [69], we think that a hole spin relaxation could be involved. However other mechanisms should be considered. The difference of the spin initialization time, faster under

quasi-resonant excitation than under resonant illumination is attributed to a fast spin relaxation of the hole during the injection from an excited state.

Chapter 5

Optical Stark Effect and Dressed States on a Mn-doped Quantum Dot

Contents

In this chapter, we present the observation of spin-dependent optically dressed states and optical Stark effect on the Mn spin. The vacuum-to-exciton or the exciton-to-biexciton transitions of the Mn-doped quantum dot are optically dressed by a strong laser field, and the resulting spectral signature is measured in photoluminescence. We demonstrate that the energy of any spin state of the Mn atom can be independently tuned by using the optical Stark effect induced by a control laser. We study the power-, polarization-, and detuning-dependent Autler-Townes splitting of each optical transition of the Mn-doped quantum dot. These dependencies are well described using the dressed atom picture of a two-level system, showing that any spin state of the Mn atom can be individually addressed and strongly coupled to a resonant laser field. First, we present the experimental configuration for these measurements and the dressed atom picture. Then, we present and discuss the experimental results.

5.1 The Dressed Atom Picture

5.1.1 Resonant Excitation of a transition in a Mn-doped Quantum Dot

Only one spin state of the Mn is addressed when a control laser is circularly polarized ($\sigma\pm$) and tuned on resonance with an emission line of the exciton-Mn (XMn) complex. The strong

coupling between the laser photons and the resonantly excited quantum dot levels results in the creation of dressed states which are split by a Rabi frequency Ω_r as shown in Fig. 5.1. Before we give a quantitative description of this phenomenon, we can give an intuitive picture. At resonance, the photons of the laser field can be coherently absorbed and emitted by the ground state and the excited state of the transition at a Rabi flopping frequency Ω_r which depends on the strength of the coupling between the laser field and the transition dipole. In other words, the unperturbed states $|Mn\rangle \otimes |n\rangle$ and $|XMn\rangle \otimes |n-1\rangle$ (n designates the n-photons state of the control laser), which are degenerate at resonance are no longer stationary solutions of the Hamiltonian. The stationary solutions, denoted $|II, n\rangle$ and $|I, n\rangle$ in Fig. 5.1 are symmetric and anti-symmetric combinations of the two unperturbed states and are split by the Rabi flopping frequency Ω_r. The laser used for the resonant excitation is a tunable continuous wave single-mode dye (Rhodamine B) laser with a spectral width smaller than $0.1\mu eV$. This laser is tunable between $590 - 640nm$, which allows resonant excitation on the ground state of our quantum dots. Also, a non-resonant laser is used to populate XMn and X_2Mn levels, in order to observe the Rabi splitting and to destroy the optical pumping performed by the resonant excitation.

5.1.2 The Dressed-Atom Picture

The dressed states and the energy splitting Ω_r can be found using a quantum description of the quantum dot levels and the laser field: this is the dressed atom formalism. We make the assumption that the Rabi splitting Ω_r and the detuning of the laser δ are smaller than the splitting ΔE between two PL lines of the quantum dot. Then, it is reasonable to calculate the dressed states resulting from the interaction between the two-levels of the quantum dot addressed by the laser (which will refer as $|G\rangle$ and $|E\rangle$ for the ground and excited state) and the resonant laser photons, while the light matter interaction with all the other levels is neglected. In Fig. 5.1, we have $|G\rangle = |Mn\rangle$ and $|E\rangle = |XMn\rangle$ with the Mn spin-state $S_z = +5/2$ and $X = +1$. In the absence of coupling, the Hamiltonian is:

$$H = \hbar\omega_{EG} |E\rangle \langle E| + \hbar\omega_L a a^\dagger \tag{5.1}$$

where a (resp. $a^\dagger$) is the annihilation (resp. creation) operator of a photon in the mode ω_L. The eigenstates of the uncoupled system are $|G, n\rangle$, $|E, n\rangle$, at an energy $\hbar n\omega_L$ and $\hbar(\omega_{EG} + n\omega_L)$. Since the detuning $\delta = \omega_L - \omega_{EG}$ is many orders of magnitude smaller than ω_L and ω_{EG}, these energy levels are grouped two by two: the energy separation within a multiplet is δ and the energy splitting between two multiplets is a multiple of $\hbar\omega_L$. These states are represented in Fig. 5.1 in the case $\delta = 0$.

The light-matter coupling originates from the dipole interaction $V = -\vec{d}.\vec{E}$ between the dipole d of the transition and E, the quantized electrical field operator. V is given in second quantization, in the rotating wave approximation by:

$$V \approx \hbar g(a |E\rangle \langle G| + a^\dagger |G\rangle \langle E|) \tag{5.2}$$

where g is the electric dipole matrix element describing the coupling between the dipole of the quantum dot transition and the mode ω_L of the electric field. The levels $|G, n\rangle$ and $|E, n-1\rangle$ of a multiplet are coupled through stimulated emission ($a^\dagger |G\rangle \langle E|$) and absorption of a photon ($a |E\rangle \langle G|$). The dressed states are found diagonalizing the total Hamiltonian within a given multiplet:

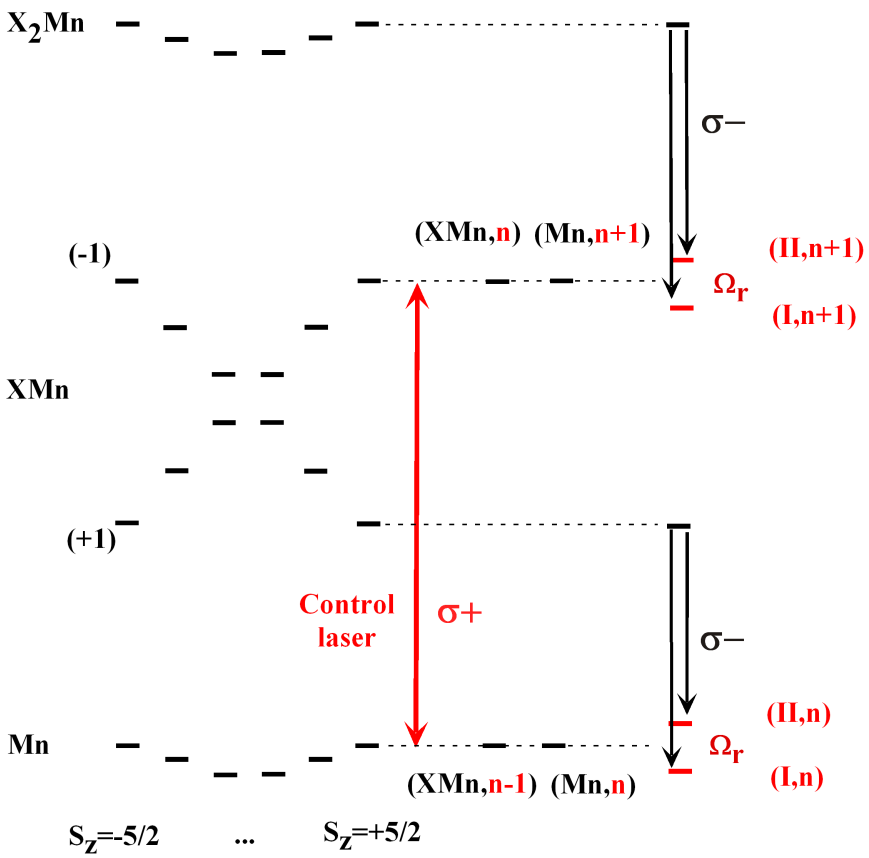

Figure 5.1: Energy levels of a Mn-doped quantum dot and formation of dressed-states. In the absence of exchange interactions with carriers (Mn or X_2Mn levels), the Mn fine structure is controlled by the strained-induced magnetic anisotropy. The bright exciton levels (XMn with X= ± 1) are split by the exchange interaction with the Mn. The quantum dot is excited by a continuous monochromatic laser tuned on a given transition of the quantum dot (here, Mn, $S_z = +5/2 \longmapsto$ XMn, X= $+1, S_z = +5/2$). Considering a mode of n photons, the levels (Mn, n) and (XMn, $n-1$) are coherently coupled through absorption and stimulated emission of a photon. The eigenstates of the coupled atom-field system (I, n) and (II, n) are entangled states which at resonance have equal contributions of the upper and the lower level of the laser-driven transition. The Rabi splitting Ω_r between these two levels can be probed in the cross-polarized PL of the exciton or the biexciton using a second non-resonant probe laser (as shown on the right part of the diagram). The splitting observed using a third level is the so-called Autler-Townes splitting.

$$H_n = \begin{pmatrix} \hbar n\omega_L & \frac{\hbar\Omega_{r,n}}{2} \\ \frac{\hbar\Omega_{r,n}}{2} & \hbar(\omega_{EG} + (n-1)\omega_L) \end{pmatrix} \tag{5.3}$$

$$= E_n^0 I_2 + \frac{\hbar}{2}\begin{pmatrix} \delta & \Omega_{r,n} \\ \Omega_{r,n} & \delta \end{pmatrix} \tag{5.4}$$

$\Omega_{r,n} = \sqrt{n}g$ is the Rabi frequency, δ the detuning and $E_n^0 = \frac{\hbar}{2}(\omega_{EG} + (2n-1)\omega_L)$ is the mean energy of the multiplet. The eigenstates of the system are given by:

$$|I, n\rangle = c\,|G, n\rangle - s\,|E, n-1\rangle \tag{5.5}$$

$$|II, n\rangle = s\,|G, n\rangle + c\,|E, n-1\rangle \tag{5.6}$$

where:

$$c = \sqrt{\frac{1}{2}\left(1 - \frac{\delta}{\sqrt{\Omega_{r,n}^2 + \delta^2}}\right)}$$

$$s = \sqrt{\frac{1}{2}\left(1 + \frac{\delta}{\sqrt{\Omega_{r,n}^2 + \delta^2}}\right)}$$

with corresponding energies:

$$E_I = E_n^0 - \frac{\hbar}{2}\sqrt{\Omega_{r,n}^2 + \delta^2} \tag{5.7}$$

$$E_{II} = E_n^0 + \frac{\hbar}{2}\sqrt{\Omega_{r,n}^2 + \delta^2} \tag{5.8}$$

$$\Delta E_{I-II} = \hbar\sqrt{\Omega_{r,n}^2 + \delta^2} \tag{5.9}$$

$$= \hbar\Omega'_{r,n}$$

$\Omega'_{r,n}$ is the generalized Rabi flopping frequency. At resonance ($\delta = 0$), $c = s = \sqrt{2}$. Then, the states $|E, n-1\rangle$ and $|G, n\rangle$ corresponding to the upper and lower levels of the transition have equal contribution to the dressed levels $|I, n\rangle$ and $|II, n\rangle$: the dressed states are entangled atom-field states.

5.1.3 Autler-Townes splitting

The Rabi splitting Ω'_r observed experimentally is given by Ω'_{r,n_L} where n_L is the average number of photons of the laser excitation. As n_L is proportional to the laser power (P), the Rabi splitting Ω_L is proportional to $\sqrt{P}$. In the following experiment, it is observed using non-resonant excitation to generate PL by a transition involving a third level and an optically dressed state as shown in Fig. 5.1. The PL of such transitions are split because, for example, spontaneous emission from $|-1, +5/2\rangle$ can occur toward any of the dressed states (II, n) and (I, n) as they contain a component of the $|+5/2\rangle$ state. The resulting PL is split by Ω'_r, this is the so-called Autler-Townes splitting [71]. As shown in Fig. 5.1, when the laser is tuned on a XMn-to-Mn

transition, an Autler-Townes splitting can also be observed by detecting the adequate biexciton PL line.

The strong coupling regime between a quantum dot transition and a laser field has been observed for the first time in 2001 by Kamada *et al.* [72], using resonant excitation on an excited state of a quantum dot. In [73, 74], Xiaodong Xu *et al.* have measured the absorption of a weak probe when the ground excitonic transition of a neutral and negatively charged quantum dot is resonantly driven by a strong pump. They have evidenced Autler-Townes and Mollow absorption spectra. Dressed states were also observed in [75] and [76]. All these experiments were performed on III-V quantum dots.

5.2 Optical Stark Effect and Dressed Exciton States in a Mn-doped Quantum Dot

5.2.1 Experimental Evidendence of Optical Stark Effect and Dressed Exciton States

Experimental data corresponding to a control laser tuned on $|+1, 5/2\rangle$ and the observation of an Autler-Townes splitting in the PL of the state $|-1, 5/2\rangle$ are presented in Fig. 5.2. Particular care is given to the effect of the detuning of the control laser from the XMn resonance [Figs. 5.2(c) and 5.2(d)] and its intensity [Figs. 5.2(e) and 5.2(f)]. At large laser detuning, the optically active transitions asymptotically approach the original excitonic transitions where the remaining energy offset is the optical Stark shift. At the resonance, an anticrossing is observed showing that the strong coupling between the laser field and the exciton creates hybrid light-matter states. As presented in the inset in Fig. 5.2(d), a good agreement with the simple dressed atom model is obtain with a Rabi energy of $\Omega_r = 180\mu eV$. On resonance, the emission from the $|-1, 5/2\rangle$ state splits into a doublet when the power of the control laser is increased. The splitting is plotted as a function of the square root of the control laser intensity in Fig. 5.2(f), showing that the splitting linearly depends on this quantity, as expected from the dressed atom model. A Rabi splitting larger than $250\mu eV$ is obtained at high excitation intensity. It is worth noting that these energy shifts can be easily larger than the magnetic anisotropy of an isolated Mn spin created by the strain in the quantum dot plane ($\approx 40\mu eV$). This optical tuning of the fine structure may lead to a control of the coherent dynamics of the isolated Mn spin.

The high energy transition of the XMn complex is twice degenerate. The corresponding optical transitions differ by the polarization of the absorbed or emitted photons. The polarization dependence of the laser-induced splitting shown in Fig. 5.2(b) confirms the Mn spin selectivity of the strong coupling with the laser field: $\sigma+$ photons couple with the state $|+5/2\rangle$ of the Mn to create two hybrid light-matter states, while no splitting of this PL line is observed when the control laser is $\sigma-$. This demonstrates that the Mn spin state $S_z = +5/2$ is not dressed by the $\sigma-$ control laser, in accordance with the dipole selection rules.

5.2.2 Individual Addressing of any Transition and Mn Spin State

The strong coupling with the control laser is also observed monitoring the PL of the biexciton. This configuration of the detection speaks for itself, as the PL lines corresponding to the six Mn spin states can be observed at the same time. A detuning dependence of the PL emission is presented in Fig. 5.3 in the case of successive resonant excitations on the XMn transitions corresponding to a Mn spin state $S_z = +1/2$, $+3/2$, and $+5/2$. In these cases, the recombination of X_2Mn probes the laser-induced splitting of a XMn level for a given spin state of the Mn. It is

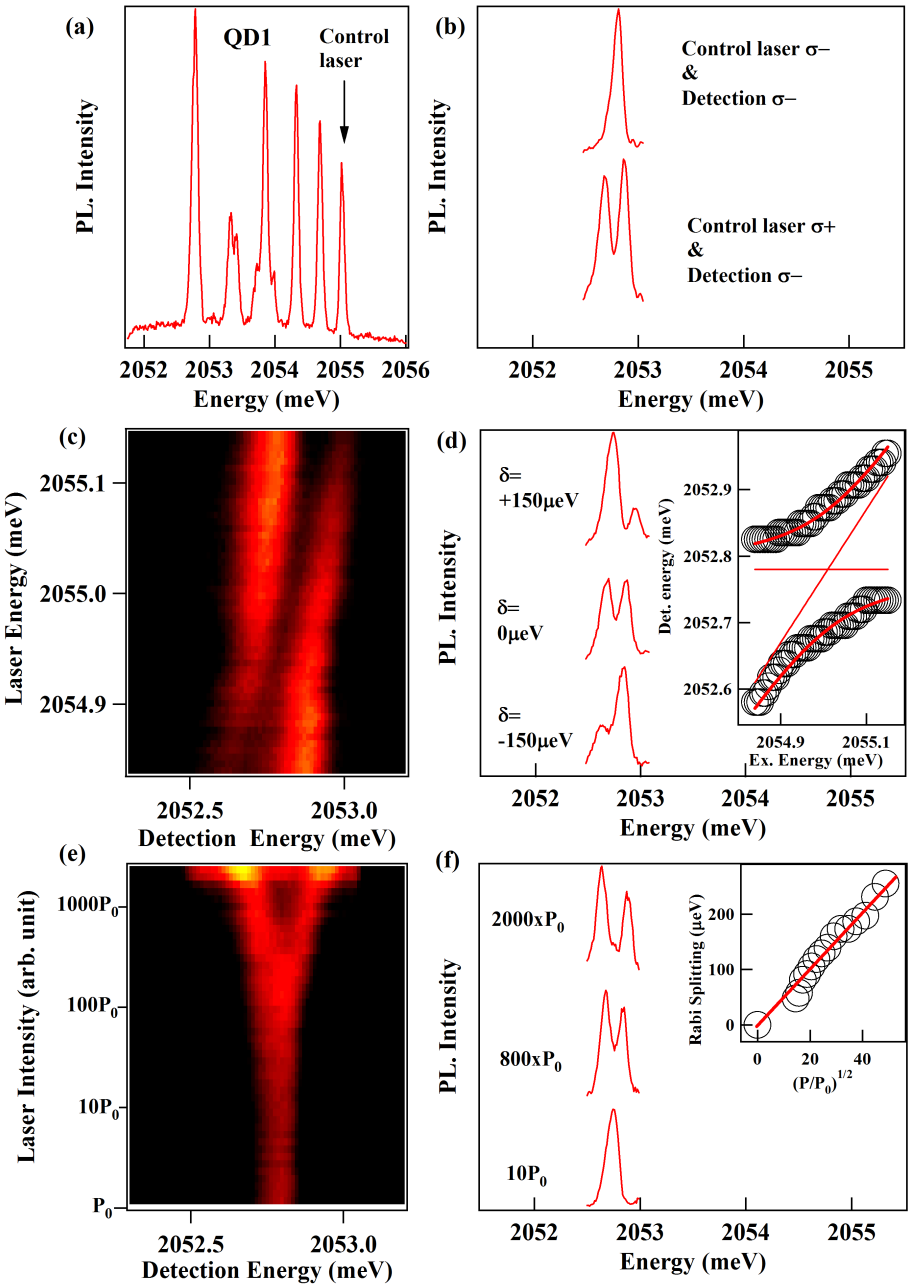

Figure 5.2: Autler-Townes splitting of the PL emission of $|-1,+5/2\rangle$ in a Mn-doped quantum dot (QD1) resonantly excited on $|+1,+5/2\rangle$. (a) shows the PL of QD1 under non-resonant excitation. (c) is the intensity map of the PL as the resonant laser is tuned around the transition. The corresponding emission line-shape is presented in (d). The inset of (d) shows the spectral position of the Autler-Townes doublet as a function of the energy of the resonant laser. The fit is obtained with a Rabi splitting $\hbar\Omega_r = 180\mu eV$. The straight lines correspond to the uncoupled exciton and laser energy. (e) is the intensity map of the PL as the resonant laser power is increased. The corresponding PL spectra are presented in (f). The inset of (f) shows the evolution of the Rabi splitting with the square-root of the resonant laser power. A linear increase is observed. (b) presents the circular polarization dependence of the Rabi splitting obtained under resonant excitation.

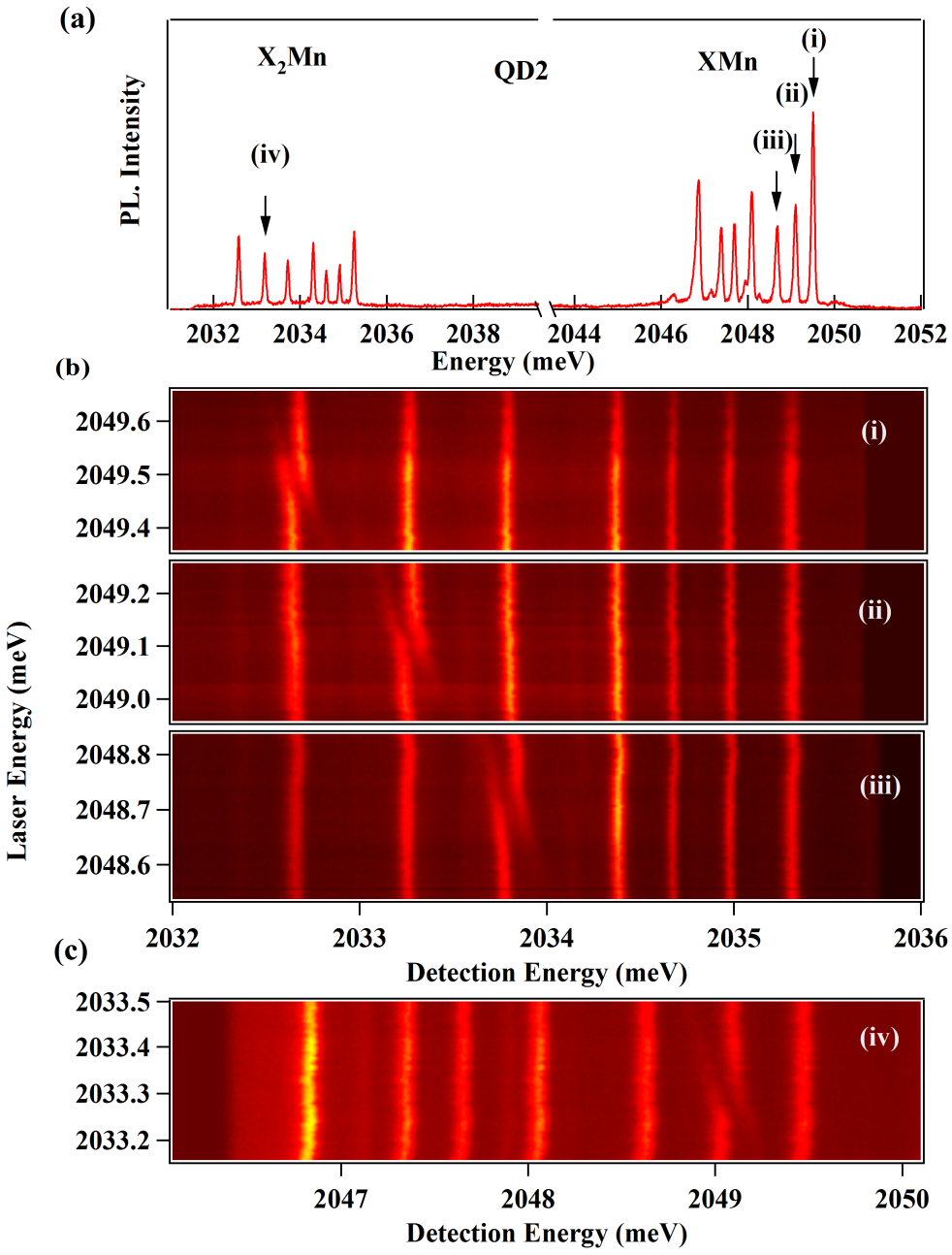

Figure 5.3: (a) PL of the exciton and biexciton in a Mn-doped quantum dot (QD2). (b) Autler-Townes splitting of the exciton in QD2 detected on the biexciton PL under resonant excitation of the ground-to-exciton transition for the Mn spin-state $S_z = +5/2$ (i), $S_z = +3/2$ (ii), $S_z = +1/2$ (iii) (arrows on the PL spectra of QD2). (c) Emission of the exciton for a dressed exciton-to-biexciton transition. The excitation is tuned around the state $S_z = +3/2$ of the biexciton (iv).

shown here that any XMn transition can be dressed, and consequently any Mn spin state can be optically shifted by a control laser tuned on resonance. By coherently driving the X_2Mn-to-XMn transition, one can also tune the energy of any state of the XMn complex as illustrated in Fig. 5.3(c) for $S_z = 3/2$. This set of experiments demonstrates that a complete optical control of the exciton-Mn system is possible.

A zoom on the detuning dependence of the dressed X_2Mn-to-XMn transition is shown in Fig. 5.4. This detuning dependence also follows the evolution predicted by the dressed atom-picture. The PL spectra observed experimentally correspond well with the spectra expected theoretically (model given in the Annex B). Note the mirror symmetry when the resonant laser is tuned on a X_2Mn-to-XMn transition while the detection is done on a XMn-to-Mn transition (or vice-versa): the anti-crossing observed in Fig. 5.4(a) and 5.3 are reversed with the one observed in Fig. 5.2 (c) where resonant excitation and detection both take place on a XMn-to-Mn transition.

5.2.3 Resonant Excitation on Mn Spin States Coupled Through Valence Band Mixing

It is also demonstrated here that the use of a resonant strong laser field allows one to individually address any spin state of the Mn even if they are coupled by the exciton through valence band mixing (VBM).

The particular situation where the Mn spin states $S_z = +1/2$ and $S_z = +3/2$ are significantly mixed is presented in Fig. 5.5. The spectrum of this quantum dot [Fig. 5.5(a)] is the one already discussed in Chap. 1 (1.3.3). Through hole-Mn short-range exchange, the VBM couples $|-1, +3/2\rangle$ with $|+2, +1/2\rangle$, and the new eigenstates (labeled (1) and (2) in Fig. 5.5 (a)) share the oscillator strength of the bright state $|-1, +3/2\rangle$. This attribution is confirmed by the calculation of the energy levels presented in Fig. 5.5(b). As shown in Figs. 5.5(c) and 5.5(d), it is possible to optically address selectively one state (and one only) of the Mn spin in the mixed bright-dark XMn levels. When the $\sigma+$ control laser is tuned on the state $|-1, +3/2\rangle$ [line (4)], an Autler- Townes splitting is observed in $\sigma-$ polarization for both components of the emission of the dark-bright excitonic complexes [lines (1) and (2) in Fig. 5.5(c)]. This arises from the control laser-induced splitting of their common final state with a Mn spin $S_z = +3/2$. With a resonant excitation on the mixed bright-dark states, only the states which share a Mn spin-state $S_z = +3/2$ are split. The dark part with a Mn spin-state $S_z = +1/2$ is not affected. This is demonstrated in Fig. 5.5(d). The $\sigma-$ control laser splits the Mn state $|+3/2\rangle$, which leads to the formation of a doublet in the $\sigma+$ PL from the state $|+1, +3/2\rangle$ [line (4)], while no splitting of the state $|+1, +1/2\rangle$ [line (3)] is observed. This experiment suggests the possibility to optically control the exciton-induced coupling between two spin states of the Mn atom. A resonant laser tuned on the transition $|-1, +3/2\rangle$-to-$|X_2, +3/2\rangle$ or $|-1, +3/2\rangle$-to-$|+3/2\rangle$ should detune the exciton level $|-1, +3/2\rangle$ from $|+2, +1/2\rangle$ and reduce the dark-bright admixing and the coupling between the two Mn spin states resulting from it.

5.2.4 Power Limitation to the Increase of the Rabi Frequency

An important question to address is whether the strong resonant excitation causes unwanted electro-static fluctuations or broadening effects. Laser excitation above the barriers is well-known to increase the pure dephasing or the spectral diffusion of the quantum dot transitions because of the photo-induced charge fluctuations in the vicinity of the quantum dot [77]. Excitation under the wetting layer (resonant on the ground state and sometimes on the first excited states) is expected to address this problem, and it has indeed been observed so far that resonant excitation

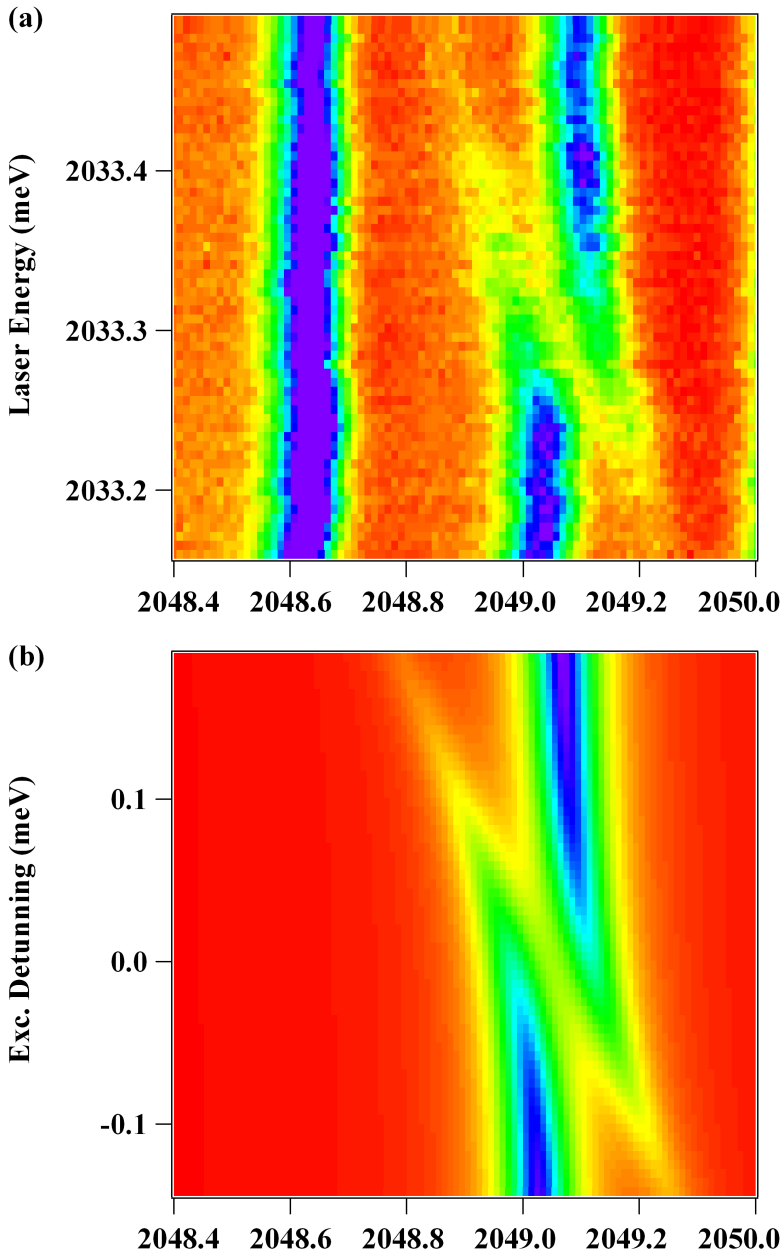

Figure 5.4: (a) presents the intensity map of the exciton PL, centered on the transition $|+1,+3/2\rangle \longmapsto |+3/2\rangle$, as the resonant laser is tunned around the exciton-to-biexciton transition $|+1,+3/2\rangle \longmapsto |X_2,+3/2\rangle$. (b) is the intensity map of the Autler-Townes splitting expected theoretically as a function of the laser detuning, in the approximation of a spin-selective excitation (i.e. only the four levels corresponding to $S_z = 3/2$ are considered). The spectra were calculated considering a Rabi splitting $\Omega_r = 140\mu eV$ and a pure dephasing term of $40\mu eV$ for all the transitions (model given in the annex B).

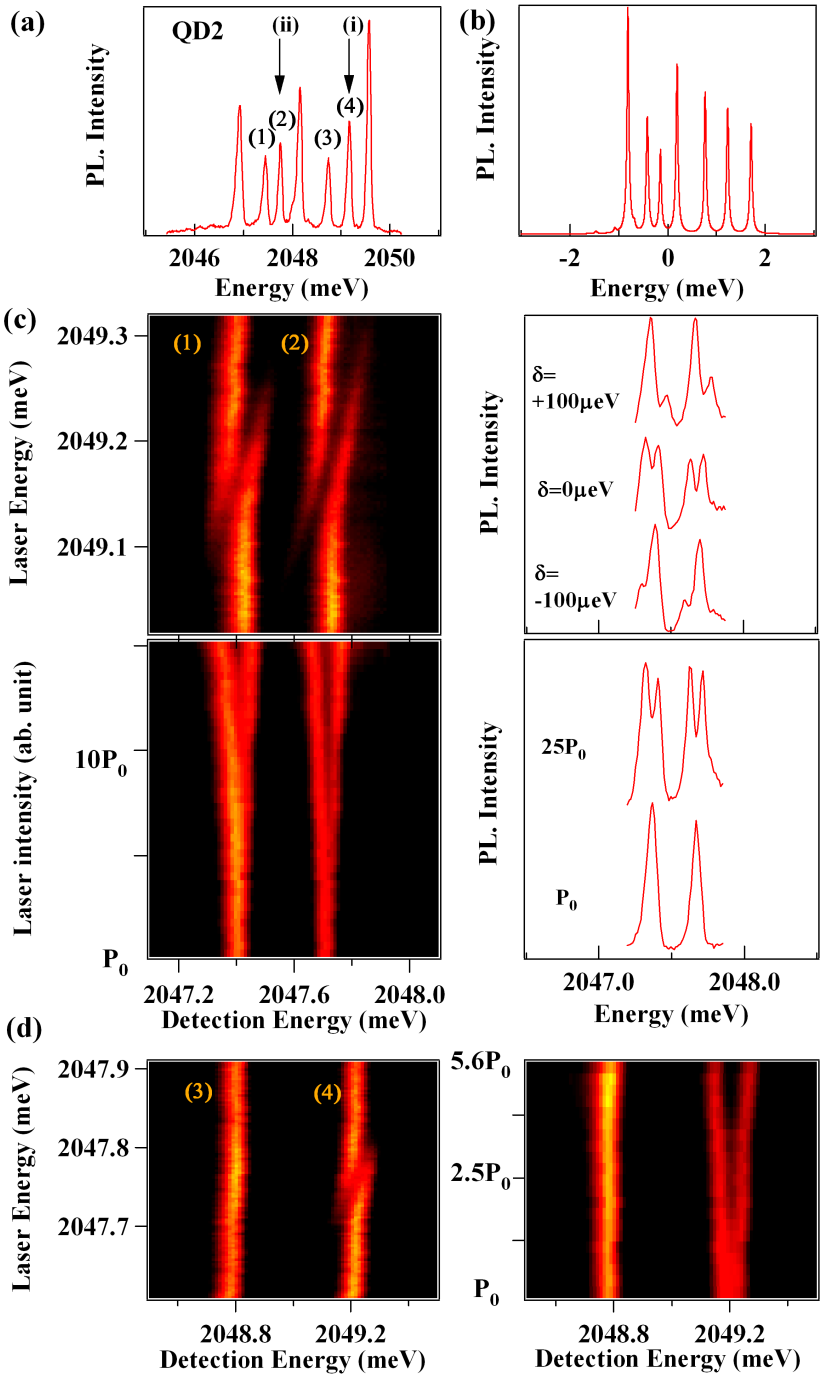

Figure 5.5: Rabi splitting obtained on a mixed bright-dark states in QD2. (a) presents the PL of QD2. The corresponding theoretical emission spectra is presented in (b). It is calculated with $I_{eMn} = 95\mu eV$, $I_{hMn} = 300\mu eV$, $I_{eh} = 900\mu eV$, $\eta = 0.1$, and $\delta_1 = 50\mu eV$ (following the notations introduced in Chap. 1). (c) presents the detuning and the excitation power dependence of the Rabi splitting obtained on a mixed bright-dark exciton under excitation on (i). (d) presents the detuning and excitation intensity dependence measured on the high energy transitions associated with the Mn spin states $S_z = +1/2$ and $S_z = +3/2$ (i.e. lines (3) and (4)) under excitation on the mixed dark-bright exciton (ii). The relevant PL lines are numbered for a sake of clarity.

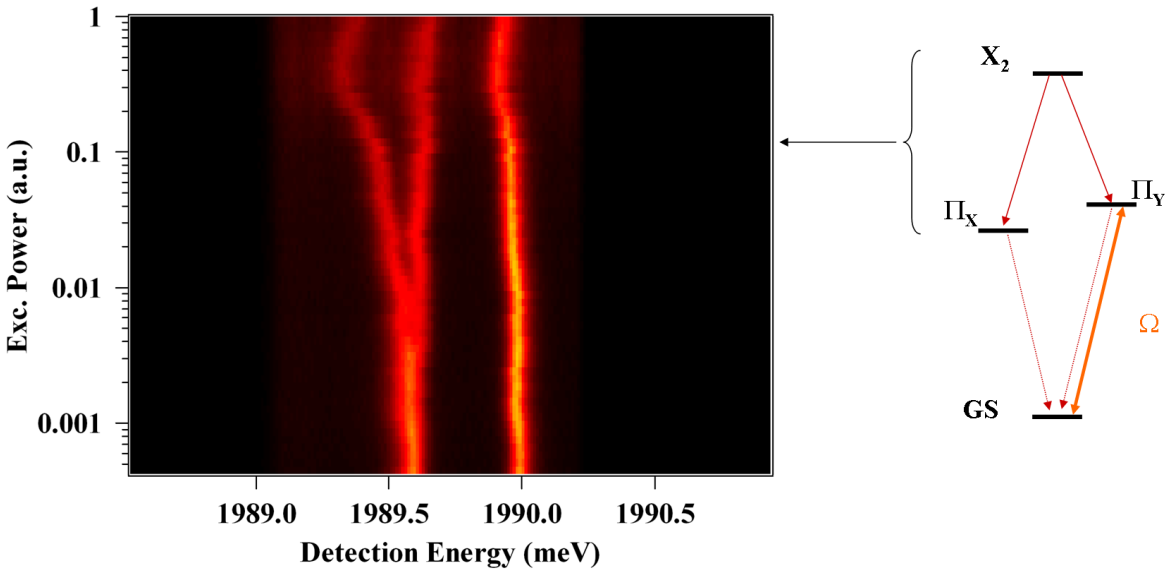

Figure 5.6: Power limitation: biexciton PL intensity map of a neutral quantum dot (no Mn) for increasing resonant laser power (the laser is tuned on the ground-to-exciton transition as shown on the right scheme). At high excitation power the emission of the PL is red-shifted.

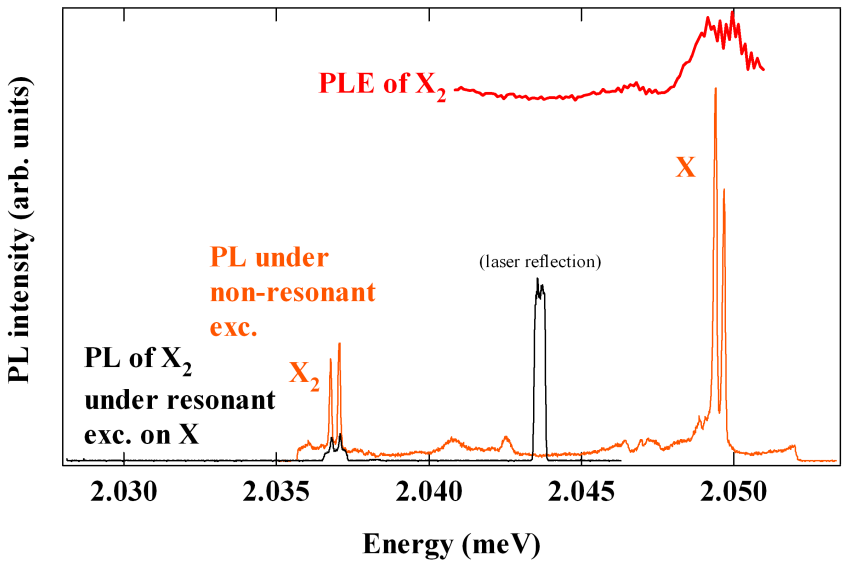

Figure 5.7: Observation of PL emission from the biexciton when exciting resonantly the exciton shown on a non magnetic quantum dot. PLE measurement is carried out and reveals the existence of a resonance close to exciton energy. The PL spectra shown are taken with the same integration time ($1s$) and the same excitation power.)

did not cause additional dephasing [76, 73, 74] even at strong power of excitation.

In the present case, the studied quantum dots have a linewidth ($\geq 60\mu eV$) which is not limited by the resolution of our set-up. No diminution of the line-width is observed under strictly resonant excitation. When the resonant excitation power is increased, broadening of the lines (others than the levels driven resonantly which are of course power broadened) is not observed for a wide range of power excitation and enables to reach Rabi splitting $\approx 300\mu eV$.

However, experimental observations show that the Rabi splitting cannot be further increased. At a certain power, further increase of the excitation power causes a red-shift and a broadening of the transitions. This is shown in Fig. 5.6, in the case of a non-magnetic quantum dot. The same behavior is of course observed on magnetic quantum dots. This limits the maximum Rabi splitting to a value of $\approx 300\mu eV$ when the laser is at resonance with the transition. We have also observed the irreversible broadening of the quantum dot PL when exciting beyond this power which is the signature of a structural change and a local deterioration of the sample due to strong laser excitation. We speculate that the reason for these observations is a heating of the sample by the laser although the sample should not be absorbent at these wavelength.

Moreover, we have observed that resonant excitation on one of the six PL line of a magnetic quantum dot produces almost systematically significant PL of the biexciton on the sample studied in this chapter. This is quite unexpected. PLE measurements of the biexciton (Fig. 5.7) has revealed the existence of a resonance close to the exciton emission (in some cases, the resonance is shifted to a few meV higher than the energy of the exciton). This behavior has been observed only on one sample, and PLE measurements of X_2 have been carried out only on a few quantum dots. Further studies are required to understand where this resonance comes from.

Conclusion

In summary, we have demonstrated that the ground, exciton, and biexciton states in a Mn-doped quantum dot can be coherently coupled to a strong resonant laser field on the optical transitions. At the resonance, hybrid matter-field states are created that should significantly influence the Mn spin dynamics. Our results demonstrate that, even under a strong optical field, the transition in a Mn-doped quantum dot behaves like isolated two-level quantum systems well described by the dressed atom picture. Only one spin-state of the Mn impurity is addressed even if the spin-states are coupled through valence-band-mixing. In the ground state, the laser-induced shift of the Mn spin could be used for a fast optical manipulation of the spin degree of freedom of the Mn atom [78]. At last, we have discussed properties of our sample under resonant excitation and have seen that the maximum Rabi splitting obtainable experimentally is limited.

Chapter 6

Spin Dynamics in n-Doped CdTe Quantum Dots

Contents

In this chapter, as a preliminary study of the influence of a Mn spin on the dynamics of a confined carrier, we discuss the properties of n-doped CdTe/ZnTe quantum dots. The samples are obtained by modulation doping: during the growth, a $20nm$ thick Al-doped ZnTe layer is grown $30nm$ above the quantum dots. The electrons from the Al donors are eventually trapped in some quantum dots, allowing the study of quantum dots with a single resident electron. First, we focus on the optical features which indicate that the quantum dots are negatively charged. Similarly to Mn-doped quantum dots, we will see that the spin of this resident carrier can be controlled by optical pumping. Then, we show that the electron is strongly coupled to the nuclear spin bath through hyperfine interaction which can efficiently depolarize the electron. On the other hand, continuous optical pumping of the electron can be used to create a dynamic polarization of the nuclei. The strong depolarization of the electron induced by nuclear spin fluctuations is then suppressed at $B = 0T$.

6.1 Optical Properties of Negatively Charged Quantum Dots

A large majority of the quantum dots in the sample studied here present a single PL line, which is the signature of a charged exciton X^+ or X^-. Moreover, these lines present a negative circular

polarization rate ranging from -20% to -60% when the laser frequency is higher than a certain value (typically $70meV$ above the PL emission). As we will explain, this is a characteristic of negatively charged quantum dots in the optical pumping regime. Another signature of X^- is the presence of a polarized fine structure in the Pholotoluminescence Excitation Spectra (PLE).

6.1.1 Polarized Fine Structure of the Excited State

We present a typical PLE spectra of these quantum dots in Fig. 6.1 (a). A negative circular polarization is observed at high energy of excitation. Also, the PLE exhibits a resonance around $2110meV$ with a strongly co- and then cross-polarized PL as the laser energy increases (Fig. 6.1 (b)). This striking feature has already been observed on InAs quantum dots by M. E. Ware *et al.* [79]. It results from optical excitation on the p-shell of the singly charged quantum dot.

The fine-structure of the p-shell (hot trion) results from the exchange interactions between the resident electron ($\uparrow_s$ or $\downarrow_s$), and the photo-created electron-hole pair ($\Uparrow_p\downarrow_p$ for $\sigma+$ excitation). The strongest exchange term is the electron-electron exchange interaction [80] which reduces to a Heisenberg Hamiltonian:

$$H_{e_s,e_p} = -\Delta_{ee}\vec{\sigma}_1.\vec{\sigma}_2 \tag{6.1}$$

This Hamiltonian splits the excited[38] singlet state S_0^* with $I = 0$ from the triplet T_{-1}, T_0, T_{+1} with $I = 1$. This splitting is typically equal to $5meV$ in InAs/GaAs quantum dots [81], [79]. The electron-hole exchange interaction Δ_0 is a smaller correction (typically $250\mu eV$ in InAs/GaAs quantum dots and $350\mu eV$ in the present case) which splits the triplet states T_1, T_0 and T_{-1} as shown in Fig. 6.2. The full Hamiltonian of the charged exciton is:

$$\begin{aligned} H_{e_s,e_p,h_p} &= \Delta_{ee}(\frac{3}{4} - \frac{I^2}{2}) + 2\Delta_0 j_z I_z + \frac{\Delta_1}{2}(j_+I_- + j_-I_+) + \frac{\Delta_2}{2}(j_+I_+ + j_-I_-) \\ &\quad +2\eta_0 j_z K_z + \frac{\eta_2}{2}(j_+K_- + j_-K_+) + \frac{\eta_1}{2}(j_+K_+ + j_-K_-) \end{aligned} \tag{6.2}$$

In this equation, we have used $\vec{K} = \vec{\sigma}_1 - \vec{\sigma}_2$ and $\vec{I} = \vec{\sigma}_1 + \vec{\sigma}_2$. The non-diagonal exchange terms Δ_1 (resp. η_1) allow a mixing between the triplet states $T_{-1} \Uparrow$ and the states $T_0 \Downarrow$ (resp $S_0^* \Downarrow$). This mixing is invoked to explain the polarized fine-structure of the p-state shown in Fig 6.1. As shown in Fig 6.1 (c), $\sigma+$ excitation selectively excites the triplet $T_0 \Uparrow$ or $T_{-1} \Uparrow$, depending on the excitation energy and the spin of the resident electron. Then relaxation to the ground state of the trion S_0 from $T_0 \Uparrow$ can occur, while relaxation from $T_{-1} \Uparrow$ requires a hole-electron flip-flop to the state $T_0 \Downarrow$ before relaxing to $S_0 \Downarrow$ resulting in a $\sigma-$ PL, controlled by the hole spin.

Relaxation from T_0 to S_0 is in fact not straightforward: the spin projection over z is conserved but the total angular momentum I of the two electrons is not conserved. The authors of [79] retain the Dzyaloshinskii-Moriya exchange term as a probable cause of the observed relaxation. This exchange term is more often encountered in magnetism than in quantum dot physics. The exchange term we have used so far are all based on the assumption that the exchange tensor is symmetric and can be diagonalized choosing proper axis (i.e. the exchange Hamiltonian could always be expressed as $H_{1,2}^{exch} = \sum_{i=x,y,z} a_i \sigma_i^1 \sigma_i^2$, where x, y, z were axis of the crystal). Dzyaloshinskii and Moriya showed that this assumption is only an approximation: there is also

[38] Excited singlet, as opposed to the ground state singlet of the trion where the two electrons are on the s shell.

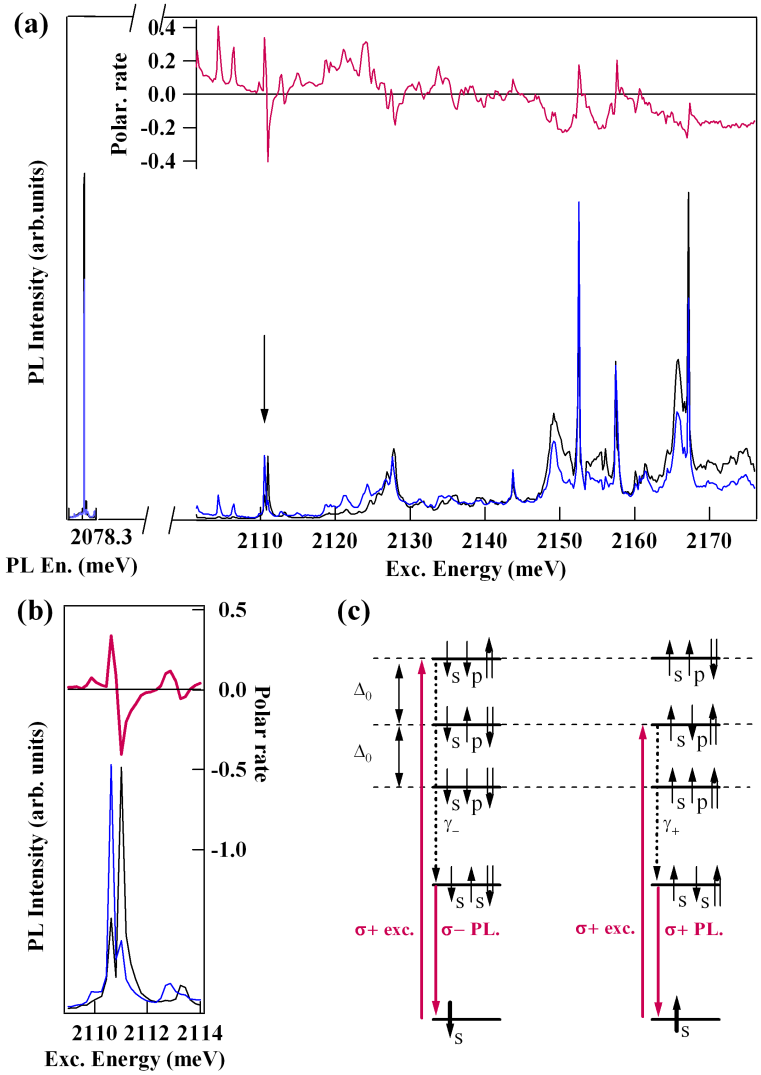

Figure 6.1: a) PLE spectra resolved in circular polarization under $\sigma+$ CW excitation. The corresponding polarization rate is displayed above. The PL is displayed on the left. b) Zoom on the polarized doublet observed in the PLE at a laser excitation around $2110meV$. c) Energy levels in a negatively charged quantum dot: (from bottom to top) the ground state (degenerate), the ground state of the trion (degenerate) the triplet state $S = 1$ (which is split by the electron-hole exchange). The representation may be over-simplified: for instance, the states denoted $\uparrow_s\downarrow_p$ stands for a symmetric spin-part for the two electrons $(\uparrow_s\downarrow_p) + (\downarrow_s\uparrow_p)$ and the excited singlet state is not represented. Only the top-two triplet states are bright. When the $\sigma+$ laser is tuned on the triplet with $S_z = 0$ (on the right part of the scheme), absorption occurs only if the resident electron is up, and relaxation to the ground singlet occurs at a rate γ_+ resulting in $\sigma+$ PL. When the laser is tuned on the triplet with $S_z = -1$ (left part of the scheme), absorption occurs only if the resident electron is down, relaxation of the electron to the ground singlet is forbidden by the Pauli principle. Relaxation is allowed through an electron-hole flip-flop (due to the assymetric part of the e-h exchange) at a rate γ_- resulting in $\sigma-$ PL.

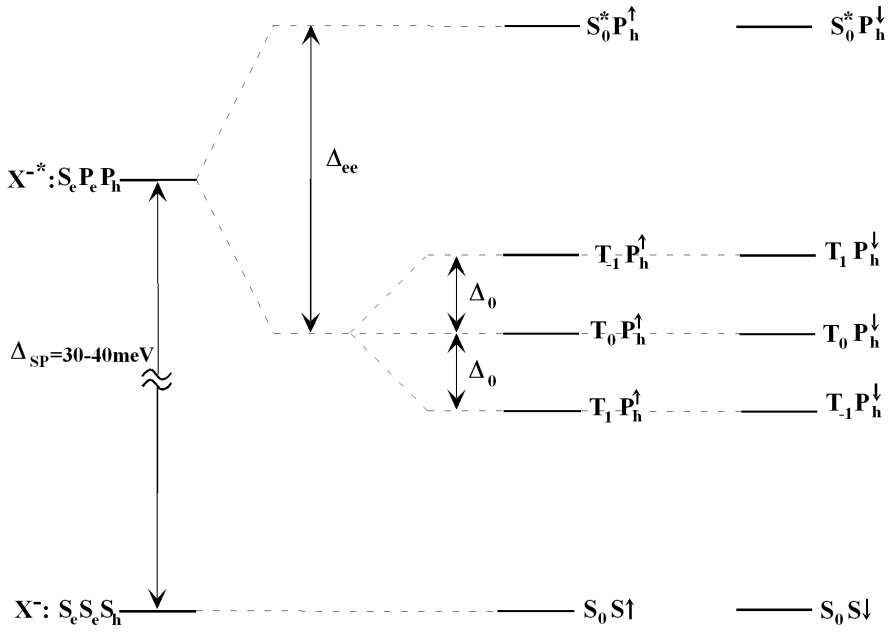

Figure 6.2: Fine structure of the negatively charged exciton.

an anti-symmetric part in the exchange tensor resulting from spin-orbit interaction. This anti-symmetric part can be expressed as a vectorial product[39]:

$$H_{1,2}^{exch,AS} = \vec{D}.(\vec{\sigma}^1 \wedge \vec{\sigma}^2) \tag{6.3}$$

where $\vec{D}$ is the so-called Dzyaloshinskii-Moriya vector. The term in $D_z(\sigma_x^1\sigma_y^2 - \sigma_y^1\sigma_x^2)$ mixes efficiently the triplet state T_0 with the excited singlet S_0^*. The authors of [79] estimate using power broadening of the transitions, the relaxation rates of each triplet to the ground singlet to be $\gamma_+ = (25ps)^{-1}$ and $\gamma_- = (310ps)^{-1}$. From these values they extract the ratio $\Delta_1/\Delta_0 = 0.24$ while $D_z/\Delta_{ee} = 1/5$ corresponding to $\Delta_2 = 60\mu eV$, $\Delta_0 = 250\mu eV$, $\Delta_{ee} = 6meV$ and $D_z = 1.2meV$. All the other anisotropic exchange term are neglected in their model. They have found that these values were compatible with *kp* calculations in a potential with a realistic anharmonicity.

We have found that the triplet splitting Δ_0 typically ranged from $350\mu eV$ to $490\mu eV$ (Fig. 6.3). This is higher than the values found by M. E. Ware *et al.* in InAs/GaAs quantum dots. This is in agreement with stronger exchange interactions in our system (for e.g. the electron-hole exchange δ_0 for the neutral exciton is typically twice the one found in InAs/GaAs quantum dots [82]). We also note in Fig. 6.1 (b) the presence of a weaker polarized doublet $\approx 3meV$ away from the first polarized doublet. This is often the case (see also the spectra shown in Fig. 6.4), and probably results from a lift of degeneracy between the orbital P states, as observed already in [48].

In the next-section, using time-decay experiments, we are going to estimate the relaxation rates γ_+ and γ_- in our quantum dots and study the spin-injection mechanism which leads, among other things, to the negative PL observed at high energy of excitation.

[39] This is just a way of re-writing the anti-symmetric exchange tensor $\overline{\overline{J}}$ (for e.g. $J_{xy} = -J_{yx} = D_z$)

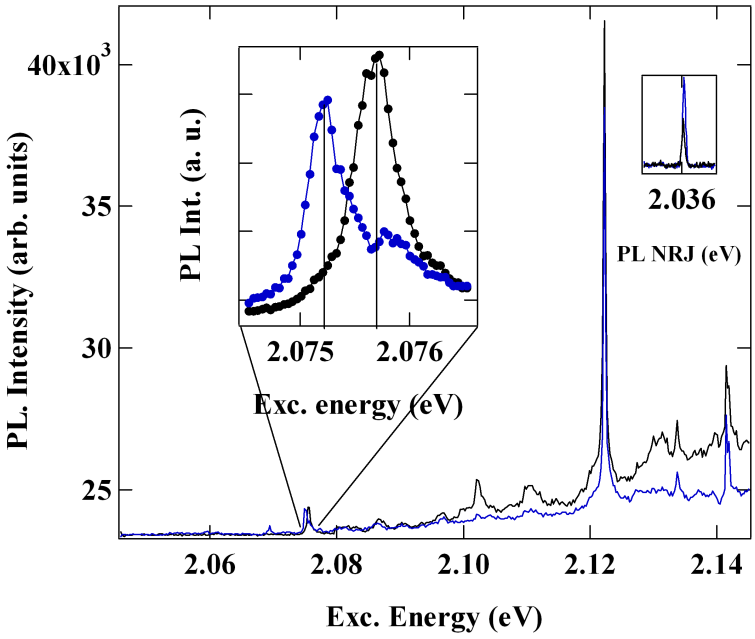

Figure 6.3: PLE spectra resolved in circular polarization under $\sigma+$ CW excitation. In inset is presented a PLE scan around the polarized fine structure, presenting a splitting $\Delta_0 = 490\mu eV$. The quantum dot under study is the same that in Fig. 6.9 (a), 6.10 (b), 6.11, 6.12 and 6.13.

6.1.2 Spin injection

In this paragraph, we consider a $\sigma+$ pulsed excitation, and discuss relaxation processes depending on the energy of the laser excitation. The PL decay measurements, and polarization-rate are qualitatively reproduced by a simple rate equation model. In this approach, relaxation of the electron within the X^- and X^{-*} complex is neglected. In the following, the numerical values should be taken with a large margin error up to 50% for the shortest times which are close to the resolution of the set-up. The PL decay curves obtained with the model are convolved with the response of the set-up and then compared to the experimental ones. The decay measurements are obtained under *ps* pulsed excitation tuned on four different excited states (see Fig. 6.4).

As shown on the PLE, the lowest excited state is fully copolarized, and at a lower energy than the P doublet. Hence, it is attributed to a forbidden transition, where the electron is injected on the S shell while the hole is on a higher shell. This transition is spin-selective: the resident electron must be $|\uparrow\rangle$. The fast initial decay of the polarization rate (Fig. 6.4, $E_{exc.1}$) is attributed to relaxation of the hole spin on the high energy shell ($\tau_{h^*} \approx 70ps$), while the slower decay is attributed to relaxation of the hole spin when it is in the S state equal to $\tau_h \approx 4ns$. This relaxation time is surprisingly short and cannot be attributed to phonon assisted processes. Tunnel coupling with photo-created carriers from the wetting layer is also unlikely at this excitation energy. Tunnel coupling with charged defects is more likely. The other parameters used to model the data are the radiative lifetime ($\tau_b = 240ps$) and hole relaxation to the S state ($\tau_{rlx} = 55ps$).

Injection on the P doublet results in the creation of an excited trion $\Uparrow_P\downarrow_P\uparrow_S$ or $\Uparrow_P\downarrow_P\downarrow_S$ depending on the spin of the resident electron. In Fig. 6.4, $E_{exc.2}$, we observe a positive polar-

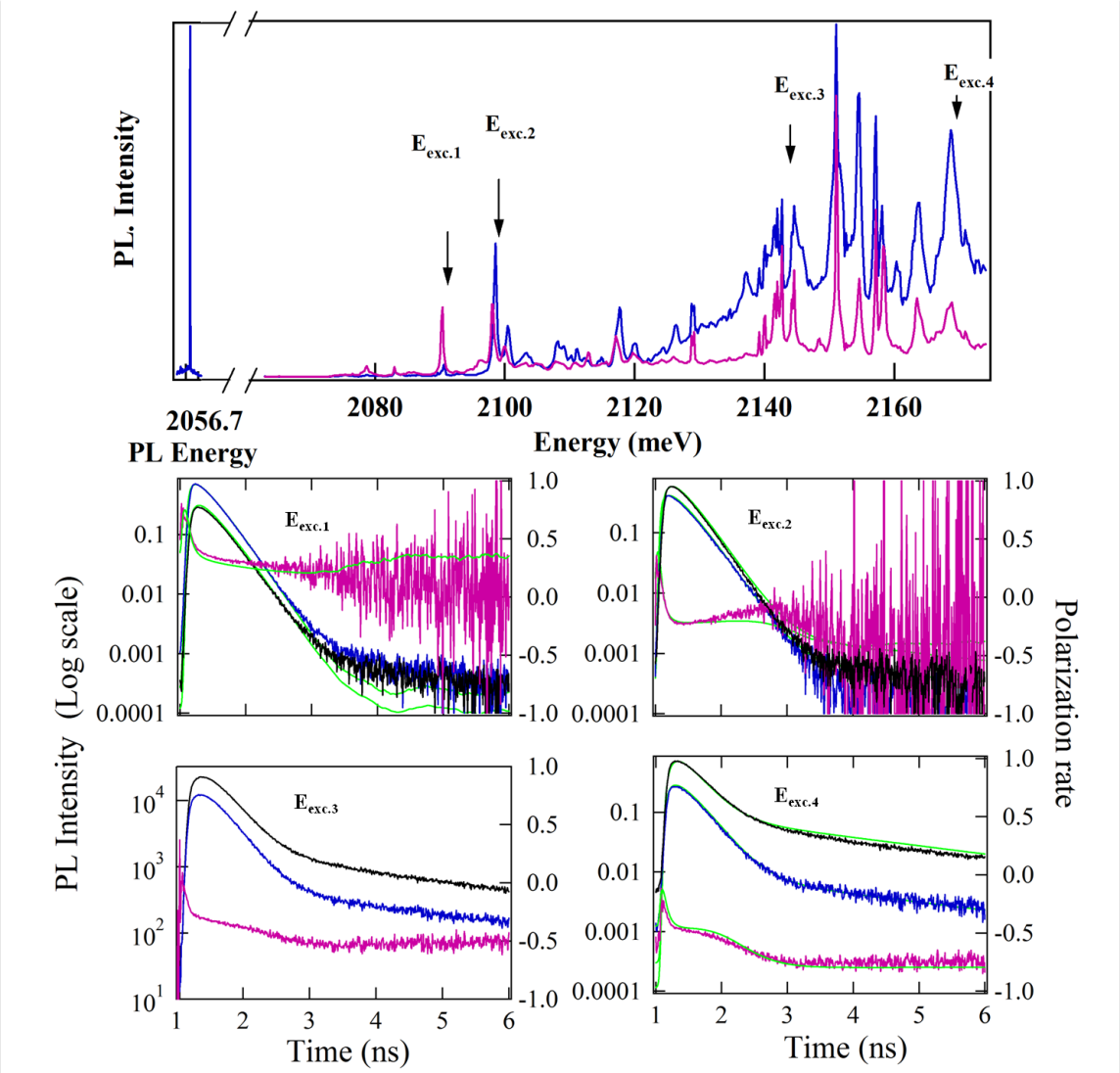

Figure 6.4: PL Decay and Time-Resolved Polarization rate measurement for different energy of excitation. The energies are shown on the PLE spectra. Three out of the four decay experiments are reproduced (green lines) using a rate equation model described in the text.

ization rate at short delays, then a fast decrease: the polarization rate becomes negative in a few tens of ps. After that, the polarization rate slowly increases on a ns time-scale. This evolution reflects the relaxation dynamics of the hot trion. The excited state $T_0 \Uparrow$ can relax quickly to the ground trion state ($\gamma_+ = (25ps)^{-1}$) and gives co-polarized PL while for the other trion state $T_{-1} \Uparrow$, relaxation to the ground state is forbidden until a hole-electron flip-flop occurs through anisotropic exchange interaction. Therefore, relaxation from the hot trion results in a positive polarization rate at short delays and negative at longer delays. For the flip-flop process, we take an effective time $\tau_{ff} \approx 50ps$. Hence we obtain $\gamma_- \approx (\tau_{ff} + \gamma_+)^{-1} = (75ps)^{-1}$, which is significantly shorter than the rate found by M.E. Ware *et al.*. This could result from stronger light/heavy hole mixing in our quantum dots, but we note that Akimov *et al.* [83] have also found ratios of Δ_1/Δ_0 between 0.44 and 0.77 in CdSe/ZnSe quantum dots[40], although they had been selecting quantum dots with small valence band mixing (low linear polarization rate of the X^- PL). To be consistent with the previous modeling and to fit the data we consider the same relaxation time of the hole spin ($\tau_h \approx 4ns$). Also, a difference in the efficiency of the injection has been considered. At the low power limit, this is ruled by the difference of oscillator strength between the two transitions (equal to 0.5) [83]. Due to the high power of the pulsed excitation we would have expected that the difference of oscillator strength could be neglected, but this is not the case and a ratio of 0.7 has been considered. At long delays, the model overestimates the negative circular polarization rate. This could result from the optical recombination of the hot trion ($\Uparrow_P \downarrow_P \downarrow_S$).

To model injection at high energy (Fig. 6.4, $E_{exc.4}$), we consider, following [81], a $0D2D$ cross-transition, where the electron is injected in the dot and the hole, in the wetting layer. Hence, the spin of the hole is completely lost ($\tau_{h_{WL}} \leq 5ps$) before it is captured by the dot with $\tau_{capt} = 30ps$. The parameters relative to the dynamics within the hot trion (P states) and the trion ground state (γ_+, τ_{ff}, τ_h and τ_b) are of course kept constant. Such conditions of excitation are well-known to be an efficient way of performing optical pumping of the resident electron down ($\downarrow$) via relaxation towards the hot trion as we will see in the next-section. Indeed we observe that our data fit with a polarization of the resident electron equal to -40% (i.e. $\langle \sigma_z \rangle = -0.2$). Such polarisation rate is consistent with CW PL experiments. We have not considered relaxation through the excited singlet states. Such relaxation should be faster than relaxation from the triplet states (a few ps). This would lead to an increase of the rise time of the PL. This has not been observed experimentally. This effect is probably within the resolution of the set-up. We find that the high energy injection and the negative circular polarization can be described qualitatevely without having to introduce the capture of dark excitons from the wetting layer (contrary to the scenario proposed in [84]).

At last, polarization of the excitation has been tuned between 90% and 95% so that the curves would adapt nicely to the data.

6.1.3 Optical orientation of the electron

We focus now on two pulses experiments (carried on another quantum dot) shown in Fig. 6.5. The pulses are of equal intensity. Measurements were performed at $B = 0T$, for two circularly polarized pulses of the same helicity (i), of opposite helicity (ii), and (iii) with the same helicity but with a transverse magnetic field $B_x = 0.13T$. The data will be qualitatively reproduced by the rate equation model described above. The response to the second pulse is modeled assuming that the formation of charged bi-exciton is negligible. An electron-hole pair is created only if

[40] The values given in [83] have been multiplied by $\sqrt{2}$. This factor arises from a difference of definition of the exchange constants.

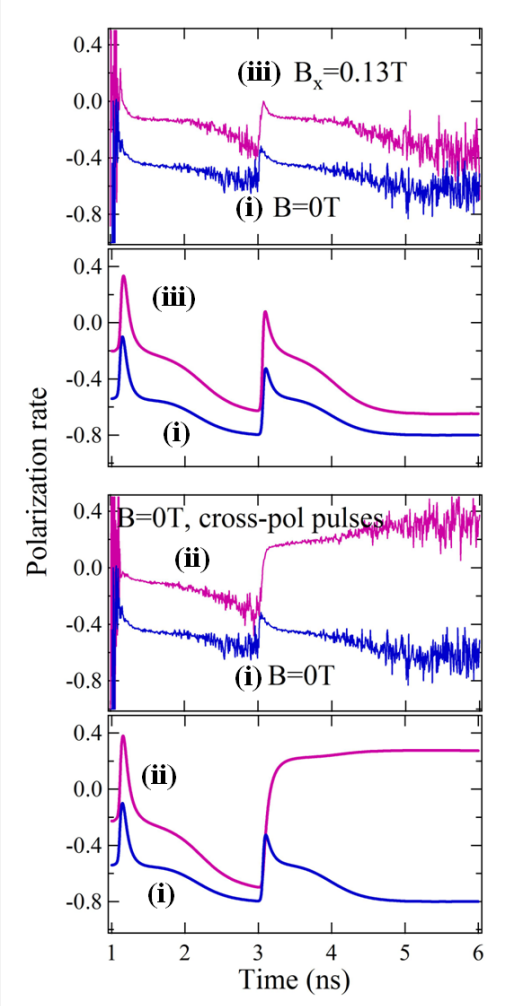

Figure 6.5: Time-Resolved Polarization rate measurement for a 2 pulses sequence. Obtained at $B_x = 0.13mT$ (iii) or at $B = 0T$ but with cross-polarized pulses (ii), in comparison with the polarization rate obtained at $B = 0T$ with two co-polarized pulses (i).

the electron was alone in the dot before the second pulse, the population of the hot trion are unchanged by the second pulse. The observed injection conditions are close to the one observed in Fig. 6.4 for $E_{exc.3}$ where we are not completely in the regime of $0D2D$ transitions, and where the injection could present some spin-selectivity. However, we will model it as if it was a simple $0D2D$ transition. A consequence is that we overestimate the population of dark triplet states and so, the amplitude of the polarization decay (relaxation from dark states contribute to a negative PL at long delays), but it will help to grasp the physics, and in fact enhance experimental features coming from dark states. The parameters used in the rate equation model are $\tau_b = 250ps$, $\tau_{h_{WL}} = 30ps$, $\tau_{capt} = 45ps$, $\tau_{ff} = 60ps$, $\gamma_+ = (25ps)^{-1}$, $\tau_h = 3ns$. Also, to reproduce the data in the case of a transverse magnetic field or with a co or cross-polarized sequence we assume a fast relaxation of the resident electron ($1ps$) when it is alone in the dot. In the case of a transverse magnetic field, it is a rather approximative way of modeling the randomization of the electron spin due to the precession in B_x between the emission of a photon and the photo-excitation by the second pulse. In the case of a co-cross polarized sequence, this is also a rough modeling of the randomization of the spin of the electron due to hyperfine interaction in the absence of nuclear spin polarization[41].

The first obvious observation is that the $0T$ polarization rate (i) is lower than the same curve obtained under transverse magnetic field $B_x = 0.13T$ (iii) or a crossed-polarized 2 pulse sequence(ii). The overall diminution of the circular polarization rate observed in (i) is attributed to the optical pumping of the resident electron resulting from the cumulative effect of the optical pulses. This cumulative effect cannot take place when the pulses are cross-polarized (in average, no angular momentum is transferred to the resident electron), and it cannot occur under transverse magnetic field because of the precession of the resident electron. Since the optical pumping is a cumulative effect observed in pulsed excitation, this means that the polarization of the resident electron is conserved at least over a few ns.

A slight diminution of the polarization measured at the beginning of the second pulse (compared to the one measured at the beginning of the first pulse) is observed in the experiment (i) and (iii). We tend to think that this diminution is real and results from the presence of dark states at the beginning of the second pulse. These dark states contribute to a negative polarization. This affects the polarization rate observed during the second pulse only during the rise-time of the PL (otherwise, the PL created by the second pulse governs the polarization rate). This decrease is observed in the calculation and over-estimated (because the population of dark states is overestimated).

In these conditions of excitation, the negative polarization of the PL gives a value of the polarization of the resident electron just after the recombination. However, we insist on the fact that (i) *the negative polarization rate is also linked to the mean value σ_z of the resident electron*, and we will systematically interpret in the following section that an increase of the polarization rate (for example from -50% to -40%) is a signature of the depolarization of the resident electron spin. Secondly, (ii) *the resident electron can be fully depolarized, even if the observed PL presents a negative circular polarization.* An experimental evidence of this is shown in Fig. 6.6(a) for $B_x = 0.13T$. In this transverse field, no polarization of the resident electron can be performed. However we still observe a negative circular polarization rate. These assumptions may require justifications.

To fix ideas, we present a simplified description of the injection dynamics reasonably consis-

[41] In the following, we will see that on this timescale, we should rather model the hyperfine interaction by the loss of the two thirds of the resident electron polarization. However, there is no point in considering these subtleties in the rate equation model presented here.

tent with the one observed in decay experiments at high excitation energy:

- The spin of the hole is fully randomized during the injection, while the photo-created electron is $\downarrow$, corresponding to σ_+ excitation.
- One electron-hole pair is injected (charged biexciton is neglected)
- Relaxation of the electrons spin is neglected, relaxation of the hole after thermalization is considered only for the dark state $\downarrow_p\downarrow_s\Downarrow$ and is neglected for the other trions because of their shorter lifetime.

Then the overall polarization rate is fixed by the following process:

1. $\uparrow_s\downarrow_p\Uparrow \longmapsto \uparrow_s\downarrow_s\Uparrow \longmapsto \sigma+ + \uparrow_s$
2. $\uparrow_s\downarrow_p\Downarrow \longmapsto \uparrow_s\downarrow_s\Downarrow \longmapsto \sigma- + \downarrow_s$
3. $\downarrow_s\downarrow_p\Uparrow \overset{\Delta_2}{\longmapsto} \downarrow_s\uparrow_s\Downarrow \longmapsto \sigma- + \downarrow_s$
4. $\downarrow_s\downarrow_p\Downarrow \overset{\tau_h}{\longmapsto} \downarrow_s\downarrow_p\Uparrow \overset{\Delta_2}{\longmapsto} \uparrow_s\downarrow_s\Downarrow \longmapsto \sigma- + \downarrow_s$

Hence, the realization of (1) and (2) is proportional to the probability for the resident electron to be $\uparrow$, while (3) and (4) depend on the probability of having the resident electron $\downarrow$. We assume that due to a process (to be discussed), the resident electron polarization between two pulses relaxes to a mean-value:

$$\langle\sigma_z\rangle = \frac{1}{2}(\rho_\uparrow - \rho_\downarrow) \tag{6.4}$$

Where $\rho_\uparrow$ and $\rho_\downarrow$ are the population of spin $\uparrow$ and $\downarrow$ before the optical injection. The polarization rate (PR) of the time-averaged PL is given by:

$$PR = -0.5 + \langle\sigma_z\rangle \tag{6.5}$$

Hence, in this simplistic approach, a polarization rate of -0.5 is expected if the electron spin relaxes completely between two absorption-emission process. If relaxation of the resident electron is negligible, a polarization rate of -1 is expected as a result of the cumulative effect of optical excitation. In practice, such low polarization rates are of course not observed. We invoke among others, effects such as: (1) Relaxation of the hole during the life-time of the cold trion and the bright hot trions, which is not completely negligible; this limits the efficiency of the optical pumping of the resident electron and increases the circular polarization rate. (2) Incomplete relaxation of the hole spin during the injection which tends to increase the circular polarization rate for $\langle\sigma_z\rangle \neq -1/2$ (3) Light-hole/Heavy-hole mixing, which affects the optical selection rules. However the equation 6.5 highlights the fact that the observation of NCP does not necessarily mean that the resident electron is polarized[42] and that a variation of the polarization of the resident electron causes a change of the circular polarization rate.

[42] NCP only means that the injection can lead to a polarization of the resident electron, but coherent processes (e.g. precession in a transverse magnetic field) or incoherent processes (e.g. spin relaxation induced by charge tunneling) can destroy the pumping process.

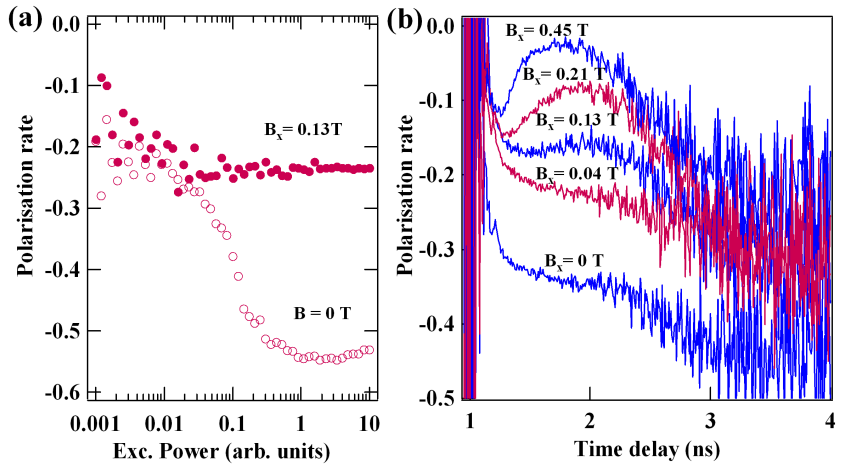

Figure 6.6: (a) Evolution of the degree of circular polarization as a function of CW excitation power. Empty circles are zero field measurements, filled circles are measurements in a transverse magnetic field $B_x = 0.13T$. (b) Time-evolution of the degree of circular polarization under pulsed-excitation for different transverse magnetic field (excitation in the Negative Circular Polarization regime).

The optical pumping of the resident electron is confirmed by the power dependence of the negative circular polarization rate obtained under continuous-wave excitation shown in Fig. 6.6 (a). As the pump power is increased, we observe a rapid decrease of the circular polarization rate, with a saturation at about -55%. The reason for this evolution is the progressive orientation of the resident electron. The remaining rate at low excitation power is controlled by the randomized injection of the hole, and the relaxation within the hot trion states, as discussed earlier. The polarization rate observed under transverse magnetic field does not depend on power, as the precession of the electron forbids the pumping process (Fig. 6.6).

We also expect the precession of the hole to play a role for sufficiently high magnetic fields. The precession of the hole during the life-time of the trion can be observed with increasing transverse magnetic field, due to the weak in-plane g factor of the hole (Fig. 6.6 (b)). At high field, this precession fully depolarizes the hole spin, affects the conditions of injection, and destroys the negative circular polarization of the PL. In Fig. 6.6 (b), we observe that the shape of the time-resolved polarization rate changes between $0.04T$ and $0.13T$. This demonstrates that the precession of the hole already contributes to a change of the PL polarization rate between $0.04T$ and $0.13T$.

6.2 Nuclear Effects in II-VI Quantum Dots

Nuclear effects have been extensively studied in III-V Quantum Dots over the past years, but few has been done in II-VI materials. It is well established that nuclear spin effects are much stronger in the former, as all the nuclei in these materials carry a spin. In III-V quantum dots, the effective field created by the polarized nuclei can be directly measured through the Zeeman splitting of the PL (Overhauser shift). This is not possible in II-VI quantum dots, where the maximum Overhauser shift is expected to be around $6\mu eV$, hidden in the linewidth of the PL transitions, but depolarization of the resident electron by unpolarized nuclei can be monitored

through the measurement of the PL polarization rate of X^-. In II-VI Quantum Dots, where the number of nuclei is typically fifty-times lower[43], fluctuations of the nuclei are also large and rule the relaxation of the resident electron spin. In this context, the control of the nuclear spin ensemble and the study of the coupled electron-nuclear spin dynamics in II-VI quantum dots deserve attention. Alternatively, nuclear spins could be suppressed completely using quantum dots based on isotopically purified II-VI materials since Zn, Cd, Mg, Se and Te all have dominant isotopes without nuclear spins.

6.2.1 Hyperfine Coupling in II-VI Quantum Dots

The nuclear spins in a semi-conductor can be controllably polarized using circularly polarized photo-excitation. This phenomenon results from the hyperfine interaction of electron and nuclear spins, enabling the transfer of angular momentum from the optically oriented electron to the nuclei. Continuous pumping of the electron can generate a dynamic nuclear spin polarization of the nuclei. The dynamically polarized nuclei produce in turn an effective magnetic field that influences the polarization of the electron in a feedback process. The electron-nuclear system is a strongly-coupled system, with a rich dynamics. We will see that this dynamics can be separated on two time-scales: a fast evolution of the electron and a slower evolution of the nuclei. The fast evolution of the electron can be grasped considering the combined action of the external magnetic field and the effective field created by the nuclei on the electron (Overhauser field B_N) and its fluctuations (B_f, which scales as $B_N^{max}/\sqrt{N}$ for an unpolarized nuclear ensemble, where N is the total number of nuclei in the quantum dot). The slow evolution of the nuclei is governed by the effective field created by the mean value of the electron spin (called Knight field, B_e), its fluctuations and the nearest neighbor interactions which result in an effective field B_{dip} due to magnetic dipole coupling between the nuclei.

The dominant contribution to the coupling between the electron and the nuclear spins originates from a Fermi contact hyperfine interaction. This term results from the direct interaction of the nuclear dipole with the electronic spin dipole and is proportional to the electron density at the position of the nucleus. Holes, which have a p-type Bloch function are not coupled to nuclei by the Fermi contact interaction. In III-V semiconductors, their coupling with the nuclei is typically ten times smaller than the electron coupling[85, 86]. Hole-nuclei hyperfine coupling will be neglected. The hyperfine interaction between the nuclei and the electron can be written as:

$$H_{hf} = v_0 \sum_i A_i \left|F_e(R_i)\right|^2 \vec{\sigma}.\vec{I_i} \tag{6.6}$$

where R_i is the position of the nucleus i, with a spin operator $\vec{I_i}$; $\vec{\sigma}$ is the electron spin operator, $F_e(r)$ is the envelope function of the electron, v_0 is the volume of a unit cell (containing N=2 atoms) and A_i is the hyperfine interaction constant given by:

$$A_i = \frac{4}{3I_i} \frac{\mu_0 \mu_B \mu_{I_i}}{v_0} \left|u_i(0)\right|^2 \tag{6.7}$$

where μ_B is the Bohr magneton, μ_{I_i} is the magneton of the nucleus i and $u_i(0)$ is the periodic Bloch function amplitude at the site of the nucleus. The derivation of this Hamiltonian can be found in [87].

[43] The small number of nuclei in II-VI QDs results from the small quantum dot volume

The hyperfine interaction constants in II-VI are not known precisely, contrary to III-V materials. The value of the nucleus magneton is known for Zn, Cd and Te [88] (c.f. Table 6.2.1), but the amplitude of the Bloch function $|u_i(0)|^2/v_0$ at the nuclear site is only known for Cd and is equal to $5.3\times10^{31}m^{-3}$ [89]. From this, we can deduce, averaging over the cadmium isotopes carrying a spin, that $A_{Cd}=-31\mu eV$. For A_{Te}, C. Testelin *et al.* have obtained a value of $-45\mu eV$ [90], assuming that the amplitude of the Bloch function was identical on Cd and Te. However, the *s*-state is anti-bonding and II-VI crystals presents an important ionicity. Consequently, we would expect that the Bloch amplitude is higher on the cation (i.e. Te) than on the anion. In III-V, the ratio $|u_{cation}|^2/|u_{anion}|^2$ is around 1.7 [91, 92]. This ratio is expected to be higher in II-VI. We take a ratio of 1.7 and find $A_{Te}\approx-80\mu eV$, which is somewhat arbitrary. Finally, we find $A_{Zn}=8.9\mu eV$ assuming $|u_{Cd}|^2/|u_{Zn}|^2=1$. The effect of Zn nuclei will be taken into account, as the fraction of Zn is expected to be $(1-x)\approx25\%$ at the center of the dot.

	Abundance (%)	I	μ_I
^{111}Cd	12.75	1/2	−0.5943
^{113}Cd	12.26	1/2	−0.6217
^{67}Zn	4.11	5/2	+0.8754
^{123}Te	0.87	1/2	−0.7357
^{125}Te	6.99	1/2	−0.8871

Table 6.1: Isotopic abundance, nuclear spin I and magneton of the nucleus μ_I for Cd, Zn and Te alloys. μ_I is given in unit of the nuclear magneton μ_N.

We are now going to discuss the dynamics of the electron-nuclei system in terms of effective field and for different timescales. Nuclear spin-dynamics tend to be much slower than electron-spin dynamics, so that the electron dynamics can be described in a frozen nuclear spin-configuration. Then, the average of all the possible nuclear spin-configuration (fluctuations around a mean value) gives the average electron-spin orientation observed experimentally (as the electron polarization, measured on a CCD camera or an APD, is an average over timescales long compared to the nuclear fluctuation time). On a longer time-scale, evolution of the mean-polarization of the nuclei will be considered. This time-scale difference relies on the fact that only one flip-flop is necessary to change the electron polarization while N flip-flops are necessary to change the polarization of the nuclear ensemble.

The Overhauser field which is the effective field created by the nuclei on the electron is defined by:

$$H_{hf}=g_e\mu_B\vec{\sigma}.\vec{B}_N \tag{6.8}$$

which gives:

$$\vec{B}_N=\frac{v_0\sum_i A_i\left|F_e(R_i)\right|^2\left\langle\vec{I}_i\right\rangle}{g_e\mu_B} \tag{6.9}$$

We can estimate roughly the maximum Overhauser field (complete polarization of the nuclei), assuming a homogeneous envelope-function for the electron normalized on a volume $V = v_0 N/2$:

$$B_N^{max} = \frac{1}{g_e \mu_B} \left(x I_{Cd} A_{Cd} p_{Cd} + (1-x) I_{Zn} A_{Zn} p_{Zn} + I_{Te} A_{Te} p_{Te} \right) \tag{6.10}$$

With $x = 0.75$, p_i the isotopic abundance of the nuclei i, I_i the spin and A_i the hyperfine coupling constant calculated earlier. Note that the maximum Overhauser field is independent on the quantum dots volume, and depends only on intrinsic parameters of the material. We take for the Lande factor in CdTe/ZnTe quantum dots $g_e = -0.5$, as measured in [27]. We estimate $B_N^{max} \approx 200mT$. This is typically forty times smaller than the maximum Overhauser field in III-V compounds. As mentioned earlier, another important parameter is the amplitude of the fluctuations of the Overhauser field for a randomly oriented nuclear ensemble, because this rules the decoherence of the electron. This results in an effective field B_f, oriented in a random direction, around which the electron precesses. On average (over the nuclear spin configurations), an electron polarized along the z axis looses 2/3 of its polarization[44] . This was predicted in [93] and observed in [94]. This decay is not a real relaxation process in the sense that the electron coherently evolves in a frozen nuclear spin configuration, but on an average measurement, we observe a fast decay of the electron polarization on a characteristic timescale $T \approx \hbar/(g_e \mu_B B_f)$ [93] which is the precession period of the electron in this nuclear field. The decay of the last third is due to true relaxation on the time-scale of a change of B_f which is longer as we will discuss shortly after. First we give an estimate of B_f at $B_N = 0$. Assuming a homogeneous envelope-function for the electron normalized on a volume $V = v_0 N/2$, it is given by [33, 95]:

$$B_f^2 = \frac{2}{(g_e \mu_B \sqrt{N})^2} (x I_{Cd}(I_{Cd}+1) A_{Cd}^2 p_{Cd} + (1-x) I_{Zn}(I_{Zn}+1) A_{Zn}^2 p_{Zn} + I_{Te}(I_{Te}+1) A_{Te}^2 p_{Te})$$

where N is the number of nuclei in the dot, regardless of their spin. We estimate this number to be roughly equal to 8000 for a quantum dot volume of $250nm^3$. This leads to $B_f \approx 12mT$. It is the same order of magnitude than the fluctuations in III-V quantum dots [96]. Consequently, electron spin relaxation by nuclei is also expected to be efficient in II-VI materials at $B_{ext} = 0T$. On a time-scale $T_e \approx 2ns$, the electron looses 2/3 of its polarization.

At $B_{ext} = 0T$, the nuclei's dynamics are ruled by the effect of the Knight field B_e (effective field created by the electron on a given nucleus) given by:

$$H_{hf} = -\sum_i \mu_i \vec{I}_i . \vec{B}_{e,i} \tag{6.11}$$

with

$$\vec{B}_{e,i} = -\frac{v_0}{\mu_I} A_i \left| F_e(R_i) \right|^2 \langle \sigma_z \rangle \vec{u}_z \tag{6.12}$$

Again, assuming a homogeneous normalized electron wave-funtion, we find:

[44] If a spin, initially $\vec{S_0}$ along z precesses around a magnetic field $\vec{B}$, the average z component overtime is $S_z(B) = (\vec{S_0}.\vec{B})(\vec{B}.\vec{u_z})/B^2 = S_0 \cos^2(\theta_B)$, where θ_B is the angle between $\vec{B}$ and the z axis. Averaging over θ_B, we find that $\langle S_z \rangle_B = S_0/3$.

$$\vec{B}_{e,i} = -\frac{2A_i}{\mu_{I_i} N} \langle \sigma_z \rangle \vec{u}_z \tag{6.13}$$

We derive an estimation of the maximum Knight field of $150mT$ for a Cd atom. This is much higher than in III-V materials, where the maximum Knight field is expected to be around a few mT [96]. This is a consequence of the difference of quantum dot size between II-VI and III-V materials. The characteristic time-scale on which a nuclei precesses in the Knight field is $T_N \approx \hbar/(\mu_{I_i} B_e)$ which is equal to $0.2\mu s$. For an unpolarized nuclei ensemble, the electron's dynamics is not extremely faster than the nuclei's. In fact we could have guessed this time-scale from the start: as the interaction of the electron with the fluctuating field scales as $H_{hf}^{max}/\sqrt{N}$ while the interaction with a single nucleus scales as H_{hf}/N, we find $T_N \approx T_e\sqrt{(N)}$. In our system, the picture of an electron evolving in a frozen nuclear spin configuration is a rougher approximation, compared to the case of III-V, where the large number of nuclei really allows to decouple the two dynamics. However, we will still use this approximation to describe qualitatively the dynamics. As the electron precesses rapidly around B_f, the nuclei only see a time-averaged Knight field, which is directed along B_f. On a time-scale T_N, the nuclei start to precess around this Knight field. The inhomogeneity of the Knight field due to the different species of nuclei and the non-uniform wavefunction F_e induces a different precession frequency for each nucleus causing a slow change of B_f. This change of direction of the fluctuating field causes the relaxation of the last third of the electron polarization.

Under optical pumping of the electron say with $\sigma+$ light, the resident electron is pumped down ($\langle \sigma_z \rangle < 0$). Spin momentum is transferred to the nuclei which acquire a polarization $\langle I_z \rangle < 0$. The dominant contribution comes from Cd and Te, presenting a hyperfine constant $A_i < 0$. With $g_e < 0$, this leads to an Overhauser field $\vec{B}_N.\vec{u}_z < 0$ while for the Knight field, we have $\vec{B}_e.\vec{u}_z > 0$. All the signs of the effective fields are reversed for Zn nuclei. The direction of these effective field is of prior importance in the experiments to come.

The last time-scale to discuss is the magnetic-dipole coupling between nuclei. This is a short-range interaction which scales as $1/r_{ij}^3$. In III-V materials, this interaction results in an effective field of $0.20mT$ with a precession period $T \approx 10^{-4}s$. This interaction is not spin-conserving and causes relaxation of the nuclei on this timescale unless a magnetic field or strain gradients affect it. In our system, the effects of this interaction is expected to be even smaller because of the low isotopic abundance of nuclei carrying a spin. Another cause of nuclear polarization relaxation is an electron-mediated nuclear spin-spin interaction which depolarizes the nuclei. This will be discussed later.

6.2.2 Evidence of strong Nuclear Spin Fluctuations

As explained earlier, the polarization rate of the PL reflects the spin polarization of the resident electron. In Fig. 6.7 (a), we show an experiment where the polarization of the electron has been measured as a function of the frequency of a $\sigma+/\sigma-$ modulation of the excitation. This experiment, carried out at low power of excitation, demonstrates the existence of a slow process ($100\mu s > T > 10\mu s$) that allows the pumping of the resident electron and hence, the decrease of the polarization rate at low modulation frequencies. This modulation frequency dependence is canceled by a magnetic field $B_z = 0.16T$, which allows a strong pumping of the resident electron, independently of the modulation frequency in the range of the scan ($0.05 - 200kHz$).

In Fig 6.7 (b), (c), we investigate the dynamics of this pumping as a function of power, and magnetic field. We find at $B = 0.19T$ a transient on a time-scale of $\approx 20ns$ to $\approx 200ns$ depending

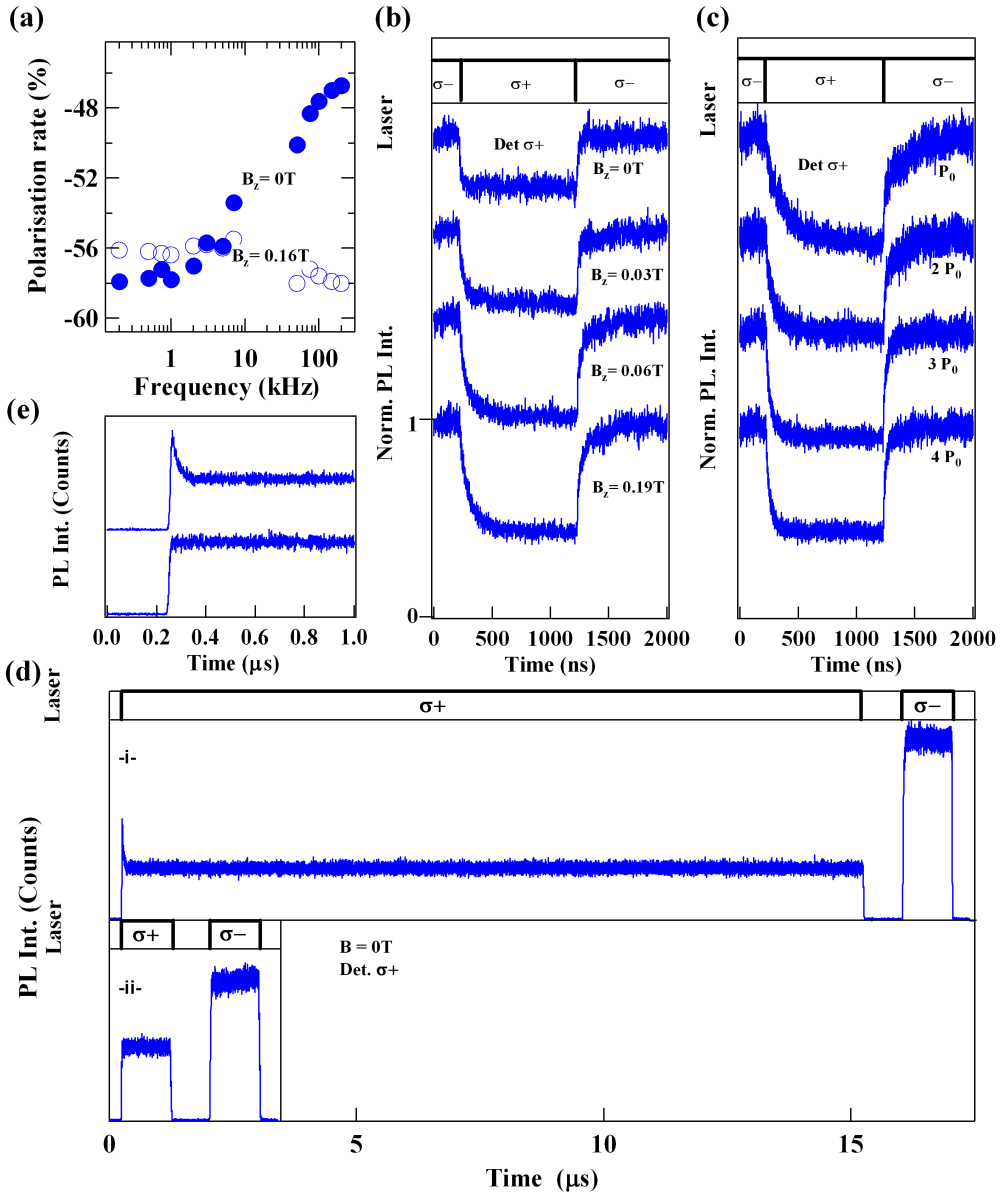

Figure 6.7: (a) Evolution of the degree of circular polarization with the frequency of the $\sigma+/\sigma-$ modulation of the excitation laser at $B_z = 0T$ and $B_z = 0.16T$ applied along the growth axis. Time-evolution of the $\sigma+$ PL excited alternatively with $\sigma+$ or $\sigma-$ light for different magnetic fields applied in the Faraday geometry (b) and for different excitations intensities at a fixed magnetic field $B_z = 0.19T$ (c). For (b) and (c), each curve is normalized to one at its highest mean-level. The curves have been shifted for a sake of clarity. The scale corresponding to one unit is given, it is the same for the two graphs. (d) Time-evolution of the $\sigma+$ PL excited alternatively with $\sigma+$ and $\sigma-$ light trains. The excitation sequence are displayed above each curve. (e) Zoom on the fast transient observed at the beginning of (d).

on power. The detection is $\sigma+$, proportional to a polarization $\langle\sigma_z\rangle$ of the resident electron. We observe a decrease of the $\sigma+$ PL (hence a decrease of the polarization of the resident electron) under $\sigma+$ excitation, and an increase under $\sigma-$ illumination. As predicted from the injection studies, the cumulative effect of $\sigma+$ (resp $\sigma-$) photon absorption tends to pump the electron $\downarrow$ (resp. $\uparrow$). The study of the pumping transient at a fixed power and for increasing magnetic field (Fig. 6.7(b)) shows a significant increase of the polarization rate with magnetic field. This demonstrates that under fast modulation, the optical pumping of the resident electron is inefficient at $B = 0T$ while the first $60mT$ of Faraday magnetic field progressively restore a strong polarization of the resident electron. This is consistent with the high frequency measurements of Fig 6.7(a). We attribute this magnetic field dependence to the existence of nuclear spin fluctuations B_f, which, in average, efficiently destroy 2/3 of the resident electron polarization between two successive photo-injection, greatly limiting the optical pumping process.

To further-confirm this hypothesis, we carry out the following experiment (Fig 6.7(d), (e)): the $\sigma+$ PL is time-resolved using two different excitation sequences. In the sequence (ii), the pulses are of equal length and power, and short enough to prevent the creation of Dynamic Nuclear Spin Polarization (DNSP). In the sequence (i), the difference of pulses length allows in average the creation of DNSP. The measurements show two striking differences. Firstly, the average circular polarization, given by the difference of the PL intensity obtained under $\sigma+$ and $\sigma-$ excitation, is higher in (i) than in (ii). Secondly, the PL of (i) exhibits PL transients reflecting an optical pumping of the resident electron. The transient observed at the beginning of the $\sigma+$ pulse is detailed in Fig. 6.7(e). These two features demonstrate directly that the Overhauser field created in (i) is strong enough to block the precession caused by the fluctuating nuclear field.

We have shown that the naive picture of smaller nuclear effects in II-VI semiconductors is subject to caution. The nuclear spin fluctuations can cause efficient electron decoherence when the nuclei are unpolarized. At first sight, these effects can be canceled by applying a Faraday field of a few tens of mT.

6.2.3 Dynamic Nuclear Spin Polarization

Direct evidence of the build-up of a DNSP can be observed using pulses of long duration (tens or hundreds of μs). As displayed in Fig. 6.8 (a), the $\sigma+$ PL recorded under $\sigma+$ excitation presents first a fast transient with a drop of the intensity due to the orientation of the resident electron spin discussed previously (a zoom on this transient is presented in Fig. 6.8 (b)). Then a slower transient is observed: the $\sigma+$ PL increases and decreases again on a few μs. This reflects a depolarization of the resident electron (increase of the circular polarization rate). This evolution has been modeled by M. Petrov *et al* [97][45]. It results from a destruction of the Overhauser field obtained at the end of the $\sigma-$ excitation pulse and the progressive build-up of an Overhauser field in the opposite direction controlled by the $\sigma+$ helicity of the excitation. During this process, the amplitude of the Overhauser fields cancels and the nuclear spin fluctuations B_f affect the resident electron. The evolution during the $\sigma-$ excitation pulse is interpreted the same way. Under $\sigma-$ excitation, the resident electron is pumped $\uparrow$. The minimum of $\sigma+$ PL observed a few μs after the beginning of the pulse corresponds to a diminution of $(\rho_\uparrow - \rho_\downarrow)$, resulting from the depolarization of the electron by the nuclear spin fluctuations.

As presented in Fig. 6.8 (d), the speed of the destruction and build-up of the DNSP can significantly increases with excitation power. This effect can be evidenced by the modulation

[45] Except the modeling was in pulsed excitation leading to subtle effects that will not be discussed here

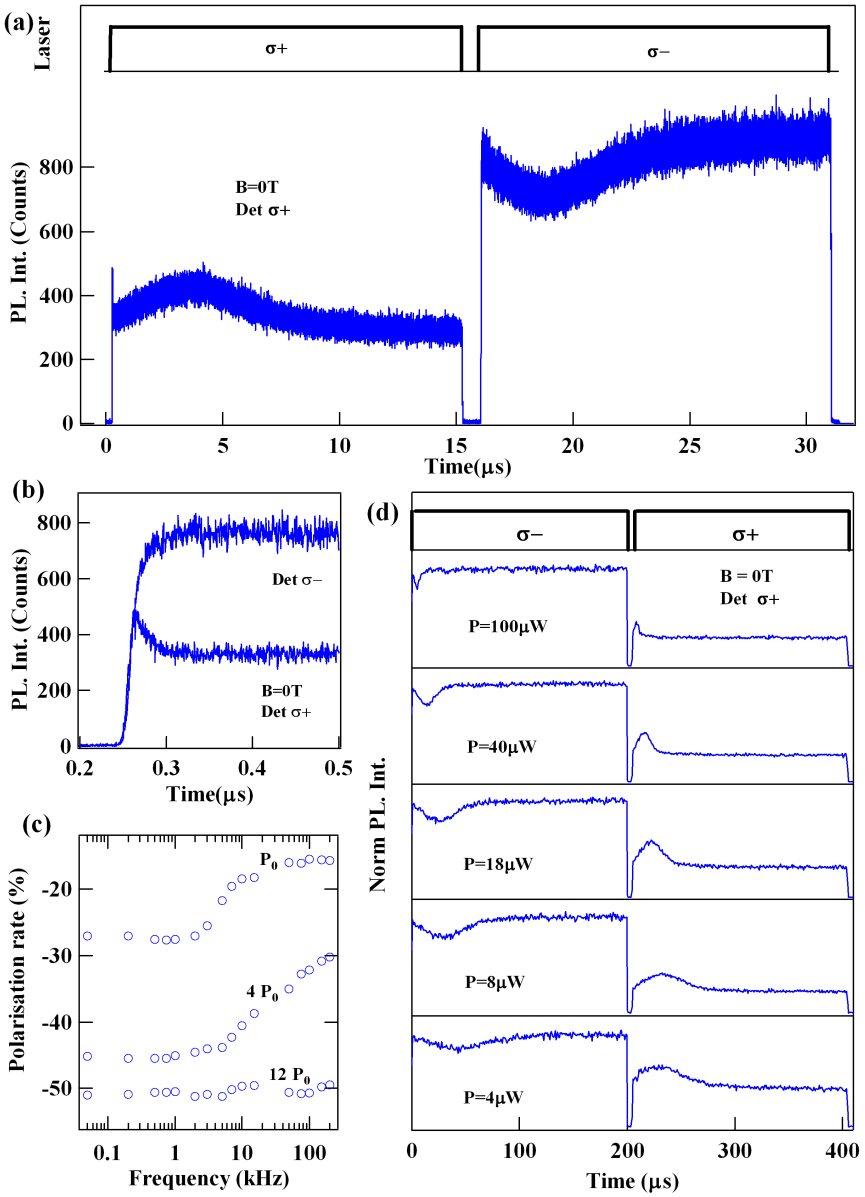

Figure 6.8: (a) Time-evolution of the $\sigma+$ PL excited alternatively with $\sigma+/\sigma-$ light. The excitation sequence is displayed above. (b) Zoom on the transient corresponding to the optical pumping of the electron. The time-evolution of the $\sigma-$ PL recorded in the same conditions of excitation is also displayed, the opposite transient is observed. (c) Circular polarization degree dependence with the $\sigma+/\sigma-$ modulation frequency of the excitation for different excitation power. (d) Time-evolution of the $\sigma+$ PL for different excitation power. The excitation sequence is displayed above.

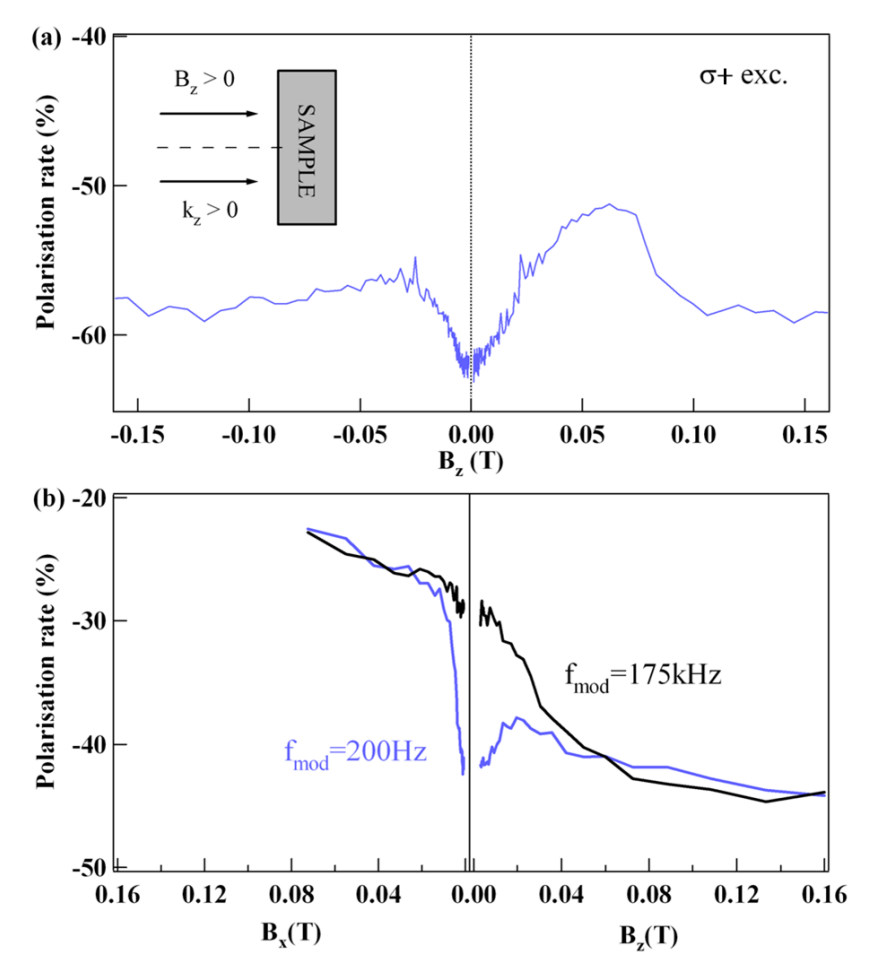

Figure 6.9: (a) Magnetic field dependence in Faraday configuration of the negative polarization rate under circularly polarized CW excitation. (b) Magnetic field dependence of the negative polarization rate in Voight (left panel) and Faraday (right panel) geometry under $\sigma+/\sigma-$ modulated excitation at low ($f_{mod} = 200Hz$) and high ($f_{mod} = 175kHz$) modulation frequency.

frequency dependence of the polarization rate displayed in Fig. 6.8 (c): the modulation frequency required to suppress the DNSP (i.e. to observe a significant increase of the polarization rate) increases with power. At low excitation intensity, a formation time of the nuclear spin polarization of $\tau_F \approx 50\mu s$ can be estimated from the modulation frequency dependence of the circular polarization. This is three orders of magnitude faster than in InAs/GaAs quantum dots where a pumping time of the nuclei at $B = 0T$ around $10ms$ has been reported [98]. At high excitation power, the polarization rate does not depend on the modulation. This is attributed to the rapidity of the pumping process which can be faster than the modulation period ($5\mu s$). This will be further confirmed and discussed during a systematic power dependence study.

6.2.4 Magnetic Field Dependence of the Negative Circular Polarisation

In order to gain knowledge about the nuclear polarization and its dependence on an external field along the spin quantization axis, we performed polarization rate measurements in the optical

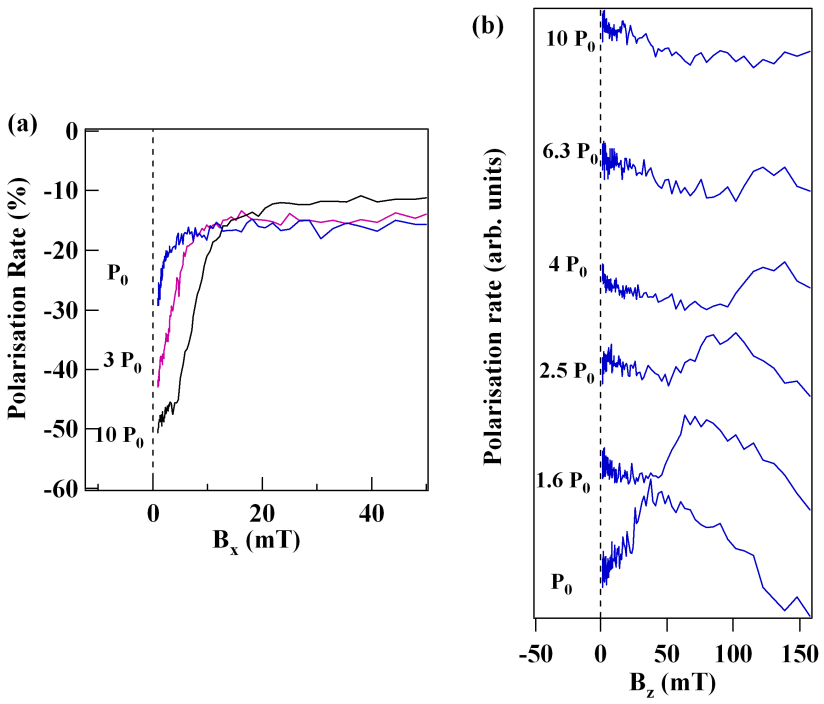

Figure 6.10: Excitation power-dependence of the negative polarization rate under magnetic field. (a) Voight configuration. (b) Faraday configuration. The excitation is CW and $\sigma+$ polarized.

pumping regime with a Faraday magnetic field under circularly polarized CW excitation and probe small variations of the polarization rate. A typical magnetic field dependence is presented Fig. 6.9 (a). The experiment are performed at low power of excitation. The asymmetry of the magnetic field dependence is a fingerprint of the presence of a nuclear spin polarization induced by the helicity of the excitation beam.

Another striking feature is the decrease of a few % of the polarization around $B = 0T$. This is in opposition to what has been observed in III-V semiconductor quantum dots, where an increase of the polarization (i.e. diminution of the resident electron spin polarization) occurs at weak magnetic field because of the dominant contribution of nuclear spin fluctuations at $B = 0T$. In the present case, these nuclear spin fluctuations are strongly suppressed by the Overhauser field resulting from the DNSP. The experiment was carried out under continuous-wave $\sigma+$ excitation, pumping the resident electron down. This leads to an average polarization of nucleus with $\langle I_z \rangle < 0$ and an Overhauser field $B_N.u_z \leq 0$.

For $B_z \geq 0$, we observe a significant increase of the circular polarization rate demonstrating an efficient depolarization of the resident electron. This behavior is attributed to compensation of the Overhauser field by the external Faraday field ($B_{ext} = -B_N$). As the electron precesses around the total field $B_{tot} = B_{ext} + B_N + B_f$, the electron dynamics are then governed by the nuclear spin fluctuations B_f, resulting in a 5% depolarisation.

Considering the left panel of Fig. 6.9 (a) (corresponding to $B_z \leq 0$), we observe at $B = 0$ a minimum in the polarization rate, then an increase of 5% and then a small decrease again. This extrema also reflects an increase of the depolarisation of the electron. This depolarisation is attributed to a compensation of the Knight field by the external magnetic field. The nuclear field is then close to zero and the electron dynamics is ruled by the sum of $B_z \approx 30mT$ and the nuclear spin fluctuations B_f. It may look rather suprising at this point that we invoke the effect of B_f since the estimation given earlier was a fluctuating Overhauser field of $12mT$. However the effect of B_f is not negligible at $30mT$ as observed in the experiment of Fig. 6.7(b), where the polarization of the PL significantly decreases as the Faraday magnetic field is increased from 0 to $60mT$.

This is further-confirmed by the following experiment: We present on the right panel of Fig. 6.9 (b) a measurement, were we have studied the polarization rate as a function of the magnetic field B_z under modulated excitation (on a different QD, hence the average polarization rate is different). The light is modulated $\sigma+/\sigma-$ at two different rates: (i) $175kHz$ ($\approx 3\mu s$ of $\sigma+$ exc., then $\approx 3\mu s$ of $\sigma-$ exc. of equal intensity) and (ii) $200Hz$ ($\approx 2500\mu s$ for a given polarization). Hence, DNSP is achieved in (ii) and not in (i) (since we are at low power of excitation). The detection is done on an APD synchronized with the modulation, and for a fixed circular polarization. We measure a 'polarization rate' by varying the excitation and not the detection. Hence, this 'polarization rate' is a sort of average of the polarization rates measured in Fig. 6.9 (a) for B_z and $-B_z$. The magnetic field dependence for (ii) is consistent with the one observed in the CW regime, with an evolution ruled by the competition between the B_z, B_N, B_e and B_f. On the other hand the magnetic field dependence (i) is only controlled by the competition between B_z and B_f. For sufficiently large external fields, the nuclear spin fluctuations B_f almost do not contribute to the total field and the electron-spin polarization does not decay. The width at half maximum is $30 \pm 5mT$. This gives an estimation of the magnitude of the nuclear spin fluctuations.

A transverse magnetic field dependence of the polarization rate is also displayed (left panel of 6.9 (b)). As the transverse magnetic field is increased, we observe in the absence of DNSP (black curve, corresponding to fast $\sigma+/\sigma-$ modulation), a progressive increase of the polarization rate over the first $80mT$. We expect two processes to contribute to the Hanle depolarization: (i) a

depolarization of the resident electron (standard Hanle depolarization controlled by the T_2 of the electron in an unpolarized nuclear spin bath. This T_2 should give rise to a half width of the hanle curve $B_{1/2} = B_f \approx 30mT$, from the Faraday measurement in Fig. 6.9 (b)) and (ii) precession of the hole during the trion life-time (expected to play a role above $40mT$ when discussing Fig. 6.6 (b)). Thus, the two processes (i) and (ii) cannot be dissociated and there is little to say about the few % of change in the circular polarization rate. More interesting is the comparison with the blue curve (slow modulation where DNSP is created). For the latter, a fast increase of the polarization rate is observed in a transverse field between 0 and $10mT$ (left panel of 6.9 (b)). The half width at half maximum is $\approx 5mT$. The fast depolarization of the resident electron is due to the precession of the elctron-nuclei system. To summarize, the magnetic field dependence in Faraday or Voigt geometry clearly depend on the creation or the absence of DNSP. The main features are:

- a depolarization of the electron-nuclei system by a transverse magnetic field of a few mT.
- a maximum of depolarization of the resident electron when $B_z \approx B_N$

We are now going to detail the power dependence of these two features.

The magnetic field dependence for $B_z > 0$ has been performed for different excitation power (Fig. 6.10 (b)). With increasing power, the dip in the negative circular polarization is shifted to higher magnetic field, evidencing an increase of the polarization of the nuclei. A significant portion of the nuclei are polarized: the dip reaches $100mT$ which could correspond to 50% of the maximum Overhauser field. However, as already discussed, the parameters of II-VI materials are not known with precision. This percentage is subject to caution.

In transverse magnetic field (Fig. 6.10 (a)), we observe that the width of the depolarization curve strongly depends on the excitation power and deviates from a Lorentzian shape at high excitation power. For the latter case, the polarization rate seems to be unaffected by the the first few mT of transverse magnetic field, and then increases. To understand this, we have to consider the electron-nuclei coupled system. This behavior could arise as the electron is pumped faster than the precession in the few mT applied ($\tau^e_{press} = 4ns$ at $B_x = 5mT$). The creation of DNSP could also be faster than the nuclei precession ($\tau^N_{press} = 5\mu s$ at $B_x = 5mT$). Then, the precession of the electron would be efficiently blocked by the Overhauser field, and the electron polarization would be conserved. Such a scenario would be specific to II-VI quantum dots, where the build-up of DNSP is fast enough to block the precession of nuclei. This requires further investigation.

The study of DNSP was complemented by adding a magnetic field in the Faraday configuration and observing the time-resolved destruction and build-up of DNSP. The slow-evolution presents also a strong assymetry in the dynamics (Fig. 6.11), depending on the relative projection of the helicity of the photon and the direction of the magnetic field. The complex non-linear dynamics of the electron-nuclei coupled system is revealed. We are unable to give a detailed explanation of this behavior. The acceleration with B_z of the dynamics observed at the beginning of the $\sigma+$ pulse could arise as B_z compensates progressively B_N, leading to an increase of the electron-nuclei flip-flop, but then, it is not clear why such an acceleration is not observed at the end of the transient observed under $\sigma-$ excitation.

6.2.5 Power Dependence of the Nuclear Polarization Build-up

In order to analyze quantitatively the build-up time and the characteristic amplitude of the transient induced by DNSP, we perform a time-resolved measurement using a $100\mu s$ pulse of a

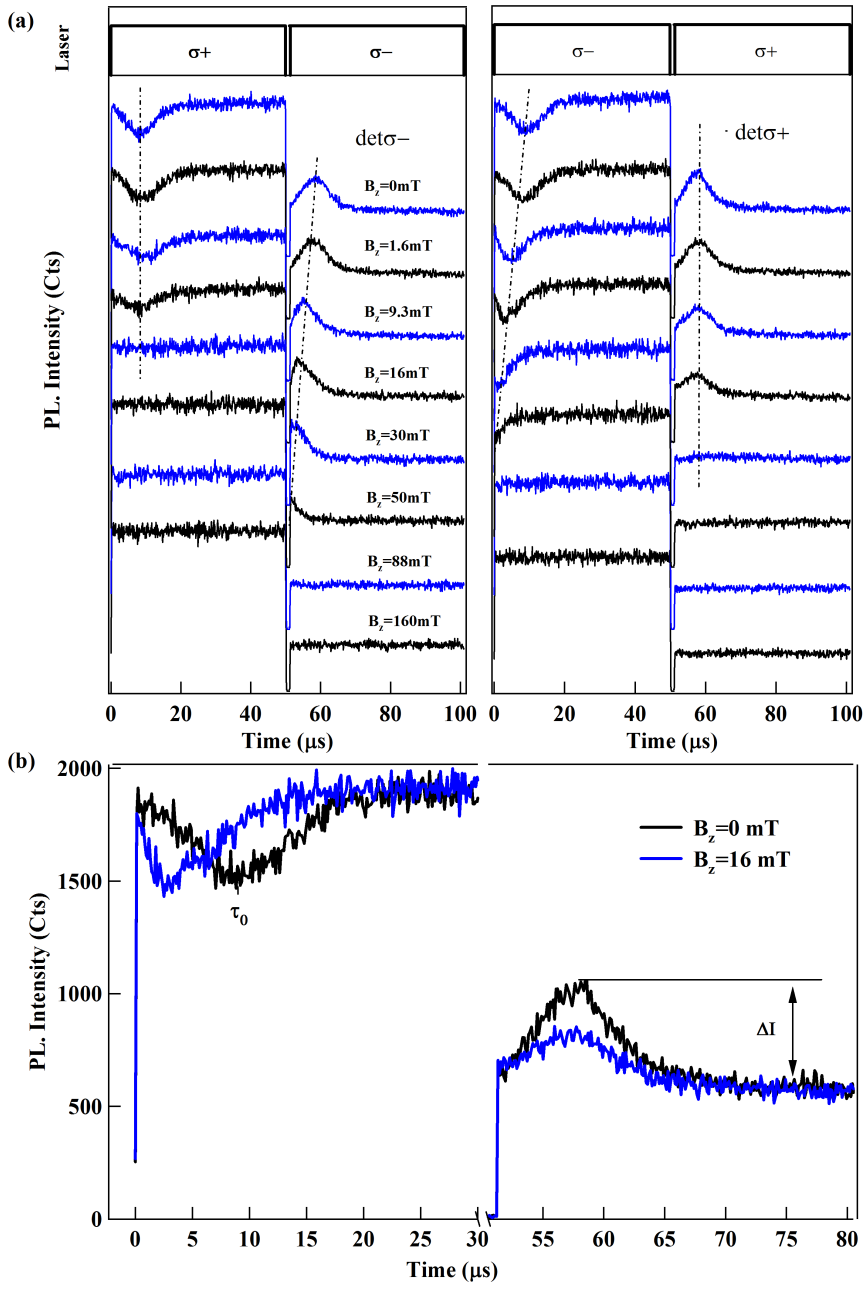

Figure 6.11: (a) Magnetic field dependence of the time-evolution of the $\sigma+$ and $\sigma-$ PL excited alternatively with $\sigma+/\sigma-$ light on a time-scale showing the destruction and build-up of the nuclear polarization. The excitation sequence is displayed above. Lines are guide to the eye. (b) Zoom on the transient corresponding to the optical pumping of the electron. The time-evolution of the $\sigma-$ PL recorded in the same conditions of excitation is also displayed. (b) A detailed view of the transients is presented.

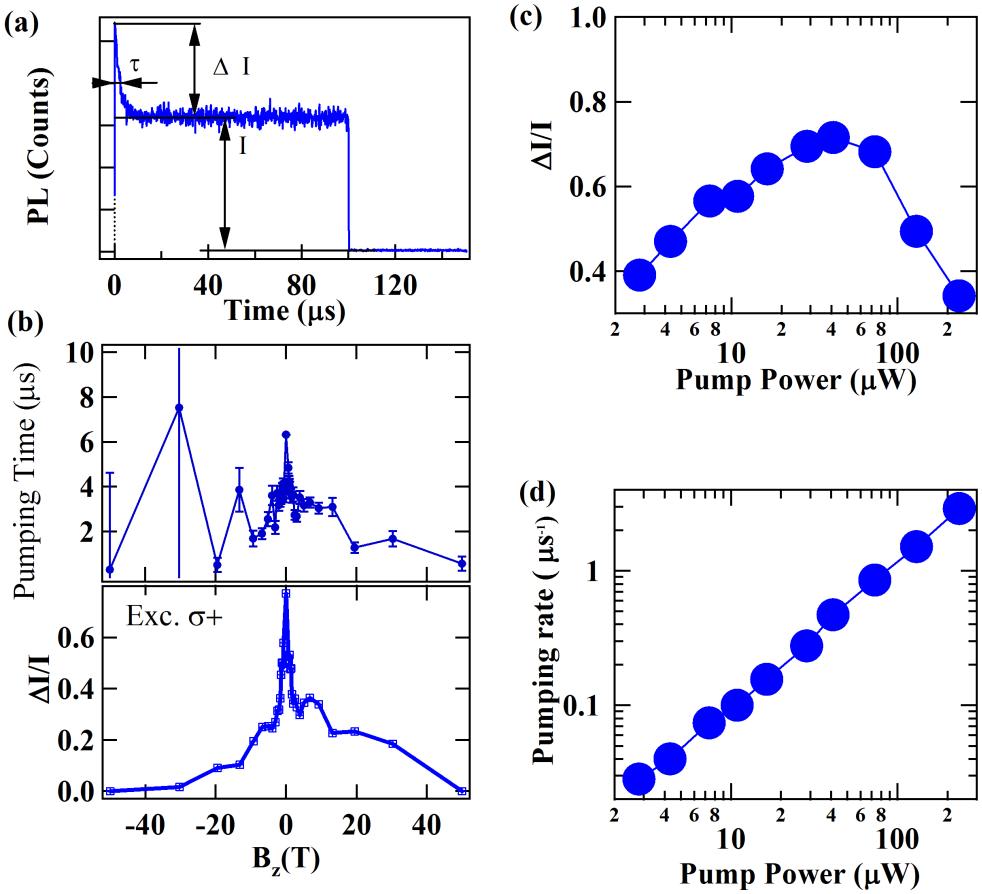

Figure 6.12: (a) DNSP transient observed under $\sigma-$ excitation after a dark time $\tau_{dark} = 50\mu s$. The amplitude (c) and rate of the transient (d) is studied as a function of power. (b) At a fixed power, the magnetic-field dependence of the amplitude of the transient and of the pumping time is shown.

$\sigma-$ helicity, followed by a $50\mu s$ dark time during which the DNSP relaxes partially (quantitative analysis of this relaxation will be done in the next section and is indeed found to occur on this time-scale for $B_z < 5mT$). This configuration enables us to fit the observed DNSP transient by an exponential variation, enabling to extract a characteristic rate $1/\tau$ and amplitude ΔI.

We observe in Fig. 6.12 (d), a linear increase of the pumping rate with power. While the build up of DNSP takes a few ms in III-V materials at $B = 0T$ [98], the observed pumping rate can be as high as a $\approx 1\mu s^{-1}$ in our case. A formation time of $30\mu s$ was already measured in CdSe/ZnSe quantum dots. Again, this results from the strong localization of the electron in II-VI quantum dots. Indeed, the built-up rate of DNSP scales as $|F_e|^4$ [99] so that we typically expect $\tau_{II-VI}/\tau_{III-V} \approx 8000^2/(10^5)^2 \approx 5.10^{-3}$.

The amplitude of the transient observed in Fig. 6.12 (c) first increases and then decreases with power. The increase is attributed to an increase of the DNSP. The decrease observed at high excitation power likely comes from a decoupling of the dynamics of the electron spin from the fluctuating nuclear spins, as the precession in the fluctuating Overhauser field is slower than the optical pumping rate of the electron.

The magnetic field dependence of $\Delta I/I$ is shown in Fig. 6.12 (b). We observe an important decrease of $\Delta I/I$ as soon as a few mT of magnetic field are applied. This decrease mainly comes from the increase of the relaxation time of the DNSP under magnetic field (this increase of the relaxation time is evidenced in Fig. 6.13 and will be further discussed). This increase of the relaxation time explains the general shape. However, the magnetic field dependence of $\Delta I/I$ (Fig. 6.12 (b)) also presents an asymmetry as the magnetic field is reversed. Similarly to the asymmetry observed in Fig. 6.9 (a), this is the signature of the creation of an effective field with well defined directions. The drop of $\Delta I/I$ likely comes from the decrease of DNSP obtained when B_{ext} screens B_e.

The pumping time (Fig. 6.12 (b)) decreases with magnetic field in the first few mT. This is consistent with a decrease of relaxation processes under magnetic field: the diminution of spin diffusion allows to reach a steady-state value more quickly. The further evolution with $B_z < 0$ cannot be clearly measured, as the signal to noise ratio increases (the amplitude of the transient diminishes). A further acceleration of the dynamics is observed for $B_z > 0$, this could be the signature of a feedback expected when B_{ext} is opposite to B_N.

6.2.6 Nuclear spin polarization decay

In order to investigate the variation of the relaxation time of the DNSP with magnetic field, we follow the protocol shown in Fig 6.13. For a given magnetic field, we prepare a DNSP and measure after a time τ_{dark} the amplitude of the transient, corresponding to the partial relaxation of the nuclear polarization. As τ_{dark} is increased, this amplitude saturates, demonstrating the full relaxation. The variation of the amplitude of the transient with τ_{dark} is used to estimate the relaxation time of DNSP at a given magnetic field. The evolution of this relaxation time is presented in Fig 6.13.(b). It ranges from $14\mu s$ at $B = 0T$ to $170\mu s$ at $B = 16mT$. The relaxation rate is one order of magnitude faster than the one observed in [100], and the one expected from nuclear dipole-dipole interactions. Furthermore, the magnetic field dependence presents a significant increase of the decay time over the first few mT, while a magnetic field of $1mT$ efficiently inhibits nuclear dipole-dipole interactions in III-V materials [98]. Since this interaction is expected to be smaller in our case, we can definitely rule out dipole-dipole interaction as a major cause of DNSP relaxation.

Co-tunneling to the close-by reservoir could be responsible for this depolarization. Via hyperfine-mediated flip-flop, the randomization of the electron spin creates an efficient relax-

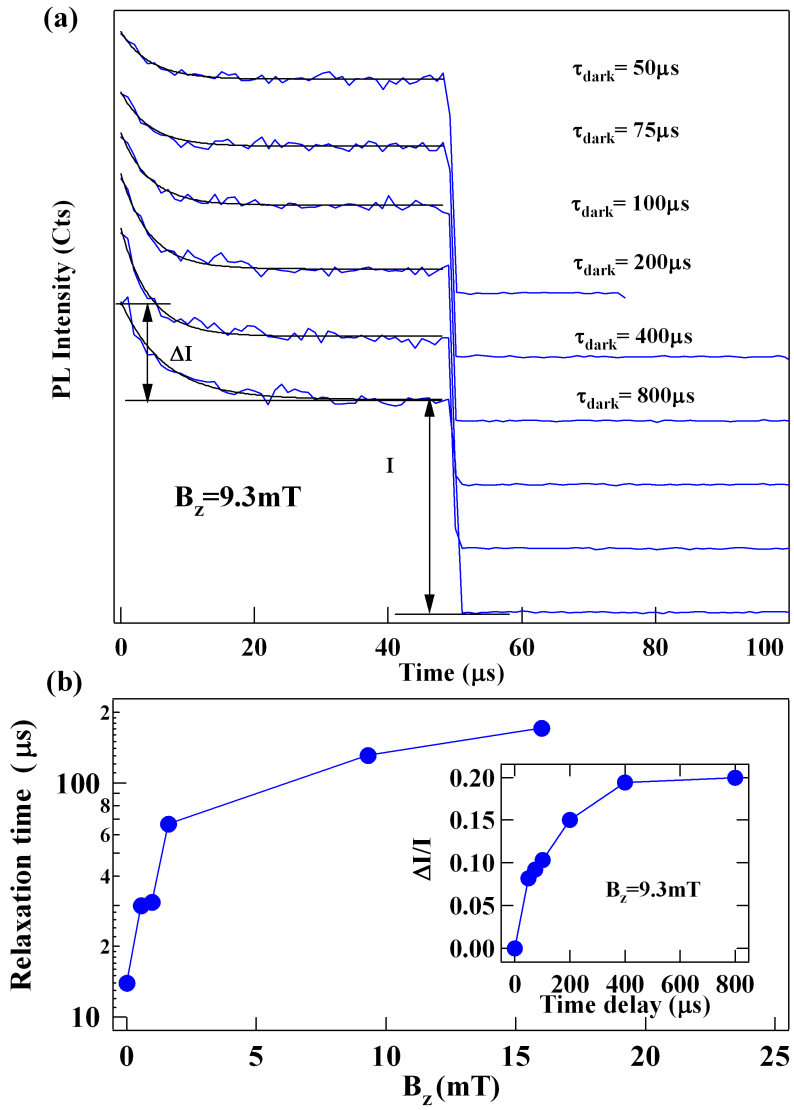

Figure 6.13: (a) Evolution of the DNSP transient, under a magnetic field $B_z = 9.3mT$, with an increasing dark time. (b) Magnetic field dependence of the nuclear spin relaxation time. The inset shows how the relaxation time is extracted (e.g. at $B_z = 9.3mT$): the amplitude of the transient is measured as a function of the time delay (i.e. τ_{dark}). The relaxation time is taken at the $1/e$ point of the time-delay dependence.

ation of the nuclei. According to [99], this relaxation time is:

$$T_{1e}^{-1} = \frac{2\left\langle \omega^2 \right\rangle \|s\|^2 \tau_c}{3[1+(\Omega\tau_c)^2]} \tag{6.14}$$

In this expression, ω is the precession frequency of the nuclei in the Knight field (equal to $2\pi/(0.2)\mu s^{-1}$), τ_c is the correlation time of the electron (in the dark), Ω is the precession frequency of the electron in the Overhauser field. At last, $\|s\|^2$ is equal to $s(s+1) = 3/4$. The fastest relaxation we expect from this process can be estimated taking $\Omega = \Omega_{fluc} = 2\pi/2ns^{-1}$ and $\tau_c = 10ns$. We obtain $T_{1e} \approx 200\mu s$ which is not fast enough. Therefore, we are tempted to conclude that co-tunneling alone cannot explain the observed dynamics.

Another mechanism to consider is the depolarization resulting from an electron-mediated nuclear dipole-dipole interaction. This results in exchange constants between the nuclei which typically scale as $A^2/(N^2\epsilon_z)$. The resulting rate of nuclear-spin depolarization is $T_{ind}^{-1} \approx A^2/(N^{3/2}\hbar\epsilon_z)$, where ϵ_z is the Zeeman splitting of the electron. This mechanism could explain a depolarization of the nuclei on a μs scale [101]. However, this expression gives only a minor bound to the relaxation time because the inhomogeneity of the Knight field can strongly inhibit this decay [102]. A magnetic field along the z axis is expected to affect this process, progressively decoupling the nuclei from the indirect coupling created by the electron, as observed in the first few mT (Fig. 6.13). The electron-induced nuclear depolarization was demonstrated in [98] in which the ms relaxation was completely suppressed using a voltage pulse on a Schottky diode in order to remove the resident electron.

Conclusion

In conclusion, we have evidenced in the photoluminescence excitation spectra of a negatively charged quantum dot the polarized fine structure of the P-shell of the hot trion. We have studied using PL decay measurements the dynamics of the injection of photocarriers as a function of the energy of the injection. Injection above the P-shell has been used to pump the resident electron on a time-scale of $10 - 100ns$ and to create a dynamic nuclear spin polarization. At $B = 0T$, the creation of the dynamic nuclear spin polarization can be as fast as a μs, and the decay of the nuclear polarization, attributed to an electron mediated relaxation, is $\approx 10\mu s$. The observed dynamics are $\approx 10^3$ faster than the ones observed in III/V quantum dots at $B = 0T$, which we attribute to the smaller quantum dot volume. The magnetic-field dependence of the PL polarization-rate revealed that the nuclear spin fluctuations were the dominant process in the dephasing of the resident electron. We proved that this dephasing was efficiently suppressed by dynamic nuclear spin polarization at $B = 0T$.

The time-resolved creation of dynamic nuclear spin polarization in a Faraday magnetic field (Fig. 6.11) has revealed an intriguant behavior. The Hanle depolarization of the coupled electron-nuclei system deviates from a Lorentzian at high excitation power, which is also unexpected. Modeling of the coherent evolution of the coupled electron-nuclei system could be helpful to a thorough comprehension.

Conclusion

In closing, we have studied in this thesis the dynamics of a single Mn spin embedded in a II-VI quantum dot. We have shown that Mn spin orientation could be achieved using light of a controlled helicity and energy. This is the first experimental demonstration of the optical pumping of a single Mn spin. Such orientation can be performed in a few tens of ns. The spin distribution obtained by such means is perfectly conserved over a few μs. This is a direct evidence that the relaxation time of a Mn spin is long, and confirms that this system has a robust spin.

We have shown that the dynamic of the Mn spin orientation at zero magnetic field is controlled by a magnetic anisotropy induced by the presence of strains at the Mn location. This magnetic anisotropy explains the saturation of the efficiency of the pumping process (at $\approx 75\%$, in the best cases) under resonant excitation. We have investigated processes responsible for the photo-induced spin-orientation. We have discussed processes involving a hole spin-flip, or carrier-Mn spin-flips. The latter have been evidenced experimentally but their physical origin needs to be clarified.

We have also evidenced dressed states on a Mn-doped quantum dot. This signature of a strong light-matter coupling, and of an optical Stark shift of the Mn spin is promising for coherent manipulation of the Mn spin. Moreover, this is the first time that dressed-states are evidenced on a II-VI quantum dots and should encourage further improvements on this class of materials.

At last, we have evidenced the coherent time-evolution of the electron-nuclei coupled system. Although no hysteresis was observed, the system presents a very rich and complex dynamics. We have observed that unpolarized nuclei could efficiently cause a rapid decoherence of the resident electron. However, these undesirable nuclear effects can in principle be completely avoided in II-VI materials through the use of isotopically purified materials.

Future experiments will involve the study of unstrained fluctuations interface quantum dots. Firstly, this system should be interesting to further-study the effect of the Mn fine structure on the optical pumping process. Also, if light-hole states are identified in these structures, we could try optical rotation of the Mn spin. Another project is the use of micro-waves. Combined with pump-probe experiments, this should allow us to directly probe transitions between the Mn fine levels and measure the magnetic anisotropy. Another way to directly probe the Mn fine structure is to use a resonant laser so as to tune a dressed state corresponding to the Mn spin-state $S_z = +5/2$ with the ground-state $S_z = +3/2$. Via resonant two-photon absorption in pulsed excitation, we should be able to probe a change in the Mn population which depends if the dressed-state is on resonance with the ground-state $S_z = +3/2$. However, before performing such experiments, we would need to considerably improve the linewidth of our samples! At last,

an interesting case to study would be the one of a hole-Mn doped quantum dot. Indeed, when an electron-hole pair is injected in the quantum dot, the Mn is left to freely flip-flop with the electron before optical recombination, thus providing a natural way to perform a fast optical pumping of the hole-Mn complex.

Conclusion (French)

En conclusion, nous avons étudié dans ce manuscrit la dynamique d'un spin unique de manganèse dans une boite quantique II-VI. Nous avons mis en évidence la possibilité d'orienter ce spin par des moyens optiques (injection de porteurs polarisés, pompage optique). Un tel processus d'orientation est réalisé en quelques dizaines de ns. Nous montrons que l'état de spin préparé optiquement est parfaitement conservé à l'échelle d'une dizaine de μs. Nous apportons la preuve expérimentale que le temps de relaxation du Manganèse est long, ce qui était bien le résultat escompté pour une impureté magnétique isolée.
Nous avons démontré qu'en champ magnétique nul, la dynamique du Manganèse seul (en l'absence d'une paire électron-trou) est contrôlée par une anisotropie magnétique induite par la présence de contraintes. La prise en compte de cette anisotropie magnétique, qui domine la structure fine du Mn, permet d'expliquer les efficacités de pompage optique rencontrées expérimentalement, qui se situent autour de 75%. Au sein du complexe exciton-Manganèse, nous avons cherché à mettre en évidence des processus rendant compte de l'orientation photo-induite. Nous avons évoqué l'hypothèse d'un processus d'orientation impliquant le spin-flip du trou, ou impliquant des relaxations de spin porteurs-Manganèse. Ces derniers ont été mis en évidence expérimentalement, et semble dominer sous excitation résonante, mais leur origine physique doit être clarifiée.
Nous avons également mis en évidence des états habillés (doublet d'Autler-Townes) sur une boîte quantique magnétique. Cette signature d'un couplage cohérent entre la lumière et les états d'une boîte quantique magnétique ouvre des perspectives de contrôle cohérent du Manganèse par des moyens optiques. De plus, c'est la première fois que des états habillés sont mis en évidence dans des boîtes II-VI, ce qui est encourageant pour cette classe de matériaux.
Enfin, nous avons étudié la dynamique cohérente du système électron-noyaux dans une boîte quantique II-VI. Bien qu'aucune hystérésis ne soit observée, ce système présente une dynamique très riche et complexe. Nous avons montré expérimentalement qu'un bain de noyaux non-polarisés causait une décohérence rapide de l'électron résident. Mais ce bain de noyaux peut être polarisé en quelques μs par le biais de l'interaction hyperfine avec un électron résidant pompé optiquement. La décohérence de l'électron induite par les noyaux peut en principe être contournée dans les matériaux II-VI, en utilisant une purification isotopique.

Nos recherches sur des boîtes dopées Mn s'orientent maintenant vers l'étude de boîtes à fluctuation d'interface non-contraintes. Tout d'abords, ce système devrait être intéressant pour observer l'influence d'une structure fine non-contrainte sur le processus de pompage optique. Aussi, si les états de trous légers sont identifiés dans ces structures, ils pourraient permettre de réaliser un contrôle cohérent du spin du Manganèse sous champ magnétique faible (un champ Faraday de quelques dizaines de mT est à priori nécessaire pour initialiser un spin de Manganèse en l'absence d'anisotropie magnétique).
Un autre projet en cours est l'utilisation de micro-ondes. Combinés à des séquences pompe-sonde, des micro-ondes nous permettraient de sonder des transitions entre deux niveaux de la

structure fine du Manganèse, et d'aller mesurer directement l'anisotropie magnétique. Un autre moyen d'aller sonder cette structure fine est d'utiliser un laser résonant pour mettre en résonance un état habillé correspondant par exemple à l'état de spin $S_z = +5/2$ avec le niveau de l'état fondamental de la boîte correspondant à $S_z = +3/2$. Via une transition résonante à deux photons (que nous réalisons en pulsé), nous devrions être capable de sonder une différence de population de l'état $+5/2$ lorsque l'état habillé est résonant avec le niveau $S_z = +3/2$. Toutefois, avant de réaliser cette expérience, il nous faudrait améliorer la largeur de raie de nos échantillons (environ $60\mu eV$) qui est comparable au l'écart énergétique attendu entre les deux niveaux de la structure fine considérés ici.
Enfin, un sujet d'étude intéressant serait les boîtes comportant un Manganèse et un trou résident. En effet, lors de l'injection d'une paire électron-trou, le Manganèse interagit avec un électron. L'évolution du spin du Manganèse est alors contrôlée par une interaction d'échange isotrope, avec des termes de flip-flop électron -Manganèse qui devraient permettre un pompage optique efficace du système trou-Mn.

Appendix A

Spin Operators

For any spin-operator S we have:

$$S_+ = S_x + iS_y \tag{A.1}$$
$$S_- = S_x - iS_y \tag{A.2}$$

Electron: $1/2$ **spin**

The spin operator for the electron are defined by:

$$\sigma_x = 0.5 \begin{pmatrix} 0 & 1 \\ 1 & 0 \end{pmatrix} \tag{A.3}$$
$$\sigma_y = 0.5 \begin{pmatrix} 0 & -i \\ i & 0 \end{pmatrix} \tag{A.4}$$
$$\sigma_z = 0.5 \begin{pmatrix} 1 & 0 \\ 0 & -1 \end{pmatrix} \tag{A.5}$$

Hole: $3/2$ **momentum**

For the hole of the Γ_8 band with a momentum $3/2$, the spin operators are defined by:

$$J_x = \begin{pmatrix} 0 & \frac{\sqrt{3}}{2} & 0 & 0 \\ \frac{\sqrt{3}}{2} & 0 & 1 & 0 \\ 0 & 1 & 0 & \frac{\sqrt{3}}{2} \\ 0 & 0 & \frac{\sqrt{3}}{2} & 0 \end{pmatrix} \tag{A.6}$$
$$J_y = \begin{pmatrix} 0 & -\frac{i\sqrt{3}}{2} & 0 & 0 \\ \frac{i\sqrt{3}}{2} & 0 & -i & 0 \\ 0 & i & 0 & -\frac{i\sqrt{3}}{2} \\ 0 & 0 & \frac{i\sqrt{3}}{2} & 0 \end{pmatrix} \tag{A.7}$$

$$J_z = \begin{pmatrix} \frac{3}{2} & 0 & 0 & 0 \\ 0 & \frac{1}{2} & 0 & 0 \\ 0 & 0 & -\frac{1}{2} & 0 \\ 0 & 0 & 0 & -\frac{3}{2} \end{pmatrix} \tag{A.8}$$

Hole in the heavy hole approximation: 1/2 isospin

For a heavy-hole of the Γ_8 band, we associate an isospin $\pm 1/2$ for heavy-holes with $J_z = \pm 3/2$. The spin operators are noted j_x, j_y and j_z. They are formally identical to σ_x, σ_y, σ_z.

Electronic spin of the Mn: 5/2 spin

The spin operators for a 5/2 are given by:

$$S_x = \begin{pmatrix} 0 & \frac{\sqrt{5}}{2} & 0 & 0 & 0 & 0 \\ \frac{\sqrt{5}}{2} & 0 & \sqrt{2} & 0 & 0 & 0 \\ 0 & \sqrt{2} & 0 & \frac{3}{2} & 0 & 0 \\ 0 & 0 & \frac{3}{2} & 0 & \sqrt{2} & 0 \\ 0 & 0 & 0 & \sqrt{2} & 0 & \frac{\sqrt{5}}{2} \\ 0 & 0 & 0 & 0 & \frac{\sqrt{5}}{2} & 0 \end{pmatrix} \tag{A.9}$$

$$S_y = \begin{pmatrix} 0 & -\frac{i\sqrt{5}}{2} & 0 & 0 & 0 & 0 \\ \frac{\sqrt{5}}{2} & 0 & -i\sqrt{2} & 0 & 0 & 0 \\ 0 & \sqrt{2} & 0 & -\frac{3i}{2} & 0 & 0 \\ 0 & 0 & \frac{3}{2} & 0 & -i\sqrt{2} & 0 \\ 0 & 0 & 0 & \sqrt{2} & 0 & -\frac{i\sqrt{5}}{2} \\ 0 & 0 & 0 & 0 & \frac{\sqrt{5}}{2} & 0 \end{pmatrix} \tag{A.10}$$

$$S_z = \begin{pmatrix} \frac{5}{2} & 0 & 0 & 0 & 0 & 0 \\ 0 & \frac{3}{2} & 0 & 0 & 0 & 0 \\ 0 & 0 & \frac{1}{2} & 0 & 0 & 0 \\ 0 & 0 & 0 & -\frac{1}{2} & 0 & 0 \\ 0 & 0 & 0 & 0 & -\frac{3}{2} & 0 \\ 0 & 0 & 0 & 0 & 0 & -\frac{5}{2} \end{pmatrix} \tag{A.11}$$

Nuclear spin of the Mn: 5/2 spin

The spin operators are noted I_x, I_y and I_z. They are formally identical to the spin operators S_x, S_y, and S_z.

Appendix B

Autler-Townes Photo-Luminescence

In this section, we compute the spontaneous emission of a three level system in the so-called V or Ξ configuration. The aim here to is to reproduce the results obtained experimentally, and to lay a foundation for further studies. The V configuration corresponds to the experiment Fig. 5.2, where resonant excitation and detection are done on the exciton (or the XMn). The Ξ configuration corresponds to Fig. 5.3(c) where resonant excitation is on a biexciton (or X_2Mn) line, and detection is made on the exciton. In fact, this problem has already been solved in [103] in the Schrödinger picture, but here, we choose to follow a calculation in the Heisenberg picture, closer to the one found for a two level system in [104] which we find less fastidious. This means that none of this section is new to the specialist, the aim is purely pedagogical.

The calculation steps will be detailed for the V configuration. To start with, we will derive the density matrix evolution equations, and solve them in the steady-state. The steady state values will be used at the end of the calculation. We will present the Langevin equations of motion, which rule the evolution of atomic operators. Then we will show that the spectrum of detected light is given by the first-order correlation function of the atomic dipole operator of the detected transition. Then, using the quantum regression theorem and a Laplace transform, we will see that the spectrum reduces to a simple algebra calculation.

B.1 Density Matrix Evolution, Stationary Solution

We consider the evolution of a three level system in the V configuration, irradiated by a classical electric field:

$$\vec{E}(z,t) = \frac{1}{2}(\varepsilon(z)e^{i(kz-\omega_L t)}\vec{u} + c.c.) \tag{B.1}$$

Where $\varepsilon(z)$ is the field amplitude, ω_L is the laser frequency, and $\vec{u}$ is the unitary vector giving the field polarization. We consider the laser is resonant or nearly resonant with the transition $1 \to 3$, with the same polarization as the transition. In the dipolar approximation and in the rotating wave approximation, the atom-laser coupling is given by:

$$\begin{aligned} H_{int} &= -\vec{D_{13}}.\vec{E} && \text{(B.2)} \\ &= \hbar\Omega(\sigma_{31}e^{-i\omega_L t} + c.h.) && \text{(B.3)} \end{aligned}$$

Where $\sigma_{31} =\mid 3\rangle\langle 1 \mid$ (more generally we define $\sigma_{ij} =\mid i\rangle\langle j \mid$). $\vec{D}_{13} = \mu_{31}\sigma_{31}\vec{u} + c.h.$ is the transition dipole operator, with μ_{31} the transition dipole. We do not restrict the problem if we

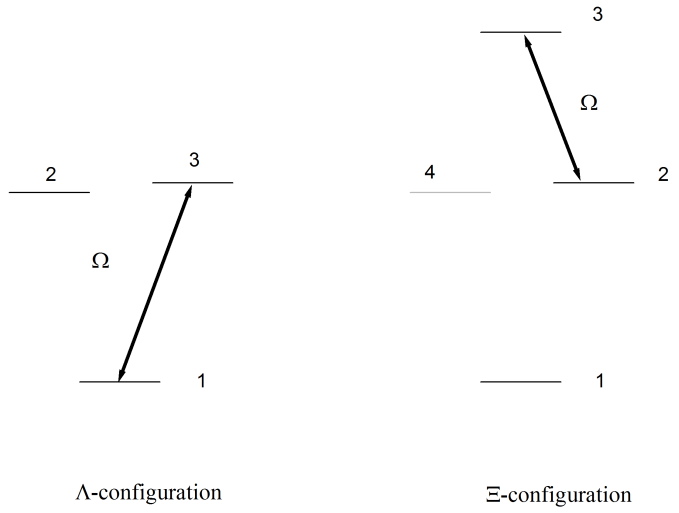

Figure B.1: Configuration of the energy levels.

take $\Omega = -\frac{1}{2}\mu_{31}\varepsilon(z)e^{ikz}$ real. The Hamiltonian of the three level system is given by:

$$H = \sum_{i=0}^{3} \hbar\omega_i\sigma_{ii} + \hbar\Omega(\sigma_{31}e^{-i\omega_L t} + c.h.) \tag{B.4}$$

The hamiltonian evolution of the density matrix can be calculated using the Liouville equation:

$$\frac{\partial\rho}{\partial t} = -\frac{i}{\hbar}[H,\rho] \tag{B.5}$$

The irreversible part of the evolution such as spontaneous emission or generation of carriers by a non-resonant laser or pure dephasing can be handled using a Lindbladien. This treatment assumes that the coupling with the environment can be treated in the Markov approximation. This approximation relies on the existence of a timescale long compared to the correlation-time of the reservoir but short compared to the decay of the system. For instance, spontaneous emission from level $2 \to 1$ is included adding (B.6) to the Hamiltonian evolution given by (B.5):

$$\left(\frac{\partial\rho}{\partial t}\right)_{irrev} = \frac{\Gamma}{2}(2\sigma_{12}\rho\sigma_{21} - \sigma_{22}\rho - \rho\sigma_{22}) \tag{B.6}$$

The first part describes the increase of the population of level 1 (ρ_{11}) due to relaxation from level 2: $\left(\frac{\partial\rho_{11}}{\partial t}\right)_{irrev} = \Gamma\rho_{22}$. The last terms describe the loss of population from level 2 at a rate Γ and the damping of the coherences linked to level 2 (ρ_{23} ρ_{21}, ρ_{32} and ρ_{12}) at a rate $\Gamma/2$. We see that, by construction, relaxation written in the Lindblald form conserves the population ($tr\rho = 1$).

When considering a pumping rate g at the limit of low pumping[46], spontaneous emission rates Γ from level 2 and 3 to level 1, and the atom-laser coupling, the full master equation is:

$$\dot{\rho}_{33} = g\rho_{11} - \Gamma\rho_{33} - (i\Omega)e^{-i\omega_L t}\rho_{13} + c.h.) \tag{B.7}$$

$$\dot{\rho}_{22} = g\rho_{11} - \Gamma\rho_{22} \tag{B.8}$$

[46] we consider $g \ll \Gamma$, population of X_2 can be neglected

$$\dot{\rho}_{32} = -(\gamma_{23} + i\omega_{23})\rho_{32} - i\Omega e^{-i\omega_L t}\rho_{12} \quad \text{(B.9)}$$
$$\dot{\rho}_{21} = -(\gamma_{12} + i\omega_{12})\rho_{21} + i\Omega e^{-i\omega_L t}\rho_{23} \quad \text{(B.10)}$$
$$\dot{\rho}_{31} = -(\gamma_{13} + i\omega_{13})\rho_{31} + i\Omega e^{-i\omega_L t}(\rho_{33} - \rho_{11}) \quad \text{(B.11)}$$
$$\rho_{11} = 1 - \rho_{33} - \rho_{22} \quad \text{(B.12)}$$
$$\rho_{23} = \rho_{32}^* \quad \text{(B.13)}$$
$$\rho_{12} = \rho_{21}^* \quad \text{(B.14)}$$
$$\rho_{13} = \rho_{31}^* \quad \text{(B.15)}$$

and where the coherence damping γ_{ij} which can include pure dephasing[47] γ_{ij}^{deph} and ω_{ij} are defined by:

$$\omega_{12} = \omega_2 - \omega_1; \quad \omega_{13} = \omega_3 - \omega_1; \quad \omega_{23} = \omega_3 - \omega_2; \quad \text{(B.16)}$$
$$\gamma_{12} = \frac{\Gamma}{2} + \frac{g}{2} + \gamma_{12}^{deph} \quad \text{(B.17)}$$
$$\gamma_{13} = \frac{\Gamma}{2} + \frac{g}{2} + \gamma_{13}^{deph} \quad \text{(B.18)}$$
$$\gamma_{23} = \Gamma + \gamma_{23}^{deph} \quad \text{(B.19)}$$

The steady state solution of these equations can be found considering that the population are constant. Note that $(\rho_{32})_{stat}$ and $(\rho_{21})_{stat}$ are equal to 0. Equation B.11 can be formally integrated:

$$(\rho_{31})_{stat}(t) = i\Omega \int_{\infty}^{t} dt' e^{-i\omega_L t'} e^{(i\omega_{13}+\gamma_{13})(t'-t)}((\rho_{33})_{stat} - (\rho_{11})_{stat}) \quad \text{(B.20)}$$
$$\text{(B.21)}$$

we find:

$$(\rho_{31})_{stat}(t) = i\Omega e^{-i\omega_L t} \frac{(\rho_{33})_{stat} - (\rho_{11})_{stat}}{\gamma_{13} + i(\omega_{31} - \omega_L)} \quad \text{(B.22)}$$
$$\text{(B.23)}$$

If we substitute this result in B.7 and use B.8 and B.12, we find the stationnary solution:

$$(\rho_{33})_{stat} = \frac{\Gamma(g+R)}{2\Gamma g + 2\Gamma R + \Gamma^2 + Rg} \quad \text{(B.24)}$$
$$(\rho_{22})_{stat} = \frac{g}{g+\Gamma}\left(1 - \frac{\Gamma(g+R)}{2\Gamma g + 2\Gamma R + \Gamma^2 + Rg}\right) \quad \text{(B.25)}$$

where R is the rate constant appearing in the rate equations:

$$R = \frac{(2\Omega)^2}{2} \frac{\gamma_{13}}{\gamma_{13}^2 + (\omega_{13} - \omega_L)^2} \quad \text{(B.26)}$$

The result B.24 will be used by the end of this section.

[47] This will be discussed in details later

B.2 What is a spectra?

From now on, we switch to a Heisenberg picture where operators depend on time. We will neglect the vectorial nature of the field operators $E(t)$ and atomic dipole operators $D(t)$. The Wiener-Khintchine theorem states that the spectrum of a stationary stochastic process is given by the Fourier transform of the two-time correlation function of the radiated field:

$$S(\omega_{det}) \propto \lim_{T\to\infty} \frac{1}{T} \int_0^T dt \int_0^T dt' \langle E^-(t) E^+(t') \rangle e^{-i\omega_{det}(t-t')} \tag{B.27}$$

where $E^+(t)$ is the positive frequency component of the electric field operator[48]. There is a simple relation between the scattered electrical field and the atomic dipole valid both in classical physics and in quantum mechanics:

$$E^+(t) \propto D^-(t - \frac{r}{c}) \tag{B.28}$$

Where the polarisation operator D^- involves in our case the contribution of the $3 \to 1$ and $2 \to 1$ transitions:

$$D^-(t) = \mu_{13}\sigma_{13}(t) + \mu_{12}\sigma_{12}(t) \tag{B.29}$$

Equation B.28 means that the time-evolution of the atomic dipole operators (and their two-time correlation function) is all that we need to solve this problem.

B.3 Langevin equations of motion

The time evolution of the atomic operators is given by the Langevin equations of motion:

$$\begin{aligned}
\dot{\sigma}_{12} &= -(\gamma_{12} + i\omega_{12})\sigma_{12} + (i\Omega)e^{-i\omega_L t}\sigma_{32} + F_{12}(t) && \text{(B.30)}\\
\dot{\sigma}_{13} &= -(\gamma_{13} + i\omega_{13})\sigma_{13} + (i\Omega)e^{-i\omega_L t}(\sigma_{33} - \sigma_{11}) + F_{13}(t) && \text{(B.31)}\\
\dot{\sigma}_{23} &= -(\gamma_{23} + i\omega_{23})\sigma_{23} - (i\Omega)e^{-i\omega_L t}\sigma_{21} + F_{23}(t) && \text{(B.32)}\\
\dot{\sigma}_{22} &= g\sigma_{11} - \Gamma\sigma_{22} + F_{22}(t) && \text{(B.33)}\\
\dot{\sigma}_{33} &= g\sigma_{11} - \Gamma\sigma_{33} - (i\Omega)e^{-i\omega_L t}\sigma_{31} + c.h.) + F_{33}(t) && \text{(B.34)}\\
\sigma_{11} &= 1 - \sigma_{33} - \sigma_{22} && \text{(B.35)}\\
\sigma_{23} &= \sigma_{32}^\dagger \;;\; \sigma_{12} = \sigma_{21}^\dagger \;;\; \sigma_{13} = \sigma_{31}^\dagger && \text{(B.36)}
\end{aligned}$$

It is the sum of a Hamiltonian evolution, relaxation terms in the Lindblald form (which give the mean effect of reservoir interactions), and the noise operator $F_{ij}(t)$ which satisfy:

$$\begin{aligned}
\langle F_{ij}(t) \rangle &= 0 && \text{(B.37)}\\
\langle F_{kl}(t) F_{ij}(t') \rangle &= 2\delta(t - t')\langle D_{klij} \rangle && \text{(B.38)}
\end{aligned}$$

We see that these equations are very similar to the ones of the matrix density (B.7-B.15), except for the presence of the $\left\{\vec{F_{ij}}\right\}_{ij}$. This comes from the fact that there is a straightforward link between the observable σ_{ij} and the matrix density coefficient ρ_{ji} in the Schrödinger picture:

$$\langle \sigma_{ij}^{Heisenberg} \rangle = tr(\sigma_{ij}\rho) = \rho_{ji}^{Schrodinger} \tag{B.39}$$

[48] We use the traditional notation: the ω vibration of $E^+(t)$ oscillates as $e^{-i\omega t}$.

The use of the $\{F_{ij}\}_{ij}$ can be justified qualitatively[49] by the fact that we need to add an "ingredient" to guarantee that the commutation rules ($[\sigma_{ij}(t), \sigma_{kl}(t)] = (\delta_{jk}\sigma_{il}(t) - \delta_{li}\sigma_{kj}(t))$) are valid at all times, even if $\langle\sigma_{ij}(t)\rangle_{stat} = 0$. We will take for granted that the $\{F_{ij}\}_{ij}$ permit to fulfill these requirements. The fact that the noise operators are δ-correlated in time is another way to formulate the Markov approximation. We won't need the explicit expression for the $\{F_{ij}(t)\}_{ij}$ and the $\{D_{klij}\}_{klij}$.

These linear equations can be considerably simplified if we manage to get rid of the explicit time dependence of the coefficients[50]. This can be done if we introduce the following operators[51]:

$$\sigma_{12} = e^{-i\omega_{12}t}S_{12}\ ;\ \sigma_{13} = e^{-i(\omega_{13}-\delta)t}S_{13}\ ;\ \sigma_{23} = e^{-i(\omega_{23}-\delta)t}S_{23}\ ; \tag{B.40}$$

$$\sigma_{21} = e^{i\omega_{12}t}S_{21}\ ;\ \sigma_{31} = e^{i(\omega_{13}-\delta)t}S_{31}\ ;\ \sigma_{32} = e^{i(\omega_{23}-\delta)t}S_{32}\ ; \tag{B.41}$$

$$\sigma_{11} = S_{11}\ ;\ \sigma_{22} = S_{22}\ ;\ \sigma_{33} = S_{33} \tag{B.42}$$

where $\delta = \omega_{13} - \omega_L$. We apply the same transformation to the $\{F_{ij}\}_{ij}$, and note $\{f_{ij}\}_{ij}$ the new noise operators . Furthermore, if we substitute $S_{11} = 1 - S_{22} - S_{33}$ in all equations, we obtain:

$$\dot{S}_{12} = -\gamma_{12}S_{12} + i\Omega S_{32} + f_{12}(t) \tag{B.43}$$

$$\dot{S}_{13} = -(\gamma_{13} + i\delta)S_{13} + i\Omega(2S_{33} + S_{22} - 1) + f_{13}(t) \tag{B.44}$$

$$\dot{S}_{21} = -\gamma_{12}S_{12} - i\Omega S_{23} + f_{21}(t) \tag{B.45}$$

$$\dot{S}_{22} = g(1 - S_{22} - S_{33}) - \Gamma S_{22} + f_{22}(t) \tag{B.46}$$

$$\dot{S}_{23} = -(\gamma_{23} + i\delta)S_{23} - i\Omega S_{21} + f_{23}(t) \tag{B.47}$$

$$\dot{S}_{31} = -(\gamma_{13} - i\delta)S_{31} - i\Omega(2S_{33} + S_{22} - 1) + f_{31}(t) \tag{B.48}$$

$$\dot{S}_{32} = -(\gamma_{23} - i\delta)S_{32} + i\Omega S_{12} + f_{32}(t) \tag{B.49}$$

$$\dot{S}_{33} = g(1 - S_{22} - S_{33}) - \Gamma S_{33} - i\Omega(S_{13} - S_{31}) + f_{33}(t) \tag{B.50}$$

$$\tag{B.51}$$

which can be written in the matrix form:

$$\frac{d}{dt}\begin{pmatrix} S_{12} \\ S_{13} \\ S_{21} \\ S_{22} \\ S_{23} \\ S_{31} \\ S_{32} \\ S_{33} \end{pmatrix} =$$

[49] A thorough explanation can be found in the chap15 of [104].
[50] This method could have been used to solve (B.11).
[51] We extract from the $\{\sigma_{ij}\}_{ij}$ the fast dipole oscillations.

$$\begin{pmatrix} -\gamma_{12} & 0 & 0 & 0 & 0 & 0 & i\Omega & 0 \\ 0 & -(\gamma_{13}+i\delta) & 0 & i\Omega & 0 & 0 & 0 & 2i\Omega \\ 0 & 0 & -\gamma_{12} & 0 & -i\Omega & 0 & 0 & 0 \\ 0 & 0 & 0 & -(\Gamma+g) & 0 & 0 & 0 & -g \\ 0 & 0 & -i\Omega & 0 & -(\gamma_{23}+i\delta) & 0 & 0 & 0 \\ 0 & 0 & 0 & -i\Omega & 0 & -(\gamma_{13}-i\delta) & 0 & -2i\Omega \\ i\Omega & 0 & 0 & 0 & 0 & 0 & -(\gamma_{23}-i\delta) & 0 \\ 0 & i\Omega & 0 & -g & 0 & -i\Omega & 0 & -(g+\Gamma) \end{pmatrix} \begin{pmatrix} S_{12} \\ S_{13} \\ S_{21} \\ S_{22} \\ S_{23} \\ S_{31} \\ S_{32} \\ S_{33} \end{pmatrix}$$

$$+ \begin{pmatrix} 0 \\ i\Omega \\ 0 \\ g \\ 0 \\ i\Omega \\ 0 \\ g \end{pmatrix} + \begin{pmatrix} f_{12} \\ f_{13} \\ f_{21} \\ f_{22} \\ f_{23} \\ f_{31} \\ f_{32} \\ f_{33} \end{pmatrix} \tag{B.52}$$

We will identify this equation with the matrix notation:

$$\dot{\Psi}(t) = L\Psi(t) + \Lambda + F(t) \tag{B.53}$$

Where the $\Psi(t)$ vector is related to the $S_{ij}(t)$ operators, L is the matrix containing the coefficients of the linear differential equations, Λ is a vector which results from the elimination of $S_{11}(t)$ in the equations, and $F(t)$ is a vector containing the noise operators.

B.4 Relevant two-time correlation function for the spectra calculation

Inserting (B.29) into (B.27), and replacing the $\sigma_{ij}(t)$ by the slow varying operator S_{ij} we obtain:

$$\begin{aligned} S(\omega) \propto \mu_{13}\mu_{31} \lim_{T\to\infty} \frac{1}{T} \int_0^T dt \int_0^T dt' \langle S_{31}(t) S_{13}(t') \rangle e^{-i(\omega-\omega_{12})(t-t')} \\ + \mu_{21}\mu_{13} \lim_{T\to\infty} \frac{1}{T} \int_0^T dt \int_0^T dt' \langle S_{21}(t) S_{13}(t') \rangle e^{i(\omega_{12}-\omega_{13})t} e^{-i(\omega-\omega_{13})(t-t')} \\ + \mu_{31}\mu_{12} \lim_{T\to\infty} \frac{1}{T} \int_0^T dt \int_0^T dt' \langle S_{31}(t) S_{12}(t') \rangle e^{i(\omega_{13}-\omega_{12})t} e^{-i(\omega-\omega_{12})(t-t')} \\ + \mu_{21}\mu_{12} \lim_{T\to\infty} \frac{1}{T} \int_0^T dt \int_0^T dt' \langle S_{21}(t) S_{12}(t') \rangle e^{-i(\omega-\omega_{12})(t-t')} \end{aligned} \tag{B.54}$$

We are interested in the solution of (B.54) in the stationary regime which means that the two-time-correlation functions involved depend only on the time difference $t - t'$. Therefore, the second and third term in (B.54) are null[52] because of the oscillating factor $e^{+i(\omega_{13}-\omega_{12})t}$ (or

[52] If we had taken in account the polarization of the transition , these terms would be trivially null because of the scalar product between the two dipole moments μ_{21} and μ_{13}.

it's c.c.). Next, we see that the first term and the last term correspond to two different set of emission lines, one centered at the frequency ω_{13} and the other at ω_{12}. In other words, the first term is the resonant fluorescence, and the last term is the emission from level 2 detected in our experiments. We will focus on the calculation of this last term:

$$S_{exp}(\omega) \propto \lim_{T\to\infty} \frac{1}{T} \int_0^T dt \int_0^T dt' \langle S_{21}(t) S_{12}(t') \rangle e^{-i(\omega-\omega_{12})(t-t')}$$

$$= \lim_{T\to\infty} \frac{1}{T} \int_0^T dt \int_{t-T}^t d\tau \langle S_{21}(\tau) S_{12}(0) \rangle e^{-i(\omega-\omega_{12})\tau}$$

$$= \lim_{T\to\infty} \frac{1}{T} \int_0^T dt \left(\int_0^t d\tau \langle S_{21}(\tau) S_{12}(0) \rangle e^{-i(\omega-\omega_{12})\tau} + \int_0^{T-t} d\tau \langle S_{21}(0) S_{12}(\tau) \rangle e^{i(\omega-\omega_{12})\tau} \right) \quad \text{(B.55)}$$

The correlation function $\langle S_{21}(0) S_{12}(\tau) \rangle$ is not null only on a finite correlation time T_{cor}. When t is greater than T_{cor}, the integral over τ which we note $F(t)$ is constant ($F(\infty)$). So, in order to get rid of the integral over t, we can decompose the integral:

$$S_{exp}(\omega) \propto \lim_{T\to\infty} \frac{1}{T} \int_{T_{corr}}^{T-T_{corr}} dt (F(\infty) + F^*(\infty))$$

$$+ \lim_{T\to\infty} \frac{1}{T} \left(\int_0^{T_{cor}} dt + \int_{T-T_{cor}}^T dt \right) (F(t) + F^*(T-t)) \quad \text{(B.56)}$$

Since the physical quantity $F(t)$ can be majored, the second limit in (B.56) tends to zero and the first limit tends toward $F(\infty) + F^*(\infty)$. Finally:

$$S_{exp}(\omega) \propto \int_0^\infty d\tau \langle S_{21}(\tau) S_{12}(0) \rangle e^{-i(\omega-\omega_{12})\tau} + c.c. \quad \text{(B.57)}$$

We introduce the Laplace transform of the two-time-correlation of the Ψ operators (using the notations introduced Eqn. B.53):

$$\Phi_{ij}(p) = \int_0^\infty e^{-p\tau} \langle \Psi_i(\tau) \Psi_j(0) \rangle \quad \text{(B.58)}$$

We see that B.57 is nothing else but the Laplace transform: $(\Phi_{13}(p))_{p=i(\omega-\omega_{12})}$.

B.5 Quantum Regression Theorem

The quantum regression theorem is an equation which gives the evolution of the two-time correlation function of atomic operators as a function of the expectation value of the system operator correlation function. Beyond this impressive name, there is a theorem which is easy to demonstrate. If we consider the operators $\{\Psi_i\}$, a time $\tau > 0$ and use Eqn. B.53:

$$\frac{d}{d\tau} \langle \Psi_i(\tau) \Psi_j(0) \rangle = \langle [L\Psi(\tau) + \Lambda]_i \Psi_j(0) \rangle + \langle F_i(\tau) \Psi_j(0) \rangle \quad \text{(B.59)}$$

The atomic operator $\Psi_j(0)$ cannot know about the future noise $F_i(\tau)$, so expectation value $\langle F_i(\tau) \Psi_j(0) \rangle$ vanishes. All is left is:

$$\frac{d}{d\tau} \langle \Psi_i(\tau) \Psi_j(0) \rangle = \langle [L\Psi(\tau) + \Lambda]_i \Psi_j(0) \rangle \quad \text{(B.60)}$$

B.6 Spectra in the Λ configuration

As we have seen Eqn. B.57, the spectra can be derived from the Laplace transform $\Phi_{31}(p)$. This quantity can be calculated if we take the Laplace transform of (B.60) for $j = 3$ and $i \in [1; 8]$ which is:

$$p\left(\Phi_{i1} - \langle\Psi_i(0)\Psi_1(0)\rangle\right) = \sum_{k=1}^{8} L_{ik}\Phi_k 1 + \frac{[\Lambda]_i}{p}\langle\Psi_1(0)\rangle \tag{B.61}$$

We can rewrite the equations (B.61) in a Matrix form. We introduce the column vector φ:

$$\varphi = \begin{pmatrix} \Phi_{11} \\ \Phi_{21} \\ \Phi_{31} \\ \Phi_{41} \\ \Phi_{51} \\ \Phi_{61} \\ \Phi_{71} \\ \Phi_{81} \end{pmatrix}$$

Then, using (B.52), and the $8 * 8$ identity matrix I_8; (B.61) are equivalent to:

$$(pI_8 - L)\varphi = \begin{pmatrix} \langle\Psi_1(0)\Psi_1(0)\rangle \\ \langle\Psi_2(0)\Psi_1(0)\rangle + i\frac{\Omega}{p}\langle\Psi_1(0)\rangle \\ \langle\Psi_3(0)\Psi_1(0)\rangle \\ \langle\Psi_4(0)\Psi_1(0)\rangle + \frac{g}{p}\langle\Psi_1(0)\rangle \\ \langle\Psi_5(0)\Psi_1(0)\rangle \\ \langle\Psi_6(0)\Psi_1(0)\rangle + i\frac{\Omega}{p}\langle\Psi_1(0)\rangle \\ \langle\Psi_7(0)\Psi_1(0)\rangle \\ \langle\Psi_8(0)\Psi_1(0)\rangle + \frac{g}{p}\langle\Psi_1(0)\rangle \end{pmatrix} \tag{B.62}$$

The expectation values $\langle\Psi_i(0)\Psi_1(0)\rangle$ and $\langle\Psi_1(0)\rangle$ can be calculated using the definition of the Ψ_i given in (B.53) and using the results of the sub-section B.1. We find that the only term which is not null is:

$$\begin{aligned} \langle\Psi_3(0)\Psi_1(0)\rangle &= \langle S_{21}(0)S_{12}(0)\rangle && \text{(B.63)} \\ &= \langle\sigma_{21}(0)\sigma_{12}(0)\rangle && \text{(B.64)} \\ &= \rho_{22} && \text{(B.65)} \\ &= \frac{g}{g+\Gamma}\left(1 - \frac{\Gamma(g+R)}{2\Gamma g + 2\Gamma R + \Gamma^2 + Rg}\right) && \text{(B.66)} \end{aligned}$$

Using Cramers'rule, we find:

$$\Phi_{31}(p) = \frac{(p + \gamma_{23} + i\delta)\rho_{22}}{\left(p + \gamma_{23} + i\delta + \frac{\Omega^2}{p+\gamma_{12}}\right)(p + \gamma_{12})} \tag{B.67}$$

and the spectrum $S_{exp}(\omega) \propto \Re e\left\{(\Phi_{31}(p))_{p=i(\omega-\omega_{12})}\right\}$ is given by:

$$S_{exp}(\omega) \propto \Re e\left\{\frac{(i(\omega-\omega_{12})+\gamma_{23}+i\delta)\rho_{22}}{\left(i(\omega-\omega_{12})+\gamma_{23}+i\delta+\frac{\Omega^2}{i(\omega-\omega_{12})+\gamma_{12}}\right)(i(\omega-\omega_{12})+\gamma_{12})}\right\} \tag{B.68}$$

B.7 Spectra calculation in the Ξ configuration

We will give the main steps and results for the Ξ configuration. The notations are the same as in the previous section, so is the index ordering to define the matrix form of the equations, and the calculation procedure[53]. But to reproduce more faithfully the experiments[54], we include incoherent population transfer towards a fourth level. This level corresponds to the other excitonic level to which the biexciton can decay[55]. This means we add a ninth component to the Ψ vector ($\Psi_9 \equiv \sigma_{44}(t) \equiv S_{44}(t)$), to Λ, to $F(t)$ and a dimention to the square matrix L. We call Γ' the relaxation rate of the decays $3 \to 2$ and $3 \to 4$, Γ the relaxation rate of the decays $2 \to 1$ and $4 \to 1$, and $\delta = \omega_{23} - \omega_L$ (levels shown Fig. B.1). We reduce the problem to:

$$\dot{\Psi}(t) = L\Psi(t) + \Lambda + F(t) \tag{B.69}$$

With the L matrix given by:

$$\begin{pmatrix}
-\gamma_{12} & i\Omega & 0 & 0 & 0 & 0 & 0 & 0 & 0 \\
i\Omega & -(\gamma_{13}+i\delta) & 0 & 0 & 0 & 0 & 0 & 0 & 0 \\
0 & 0 & -\gamma_{12} & 0 & 0 & -i\Omega & 0 & 0 & 0 \\
0 & 0 & 0 & -(\Gamma+2g) & i\Omega & 0 & -i\Omega & \Gamma'-g & -g \\
0 & 0 & 0 & i\Omega & -(\gamma_{23}+i\delta) & 0 & 0 & -i\Omega & 0 \\
0 & 0 & -i\Omega & 0 & 0 & -(\gamma_{13}-i\delta) & 0 & 0 & 0 \\
0 & 0 & 0 & -i\Omega & 0 & 0 & -(\gamma_{23}-i\delta) & i\Omega & 0 \\
0 & 0 & 0 & g & -i\Omega & 0 & i\Omega & -2\Gamma' & g \\
0 & 0 & 0 & -g & 0 & 0 & 0 & \Gamma'-g & -2g
\end{pmatrix}$$

And the Λ vector given by:

$$\Lambda = \begin{pmatrix} 0 \\ 0 \\ 0 \\ g \\ 0 \\ 0 \\ 0 \\ 0 \\ g \end{pmatrix} \tag{B.70}$$

[53] We eliminate the variable S_{11} like we did for (B.43-B.50).

[54] In particular, the drop of PL signal as the Rabi frequency Ω is increased.

[55] The polarisations $\{\sigma_{4i}, h.c.\}_i$ linked to level 4 could be added but it would not change the calculated spectra emitted by the dipole D_{12}. Of course, this is not the case for the other transitions.

The spectra is given by the Laplace transform $\Phi_{31}(p)$ which is an unknown in the following linear system of equations:

$$(pI_9 - L)\begin{pmatrix} \Phi_{11} \\ \Phi_{21} \\ \Phi_{31} \\ \Phi_{41} \\ \Phi_{51} \\ \Phi_{61} \\ \Phi_{71} \\ \Phi_{81} \\ \Phi_{91} \end{pmatrix} = \begin{pmatrix} \langle\Psi_1(0)\Psi_1(0)\rangle \\ \langle\Psi_2(0)\Psi_1(0)\rangle \\ \langle\Psi_3(0)\Psi_1(0)\rangle \\ \langle\Psi_4(0)\Psi_1(0)\rangle + \frac{g}{p}\langle\Psi_1(0)\rangle \\ \langle\Psi_5(0)\Psi_1(0)\rangle \\ \langle\Psi_6(0)\Psi_1(0)\rangle \\ \langle\Psi_7(0)\Psi_1(0)\rangle \\ \langle\Psi_8(0)\Psi_1(0)\rangle \\ \langle\Psi_9(0)\Psi_1(0)\rangle + \frac{g}{p}\langle\Psi_1(0)\rangle \end{pmatrix} \tag{B.71}$$

We calculate the expectation values in the inhomogeneous vector of (B.71) and find out:

$$\begin{pmatrix} \langle\Psi_1(0)\Psi_1(0)\rangle \\ \langle\Psi_2(0)\Psi_1(0)\rangle \\ \langle\Psi_3(0)\Psi_1(0)\rangle \\ \langle\Psi_4(0)\Psi_1(0)\rangle + \frac{g}{p}\langle\Psi_1(0)\rangle \\ \langle\Psi_5(0)\Psi_1(0)\rangle \\ \langle\Psi_6(0)\Psi_1(0)\rangle \\ \langle\Psi_7(0)\Psi_1(0)\rangle \\ \langle\Psi_8(0)\Psi_1(0)\rangle \\ \langle\Psi_9(0)\Psi_1(0)\rangle + \frac{g}{p}\langle\Psi_1(0)\rangle \end{pmatrix} = \begin{pmatrix} 0 \\ 0 \\ (\rho_{22})_{stat}(0) \\ 0 \\ 0 \\ (\rho_{23})_{stat}(0) \\ 0 \\ 0 \\ 0 \end{pmatrix} \tag{B.72}$$

Finally, using Cramer's rule we find:

$$S_{exp}(\omega) \propto \Re e\left\{\frac{(i(\omega-\omega_{12})-i\delta+\gamma_{13})(\rho_{22})_{stat}(0)+i\Omega(\rho_{23})_{stat}(0)}{(i(\omega-\omega_{12})+\gamma_{12})(i(\omega-\omega_1 2)-i\delta+\gamma_{13})+\Omega^2}\right\} \tag{B.73}$$

with:

$$(\rho_{22})_{stat}(0) = \frac{(2\Gamma'+R-\frac{2g\Gamma'}{2g+\Gamma})(\frac{g}{g+\Gamma'})}{g+R+\frac{g\Gamma}{2g+\Gamma}+\frac{\Gamma+g}{\Gamma'+g}(2\Gamma'+R-\frac{2g\Gamma'}{2g+\Gamma})} \tag{B.74}$$

$$(\rho_{23})_{stat}(0) = \frac{i\Omega}{\gamma_{23}+i\delta}\left(\frac{g}{g+\Gamma'}-\frac{2g+\Gamma+\Gamma'}{g+\Gamma'}(\rho_{22})_{stat}\right) \tag{B.75}$$

$$R = \frac{(2\Omega)^2}{2}\frac{\gamma_{23}}{\gamma_{23}^2+(\omega_{23}-\omega_L)^2} \tag{B.76}$$

This equation has been used to model the experimental data in Fig. 5.4.

B.8 General Remarks

The aim here is to generalise the calculations to the case of resonant fluorescence and to explicit a numerical handling. As shown in the sub-section B.4, the spectrum is the sum of the spectra of each dipole provided the fact that these dipole have different transition frequencies. Each dipole

emission can be calculated seperatly using the method described above. For each dipole σ_{ij} of a three level system, we arrive at a matrix formulation of the problem of the type:

$$(pI_8 - L)\varphi = \chi + \frac{\Lambda}{p}\langle\sigma_{ji}(t=0)\rangle \tag{B.77}$$

In fact this problem can also be solved using the inverse of the matrix $(pI_8 - L)$:

$$\varphi = (pI_8 - L)^{-1}\left(\chi + \frac{\Lambda}{p}\langle\sigma_{ji}(t=0)\rangle\right) \tag{B.78}$$

The problem in (B.78) is that if $\langle\sigma_{ji}(t=0)\rangle \neq 0$, it diverges for $p = 0$. In the previous spectra calculation, we were not bothered by this term, since the relevent dipole always satisfied $\langle\sigma_{ji}(t=0)\rangle \neq 0$. This is because there was no resonant laser driving it, so the dipole mean value would tend to zero in the stationnary regime, and the spectrum would be given by the dipole fluctuation around zero. However, if detection is resonant with the laser, the atomic dipole is in a forced oscillation regime at the frequency of the laser. Since the coherence time of the laser is infinite (c.f. (B.1)), this results in a Dirac delta function in the spectra. This elastic scattering know as the Rayleigh peak would be the only componant of the spectra if we considered a purely Hamiltonian evolution where energy is conserved. The coherent Rayleigh scattering can be removed, an expression easy for computation can be derived:

$$\begin{aligned}
\varphi^{inc} &= (pI_8 - L)^{-1}\left(\chi + \frac{\Lambda}{p}\langle\sigma_{ji}(t=0)\rangle\right) - \frac{1}{p}\lim_{p\to 0} p((pI_8 - L)^{-1})\frac{\Lambda}{p}\langle\sigma_{ji}(t=0) && \text{(B.79)}\\
&= (pI_8 - L)^{-1}\chi + \left((pI_8 - L)^{-1} + L^{-1}\right)\frac{\Lambda}{p}\langle\sigma_{ji}(t=0)\rangle && \text{(B.80)}\\
&= (pI_8 - L)^{-1}\chi + (pI_8 - L)^{-1}L^{-1}\Lambda\langle\sigma_{ji}(t=0)\rangle && \text{(B.81)}
\end{aligned}$$

For the last step, we have used the fact that the matrix $(pI_8 - L)^{-1}$ and L^{-1} commute. Equation B.81 can be used to compute the incoherent emission of a dipole excited (or not) by a resonant laser.

B.9 Autler-Townes PL in the limit of a slow spectral diffusion

An interesting application to this calculation is to consider the case of a quantum dot subject to a slow spectral diffusion. This situation arises because of charge fluctuations in the quantum dot neighborhood which Stark shift the transition. The energy shift Σ depends on the level considered.

We suppose that for a given charged environment, the energy shift of the ground state is zero, while the excitonic levels are shifted by Σ and the biexciton by 2Σ (which is fairly realistic in this system [105]). We assume that the correlation time τ_c is greater than the radiative lifetime of the levels but short compared to the integration time of the detector, and that the energy shift follows a poissonian distribution characterized by $\Sigma_0 = 60\mu eV$. Under these assumptions, the PL spectra can be calculated considering the sum over the different configurations. The result for various Rabi is presented in Fig. B.2. We see a variation of the linewidth within the Autler-Townes splitting, which depends on the configuration of the detection (Ξ or Λ). This effect can easily be understood physically. We assume a zero detuning (when $\Sigma = 0$!) to facilitate the discussion. In the Λ configuration for instance (lower panel of Fig. B.2), the control laser admixes the states 3 and 1. The two levels 3 and 2 jitter (on the detection time scale). This

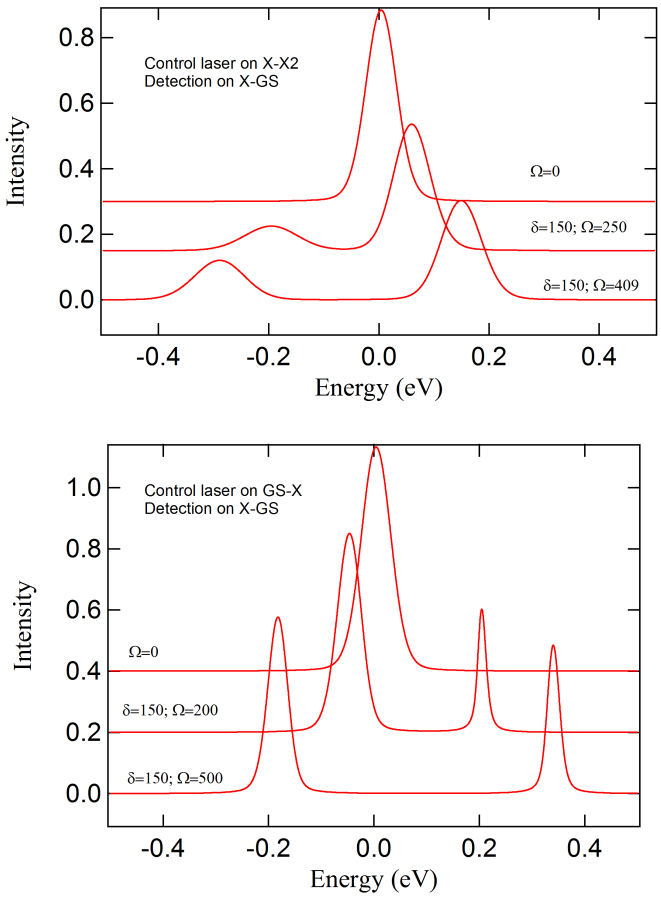

Figure B.2: Autler-Townes PL for a 4 level system analogue to a neutral quantum dot where the excitonic states are split by anisotropic exchange. Spectral diffusion with $\tau_c >> \Gamma$ is considered.

jitter is time-correlated for the two-levels. The states dressed by the laser jitter twice as less. Then, recombination from level 2 to the dressed state is less broadened. Considering a detuning $\delta \neq 0$, this effect leads to a difference of linewidth between the two PL lines: recombination from level 2 towards the dressed state which is more excitonic character has a smaller linewidth.

This effect has not been observed experimentally. In fact, presently, we do not know what is the lineshape of our quantum dots (Lorentzian or Gaussian).

Bibliography

[1] K.C. Nowack, F. H. L. Koppens, Yu. V. Nazarov, et L. M. K. Vandersypen, "*Coherent Control of a Single Electron Spin with Electric Fields*", *Science* (2007), vol. **318**, p. 1730.

[2] F. H. L. Koppens, C. Buizert, K. J. Tielrooij, I. T. Vink, K. C. Nowack, T. Meunier, L. P. Kouwenhoven, et L. M. K. Vanderypen, "*Driven coherent oscillations of a single electron spin in a quantum dot*", *Nat.* (2006), vol. **766**, p. 766.

[3] Brian D. Gerardot, Daniel Brunner, Paul A. Dalgarno, Patrick Ohberg, Stefan Seidl, Martin Kroner, Khaled Karrai, G. Stoltz, Nick, M. Petroff, Pierre, et Richard J. Warburton, "*Optical pumping of a single hole spin in a quantum dot*", *Nature* (2008), vol. **451**, p. 441.

[4] Mete Atatüre, Jan Dreiser, Antonio Badolato, et Atac Immamoglu, "*Observation of Faraday rotation from a single confined spin*", *Nat. Phys.* (2007), vol. **3**, p. 101.

[5] M. H. Mikkelsen, J. Berezovsky, N. G. Stoltz, L. A. Coldren, et D. D. Awschalom, "*Optically detected coherent spin dynamics of a single electron in a quantum dot*", *Nat. Phys.* (2007), vol. **3**, p. 770.

[6] Kristiaan De Greve, Peter L. McMahon, David Press, Thaddeus D. Ladd, Dirk Bisping, Christian Scheider, Martin Kamp, Lukas Worschech, Sven Höfling, Alfred Forchel, et Yoshihisa Yamamoto, "*Ultrafast coherent control and suppressed nuclear feedback of a single quantum dot hole qubit*", *Nat. Phys.* (2011, DOI10.1038/nphys2078).

[7] D. Press, Kristiaan De Greve, Peter L. McMahon, Thaddeus D. Ladd, Benedikt Friess, Christian Schneider, Martin Kamp, Sven Höfling, Alfred Forchel, et Yoshihisa Yamamoto, "*Ultrafast optical spin echo in a single quantum dot*", *Nat. Phot.* (2010), vol. **4**, p. 367.

[8] D. Scalbert, J. Cernogora, et C. Benoit a la Guillaume, "*Spin-Lattice Relaxation in Paramagnetic CdMnTe*", *Sol. Stat Comm.* (1988), vol. **66**, no. 6, p. 571.

[9] T. Dietl, P. Peyla, W. Grieshaber, et Y. Merle d'Aubigné, "*Dynamics of Spin Organization in Diluted Magnetic Semiconductors*", *Phys. Rev. Lett.* (1995), vol. **74**, no. 3, p. 474.

[10] Lucio Robledo, Liliane Childress, Hannes Bernier, Bas Hensen, Paul F.A. Alkemade, et Ronald Hanson, "*High-fidelity projective read-out of a solid-state quantum register*", *Nature* (2011), vol. **477**, p. 574.

[11] D. E. Reiter, T Kuhn, V. M. Axt, et P. Machnikowski, "*Dynamics of a single Mn spin in a quantum dot: the role of magnetic fields in Faraday and Voigt geometry.*", *Journal of Physics, Conf. Series* (2009), vol. **193**, p. 012101.

[12] Y. Léger, L. Besombes, L. Maingault, et H. Mariette, "*Valence-band mixing in neutral, charged, and Mn-doped self-assembled quantum dots*", *Phys. Rev. B* (2007), vol. **76**, p. 045331.

[13] O.A. Kane, "*Band structure of indium antimonide*", *J. Phys. Chem. Solids* (1957), vol. **1**, no. 4, pp. 249–261.

[14] Soline Richard, *Modelisation physique de la structure électronique, du transport et de l'ionisation par choc dans les materiaux IV-IV massifs, contraints et dans les puits quantiques.* PhD thesis, 2004.

[15] J. M. Luttinger, "*Quantum Theory of Cyclotron Resonance in Semiconductors: General Theory*", *Phys. Rev.* (1956), vol. **102**, no. 4, p. 1030.

[16] G.L. Bir et G.E. Pikus, *Symmetry and stained-induced effects in semi-conductors.* John Wilhey & sons, new york ed., 1974.

[17] J. Allègre, B. Gil, J. Calatatud, et H. Mathieu, "*Deformation potentials of CdTe epilayers from piezo and wavelength modulation reflectivity spectra analysis*", *J. Crys. Growth* (1990), vol. **101**, p. 603.

[18] Guy Fishman, *Semi-conducteurs: les bases de la théorie k.p.* Les Editions de l'Ecole Polytechnique, Avril 2010.

[19] J. M. Luttinger et W. Kohn, "*Motion of Electrons and Holes in Perturbed Periodic Fields*", *Phys. Rev.* (1955), vol. **97**, no. 4, p. 869.

[20] J-L Basdevant et J Dalibard, *Mécanique Quantique*, ch. 2, p. 80. Les éditions de l'école Polytechnique, 2002.

[21] Ivan Favero, *Décohérence, Symmétries et Relaxatation de spin dans les boîtes quantiques de semiconducteur*, ch. 4, p. 130. PhD Thesis, Université Pierre et Marie Curie, Paris VI, 2005.

[22] W. Wardzynski et M. Suffczynski, "*Dependence of the exchange splitting in excitons on the interatomic distance*", *Sol. State Com.* (1972), vol. **10**, p. 417.

[23] J.C. Merle, R. Sooryakumar, et M. Cardona, "*Resonant Brillouin Scattering in Cadmium-Telluride*", *Phys. Rev. B.* (1984), vol. **30**, p. 3261.

[24] Gabriel Bester et Alex Zunger, "*Cylindrically shaped zinc-blende semiconductor quantum dots do not have cylindrical symmetry: Atomistic symmetry, atomic relaxation, and piezoelectric effects*", *Phys. Rev. B* (2005), vol. **71** , p. 045318.

[25] Gabriel Bester, Selvakumar Nair, et Alex Zunger, "*Pseudo-potential calculation of the excitonic fine structure of a million-atom self-assembled $In_{1-x}Ga_xAs/GaAs$ quantum dots*", *Phys. Rev. B* (2003), vol. **67**, p. 161306.

[26] T. Takagahara, "*Theory of exciton doublet structures and polarisation relaxation in single quantum dots*", *Phys. Rev. B* (2000), vol. **62**, no. 24, p. 16840.

[27] Y. Léger, *Détection de spin individuels dans les boîtes quantiques magnétiques.* Université Joseph Fourier, Grenoble 1: PhD thesis, 2007.

[28] F. Patella, S. Nufris, F. Arciprete, Fanfoni M., Placidi E., A. Sgarlata, et A. Balzarotti, "*Tracing the two- to three-dimensional transition inthe InAs/GaAs(001) heteroepitaxial growth*", *Phys. Rev. B* (2003), vol. **67**, p. 205308.

[29] F. Tinjod, B. Gilles, S. Moehl, K. Kheng, et H. Mariette, "*II-VI quantum dot formation induced by surface energy change of a strained layer*", *Appl. Phys. Lett.* (2003), vol. **82**, p. 4340.

[30] A. Kudelski, A. Lemaître, A. Miard, Voisin P., T. C. M. Graham, R. J. Warburton, et O. Krebs, "*Optically Probing the Fine Structure of a Single Mn Atom in an InAs Quantum Dot*", *Phys. Rev. Lett.* (2007), vol. **99**, p. 247209.

[31] Y.R. Lee, A.K. Ramdas, et R.L. Aggarwal, "*Origin of the Mn^{2+} optical transition in Mn-based II-VI diluted magnetic semiconductors*", *Phys. Rev. B* (1986), vol. **33**, no. 10, p. 7383.

[32] A.V. Komaronv, S.M. Ryabchenko, O.V. Terletskii, I.I. Zheru, et R.D. Ivanchuk, *Sov. Phys. JETP* (1977), vol. **46**, p. 318.

[33] M. I. Dyakonov, *Spin physics in Semiconductors.* Springer, 2008.

[34] J.K. Furdyna, "*Diluted Magnetic Semiconductors*", *J. Appl. Phys.* (1988), vol. **64**, p. R29.

[35] J.R. Schrieffer et P. A. Wolff, "*Relation between the Anderson and Kondo Hamiltonians*", *Phys. Rev.* (1966), vol. **149**, no. 2, p. 491.

[36] Rémi Beaulac et Daniel R. Gamelin, "*Two-center formulation of Mn^{2+} electron s-d exchange coupling in bulk and quantum-confined diluted magnetic semiconductor*", *Phys. Rev. B* (2010), vol. **82**, p. 224401.

[37] I.A. Merkulov, D.R. Yakovlev, A. Keller, W. Ossau, J. Geurts, A. Waag, Landwehr G., G. Karczewski, T. Wojotowicz, et J. Kossut, "*Kinetic Exchange between the Conduction Band Electrons and Magnetic Ions in Quantum-Confined Structures*", *Phys. Rev. Lett.* (1999), vol. **83**, no. 7, p. 1431.

[38] A.K. Battacharjee, "*Magneto-Optics near the L point of the brillouin zone in semimagnetic semiconductors*", *Phys. Rev. B* (1990), vol. **41**, p. 5996.

[39] A. K. Bhattacharjee, "*Confinement-induced reduction of the effective exchange parameters in semimagnetic semiconductor nanostructures*", *Phys. Rev. B* (1998), vol. **58**, no. 23, p. 15660.

[40] Laurent Maingault, *Insertions d'ions magnétiques dans les boîtes quantiques de semiconducteur II-VI.* Université Joseph Fourier, Grenoble 1: PhD thesis, 2006.

[41] Gerald D. Mahan, *Many-particle Physics*, ch. 1.4, pp. 54–60. Plenum Press, New York, 1990.

[42] L. Besombes, Y. Leger, L. Maingault, D. Ferrand, et H. Mariette, "*Carrier-induced spin splitting of an individual magnetic atom embedded in a quantum dot*", *Phys. Rev. B* (2005), vol. **71**, p. 161307.

[43] J. Fernandez-Rossier, *Private Communication.*

[44] Laurent Maingault, L. Besombes, Y. Léger, C. Bougerol, et H. Mariette, "*Inserting one single Mn ion into a quantum dot*", *Appl. Phys. Lett.* (2006), vol. **89**, p. 193109.

[45] D. T. F. Marple, "*Refractive index of ZnSe, ZnTe and CdTe*", *J. of Appl. Phys.* (1964), vol. **35**, no. 3, p. 539.

[46] W. L. Barnes, G. Björk, J. M. Gérard, P. Jonsson, J. A. E. Wasey, P. T. Worthing, et V. Zwiller, "*Solid-state single photon sources: light collection strategies*", *Eur. Phys. J. D* (2002), vol. **18**, pp. 197–210.

[47] Alexander O. Govorov et Alexander V. Kalameitsev, "*Optical properties of a semiconductor quantum dot with a single magnetic impurity: photo-induced spin orientation*", *Phys. Rev. B* (2005), vol. **71**, p. 035338.

[48] M. M. Glazov, E. L. Ivchenko, L. Besombes, Y. Léger, L. Maingault, et H. Mariette, "*Fine structure of exciton excited levels in a quantum dot with a magnetic ion*", *Phys. Rev. B* (2007), vol. **75**, p. 205313.

[49] Mete Atatüre, Jan Dreiser, Antonio Badolato, Alexander Högele, Khaled Karrai, et Atac Immamoglu, "*Quantum-Dot Spin-State Preparation with Near-Unity Fidelity*", *Science* (2006), vol. **312**, no. 5773, p. 551.

[50] L. Besombes, K. Kheng, L. Marsal, et H. Mariette, "*Acoustic phonon broadening mechanism in single quantum dots*", *Phys. Rev. B* (2001), vol. **63**, p. 155307.

[51] L. Besombes, Y. Leger, J. Bernos, H. Boukari, H. Mariette, J.P. Poizat, T. Clement, J. Fernandez-Rossier, et R. Aguado, "*Optical Probing of Spin Fluctuations in a Single Paramagnetic Mn atom in a Semiconductor Quantum Dot*", *Phys. Rev. B* (2008), vol. **78**, p. 125324.

[52] M. Qazzaz, G. Yang, S.H. Xin, L. Montes, H. Luo, et J. K. Furdyna, "*Electron Paramagnetic Resonance of Mn^{2+} in Strained-Layer Semiconductir Superlattices*", *Sol. Stat. Comm.* (1995), vol. **96**, no. 6, p. 405.

[53] M. T. Causa, M. Tovar, S. B. Oseroff, R. Calvo, et W. Giriat, "*Spin-Lattice coefficients of Mn^{2+} in II-VI compounds*", *Phys. Lett.* (1980), vol. **A77**, no. 6, p. 473.

[54] C.M. Simon, *Contrôle Optique de l'exciton dans des boîtes individuelles.*, ch. 3, p. 106. PhD thesis, 2010.

[55] R. D. Greenough et S. B. Palmer, "*The elastic constants and thermal expansion of single-crystal CdTe*", *J. Phys. D: Appl. Phys.* (1973), vol. **6**, no. 53, p. 587.

[56] R. C. Myers, M. H. Mikkelsen, J.-M. Tang, A. C. Gossard, Flatté M. E., et D.D. Awschalom, "*Zero field optical manipulation of magnetic ions in semiconductors*", *Nat. Mat.* (2008), vol. **7**, p. 203.

[57] M. Scheibner, T. A. Kennedy, L. Worschech, A. Forchel, G. Bacher, T. Slobodskyy, G. Schmidt, et L. W. Molenkamp, "*Coherent dynamics of locally interacting spins in self-assembled $Cd_{1-x}Mn_xSe/ZnSe$ quantum dots*", *Phys. Rev. B* (2006), vol. **73**, p. 081308.

[58] Y. Léger, L. Besombes, L. Maingault, D. Ferrand, et H. Mariette, "*Geometrical Effects on the Optical Properties of a Quantum Dot Doped with a Single Magnetic Atom*", *Phys. Rev. Lett.* (2005), vol. **95**, p. 047403.

[59] I. Favero, G. Cassabois, C. Voisin, C. Delalande, Ph. Roussignol, R. Ferreira, C. Couteau, J.P. Poizat, et J.M. Gérard, "*Fast exciton spin relaxation in single quantum dots*", *Phys. Rev. B* (2005), vol. **71**, p. 233304.

[60] T. Müller, T. Moldaschl, W. Parz, S. Golka, G. Strasser, et K. Unterrainer, "*Femtosecond Spectral Hole Burning Spectroscopy as a Probe for Exciton Spin Dynamics in Quantum Dots*", *Acta Phys. Pol. A* (2008), vol. **113**, p. 777.

[61] Yu-Huai Liao, Juan I. Climente, et Shun-Jen Cheng, "*Dominant channels of exciton spin relaxation in photo-excited self-assembled (In,Ga)As quantum dots*", *Phys. Rev. B* (2011), vol. **83**, p. 165317.

[62] K. Kowalik, O. Krebs, A. Lemaitre, J. A. Gaj, et P. Voisin, "*Optical alignment and polarization conservation of the neutral-exciton spin in individual InAs/GaAs quantum dots*", *Phys. Rev. B* (2008), vol. **77**, p. 161305.

[63] L. M. Woods, T. L. Reinecke, et Y. Lyanda-Geller, "*Spin relaxation in quantum dots*", *Phys. Rev. B* (2002), vol. **66**, p. 161318.

[64] E. Tsitsishvili, R. V. Baltz, et H. Kalt, "*Exciton spin relaxation in single semiconductor quantum dots*", *Phys. Rev. B* (2003), vol. **67**, p. 205330.

[65] Anna Grodecka, Lucjan Jacak, Paul Machnikowski, et Katarzyna Roszak, "*Phonon impact on the coherent control of quantum states in semiconductor quantum dots*", *arXiv* (2004), vol. **0404364**, no. v1.

[66] K. Roszak, V. M. Axt, T. Kuhn, et P. Machnikowski, "*Exciton spin decay in quantum dots to bright and dark states*", *Phys. Rev. B* (2007), vol. **76**, p. 195324.

[67] N. Vagelatos, D. Wehe, et J.S. King, "*Phonon dispersion and phonon densities of states for ZnS and ZnTe*", *J. Chem. Phys.* (1975), vol. **60**, p. 3613.

[68] C. Le Gall, R. S. Kolodka, C. L. Cao, H. Boukari, H. Mariette, J. Fernandez-Rossier, et L. Besombes, "*Optical initialization, readout, and dynamics of a Mn spin in a quantum dot*", *Phys. Rev. B* (2010), vol. **81**, p. 245315.

[69] Lukasz Cywinsky, "*Optical Orientation of a single Mn spin in a quantum dot: Role of carrier spin relaxation*", *Phys. rev. B* (2010), vol. **82**, p. 075321.

[70] M. Goryca, P. Plochocka, W. Kazimierczuk, Wojnar, G. Karczewski, J. A. Gaj, M. Potemski, et P. Kossacki, "*Brightening of dark excitons in a single CdTe quantum dot containing a single Mn^{2+} impurity.*", *Phys. Rev. B* (2010), vol. **82**, p. 165323.

[71] S. H. Autler et C. H. Townes, "*Stark Effect in Rapidly Varying Fields*", *Phys. Rev.* (1955), vol. **100**, p. 103.

[72] H. Kamada, H. Gotoh, J. Temmyo, T. Takagahara, et H. Ando, "*Exciton Rabi Oscillations in a Single Quantum Dot*", *Phys. Rev. Lett.* (2001), vol. **87**, no. 24, p. 246401.

[73] Xiaodong Xu, Bo Sun, Paul R. Berman, Duncan G. Steel, Allan S. Bracker, Dan Gammon, et L. J. Sham, "*Coherent Spectroscopy of a Strongly Driven Quantum Dot*", *Science* (2007), vol. **317**, p. 929.

[74] Xiadong Xu, Bo Sun, Erik D. Kim, Katherine Smirl, P. R. Berman, D. G. Steel, A. S. Bracker, D. Gammon, et L. J. Sham, "*Single Charged Quantum Dot in a Strong Optical Field: Absorption, Gain and the ac-Strark Effect*", *Phys. Rev. Lett.* (2007), vol. **101**, p. 227407.

[75] M. Kroner, C. Lux, S. Seidl, A.W. Holleitner, K. Karrai, A. Badolato, P.M. Petrofff, et R. J. Warburton, "*Rabi splitting and ac-Stark shift of a charged exciton*", *Appl. Phys. Lett.* (2008), vol. **92**, p. 031108.

[76] Gregor Jundt, Lucio Robledo, Alexander Högele, Stefan Fält, et Atac Immamoglu, "*Observation of Dressed Excitonic States in a Single Quantum Dot*", *Phys. Rev. Lett.* (2008), vol. **100**, p. 177401.

[77] A. Berthelot, I. Favero, G. Cassabois, C. Voisin, C. Delalande, Ph. Roussignol, R. Ferreira, et J. M. Gérard, "*Unconventional motional narrowing in a semiconductor quantum dot*", *Nature Physics* (2006), vol. **2**, p. 759.

[78] David Press, Thaddeus D. Ladd, Bingyang Zhang, et Yoshihisa Yamamoto, "*Complete quantum control of a single quantum dot spin using ultrafast optical pulses*", *Nature* (2008), vol. **456**, p. 218.

[79] M. E. Ware, E.A Stinaff, D. Gammon, M. F. Doty, A. S. Bracker, D. Gershoni, V. L. Korenev, S. C. Badescu, Y. Lyanda-Geller, et T. L. Reinecke, "*Polarized Fine structure in the Photoluminescence Excitation Spectrum of a Negatively Charged Quantum Dot*", *Phys. Rev. Lett.* (2005), vol. **95**, p. 177403.

[80] B. Urbaszek, R. J. Warburton, K. Karrai, B. D. Gerardot, P. M. Petroff, et J. M. Garcia, "*Fine structure of Highly Charged Excitons in Semiconductor Quantum Dots*", *Phys. Rev. Lett.* (2003), vol. **90**, no. 24, p. 247403.

[81] O. Cortez, S. ans Krebs, S. Laurent, M. Senes, X. Marie, P. Voisin, R. Ferreira, G. Bastard, Gerard J-M., et T. Amand, "*Optically Driven Spin Memory in n-doped InAs-GaAs Quantum Dots*", *Phys. Rev. Lett.* (2002), vol. **89**, no. 20, p. 207401.

[82] M. Bayer, G. Ortner, O. Stern, A. Kuther, A. A. Gorbunov, A. Forchel, P. Hawarylak, S. Fafard, K. Hinzer, T. L. Reinecke, Walck S. N., J. P. Reithmaier, Klopf F., et F. Schafer, "*Fine structure of neutral and charged excitons in self-assembled In(Ga)As/(Al)GaAs quantum dots*", *Phys. Rev. B* (2002), vol. **65**, p. 195315.

[83] I. A. Akimov, K. V. Kavokin, A. Hundt, et F. Henneberger, "*Electron-hole exchange interaction in a negatively charged quantum dot*", *Phys. Rev. B.* (2005), vol. **71**, p. 075326.

[84] Andrew Shabaev, Eric A. Stinaff, Allan S. Bracker, Daniel Gammon, Alexander L. Efros, Vladimir L. Korenev, et Igor Merkulov, "*Optical pumping and negative luminescence polarization in charged GaAs quantum dots*", *Phys. Rev. B* (2009), vol. **79**, p. 035322.

[85] P. Desfonds, B. Eble, F. Fras, C. Testelin, F. Bernardot, M. Chamarro, B. Urbaszek, T. Amand, X. Marie, J. M. Gérard, V. Thierry-Mieg, A. Miard, et A. Lemaître, "*Electron and hole spin cooling efficiency in InAs quantum dots: The role of nuclear field*", *Appl. Phys. Lett.* (2010), vol. **96**, p. 172108.

[86] E. A. Chekhovich, A. B. Krysa, M. S. Skolnick, et A. I. Tartakovskii, "*Direct Measurement of the Hole-Nuclear Spin Interaction in Single InP/GaInP Quantum Dots Using Photoluminescence Spectroscopy*", *Phys. Rev. Lett.* (2011), vol. **106**, p. 027402.

[87] A. Abragam, *Principles of Nuclear Magnetism.* Oxford University Press, 1961.

[88] American Institute of Physics, *American Institute of Physics Handbook.* McGraw-Hill, third edition ed., 1972.

[89] A. Nakamura, D. Paget, C. Hermann, C. Weisbuch, et G. Lampel, "*Optical Detection of Electron Spin Resonance in CdTe*", *Sol. State. Comm.* (1979), vol. **30**, p. 411.

[90] C. Testelin, B. Elbe, F. Bernardot, G. Karczewski, et M. Chamarro, "*Signature of the Overhauser field on the coherent spin dynamics of donor-bound electrons in a single CdTe quantum well*", *Phys. Rev. B* (2008), vol. **77**, p. 235306.

[91] D. Paget, G. Lampel, B. Sapoval, et V.I. Safarov, "*Low field elctron-nuclear spin coupling in gallium arsenide under optical pumping conditions*", *Phys. Rev. B* (1977), vol. **15**, no. 12, p. 5780.

[92] M. Gueron, "*Density of the conduction electrons at the nuclei in indium antimonide*", *Phys. Rev.* (1964), vol. **135**, no. 1A, p. 200.

[93] I.A. Merkulov, Al. L. Efros, et M. Rosen, "*Electron relaxation by nuclei in semiconductor quantum dots*", *Phys. Rev. B* (2002), vol. **65**, p. 205309.

[94] P.-F. Braun, X. Marie, L. Lombez, B. Urbaszek, P. Renucci, V.K. Kalevich, K.V. Kavokin, O. Krebs, P. Voisin, et Y. Masumoto, "*Direct observation of the electron spin relaxation induced by nuclei in quantum dots*", *Phys. Rev. Lett.* (2005), vol. **94**, p. 116601.

[95] Benoît Elbe, *Interaction hyperfine dans les boîtes quantiques d'InAs/GaAs sous pompage optique orienté.* Université Pierre et Marie Curie, Paris VI: PhD Thesis, 2006.

[96] T. Auer, R. Oulton, A. Bauschulte, D.R. Yakovlev, M. Bayer, S. Yu. Verbin, R. V. Cherbunin, D. Reuter, et A. D. Wieck, "*Measurement of the knight field and local nuclear dipole-dipole field in InGaAs/GaAs quantum dot ensemble*", *Phys. Rev. B* (2009), vol. **80**, p. 205303.

[97] M. Yu. Petrov, G. G. Kozlov, R. V. Ignatiev, I. V. Cherbunin, D. Yakovlev, et M. Bayer, "*Coupled electron-nuclear spin dynamics in quantum-dots: A graded box model approach*", *Phys. Rev. B* (2009), vol. **80**, p. 125318.

[98] P. Maletinsky, A. Badolato, et A. Immamoglu, "*Dynamics of Quantum Dot Nuclear Spin Polarization Controlled by a Single Electron.*", *Phys. Rev. Lett.* (2007), vol. **99**, p. 056804.

[99] I. A. Merkulov, G. Alvarez, D. R. Yakovlev, et T. C. Schulthess, "*Long-term dynamics of the electron-nuclear spin system of a semiconductor quantum dot*", *Phys. Rev. B* (2010), vol. **81**, p. 115107.

[100] D. H. Fend, I. A. Akimov, et F. Henneberger, "*Non-equilibrium Nuclear-Electron Spin Dynamics in Semiconductor Quantum Dots*", *Phys. Rev. Lett.* (2007), vol. **99**, p. 036604.

[101] D. Klauser, W. A. Coish, et D. Loss, "*Nuclear spin state narrowing via gate-controlled Rabi oscillations in a double quantum dot.*", *Phys. Rev. B* (2006), vol. **73**, p. 205302.

[102] Changxue Deng et Xuedong Hu, "*Nuclear spin diffusion in quantum dots, effects of inhomogeneous hyperfine interaction*", *Phys. Rev. B* (165333), vol. **72**, p. 165333.

[103] L. M. Narducci, M. O. Scully, G.-L. Oppo, P. Ru, et Tredicce J. R., "*Spontaneous emission and absorpion properties of a driven three-level system*", *Phys. Rev. A.* (1990), vol. **42**, no. 3, p. 1630.

[104] P. Meystre et M. Sargent, *Elements of Quantum Optics.* Springer, 4th ed., 2007.

[105] L. Besombes, K. Kheng, L. Marsal, et H. Mariette, "*Few-particle effects in single CdTe quantum dots*", *Phys. Rev. B* (2002), vol. **65**, p. 121314.

Résumé

Nous avons étudié les propriétés dynamiques d'un spin individuel dans une boite quantique de semiconducteur II-VI (spin d'un atome de Mn ou electron résident). Une boîte quantique comportant un atome de manganese présente six raies qui permettent de sonder optiquement l'état de spin du Manganese. Des expériences pompe-sonde réalisées sur boîte unique ont permit de montrer que le spin du Mn peut être orienté optiquement en quelques dizaines de ns, que le temps de vie T_1 de ce spin est supérieur à la μs, et que le pompage optique en champ nul est controlé par une anisotropie magnétique induite par les contraintes. Par ailleurs, dans le but d'identifier les mécanismes du pompage optique, nous avons mis en évidence des processus de relaxation de spin au sein du système exciton-manganese, durant la durée de vie de ce dernier. Enfin, nous avons réalisé un effet Stark optique sur chacune des raies d'une boîte quantique magnétique. Concernant la dynamique d'un électron dans une boîte quantique II-VI, nous avons mis en évidence le pompage du spin de l'électron résident ainsi que des noyaux.

Mots-clés: Boîte quantique, semiconducteur magnétique dilué, manganèse, spin individuel, pompage optique, effet Stark optique, champ Overhauser.

Abstract

We have studied the dynamic properties of a single spin (Mn impurity or resident electron) in a II-VI semiconductor quantum dot. A quantum dot doped with a single Mn atom presents six lines which allow to probe optically the spin-state of the Mn atom. Pump-probe experiments at a single dot level were carried out to demonstrate that the Mn spin could be oriented in a few tens of ns, and that the spin-distribution prepared by such means was perfectly conserved over a few μs. The optical pumping of the Mn spin at zero magnetic field is controlled by a strain-induced magnetic anisotropy. Furthermore, seeking for a microscopic mechanism controlling the optical pumping of the Mn atom, we have evidenced spin relaxation channels within the exciton-Mn complex. At last, we have demonstrated an optical Stark effect on any of the lines of a Mn-doped quantum dot. Concerning the dynamics of an electron in a II-VI quantum dot, we have evidenced optical pumping of the resident electron, and dynamic nuclear spin polarization.

Keywords: Quantum dot, diluted magnetic semiconductor, manganese, single spin, optical pumping, optical Stark effect, Overhauser field.